

University of Southampton Research Repository

Copyright © and Moral Rights for this thesis and, where applicable, any accompanying data are retained by the author and/or other copyright owners. A copy can be downloaded for personal non-commercial research or study, without prior permission or charge. This thesis and the accompanying data cannot be reproduced or quoted extensively from without first obtaining permission in writing from the copyright holder/s. The content of the thesis and accompanying research data (where applicable) must not be changed in any way or sold commercially in any format or medium without the formal permission of the copyright holder/s.

When referring to this thesis and any accompanying data, full bibliographic details must be given, e.g.

Thesis: Author (Year of Submission) "Full thesis title", University of Southampton, name of the University Faculty or School or Department, PhD Thesis, pagination.

Data: Author (Year) Title. URI [dataset]

UNIVERSITY OF SOUTHAMPTON

Faculty of Engineering and Physical Sciences
Department of Aeronautical and Astronautical Engineering

**Time-of-Flight Characterisation of
Alternative Propellants for Porous
Electrospray Thrusters**

by

Szymon Dworski

MEng

ORCID: 0000-0003-4787-9289

*A thesis for the degree of
Doctor of Philosophy*

March 2025

University of Southampton

Abstract

Faculty of Engineering and Physical Sciences

Department of Aeronautical and Astronautical Engineering

Doctor of Philosophy

Time-of-Flight Characterisation of Alternative Propellants for Porous Electro spray Thrusters

by Szymon Dworski

Electrospray propulsion is a type of small satellite propulsion which could have a significant impact on the space industry due to, among other reasons, its high specific impulses. High specific impulses are enabled by the evaporation of high charge-to-mass ratio ions from the surface of a liquid under the influence of a sufficiently strong electric field. This process of ion evaporation is called electro spray ionisation and is enabled by the use of room temperature molten salts, termed ionic liquids, typically comprised of a cation and anion. However, the fundamental physics of ion emission is not well understood, especially the factors determining the charge-to-mass ratios of these ions. A better understanding of the factors determining ion emission would allow for a more informed selection of these ionic liquids, therefore enable better electro spray thruster design. In order to investigate ion cluster emission, a single emitter porous electro spray thruster was tested with seven different ionic liquids. Three different instruments were used to characterise the thruster: a full plume current collector, a retarding potential analyser and a time-of-flight mass spectrometer. The last instrument contained a large current collector, a 'reflecting' gate and a flight length of 550 mm.

Eleven different emitters were tested with the seven ionic liquids in order to characterise a broad liquid property range. Three of the ionic liquids were called metal/metalloid ionic liquids, ionic liquids comprised of EMI^+ cations and anions comprised of a central metal/metalloid atom surrounded by halogens. These were: EMI-BF_4 , EMI-FeCl_4 and EMI-SbF_6 . The remaining four ionic liquids were comprised of ions which contained more than one charge, termed multiply-charged ionic liquids. These were: $(\text{EMI})_2\text{-Co(SCN)}_4$, $\text{C}_6(\text{mim})_2\text{-(Im)}_2$, $\text{C}_6(\text{mim})_2\text{-Co(SCN)}_4$ and $(\text{C}_6\text{mim})_3\text{-Dy(SCN)}_6$. Five out of seven of these ionic liquids have not been previously tested.

Current-voltage tests showed a large range of currents. EMI-FeCl_4 emitted an especially large amount of current, with over 50 μA recorded for a single emitter. EMI-BF_4 , EMI-SbF_6 , $(\text{EMI})_2\text{-Co(SCN)}_4$ and $\text{C}_6(\text{mim})_2\text{-Co(SCN)}_4$ were found to emit similar currents, 10 to 20 μA , despite a large difference in conductivity. $\text{C}_6(\text{mim})_2\text{-(Im)}_2$ and $(\text{C}_6\text{mim})_3\text{-Dy(SCN)}_6$ were found to emit the least current but were also found to have great high voltage stability, emitting at voltages exceeding 4000 V. However, further current-voltage characterisation is required to reliably confirm these characteristics.

Time-of-Flight tests showed that the emitted ion cluster sizes were similar, with most of the plumes being comprised of monomers, dimers and trimers. The charge-to-mass ratios were found to be similar for all the ionic liquids tested, despite having large differences in conductivities and viscosities. It was also shown that the average charge-to-mass ratio did not change with volumetric flow rate, remaining constant for most tests completed. An ion cluster emission model was introduced to predict the ion cluster distributions of the plume, however this was found to be inaccurate. This showed that the ionic liquid properties do not provide a reliable method for predicting charge-to-mass ratio of the ion clusters emitted.

Acknowledgements

Over these four years that I have worked on a PhD, there have been too many people to thank just in a short section in my thesis. So if you do for some reason decide to read this thesis and I have not mentioned you, I am sorry and know that you are in my memory.

A large part of my PhD was spent working on the PET-50 project as part of a collaboration between the University of Southampton, AVS UK and RHP Austria. During this project I learned a lot about electrospray thrusters, diagnostics and spacecraft propulsion in general. I would like to thank AVS UK and RHP Austria for enabling this project which taught me so much in my journey as a researcher.

I would like to thank my supervisor Dr Charlie Ryan for allowing me this journey. Although it is not always easy to work with me, you have remained patient and provided support for me the entire time. Even when I have had some of my more outlandish ideas, you have guided me through to arrive at the best outcome. Thank you for teaching me so much, it has been a great journey and I could not have finished it without you.

To my lab mates, just to name a few, Chengyu, Tom, Nazli and Arsad, thank you for putting up with my constant chatter throughout these years. Our conversations helped me a lot, whether to deal with the occasional tedium of lab work or to help me with working out new ideas. Equally I'd like to thank the technicians at our university, especially Simon Beever and Gus Gillam, for helping me throughout the PhD to engineer my various designs. You have also taught me a lot about manufacturing which is vital for building my ideas, and is learned best practically.

Thank you to my family, especially my mum and my dad, and my friends for being there for me when I needed it. I know I am not always the easiest to be with, but yet when I needed that trip to the pub for a beer or two, you have always been there for me. Whenever I required company, you have never failed me. Thank you. Finally, thank you to my Church, Father Anthony and my local parish community for always being there for me. Sometimes things looked bleak, yet you have always been my unbreakable bedrock when I needed you the most.

Contents

Acknowledgements	iii
List of Figures	ix
List of Tables	xiii
Declaration of Authorship	xv
1 Introduction	1
1.1 Spacecraft Propulsion	1
1.2 Electrospray Thrusters as Spacecraft Propulsion	8
1.3 Thesis Aims and Motivations	14
2 Emission and Plume Evolution of Porous Electrospray Thrusters	15
2.1 The Taylor Cone and Emission	15
2.1.1 Droplet emission	15
2.1.2 Pure-Ion Emission	18
2.2 Ion Evaporation	19
2.2.1 Ion Evaporation Kinetics	19
2.2.2 Ion Current in Pure-Ion Emission	23
2.3 Ion Cluster Size	31
2.3.1 Predicting Cluster Sizes	32
2.3.2 Comparison with Experimental Data	35
2.3.3 Considerations for Ionic Emission	38
2.3.4 Alternative Propellants	45
2.3.5 Ion Cluster Fragmentation	50
2.3.5.1 Field-free Fragmentation	52
2.3.5.2 Acceleration Region Fragmentation	53
2.4 Investigating Alternative Propellants for Porous Electrospray Thrusters	55
3 Experimental Methods	57
3.1 Current Collection	57
3.2 Retarding Potential Analysis	62
3.2.1 RPA Expected Results	63
3.2.1.1 Field-Free Fragmentation	65
3.2.1.2 Acceleration Region Fragmentation	66
3.3 Time of Flight Mass Spectrometry	68
3.3.1 TOF Expected Results	69

3.3.2	TOF Electrostatic Gates	73
3.3.3	TOF Current Collection	76
3.3.4	TOF Systems in the Literature	81
3.4	Diagnostic Setups for Electrospray Experiments	82
4	Experimental Setup	83
4.1	Diagnostic Tools	83
4.1.1	Current Collector	84
4.1.2	Retarding Potential Analyser	85
4.1.3	Time-of-Flight Mass Spectrometer	86
4.1.3.1	Design of the Electrostatic Gate	87
4.1.3.2	Design of the Collector Plate	88
4.1.3.3	Assembled TOF System	89
4.2	Electrospray Thruster	90
4.3	Combined Experimental System	93
4.4	Data Analysis	95
4.4.1	Collector Current	95
4.4.2	RPA	96
4.4.3	TOF	97
4.5	Methodology	101
4.6	Summary	103
5	Experimental Results	105
5.1	Experimental Conditions	105
5.1.1	Ionic Liquids	105
5.1.2	Emitters Used for Testing	108
5.2	Metal/Metalloid Halides	111
5.2.1	EMI-BF ₄	111
5.2.1.1	Current-Voltage	111
5.2.1.2	Time-of-Flight	113
5.2.1.3	Retarding Potential Analysis	116
5.2.2	EMI-FeCl ₄	120
5.2.2.1	Current-Voltage	120
5.2.2.2	Time-of-Flight	124
5.2.2.3	Retarding Potential Analysis	129
5.2.3	EMI-SbF ₆	131
5.2.3.1	Current-Voltage	131
5.2.3.2	Time-of-Flight	132
5.2.3.3	Retarding Potential Analysis	135
5.2.4	Summary	138
5.3	Multiply-Charged Ionic Liquids	139
5.3.1	(EMI) ₂ -Co(SCN) ₄	140
5.3.1.1	Current-Voltage	140
5.3.1.2	Time-of-Flight	142
5.3.1.3	Retarding Potential Analysis	147
5.3.2	C ₆ (mim) ₂ -(IM) ₂	152
5.3.2.1	Current-Voltage	152

5.3.2.2	Time-of-Flight	153
5.3.2.3	Retarding Potential Analysis	157
5.3.3	$C_6(\text{mim})_2\text{-Co(SCN)}_4$	159
5.3.3.1	Current-Voltage	162
5.3.3.2	Time-of-Flight	163
5.3.4	$(C_6\text{mim})_3\text{-Dy(SCN)}_6$	163
5.3.4.1	Current-Voltage	163
5.3.4.2	Time-of-Flight	166
5.3.4.3	Retarding Potential Analysis	168
5.4	Combined Current	169
5.5	Analysis of TOF data	174
5.5.1	Comparison with Droplet Charge-to-Mass Ratio	174
5.5.2	Comparison with Ion Emission Model	178
5.5.2.1	EMI- BF_4	178
5.5.2.2	EMI- FeCl_4	180
5.6	Summary	182
6	Conclusions and Future Work	185
6.1	Future Work	188
7	Appendix	193
7.1	Appendix A: Review of electrospray thrusters	193
7.1.1	Capillary Thrusters	194
7.1.2	Externally Wetted Thrusters	195
7.1.3	Porous Electrospray Thruster	196

List of Figures

1.1	Specific impulses of different types of propulsion systems used in small satellites	3
1.2	The relationship of the exhaust velocity and the chamber temperature divided by the molecular weight, plotted for three different specific heats.	6
1.3	The relationship of the exhaust velocity with the charge-to-mass ratio and the voltage, with range of voltages between 200 to 2000 V.	7
1.4	Three different designs of electro spray thruster emitters	9
1.5	Molecular structure of EMI-BF ₄	10
1.6	Performance of different types of specific impulses against thrust for various electro spray thrusters plotted on similar axes to Figure 1.1.	12
2.1	Four pictures showing the Taylor cone (a) and the subsequent collapse of it (b-d)	16
2.2	Two different modes of operation for an electro spray source showing droplet emission on the left hand side and ion emission on the right hand side.	18
2.3	The conical shape of a highly stressed meniscus takes a non-circular shape, however when the meniscus tip is sufficiently magnified it is assumed to take the shape of a circle.	25
2.4	Variation of ion current with the electric field strength and ion solvation energy	26
2.5	The current estimated to be emitted by EMI-BF ₄ assuming a constant area of emission using Equation 2.21. The ion solvation energy was varied between 1.2 and 2.0 eV.	28
2.6	Current estimated to be emitted by an ionic liquid with a conductivity varying from 0.1 to 1.5 Sm ⁻¹	29
2.7	Current estimated to be emitted by an ionic liquid with a surface tension varying from 40 to 60 mNm ⁻¹	30
2.8	Current estimated to be emitted by an ionic liquid with a relative permittivity range of 10 to 90.	31
2.9	In solvation energy required to emit an ion of various ion radii	33
2.10	The gradient of the ion solvation energy required to emit an ion of varying ion radius	33
2.11	Probability distribution function for EMI-BF ₄ positive ion emission	35
2.12	Probability distribution function for EMI-BF ₄ positive ion emission with a varying surface tension from 0.044 to 0.06 Nm ⁻¹	39

2.13	Probability distribution function for EMI-BF ₄ positive ion emission with a varying relative permittivity from 4 to 20. As the relative permittivity increases, the curves shifts further right cat a hgiher n value, corresponding to larger ion emission	41
2.14	Probability distribution function for EMI-BF ₄ positive ion emission with a varying density from 1000 to 1400 kgm ⁻³ . Larger ions are more likely to be emitted as the density increases.	42
2.15	Percentage change in surface tension, relative permittivity and density for EMI-BF ₄	43
2.16	Probability distribution function for EMI-BF ₄ positive ion emission with a temperature varying from 293 to 613 K	44
2.17	Fragmentation within an electrospray thruster, alongside the two regions where fragmentation occurs.	50
3.1	Three variants a basic current collection setup.	58
3.2	Key geometrical considerations for designing an electrospray thruster current collector.	60
3.3	A four grid RPA, showing to what grid each potential is applied to. From the left hand-side the grids are as follows: floating, electron repelling, retarding and secondary electron suppression.	62
3.4	The effects of an acceleration efficiency of 0.9 On RPA data.	64
3.5	An ideal energy distribution, shown in the dotted line, with a more realistic energy distribution shown in the solid line showing the effects of field-free fragmentation.	65
3.6	An idealised version of RPA data, including the effects of acceleration efficiency, field-free fragmentation and acceleration region fragmentation.	66
3.7	Example RPA data from a thruster which has similar emitters to the emitters tested in this thesis	67
3.8	A basic TOF system showing the two components, the gate and the collector, alongside a plume comprising of monomers, dimers and trimers.	69
3.9	An example plot of TOF data assuming monomer, dimer and trimer EMI-BF ₄ cations. The current drops correspond to the arrival of a given ion species.	70
3.10	An example TOF plot which includes the effects of acceleration region fragmentation.	71
3.11	Example TOF data showing the effect of gate noise	72
3.12	Two most common TOF gates used in literature	74
3.13	Design of an interleaved comb gate used in TOF	75
3.14	Time spread induced due to the width of a collector plate assuming a flight length of 500 mm. As the collector plate diameter is increased, the time spread increases. The time spread is also higher for the heavier ion clusters.	77
3.15	A schematic of a typical Faraday cup used for ion detection.	78
3.16	Effects of off-axis emission for TOF. On-axis emission into a TOF gate is shown in (a) while (b) shows the off-axis emission. During off-axis emission, a significant proportion of the current may be lost due to the misalignment between the beamlets and the TOF gate entrance aperture.	79
3.17	Use of electron amplification to amplify the current of an incoming ion	80

4.1	An example circuit using a TVS diode, made using LTSpice.	85
4.2	The schematics of the FC-72 used as an RPA.	86
4.3	The previous TOF gate design, shown on the left, with an improved design shown on the right. The area of the gate was reduced between the two designs in order to decrease the capacitance of the system.	88
4.4	The large collector plate designed for use with TOF system.	89
4.5	The assembled TOF system	90
4.6	The designed dimensions of each porous glass emitter.	91
4.7	A block of 16 emitters after CNC manufacturing	92
4.8	Cut-out of the thruster with the main components annotated.	92
4.9	PET-RTS with the porous electrospray source mounted on the rotary stage. The respective diagram of each of the instruments is shown here with their electrical connections.	94
4.10	The thruster, centre, mounted on the rotary stage. On the left hand-side the TOF gate can be seen, positioned behind the thruster is the rotary stage and finally in the bottom right corner is the RPA.	94
4.11	Current-Voltage data using EMI-BF ₄ , with both the current collected and the voltage applied to the emitter.	95
4.12	Raw RPA data using EMI-BF ₄ including the retarding voltage applied.	96
4.13	TOF data recorded without the thruster operating, showing the gate noise occurring after the switching of the gate at 0 μs.	98
4.14	Raw TOF with no corrections or filtering while the thruster is operating showing a typical TOF curve.	98
4.15	Reduced noise TOF data, removing the effect of the gate noise by subtracting the gate noise from the raw TOF data.	99
4.16	Filtered and transformed TOF data. The points indicate where the proportions of each species were calculated.	100
5.1	Appearance of the different ionic liquids, from left to right; EMI-BF ₄ , EMI-FeCl ₄ , EMI-SbF ₆ , (EMI) ₂ -Co(SCN) ₄ , C ₆ (mim) ₂ -(Im) ₂ , (C ₆ mim) ₃ -Dy(SCN) ₆ and C ₆ (mim) ₂ -Co(SCN) ₄	108
5.2	The ions present in the ionic liquids which were tested in this paper. Each ionic liquids is represented by: EMI-BF ₄ - green, EMI-FeCl ₄ - black, EMI-SbF ₆ - purple, (EMI) ₂ -Co(SCN) ₄ - orange, C ₆ (mim) ₂ -(Im) ₂ - red, (C ₆ mim) ₃ -Dy(SCN) ₆ - yellow and C ₆ (mim) ₂ -Co(SCN) ₄ - blue. The molecular diagrams were sourced from PubChem(https://pubchem.ncbi.nlm.nih.gov/).	109
5.3	Current-voltage for data emitter 2 using EMI-BF ₄	111
5.4	Current-voltage data for emitter 3 using EMI-BF ₄	112
5.5	TOF data for emitter 2 using EMI-BF ₄ for both polarities	114
5.6	TOF data for emitter 3 using EMI-BF ₄ for both polarities.	115
5.7	Long period positive polarity TOF data for emitter 2.	116
5.8	RPA data for emitter 2 using EMI-BF ₄ for both polarities.	117
5.9	RPA data for emitter 3 using EMI-BF ₄ for both polarities.	119
5.10	Current-voltage data for emitter 17 using EMI-FeCl ₄ , showing a similar magnitude of current emitted to EMI-BF ₄ , albeit at a significantly lower voltage.	120
5.11	Estimated onset voltages for EMI-BF ₄ and EMI-FeCl ₄ ,	121

5.12	Current-voltage data for emitter 4 using EMI-FeCl ₄	122
5.13	A repeat test of emitter 4 after three days.	123
5.14	Combined collector current data for all current data shown.	124
5.15	TOF data for emitter 4 using EMI-FeCl ₄ for both polarities.	126
5.16	TOF data for emitter 17 using EMI-FeCl ₄ for both polarities	127
5.17	Angular current distributions for emitter 17 using EMI-FeCl ₄	129
5.18	RPA data for emitter 4 using EMI-FeCl ₄ for both polarities	130
5.19	Current-voltage for data emitter 14 using EMI-SbF ₆	131
5.20	Positive polarity TOF data for EMI-SbF ₆	133
5.21	Negative polarity TOF data for EMI-SbF ₆ at a voltage of -2600 V.	135
5.22	The RPA data for emitter 14 for both polarities.	136
5.23	The critical electric field calculated with different ion charges.	140
5.24	Current-voltage for data emitter 1 using (EMI) ₂ -Co(SCN) ₄	141
5.25	Current-voltage for data emitter 10 using (EMI) ₂ -Co(SCN) ₄	142
5.26	TOF data for emitter 1 using (EMI) ₂ -Co(SCN) ₄ for both polarities.	144
5.27	TOF data for emitter 10 using (EMI) ₂ -Co(SCN) ₄ for both polarities.	145
5.28	RPA data for emitter 1 using (EMI) ₂ -Co(SCN) ₄ for both polarities.	149
5.29	RPA data for emitter 10 using (EMI) ₂ -Co(SCN) ₄ for both polarities.	150
5.30	Current-voltage for data emitter 6 using C ₆ (mim) ₂ -(IM) ₂	153
5.31	Current-voltage for data emitter 15 using C ₆ (mim) ₂ -(IM) ₂	153
5.32	TOF data for emitter 6 using C ₆ (mim) ₂ -(IM) ₂ for both polarities.	155
5.33	Negative polarity TOF Data for emitter 15 using C ₆ (mim) ₂ -(IM) ₂	156
5.34	RPA data for emitter 6 using C ₆ (mim) ₂ -(Im) ₂ for both polarities.	158
5.35	A kapton heater mounted on the extractor of the thruster.	160
5.36	Emitter 16 after the filling process.	161
5.37	Current-voltage for data emitter 16 using C ₆ (mim) ₂ -Co(SCN) ₄	162
5.38	Positive polarity TOF data for C ₆ (mim) ₂ -Co(SCN) ₄ at a voltage of 3300 V.	164
5.39	Current-voltage for data emitter 9 using (C ₆ mim) ₃ -Dy(SCN) ₆	165
5.40	TOF data for the negative polarity for (C ₆ mim) ₃ -Dy(SCN) ₆	167
5.41	The RPA data for emitter 9 for both polarities.	169
5.42	Current against voltage for the ionic liquids	170
5.43	Current data with a voltage normalised to the onset voltage.	172
5.44	Average charge-to-mass ratios against the conductivity per volumetric flow rate for five different ionic liquids.	175
7.1	Performance of different capillary thrusters. The specific impulse, thrust and power are found in Tab. 7.1.	194
7.2	Performance of different externally wetted thrusters. The specific impulse, thrust and power are found in Tab. 7.2.	195
7.3	Performance of different porous thrusters. The specific impulse, thrust and power are found in Tab. 7.3.	197

List of Tables

1.1	Examples of the different types of ion clusters that can be emitted from electrospray thrusters.	11
2.1	Monomer, dimer and trimer distributions using the Boltzmann ion cluster distribution.	36
2.2	Experimental monomer, dimer and trimer distributions using EMI-BF ₄	37
2.3	Ion cluster size distributions calculated to take into account the effect of temperature.	45
2.4	Comparison of modelled ion cluster size and experimental ion cluster sizes for EMI-Im assuming T = 293 K.	46
2.5	The different propellant properties for the ionic liquids tested by Legge <i>et al</i>	47
2.6	Different propellant properties for the ionic liquids tested by Castro <i>et al</i>	48
3.1	Summary of the design choices of different TOF systems in literature. The 'Emitter' and 'Extractor' gates reference to systems where the gate switch is used on the emitter and extractor.	81
4.1	Calculated ion proportions and their uncertainties for the example TOF data.	101
5.1	The conductivities, K , viscosities, μ , surface tensions, γ , masses, m and charges, q , for the ionic liquids tested in this thesis. is solid, therefore the liquid properties are not provided. All the conductivities unless otherwise stated were tested with a Horriba LAQUAtwin EC-33 conductivitymeter. Anion masses were obtained from PubChem, https://pubchem.ncbi.nlm.nih.gov/	106
5.2	Tip radii and heights of different emitter tips used in testing.	110
5.3	The various different types of ions calculated which could have been emitted by EMI-BF ₄	116
5.4	Various different types of ions calculated which could have been emitted by EMI-FeCl ₄	125
5.5	Various different types of ions calculated which could have been emitted by EMI-SbF ₆	134
5.6	Various different types of ions calculated which could have been emitted by (EMI) ₂ -Co(SCN) ₄	146
5.7	Various different types of ions calculated which could have been emitted by C ₆ (mim) ₂ -(IM) ₂	157
5.8	Various different types of ions calculated which could have been emitted by C ₆ (mim) ₂ -Co(SCN) ₄	164

5.9	The various different types of ions calculated which could have been emitted by $(\text{C}_6\text{mim})_3\text{-Dy}(\text{SCN})_6$	167
5.10	Modelled ion cluster size distribution for EMI- BF_4	178
5.11	Experimental ion cluster size distributions for emitter 3 using EMI- BF_4	179
5.12	Experimental ion cluster size distributions for emitter 2 using EMI- BF_4	179
5.13	Modelled ion cluster size distribution for EMI- FeCl_4	180
5.14	Experimental ion cluster size distributions for emitter 4 using EMI- FeCl_4	181
5.15	Experimental ion cluster size distributions for emitter 17 using EMI- FeCl_4	181
7.1	Summary of the thruster parameters from various sources for capillary thrusters.	195
7.2	Summary of the thruster parameters from various sources for externally wetted thrusters.	196
7.3	Summary of the thruster parameters from various sources for porous thrusters.	197

Declaration of Authorship

I declare that this thesis and the work presented in it is my own and has been generated by me as the result of my own original research.

I confirm that:

1. This work was done wholly or mainly while in candidature for a research degree at this University;
2. Where any part of this thesis has previously been submitted for a degree or any other qualification at this University or any other institution, this has been clearly stated;
3. Where I have consulted the published work of others, this is always clearly attributed;
4. Where I have quoted from the work of others, the source is always given. With the exception of such quotations, this thesis is entirely my own work;
5. I have acknowledged all main sources of help;
6. Where the thesis is based on work done by myself jointly with others, I have made clear exactly what was done by others and what I have contributed myself;
7. Parts of this work have been published as: See the following page.

Signed:.....

Date:.....

List of Publications

First Author Publications

Journal Papers

Part of this work was published in the journal paper:

S. Dworski and C.N. Ryan, "Investigating the ions emitted by multiply charged ionic liquids from a porous electrospray ion source," *Journal of Applied Physics*, vol. 136, p. 133301, 10 2024.

Conference Papers

Part of this work was also published in the conference paper:

S. Dworski and C. Ryan, "Analysis of Plumes Produced by Novel Ionic Liquids in Electrospray Thrusters," in *38th International Electric Propulsion Conference*, Toulouse, France, 2024.

Work on the PET-50 project, which contributed to the development of the diagnostics equipment, was published in the conference papers:

S. Dworski, A. Quraishi, E. Batchelor, A.G. Machado, C. Ryan, A. Ferreri, G. Vincent, A. Croos, D. Shcherbak, J. Sadler, A. Garbayo, M. Vozárová and E. Neubauer, "Performance of a 50 W Porous Electrospray Thruster in Preparation for Flight," in *38th International Electric Propulsion Conference*, Toulouse, France, 2024.

A further conference paper which contributed to the development of the diagnostics equipment:

S. Dworski, C. Ma and C. Ryan, "Effects of Propellant Temperature on Fragmentation in the Plume of a Porous Electro spray Thruster," in *37th International Electric Propulsion Conference*, Boston, MA, USA, 2022.

Second/Co-Author Publications

Journal Papers

The diagnostic equipment developed in this thesis was used in:

N. Turan, S. Dworski, N.J. Wells and C.N. Ryan, "Detailed Analysis of Ionic Liquid Mixtures as Alternative Propellants for Porous Electro spray Thrusters," *Journal of Applied Physics*, Submitted for Publication.

Conference Papers

The diagnostic equipment developed in this thesis was used in:

N. Turan, S. Dworski, and C. Ryan, "Investigation of cation and anion emission mechanisms from porous electro spray thrusters using ionic liquid mixtures," in *38th International Electric Propulsion Conference*, Toulouse, France, 2024.

Further work on the PET-50 project which contributed to the development of the diagnostic equipment was presented in the following conferences:

A. Quraishi, S. Dworski, E. Batchelor, A. Gonzalez Machado, C. Ryan, A. Ferreri, G. Vincent, A. Croos, A. Garbayo, M. Vozárová and E. Neubauer, "Development of a 50 w porous emitter electro spray thruster towards flight," in *74th International Astronautical Congress*, Baku, Azerbaijan, 2023.

A. Quraishi, S. Dworski, C. Ma, C. N. Ryan, A. Ferreri, G. Vincent, H. Larsen, E. R. Azevedo, E. Dingle, A. Garbayo, M. Vozárová and E. Neubauer, "Designing and commercialization of porous emitter electro spray thruster for space applications," in *AIAA SCITECH 2023 Forum*, National Harbor, MD, USA, 2023.

A. Quraishi, S. Dworski, C. Ma, C. Ryan, A. Ferreri, G. Vincent, H. Larsen, E. R. Azevedo, E. Dingle, A. Garbayo, et al., "Development of porous emitter electro spray

thruster using advanced manufacturing processes," in *37th International Electric Propulsion Conference*, Boston, MA, USA, 2022.

Chapter 1

Introduction

The space industry in the 21st century is a rapidly expanding sector. From small satellites enabling smaller entities to access space, to envisioning the first human interplanetary travel, the ambition of space agencies and the space industry is constantly increasing. However, as this growth accelerates these endeavours are encountering challenges such as within the local space environment, where space debris in low earth orbit could endanger future space travel. These ambitions and problems are leading the way for continually increasing demands from spacecraft to last longer, fly further and collect more data. These demands feed into spacecraft requirements meaning that spacecraft subsystems have continually more demanding specifications. One of these subsystems which is increasingly important is on-orbit spacecraft propulsion.

1.1 Spacecraft Propulsion

Spacecraft propulsion is a system that provides a spacecraft with thrust by accelerating a propellant to a high velocity, enabling the spacecraft to move. Spacecraft propulsion can be categorised into two categories: launch vehicle and on-orbit propulsion. The former is used to launch a spacecraft from Earth into space, and is not explored in this thesis, while the latter typically provides two essential functions: attitude control and orbital manoeuvring.

Attitude control is the prediction and reaction to a spacecraft's orientation, referring to its three-dimensional rotational position, which is crucial to fulfil mission pointing

requirements. Orbital manoeuvring involves altering elements of an orbit, such as the altitude, the inclination, or the eccentricity, and is employed for tasks such as orbit insertion, de-orbiting or space debris mitigation and collision avoidance. Attitude control and orbital manoeuvring play a critical role in enabling a spacecraft to achieve its mission objectives, with spacecraft propulsion forming an essential part of most spacecraft.

To achieve these functions, propulsion requires an energy source to accelerate the propellant. This energy can be provided from three energy sources: chemical, electric and nuclear, with these energy sources typically being used to characterise the types of propulsion systems. Chemical propulsion liberates energy from an exothermic chemical reaction to increase the enthalpy of the propellant therefore allowing it to be accelerated. Similarly, nuclear propulsion uses the energy produced by nuclear fission (in the future possibly fusion as well) to increase the enthalpy of the propellant and then accelerate it. Finally, electric propulsion utilises electrical energy to accelerate the propellant with power typically supplied by solar panels, though it can also be supplied by chemical and nuclear power sources. However, the acceleration for electric propulsion is ultimately provided by the utilisation of electrical energy irrespective of its power source.

Figure 1.1 shows the thrusts and specific impulses of various different electric and chemical propulsion systems for small satellites. Chemical propulsion systems, such as cold-gas and chemical propulsion, generally produce higher thrusts but lower specific impulses compared to electric propulsion systems, which are represented by the other groups in the figure.

Chemical propulsion systems provide high thrusts and low to moderate specific impulses, with chemical thrusters typically reaching < 450 s [1]. Meanwhile current electric propulsion systems provide moderate to very low thrusts and low to very high specific impulses (up to 4000 s), as Figure 1.1 illustrates. It can be seen that the performances of various thrusters significantly vary, with specific impulses changing by three orders of magnitude and thrusts varying by almost seven orders of magnitude. The high thrust of chemical propulsion sources makes them suitable for quick and impulsive orbital manoeuvres and rapid transit times, while electric propulsion can produce similar impulses for less propellant at the cost of longer transit times.

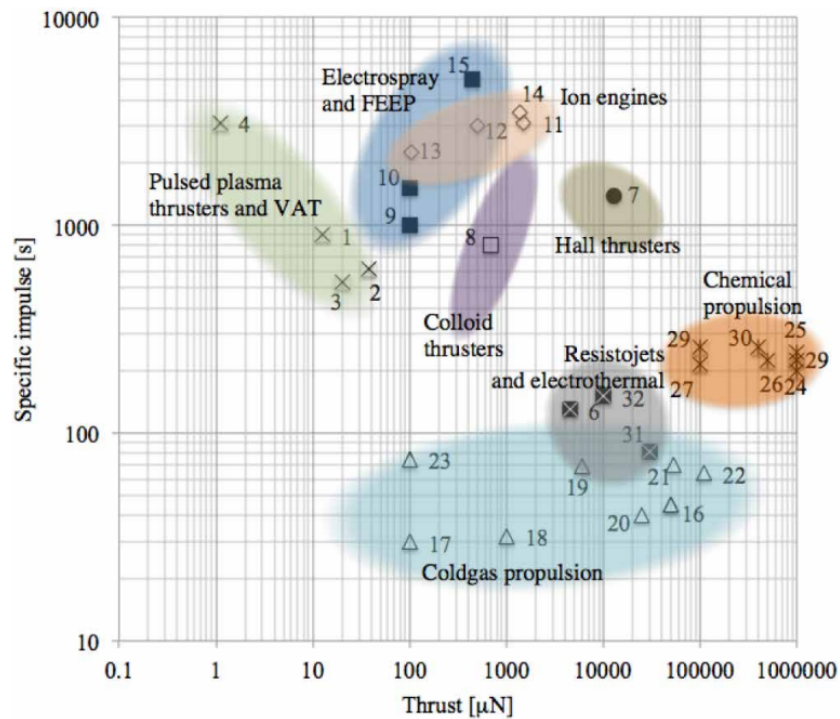


FIGURE 1.1: Specific impulses of different types of propulsion systems used in small satellites [2].

With the high varying performance, and other merits and disadvantages of each propulsion type, it can be unclear which spacecraft propulsion system could be the most impactful in the space industry in the near future. Chemical propulsion has been the principle form of propulsion for use in space since the first spacecraft and has the most flight heritage of any spacecraft propulsion system. However, chemical propulsion is fundamentally limited by the energy stored in the chemical bonds of its propellant meaning that its specific impulse is also fundamentally limited.

An alternative propulsion type to chemical is nuclear propulsion. Higher specific impulses for nuclear propulsion of up to 900 s [3] can be achieved, while maintaining similar thrust levels to chemical propulsion. Although the higher specific impulse addresses the issue of limited energy by utilising the more energetic process of nuclear fission, there are still many difficulties in developing such technology for use in space. However, nuclear propulsion has recently gained prominence for use in space for example with the DRACO program, a program to develop a nuclear thermal rocket and demonstrate its use in orbit by 2027 [4].

Finally, the specific impulse of electric propulsion is limited only by the power available

to the electric propulsion system. However, with current power sources for spacecraft the practical specific impulse is limited to $\sim 3000 - 4000$ seconds, approximately an order of magnitude higher than chemical propulsion. Electric propulsion also shares a long flight heritage with chemical propulsion, with the first flight of an electric propulsion system in 1964 by SERT-1, albeit only recently gaining prominence for use in spacecraft [5].

This high specific impulse and heritage has led to electric propulsion gaining increasing usage as a satellite propulsion system. An example application of electric propulsion are all-electric communication satellites, where all propulsion requirements for the satellite are provided by electric propulsion. The high specific impulse of electric propulsion reduces the mass of the propulsion subsystem therefore providing savings in satellite costs. All-electric communication satellites provide other benefits, such as the mass savings from using electric propulsion enabling improvements on the payload performance hence increasing the revenue produced by the satellite [6]. The mass saving capabilities of electric propulsion are especially impactful for interplanetary flight [7]. One example of the impact of electric propulsion on interplanetary travel is the Dawn mission. The aim of the mission was to visit and study two interplanetary bodies: the asteroid Vesta and the dwarf planet Ceres [8]. An electric propulsion system was selected instead of a chemical propulsion system for this mission, reducing the required propellant mass to 400 kg of Xenon compared to over 6000 kg if a chemical propulsion system was used [9].

Electric propulsion systems can also be categorised based on the way the electrical energy is converted to produce thrust. Electrothermal electric propulsion systems utilise electrical energy by converting it into heat, such as by using a heater, and thus increasing the enthalpy of the propellant similar to chemical and nuclear thrusters. Electrostatic propulsion systems utilise the electrical energy to produce ions, that are then accelerated by electrodes which directly apply a static electric field. Finally, electromagnetic thrusters use the Lorentz force to ionise and accelerate the propellant, with the force arising from interaction between the plasma and the magnetic field provided by the thruster.

The three sub-categories for electric thrusters also have varying thrust and specific impulse capabilities, in order from lower specific impulse to higher specific impulse: electrothermal (resistojets and electrothermal), electromagnetic (pulsed plasma, Vacuum Arc Thrusters (VAT) and hall thrusters) and electrostatic (electrospray, Field Emission Electric Propulsion shortened to FEEP, colloid and ion engines), shown in Figure 1.1. The differences in specific impulses of each spacecraft propulsion type allows for further specialisation in their function, in a similar manner as looking at the differences between chemical, nuclear and electrical systems. There are other characteristics which are important, such as reliability, safety and lifetime however for brevity these will not be discussed.

In order for electric propulsion to produce thrust, a propellant has to be used, the properties of which play a key role in thruster performance. Examples of propellants used in electric propulsion systems include; xenon or krypton, or other inert noble gases, used by hall thrusters and ion engines, molten metals such as indium used by FEEPs and organic liquids for electrosprays and colloid thrusters. The broad range of propellants highlights that alongside electrical energy transfer, the propellants used are intrinsic to the type of electric propulsion system used hence are crucial to consider.

The importance of the selection of propellants is highlighted when investigating the exhaust velocity, v_{ex} , a fundamental parameter in spacecraft propulsion systems affecting both the thrust, T , and the specific impulse of the thruster, I_{sp} . The thrust and specific impulse can be described as a function of the exhaust velocity by:

$$T = \dot{m}v_{ex}, \quad (1.1)$$

$$I_{sp} = \frac{v_{ex}}{g_0}, \quad (1.2)$$

where \dot{m} is the mass flow rate of the propellant and g_0 is the standard acceleration of gravity. To increase the specific impulse the exhaust velocity of the propellant can be increased and, similarly, to achieve a higher thrust the mass flow rate can be increased, which for electric propulsion is typically linked to the total power available to thruster. Also for the thrust, it initially appears that increasing the exhaust velocity increases the thrust, however the exhaust velocity has a more complex relationship with thrust that typically means that higher exhaust velocities decrease the thrust, which will be

discussed for electrostatic thrusters later in this chapter. The exhaust velocity is defined in three different ways given that there are three different types of electric propulsion systems, however only two will be provided here.

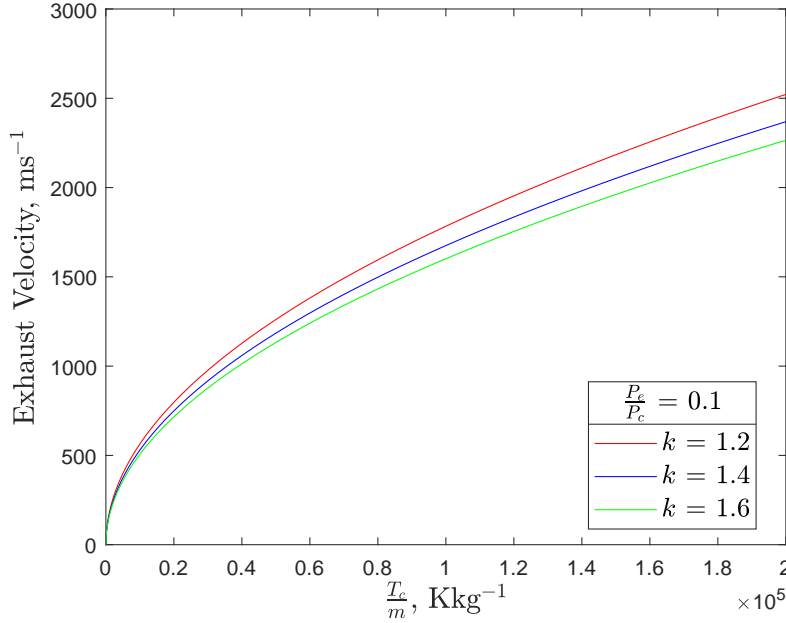


FIGURE 1.2: The relationship of the exhaust velocity and the chamber temperature divided by the molecular weight, plotted for three different specific heats.

The electrothermal exhaust velocity, $v_{ex,et}$, is defined by the propellant molecular mass, m , chamber pressure, P_c , and the chamber temperature, T_c . The ratio of specific heats, k , which is another propellant property, also contributes to the electrothermal exhaust velocity equation. The electrothermal exhaust velocity is defined as [10]:

$$v_{ex,et} = \sqrt{\frac{R}{m} \frac{2k}{k-1} T_c \left(1 - \left(\frac{P_e}{P_c} \right)^{\frac{k-1}{k}} \right)}, \quad (1.3)$$

where R is the universal gas constant and P_e is the exhaust pressure. Equation 1.3 has been plotted in Figure 1.2 and shows how the electrothermal exhaust velocity varies with varying k and $\frac{T_c}{m}$. The exhaust velocity can be increased by increasing the chamber temperature and the propellant molecular mass. It can also be varied the ratio of specific heats and the chamber pressure, although these have a marginal effect. Nonetheless, Figure 1.2 highlights that propellant properties have an effect on the exhaust velocity of electrothermal thrusters.

Similarly, the electrostatic exhaust velocity, $v_{ex,es}$, can be defined as a function of the ion charge q and the potential which an ion is accelerated by, ϕ . This is shown by,

$$v_{ex,es} = \sqrt{\frac{2q\phi}{m}}. \quad (1.4)$$

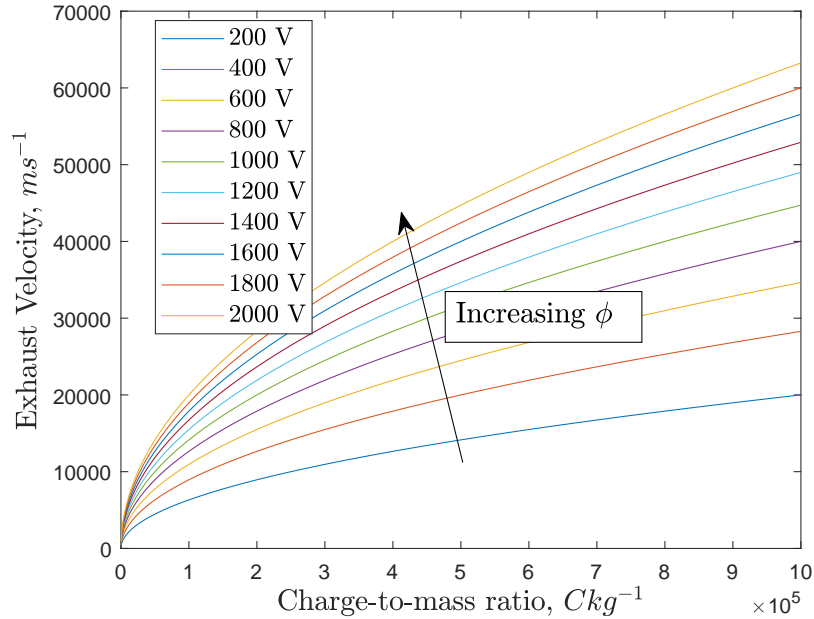


FIGURE 1.3: The relationship of the exhaust velocity with the charge-to-mass ratio and the voltage, with range of voltages between 200 to 2000 V.

Figure 1.3 shows Equation 1.4 plotted for various charge-to-mass ratios and acceleration potentials. The effect of the charge-to-mass ratio, $\frac{q}{m}$, can be seen to be significant on the exhaust velocities, with a typical electric propulsion ion of Xe^+ , with a charge-to-mass ratio of $7.34 \times 10^5 \text{ Ckg}^{-1}$, having an exhaust velocity of over $10,000 \text{ ms}^{-1}$ for all voltages. Typically for electrostatic type thrusters the charged particles are singly charged and the charge does not change after emission, thus the mass of the ion is the main determining factor of the exhaust velocity. As with the electrothermal type of propulsion, a smaller mass will increase the exhaust velocity and therefore the specific impulse. Although this is a very simplified model of how the propellant properties affect the performance, it highlights that even in these fundamental equations for different types of thrusters the propellant properties play a significant role in determining the performance of the thruster.

From the data included in Figure 1.1, the propulsion systems with the highest specific impulses are electrospray, FEEP and gridded ion thrusters, with all of these being a type of electrostatic thruster. These high specific impulses could offer the largest savings on propellant mass, which could be useful to most space missions, with the downside of having a significantly lower thrust than other types of thrusters.

Although the ion acceleration method for gridded ion thrusters, electrospray thrusters and FEEPs is the same, their characteristics vary considerably. Electrosprays and FEEP thrusters are scalable to micro and nano-meter scales [11] without a loss in efficiency due to their electrohydrodynamic ionisation, which can operate at these scales without significant losses. With the increasing use of small satellites in space, especially standardised small satellites called CubeSats [12], the miniturisation of a propulsion system has gained significance. As a result, FEEP and electrospray thrusters have emerged as a promising solution to meet this requirement. Of these two propulsion systems, FEEP has found the most use due to the high current produced by it and therefore good thrust, with the company Enpulsion having already launched over 100 FEEP thrusters into space [13]. However, as will be shown in the next section, electrospray thrusters offer a good alternative to FEEP thrusters, with the unique molecular propellants used by electrospray thrusters allowing high levels of both specific impulse and thrust-to-power ratio.

To summarise, for spacecraft propulsion systems, one of the key requirements is a certain level of specific impulse, with a higher specific impulse now typically being preferred. Electric propulsion systems have the highest specific impulses currently available (especially gridded ion thrusters, electrospray and FEEP thrusters) potentially leading to significant mass savings when using them. Electrospray and FEEP thrusters offer an almost infinite scalability, with the scalability offering an advantage with the increasing implementation of small satellites.

1.2 Electrospray Thrusters as Spacecraft Propulsion

Electrospray thrusters are a type of electrostatic propulsion device that utilise the electrospray effect to produce charged particles from a liquid. The two most fundamental

components of an electrospray thruster are the emitter and the extractor. The extractor is a thin grounded conductive plate placed close to the emitter with a small aperture through which ions are transmitted. The emitter of an electrospray thruster is a small, very sharp needle-shaped object where a high voltage, termed the emitter voltage, is applied. Liquid feeding is also enabled by the emitter tip, which is key to sustain charged particle emission. The emitter is typically made from ceramic or metal. A very strong electric field is produced between the emitter and the extractor, causing the propellant to undergo charged particle emission, with the electric field then accelerating the charged particles to very high velocities.

Three types of emitters exist, capillary, externally wetted and porous emitters, illustrated in Figure 1.4. A capillary emitter is comprised of a sharpened capillary through which propellant is fed. The second type of emitter is called an externally wetted emitter, where a solid needle-like structure is used to feed the propellant, with the roughness of this tip controlled to vary the flow rate of propellant over it. The third type of emitter is the porous emitter where propellant flows through a porous structure to a sharp tip, with the pore sizes being used to enable and control the propellant flow to the tip.

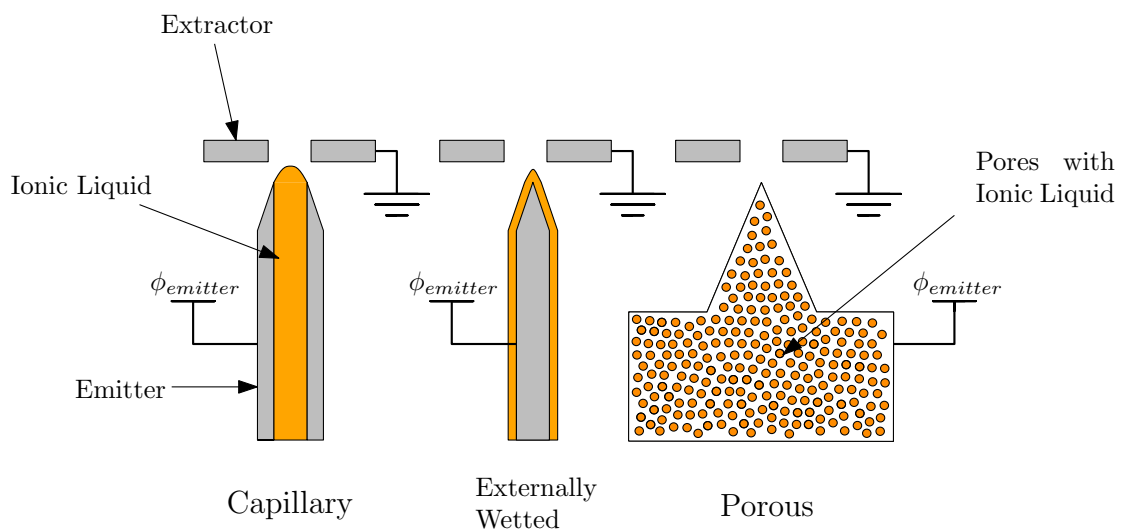


FIGURE 1.4: Three different designs of electrospray thruster emitters. The emitters are used to amplify the electric field at the tip and to transport propellant to the tip. The orange represents the propellant in the emitter.

The most common propellants used in electrospray thrusters are room temperature molten salts, termed 'ionic liquids', comprised of molecular positively and negatively charged ions, typically a cation and an anion. One of the most common ionic liquids

is 1-ethyl-3-methylimidazolium tetrafluoroborate (EMI- BF_4), the molecular structure of which is shown in Figure 1.5. The figure shows the anion BF_4^- ionically bonded to the large molecular cation EMI^+ , an organic cation, forming a neutral pair. The molecular nature of these ions makes ionic liquids more chemically complex than other typical electric propulsion propellants, which are usually atomic propellants.

The complexity provides some unique properties to electro spray thrusters using ionic liquids. One of these properties is that given its molecular nature, the number of possible ionic liquids is practically infinite, with up to 10^{18} combinations possible [14].

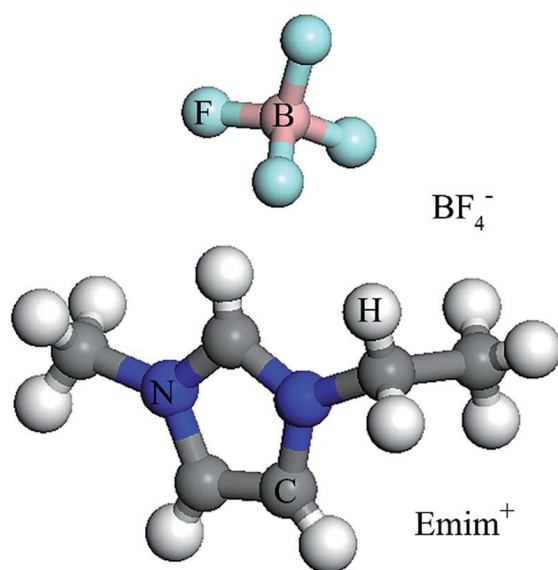
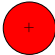
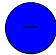
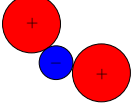
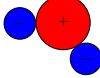
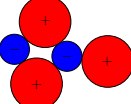
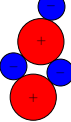


FIGURE 1.5: Molecular structure of EMI-BF_4 [15].

Another unique property of electro spray thruster emission when using ionic liquids is the complexity of the ions emitted. Ionic emission from an electro spray thruster produces clusters of ions that have an anion or a cation clustered with n number of neutrals. One way to easily represent these ions is by using nomenclature from Larriba *et al* [16], where cations are represented by A^+ and anions are represented by B^- , and neutrals are A^+B^- . As an example, in Figure 1.5 the A^+ and B^- correspond to the cation EMI^+ and anion BF_4^- respectively, and the ionically bonded pair, EMI-BF_4 , corresponds to the neutral A^+B^- . Using this nomenclature, the cations emitted by electro spray ionisation can be emitted in clusters of unique forms. They are normally described in terms of monomers, A^+ , dimers, $\text{A}^+[\text{A}^+\text{B}^-]$, trimers, $\text{A}^+[\text{A}^+\text{B}^-]_2$, quadramers, $\text{A}^+[\text{A}^+\text{B}^-]_3$, and so forth. The negatively charged anion molecular ions take the a similar form, albeit with an anion providing the charged component to the ion cluster. A visualisation of

TABLE 1.1: Examples of the different types of ion clusters that can be emitted from electrospray thrusters.

Ion name	Ion type	Cation	Anion
Monomer	$n = 0$		
Dimer	$n = 1$		
Trimer	$n = 2$		

these ion clusters is shown in Tab. 1.1, with the variable n corresponding to the amount of neutrals, A^+B^- , attached to the ion cluster.

As the sizes of ion clusters increase, referring in this thesis to clusters with a higher n hence a lower charge-to-mass ratio, they eventually become droplets. These droplets have a significantly reduced charge-to-mass ratio leading to a low specific impulse. The exact definition of droplets is not clear, with an arbitrary but practical definition for this thesis being that a droplet is any charged particle with a charge-to-mass ratio lower than $5 \times 10^4 \text{ Ckg}^{-1}$ for EMI-BF₄. In terms of the physics, ion clusters can be considered gaseous based on the considerations of the processes during emission [17], where a liquid phase ion in the meniscus is evaporated into a gaseous phase ion. Meanwhile, droplets can be considered liquid phase due to no phase change occurring during emission. However, the lower limit of the charge-to-mass ratios of an ion cluster and the upper limit of the charge-to-mass ratios of a droplet are unclear, making distinction between the two at times difficult.

The emission of these unique ion clusters and droplets by electrospray thrusters results in a very broad range of performances, encompassing high and low specific impulses, $\sim 90 \text{ s} - \sim 5500 \text{ s}$, and also very low to moderate thrusts, $<1 \text{ nN} - \sim 150 \text{ }\mu\text{N}$, relative to other types of thrusters shown in Figure 1.1. Figure 1.6 shows the thrusts and specific impulses of various electrospray laboratory experiments and thrusters. The specific impulses vary by approximately two orders of magnitude and the thrust by approximately five orders of magnitude across different thrusters, exemplifying the wide performance range of electrospray thrusters. The particular details of these data,

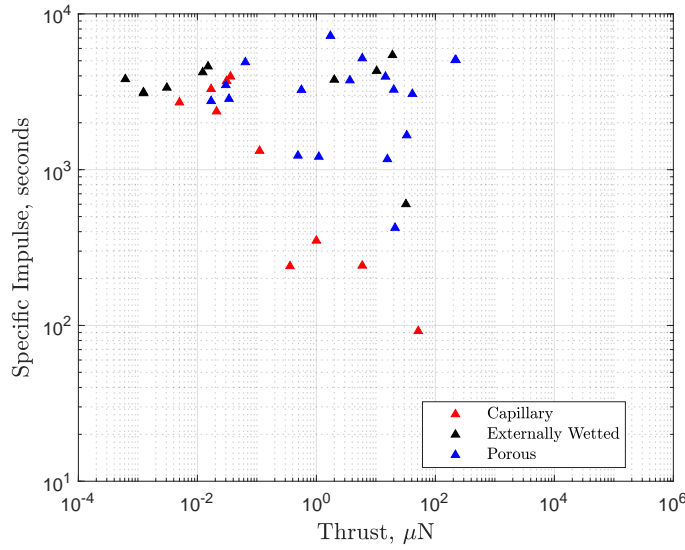


FIGURE 1.6: The specific impulses against thrust for various electro spray thrusters plotted on similar axes to Figure 1.1. The data for this figure was collected from a range of sources in and plotted in this figure [18, 19, 20, 21, 22, 23, 24, 25, 26, 27, 28, 29, 30, 31, 32, 33, 34, 35, 36, 37, 38, 39]. Where the thrust and specific impulse are not explicitly stated in the literature, they were calculated using Equations 1.4 and 1.5

including which source each point corresponds to, can be found in Appendix A, section 7.1.

In order to explain this broad range of performances for electro spray thrusters, the equations for thrust and specific impulse for electrostatic (hence electro spray) thrusters are required. The thrust equation, Equation 1.1, can be rewritten specifically for electrostatic thrusters using the electrostatic exhaust velocity equation, Equation 1.4, and by also taking into account that the mass flow rate can be defined using the current emitted by the thruster, $I, \dot{m} = \frac{mI}{q}$. The specific impulse equation can be simply derived by substituting Equation 1.4 into Equation 1.2. These two steps produce the equations:

$$T = I\sqrt{2\phi_{emitter}}\sqrt{\frac{m}{q}}, \quad (1.5)$$

$$I_{sp} = \frac{1}{g_0}\sqrt{2\phi_{emitter}}\sqrt{\frac{q}{m}}. \quad (1.6)$$

For both of these equations it was assumed that the acceleration potential is the same as the emitter potential, i.e. $\phi = \phi_{emitter}$. Three parameters from Equation 1.5 and 1.6

can be seen to drive the equations: current emitted, I , the emitter voltage, $\phi_{emitter}$ and the charge-to-mass ratio of emitted ions, $\frac{q}{m}$. Thrust is increased by a higher current, a higher acceleration potential and a lower charge-to-mass ratio. Meanwhile the specific impulse is increased by a higher acceleration potential and a higher charge-to-mass ratio. All three of these parameters are controlled by two aspects of the thruster's design (the thruster's emitter, extractor and propellant feeding design) and the propellant used.

The effects of different emitter, extractor, and propellant feeding designs have been well-characterised in literature. The emitter tip radius has been found to significantly vary the amount of current emitted, with sharper emitters leading to a lower current [40, 41, 42] and the voltage at which the thruster begins to emit ions, termed the onset voltage, V_{onset} , reducing as the emitter becomes sharper [40, 41, 42]. Increasing the distance between the emitter and the extractor also increases the onset voltage, so that thrusters with larger extractor distances operate at higher voltages [43]. The flow rate through the emitters has a significant effect on the current emitted, where increasing the flow rate usually increases the current (although not always) but decreases the charge-to-mass ratios of emitted ion clusters and droplets [18, 44, 45, 46].

The effects of using different propellants have been less conclusively characterised in the literature. To briefly summarise the results from the literature, it is expected that a more conductive propellant with higher surface tension is generally more likely to produce ion clusters and droplets with a higher charge-to-mass ratio [25, 47]. However, for recent experimental data these relationships are not well followed [25, 28, 48], except for work by Villegas-Prados *et al* [49] which found that following a guideline of higher conductivity and surface tension promoted higher charge-to-mass ion emission. For all of these studies the consistent rule was that higher conductivity ionic liquids emitted more current, which was verified in the experimental data [25, 28, 48, 49].

Investigating the causes of the different charge-to-mass ratio ion clusters in different propellants could lead to a better understanding of the physics of ion emission in electrospray thrusters. This would allow ionic liquids, and therefore electrospray thrusters, to be able to more predictably perform in a variety of different regimes, for example higher thrust, lower specific impulse or higher specific impulse, lower thrust. Changing from either of these regimes for an electrospray thruster would be much easier

than any other thruster as only the propellant would have to be changed, meaning the same thruster could be used for many different purposes. It would also help in other fields where electrosprays are used, such as focused ion beams, as the necessary beam properties could be predicted beforehand.

1.3 Thesis Aims and Motivations

The available models for electrospray thruster ionic emission currently rely on a few key propellant properties, particularly conductivity and surface tension. However, experiments have mostly not been able to produce results which could be predicted by these properties, other than the current. One of the least predictable properties is the charge-to-mass ratio of emitted ion clusters, especially in pure ion emission, and what determines this based on the propellant. In this thesis, the main aim is to investigate the properties that affect the charge-to-mass ratios of emitted ion clusters using Time-of-Flight Mass Spectrometry of a single emitter porous electrospray thruster. The important aims in this are stated here:

- Create an experimental setup which includes a Time-of-Flight Mass Spectrometer.
- Identify alternative propellants which allow for testing a broad range of propellant properties.
- Show the key characteristics of a porous electrospray thruster operating on each propellant:
 - Current Emitted.
 - Plume energy.
 - Charge-to-mass ratios of ion clusters and their proportions.
- Utilise the experimental results to investigate the predictors of ion clustering size and therefore the charge to mass ratio.
 - Knowledge of these predictors would indicate what further research would have to be done in order to reveal relationships in ion cluster sizing.

Chapter 2

Emission and Plume Evolution of Porous Electrospray Thrusters

To investigate the ionic clustering of different propellants in porous electrospray thrusters, the physics of porous electrospray thrusters need to be understood sufficiently. In this chapter, an understanding of the ion evaporation process will be developed, beginning with the Taylor cone, followed by ion kinetics and the energy involved in the ion evaporation process. Then the ion kinetics will be applied to predictions of the current emitted by electrospray sources that have the most mature theoretical understanding. Next, the ion evaporation process will be used to investigate how possible sizing of clusters could be predicted and to create a qualitative understanding of the factors affecting ion clustering. Finally, the break-up of ion clusters in the plume of an electrospray thruster, termed fragmentation, will be discussed as it is a phenomena that plays a vital role in both thruster performance and interpreting experimental data.

2.1 The Taylor Cone and Emission

2.1.1 Droplet emission

Electrospraying involves the production of charged particles from the surface of a liquid due to the presence of a strong electric field. The advantage of this method of

ionisation, other than its scalability, is that it is a 'soft' ionisation method, meaning that little energy is imparted into the emitted charged particle. Soft ion emission means that much larger and stable charged particles can be formed, allowing for the easy creation of clusters of molecular ions. This is in contrast to other forms of ionisation such as electron impact ionisation, a 'hard' ionisation method that typically disassociates larger molecules when ionised. An effect of 'soft' ionisation is that a broad range of charge-to-mass ratio charged particles can be emitted, which leads to a broad range of thrusts and specific impulses, shown in Equations 1.5 and 1.6.

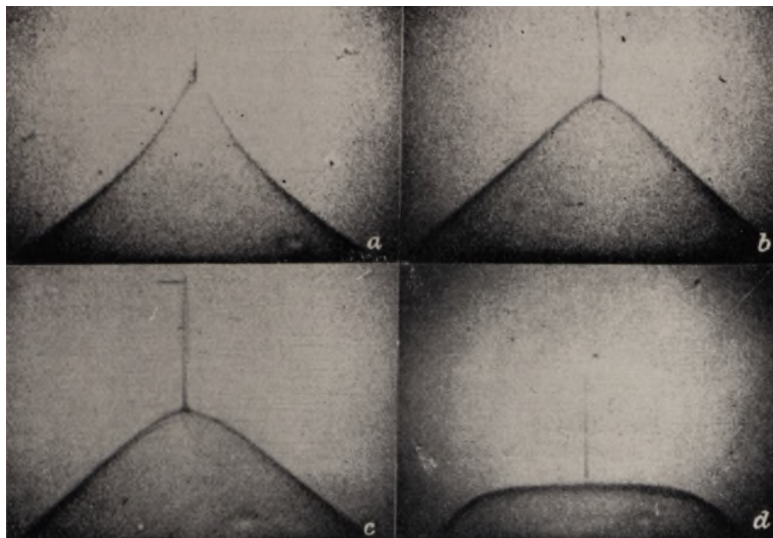


FIGURE 2.1: Four pictures showing the Taylor cone (a) and the subsequent collapse of it (b-d) [50].

At the core of the electro spraying phenomenon is the distortion of the surface of a liquid into a shape called a 'Taylor Cone'. When a conductive liquid is subjected to a strong electric field, the liquid meniscus responds to this field by distorting its shape. The meniscus distortion was investigated by Taylor in 1964 [50], who used a capillary with various liquids and applied an electric potential to it. Taylor showed theoretically and experimentally that the liquid meniscus forms a cone with a half angle of 49.3° , as illustrated in Figure 2.1. The impact that Taylor's studies had on the electrohydrodynamic behaviours of liquids led to the liquid meniscus created during electro spraying to be termed a 'Taylor' cone.

One of the important studies of the physics of electro spraying was the fundamental study of electro spraying by De la Mora and Loscertales [51]. In this paper, a series of experiments were completed on capillary sources to investigate the current emitted by an electro spray source. Six different liquids were tested to investigate a variety

of different propellant properties, with some of these being doped with salts to allow for a greater variation of the propellant conductivity. These sources were then electro-sprayed and their currents were recorded.

The experiments showed a relation between the emitted current and the volumetric flow rate applied to the capillary source. Furthermore, current was also related to the conductivity, surface tension and relative permittivity. The relationship found is:

$$I = f(\epsilon) \left(\frac{\gamma K Q}{\epsilon} \right)^{\frac{1}{2}}, \quad (2.1)$$

where I is the current, $f(\epsilon)$ is a function of the relative permittivity, γ is the surface tension, K is the conductivity, Q is the volumetric flow rate and ϵ is the relative permittivity. Furthermore, the charge-to-mass ratio can also be described as a function of conductivity and volumetric flow rate [47]:

$$\frac{q}{m} \propto \left(\frac{K}{Q} \right)^{0.429}. \quad (2.2)$$

Equations 2.1 and 2.2 have significant implications on the selections of propellants for capillary electro-spray thrusters, notably that the conductivity seems to play a vital role in determining the current and the charge-to-mass ratios of the emitted charged particles. In these early capillary sources, the charged particles emitted were typically primarily very low charge-to-mass ratio droplets, for example 41.7 Ckg^{-1} [44], leading to early thrusters having a very low specific impulse. For propellants, the important aim became increasing the conductivity as this would allow for an increase in current and a reduction in the size of the emitted charged particles translating to a higher thrust and specific impulse.

A continuous increase of conductivity of a propellant eventually leads Equation 2.2 to its 'maximum', where an electro-spray thruster only emits high charge-to-mass ratio ion clusters, achieved first by Romero-Sanz *et al* [18]. The pure-ion emission, a term applied to plumes that only emit high charge-to-mass ratio ion clusters, was facilitated by the use of a new type of propellant. This type of propellant was ionic liquids, specifically EMI-BF₄ for the experiment by Romero-Sanz *et al*. EMI-BF₄ has a high conductivity of

1.4 Sm^{-1} hence it was expected to produce a high current and high charge-to-mass ratio charged particles, therefore a high thrust and specific impulse.

However, conductivity does not always influence the charge-to-mass ratios of charged particles as shown in Equation 2.2. Gamero-Castaño and De La Mora [52] tested an even higher conductivity liquid, with a conductivity of 2.2 Sm^{-1} , which was found to emit the highest charge-to-mass ratio charged particles out of the other liquids tested in this experiment. However, pure-ion emission was not achieved by the liquid, despite it having a higher conductivity than EMI-BF_4 . This result seemed to indicate a diminished influence of the conductivity on pure-ion emission [18].

2.1.2 Pure-Ion Emission

One possible reason for the discrepancy of the factors influencing charged particle emission for different thrusters could be that the older electro spray thrusters often emitted mostly droplets, while current electro spray thrusters emit primarily ion clusters in pure-ion emission. Of the electro spray thrusters currently being developed or those which have been developed, including the PET-50 [53], the BET-300p [54] and a thruster by ienai space company [49], all of them emit a significant proportion of ion clusters.

The fundamental emission mechanism observed in pure-ion emission is different from that observed in droplet emission. These differences are highlighted in Figure 2.2, showing the shape of the meniscus during droplet emission, called cone-jet emission, and during pure-ion emission. For droplet emission, the mechanism of emission is based primarily on hydrodynamics and the propellant properties. A jet forms at the

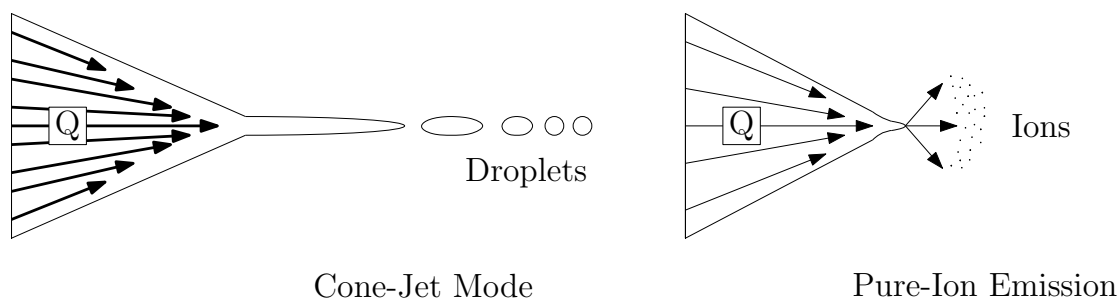


FIGURE 2.2: Two different modes of operation for an electro spray source showing droplet emission on the left hand side and ion emission on the right hand side.

tip of the Taylor cone meniscus that breaks apart due to the electric field and surface tension, producing small accumulations of neutral and charged molecules.

However, as the flow rate of the ionic liquid to the electrospray is reduced, the source begins to produce higher charge-to-mass ratio charged particles [47]. At a certain point, the emission of large droplets is completely suppressed, causing the cone-jet mode to transform into a pure-ion mode where the meniscus forms a small protrusion with a reduced volume [55], shown in Figure 2.2 on the right hand side. The process which emits these ions from the Taylor cone tip is called ‘ion evaporation’. During this process, an ion becomes energetic enough to exceed a certain energy threshold, called the ion solvation energy ΔG_s . Once this threshold is exceeded, the ion is emitted directly from the surface of a liquid meniscus. The energy for this emission is provided by the strong electric field produced in electrospray thrusters.

The process of electrospray ion emission was first investigated by Iribarne and Thomson [17], where the ion emission from the surface of a droplet was investigated. Although ion emission from the surface of a droplet is not fully reflective of pure-ion emission, due to pure-ion emission occurring on the surface of the meniscus, it is assumed that the process of electrospray ion emission is the same irrespective of the origin. Therefore, Iribarne and Thomson’s work is fundamental to pure-ion emission and will form the basis in the theoretical analysis in the next section.

2.2 Ion Evaporation

2.2.1 Ion Evaporation Kinetics

So far some equations have been introduced which indicate how current and charge-to-mass ratio of droplets and possibly ion clusters vary, however these equations consider plumes that emitted mostly or only droplets. As the process of ion emission is different, new equations will be introduced to attempt to describe how the current and charge-to-mass ratio of ion clusters may vary. This section will describe the fundamental kinetics of ion emission in order to begin to understand the process leading to ion cluster emission.

Ion emission in electrospray thrusters occurs due to the 'evaporation' of individual or clusters of ions from the surface of a liquid due to the presence of a strong electric field. For evaporation to occur, the ion or ion cluster has to overcome a certain level of energy called the ion solvation energy, ΔG_s . The ion solvation energy represents the energy required to take a liquid-phase ion (an ion within the ionic liquid) into a gas-phase ion, with this energy being determined by the strength of the chemical bonds that the ion has to the molecules within the liquid. This energy for an ionic liquid is typically assumed to be 1-2 eV [52], although this range is based from measurements of a non-ionic liquid. The energy required to emit these ions is generally too high for any meaningful amount of evaporation to occur from a purely thermal process (i.e. by heating up the ionic liquid).

In order to emit a significant ion current in an electrospray thruster, the ion solvation energy is reduced by the presence of an electric field. This reduction energy, called the energy reduction due to the presence of an electric field, ΔG_e , allows for the ions to be evaporated at a sufficiently high electric field strength. These two terms form the equation for the total energy of the system in the presence of the electric field, ΔG :

$$\Delta G = \Delta G_s - \Delta G_e. \quad (2.3)$$

The case for which significant ion evaporation begins to occur is when the reduction of energy due to the electric field exceeds the ion solvation energy, $\Delta G_e > \Delta G_s$. This condition produces an estimate of the electric field strength at which significant ion evaporation occurs, which typically is $\sim 1 \text{ Vnm}^{-1}$. To arrive at this number, ΔG_e needs to be described more fully. The image charge potential model can be applied [45], which describes ΔG_e as:

$$\Delta G_e = \sqrt{\frac{(n_q e)^3 E}{4\pi\epsilon_0}}, \quad (2.4)$$

where n_q is the number of charges in the ion (i.e. what charge does the cation and anion have in the ionic liquid, for example the EMI-BF₄ ions both have an $n_q = 1$), e is the elementary charge and E is the normal electric field strength at the tip of the meniscus. For most ionic liquids n_q is 1, which represents a single charge in the ion, however ions

that contain more than one charge exist and will be reviewed within this thesis. Taking the condition that the reduction in energy must be greater than the ion solvation energy, Equation 2.4 can be used to describe the electric field strength required for significant ion emission:

$$E_{crit} = \frac{4\pi\epsilon_0\Delta G_s^2}{(n_q e)^3}. \quad (2.5)$$

Equation 2.5 shows that the critical electric field for significant ion evaporation increases with the ion solvation energy, meaning that the molecular bonding of the ionic liquid plays a significant role in the onset of emission of ions.

A precise model of ion solvation energy, ΔG_s , for ionic liquids is not known, with previous attempts to use certain models being somewhat unsuccessful in predicting ion emission properties [16]. However, the models for ion solvation energy will be introduced here to at least provide a qualitative understanding of how the ion solvation energy may change with varying properties of ionic liquids. The most basic method to determine a form of ion solvation energy is to use the Born equation for ion solvation. The Born equation is [56]:

$$\Delta G_s \approx \Delta G_{Born} = \frac{(n_q e)^2}{8\pi\epsilon_0 r_i} \left(1 - \frac{1}{\epsilon}\right), \quad (2.6)$$

where r_i is the radius of the ion. It can be already seen from Equation 2.6 that some propellant properties have an impact on the ion solvation energy, specifically the charge state of the ions within the ionic liquid, the radius of the emitted ions and the relative permittivity of the ionic liquid. Two of these properties, n_q and r_i , are related to the molecular properties of the ion, instead of the bulk properties of the ionic liquid, already showing a deviation from droplet emission. However, this method of ion solvation energy prediction is inaccurate for use in ion electrospray emission. The main reason for this is the formula assumes an ion in a dielectric medium, meaning that electrostatic interactions would not affect the ion solvation energy. For ionic liquids, this is not the case as the ions will be relatively mobile in the liquid meaning that the intermolecular electrostatic interactions would be common, therefore affecting the ionic liquid solvation energy.

As an example, Equation 2.6 will be used to estimate the ion solvation energy for the EMI^+ ion. The radius of the ion is not trivial to determine, however a spherical estimate will be used here as was used by Larriba *et al* [16]:

$$r_i = \left(\frac{3m}{4\pi\rho} \right)^{\frac{1}{3}}, \quad (2.7)$$

where m is the molecular mass of the ion and ρ is the density. Taking the density of EMI-BF_4 (1240 kgm^{-3}) and the molecular mass¹ of EMI^+ (111.17 AMU) the ion radius is estimated as 0.329 nm. Finally, the ion solvation energy estimated by Equation 2.6 for EMI^+ is 2.018 eV, where the dielectric constant for EMI-BF_4 is 12.8 [57]. For EMI-BF_4 positive emission, the onset of emission was simulated at an electric field strength of $1.2 \times 10^9 \text{ Vm}^{-1}$ [58], corresponding to an ion solvation energy of 1.31 eV from Equation 2.4. The difference between the values of 1.31 and 2.018 eV are significant, especially when considering the evaporation equations in the next section, therefore this disagreement highlights the limitations of the ion solvation energy model.

A further refinement of this equation considers the inclusion of the effect of surface tension to the total ion solvation energy. The Born equation only estimates the energy that is required to change a liquid phase ion into a gas phase ion. However, this neglects some effects that occur during the emission process. One of these effects is the additional energy required to break the surface tension for an ion cluster to be emitted. Equation 2.6 can be refined by adding a surface tension component to represent the breaking of the surface tension, which can be shown by,

$$\Delta G_{\text{Born}, \gamma} = \frac{(n_q e)^2}{8\pi\epsilon_0 r_i} \left(1 - \frac{1}{\epsilon} \right) + 4\pi\gamma r_i^2. \quad (2.8)$$

The extra term on the right hand side of Equation 2.8 can only be positive, therefore the energy required to emit an ion cluster only increases when surface tension is considered. In order to produce a more reliable estimate of ion solvation energy, more factors would have to be considered that effect the ion solvation energy. However, even though Equation 2.8 produces incorrect results, it may be a useful tool to compare

¹From this point forward, except when specified otherwise, all the ion masses will be taken from <https://pubchem.ncbi.nlm.nih.gov/>.

the differences between different ionic liquids and therefore it will be applied to see how different ionic clustering may vary with different properties.

2.2.2 Ion Current in Pure-Ion Emission

Having investigated the kinetics of the ion emission process, the current emitted by the electrospray source can now be investigated. As ion emission requires a certain level of energy to be exceeded, it can be described by the Arrhenius equation. The rate of ion emission, N , can be described by [17]:

$$N = \frac{kT}{h} e^{-\frac{\Delta G}{kT}}, \quad (2.9)$$

where k is the Boltzmann constant, T is the temperature of the meniscus and h is Planck's constant. This equation is typically shown as the current density equation of the meniscus, where the reaction rate is multiplied by the charge density at the meniscus, σ , to produce current density, j :

$$j = \sigma \frac{kT}{h} e^{-\frac{\Delta G}{kT}}. \quad (2.10)$$

Equation 2.10 shows a clear correlation between the kinetics of the ion emission process, represented by ΔG , and the current emitted by the thruster. Furthermore, the temperature plays a key role in the ion current emitted by the thruster. The final component that is necessary in developing a model for current emission is the surface charge density of the meniscus. Although the exact surface charge density is not typically known, a method to model it is [59]:

$$\sigma = \epsilon_0(E - \epsilon E_n^i), \quad (2.11)$$

where E_n^i is the normal electric field strength inside the liquid. Equation 2.11 can be substituted into Equation 2.10 in order to create a more developed equation for the current density:

$$j = \epsilon_0(E - \epsilon E_n^i) \frac{kT}{h} e^{-\frac{\Delta G}{kT}}. \quad (2.12)$$

However, the internal electric field strength is difficult to determine, therefore one approach which has been developed to address this is by assuming that the current emitted by an electro spray thruster can be determined by Ohm's law, described by the equation

$$j = KE_n^i, \quad (2.13)$$

where K is conductivity. Comparing Equations 2.12 and 2.13, the two equations are equal to each other, therefore the equations can be rearranged in order to derive an expression for E_n^i :

$$\begin{aligned} j &= KE_n^i = \epsilon_0(E - \epsilon E_n^i) \frac{kT}{h} e^{-\frac{\Delta G}{kT}} \\ E_n^i(K + \epsilon_0 \epsilon \frac{kT}{h} e^{-\frac{\Delta G}{kT}}) &= \epsilon_0 E \frac{kT}{h} e^{-\frac{\Delta G}{kT}} \\ E_n^i &= \frac{\epsilon_0 E \frac{kT}{h} e^{-\frac{\Delta G}{kT}}}{(K + \epsilon_0 \epsilon \frac{kT}{h} e^{-\frac{\Delta G}{kT}})} = \frac{E/\epsilon}{1 + K\epsilon_0 \frac{kT}{h} e^{-\frac{\Delta G}{kT}}}. \end{aligned} \quad (2.14)$$

Finally, the current density can be expressed in terms which are known by substituting Equation 2.14 into Equation 2.13:

$$j = \frac{KE/\epsilon}{1 + K\epsilon_0 \frac{kT}{h} e^{-\frac{\Delta G}{kT}}}. \quad (2.15)$$

Equation 2.15 already shows that the current density will be affected by a lot of key parameters describe so far in this thesis, including the conductivity and the ion kinetics. However, Equation 2.15 can be further developed into an actual estimate for the current emitted by a meniscus undergoing ion emission. Firstly, the current I can be represented as the product of the current density multiplied by the area of emission from the meniscus, A_{em} :

$$I = jA_{em}. \quad (2.16)$$

Representing the area of emission from the meniscus for electrospray thrusters is a non-trivial task due to the fact that the meniscus can take non standard shapes, such as the one shown in Figure 2.3, similar to the menisci simulated by Coffmann *et al* [55]. Initially a simplifying assumption will be that the tip of the meniscus can be considered a hemi-sphere with radius r_{em} .

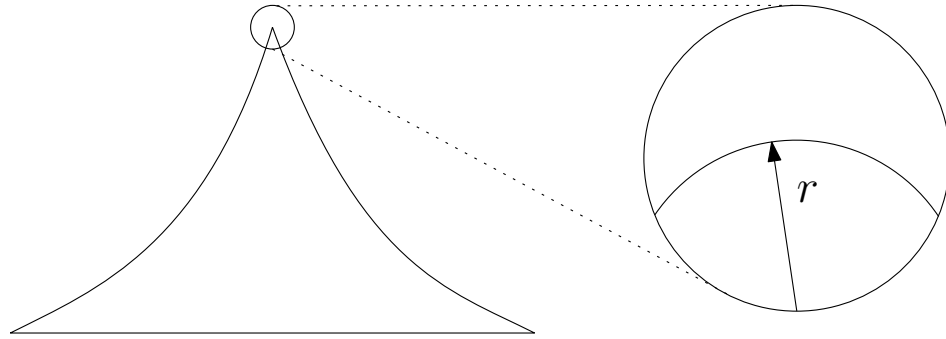


FIGURE 2.3: The conical shape of a highly stressed meniscus takes a non-circular shape, however when the meniscus tip is sufficiently magnified it is assumed to take the shape of a circle.

In order to determine r_{em} , the balance between electric stress and the surface tension on surface of the meniscus must be considered. The equation for the balance of the forces is:

$$\frac{1}{2}\epsilon_0 E^2 = \frac{\gamma}{r_{em}}, \quad (2.17)$$

which shows the the ‘stress’ created by the electric field must equal the force produced by the surface tension. Equation 2.17 can be re-arranged for the radius to be the subject of the equation, showing that:

$$r_{em} = \frac{4\gamma}{\epsilon_0 E^2}. \quad (2.18)$$

Equation 2.18 is only valid when there is a balance between the two forces. The area of emission will therefore be provided by the equation:

$$A_{em} = 2\pi r_{em}^2 = 2\pi \left(\frac{4\gamma}{\epsilon_0 E^2} \right)^2. \quad (2.19)$$

Hence an equation for current emission can be derived with known parameters by substituting Equation 2.19 and 2.15 into Equation 2.16:

$$I = 2\pi \left(\frac{4\gamma}{\epsilon_0 E^2} \right)^2 \frac{KE/\epsilon}{1 + K\epsilon\epsilon_0 \frac{kT}{h} e^{-\frac{\Delta G}{kT}}}$$

$$I = \frac{32\pi K\gamma^2}{\epsilon\epsilon_0^2 E^3 \left(1 + K\epsilon\epsilon_0 \frac{kT}{h} e^{-\frac{\Delta G}{kT}} \right)}. \quad (2.20)$$

However, Equation 2.20 shows some problems with the assumption that the radius of the meniscus varies with the electric field shown in Equation 2.18. The main problem is that the current decreases with an increasing electric field, as seen in Figure 2.4, whereas one would expect the inverse to be true from any experimental data due to the current increasing with the emitter potential.

Multiple solvation energies have been included in Figure 2.4 to investigate the effect of varying the solvation energy. It can be seen that the current emitted decreases with increasing electric field until it reaches a certain critical electric field, at which point the

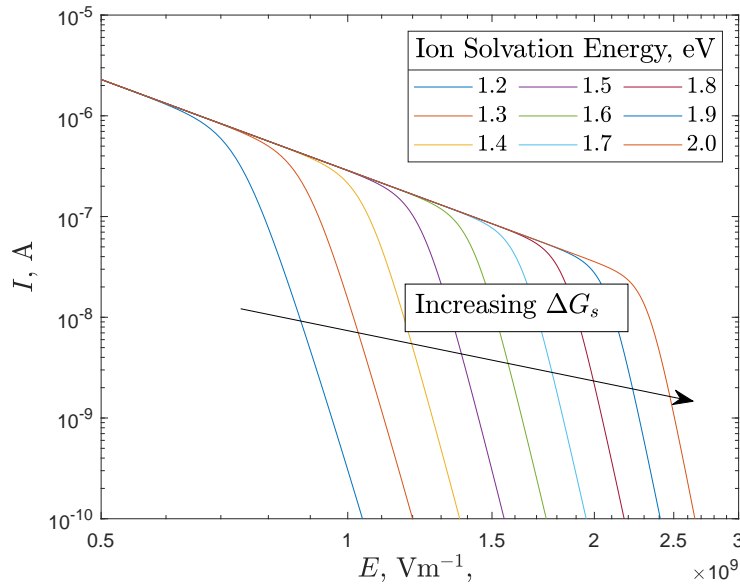


FIGURE 2.4: Variation of ion current with the electric field strength using Equation 2.20. The ion solvation energy was varied between 1.2 and 2.0 eV. As the electric field strength increases, the current decreases which is the inverse of what is seen during electro spray experiments.

current rapidly decreases to zero. Increasing the ion solvation energy does not reduce the current emitted as might be expected, however it allows for the ‘non-critical’ electric field range to be extended, so that the current begins to rapidly reduce at a higher electric field. Clearly this behaviour is non-physical as the kinetics of evaporation show that a lower ion solvation energy should increase the amount of ions emitted for a given electric field strength, therefore increasing the ion current. However, it could be possible that the higher ion solvation energy could allow for a more stable meniscus which may be hinted by Figure 2.4. This could be because the ion current is emitted at a lower rate and which perturbs the meniscus less, allowing for higher electric field operation.

A simple solution to this problem is to assume that the area of emission does not change as the electric field increases. In this assumption, although the radius of the meniscus may change, the actual area of emission does not. It will be assumed that the area of the emission will be the area of a circle taken by the meniscus where the radius of the circle is the radius of the meniscus at onset of emission, r_{onset} . Assuming that the liquid used is EMI-BF₄, the surface tension is 52.8 mNm⁻¹ [60] and the onset electric field strength is taken as 1 Vnm⁻¹. Using these two assumptions, r_{onset} is calculated as 23.9 nm using Equation 2.18, which corresponds to an area of 3.57×10^{-15} m². The constant area term will be termed A , hence Equation 2.20 can be rewritten as

$$I = A \frac{KE/\epsilon}{1 + K\epsilon\epsilon_0 \frac{kT}{h} e^{-\frac{\Delta G}{kT}}}. \quad (2.21)$$

Equation 2.21 is plotted in Figure 2.5, with a conductivity of 1.4 Sm⁻¹, surface tension of 52.8 mNm⁻¹ and a relative permittivity of 12.8. For the remainder of this section, these will be the default values used in the various examples. The figure shows that keeping the area constant ensures that as the normal electric field strength is increased, the current also increases, which seems to agree with experimental results. However, as with the changing emission area, the current emitted begins to rapidly decrease after the normal electric field strength exceeds a certain critical value. This critical value increases with increasing ion solvation energy, which could again suggest that a higher ion solvation energy enables emission at higher electric field strengths.

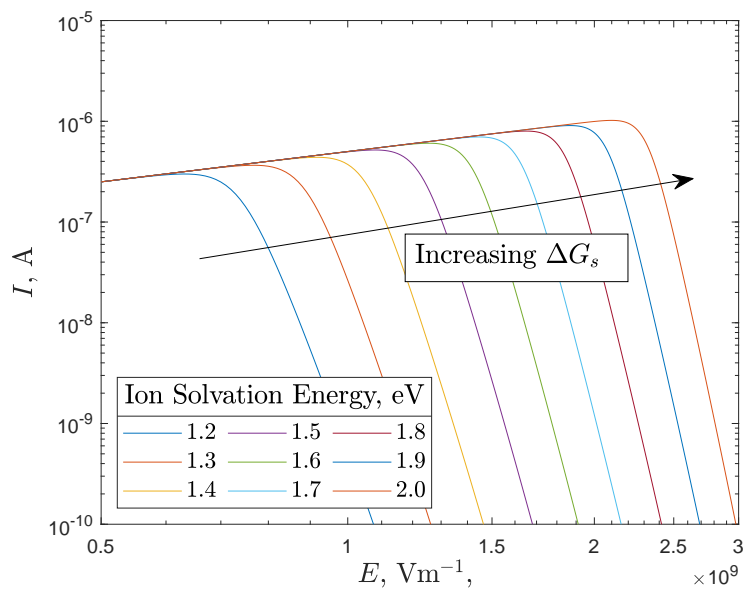


FIGURE 2.5: The current estimated to be emitted by EMI-BF₄ assuming a constant area of emission using Equation 2.21. The ion solvation energy was varied between 1.2 and 2.0 eV.

Although the model has been shown to produce results which do not seem physical, such as the varying the ion solvation energy not producing significantly different current results, the model will be used in order to investigate how certain propellant properties will vary the current emitted, specifically K , γ and ϵ . Alternative current models for electro spray thrusters exist, one of which is the multiple emission site model [61]. It reproduces experimental data accurately by assuming a constant current is produced by a single meniscus. However, multiple menscii appear as the voltage increases causing the total current to rise. This model will not be investigated further, however relevant texts are provided in the following references [61, 62].

The first propellant property which will be varied with Equation 2.21 will be the conductivity, K . It will be assumed for the three different propellant properties that the ion solvation energy is 1.8 eV. The conductivity has been experimentally shown to have significant influence on the current [25, 28, 49], therefore it is expected for Equation 2.21 to follow this relationship.

Figure 2.6 shows the variation of the current as the conductivity is varied, calculated using Equation 2.21. It can be seen that at a constant electric field as the conductivity

is increased the current increases, with the rate of change decreasing at higher conductivities. The figure agrees with experimental results at least in a qualitative sense as an increase in conductivity is expected to produce a higher current. However, as conductivity increases, the sensitivity of the current to the conductivity decreases, shown by the higher conductivity curves being closer together in Figure 2.6. This correlation does not agree with experimental data, for example Miller *et al* tested an ionic liquid with a conductivity approximately ten times the conductivity of EMI-BF₄ [32], finding the current was approximately ten times higher than the thruster operating on EMI-BF₄. Similarly, Villegas-Prados *et al* found that for seven different ionic liquids, the current for a given emitter voltage seemed to increase with an approximately quadratic relationship to the conductivity [49]. The lack of the model's predictive power is therefore highlighted by the disagreement with experimental data.

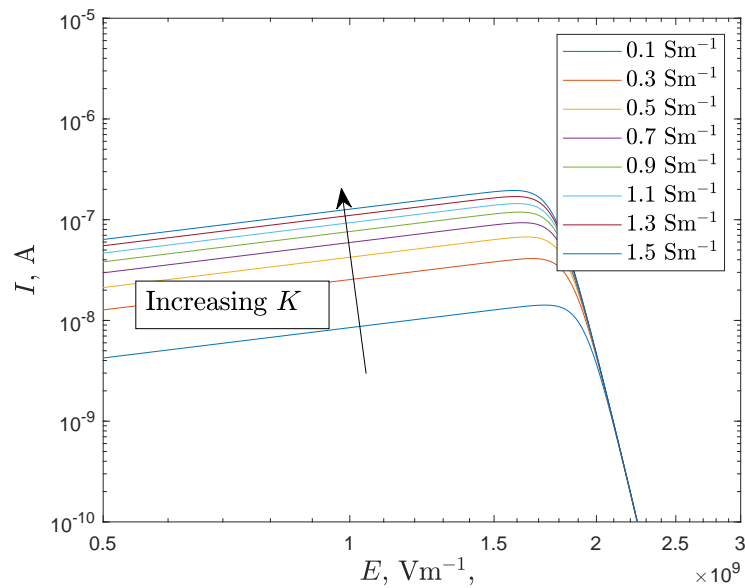


FIGURE 2.6: Current estimated to be emitted by an ionic liquid with a conductivity varying from 0.1 to 1.5 Sm^{-1} . It can be seen that as conductivity increases, the current increases although the rate decreases at higher conductivities.

Surface tension is another variable which seems to have a significant impact on the determination of the ion solvation energy and the area of emission, both being significant components in determining the ion current. Therefore, the effect of surface tension will also be investigated here, however due to the difficulty of separating the effects of surface tension and conductivity in ionic liquids it is difficult to cite experimental data which clearly demonstrates the effect of surface tension. From the considerations of

onset voltage, it is expected that as the surface tension increases, the current emitted will be lower, due to it increasing the onset voltage [40].

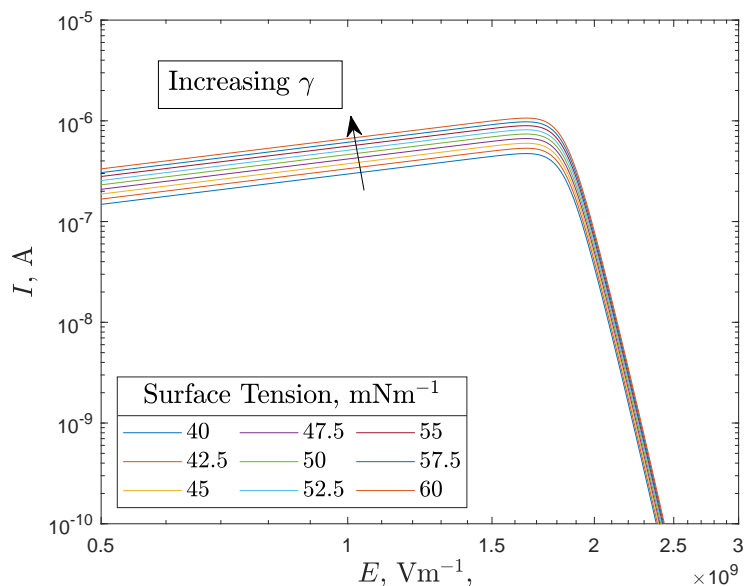


FIGURE 2.7: Current estimated to be emitted by an ionic liquid with a surface tension varying from 40 to 60 mNm^{-1} . As the surface tension increases, the current increases which is inaccurate due to the considerations of the onset voltage.

Figure 2.7 shows the effect of increasing the surface tension on the emitted current. As the surface tension is increased, the current emitted by the meniscus is also increased. As with the ion solvation energy, this does not seem to agree with the expected result considering the effects of increasing surface tension on the onset voltage. The surface tension could be considered as a macroscopic representation of the strength of the intermolecular bonds of the ions at the surface of the meniscus, therefore it might be expected that as surface tension increases, current decreases.

The final propellant property varied was the relative permittivity, shown in Figure 2.8, which decreases the current emitted as the relative permittivity is increased. Since the relative permittivity is an indicator of the reduction in strength of the electric field relative to the strength of the electric field in vacuum, it would be expected that increasing the relative permittivity decreases the ion current. This is because relative permittivity can be considered as reducing the electric field within the meniscus, in agreement with Equation 2.21.

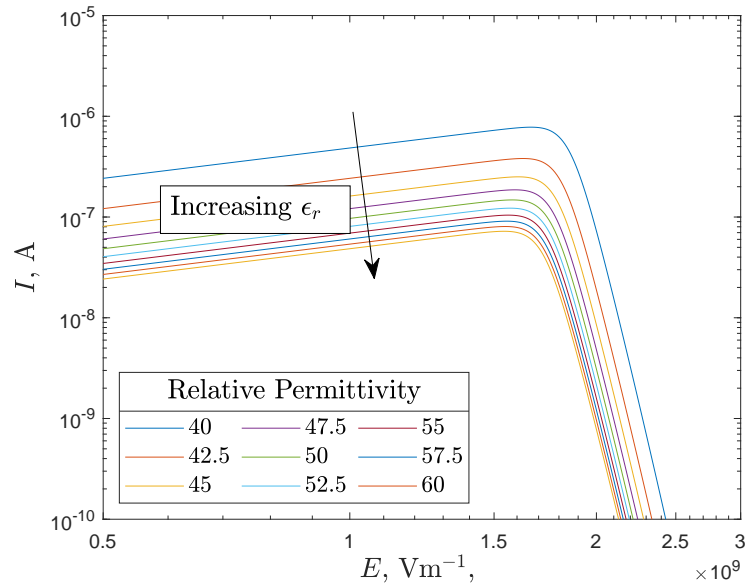


FIGURE 2.8: Current estimated to be emitted by an ionic liquid with a relative permittivity range of 10 to 90. As the relative permittivity is decreased, the current increased which reflects the expected behaviour of the ion current.

To summarise, the ion current equation (Equation 2.21) suggests that the best propellant has a high conductivity and surface tension while minimising the relative permittivity. Practically, it is difficult to measure the relative permittivity, therefore the typical propellant properties that are considered are the conductivity and surface tension. The most significant effect on the current was produced by varying conductivity, in agreement with previous experimental work focusing on varying this propellant property. However, the relative permittivity could still have a significant effect on the emitted current. For the purposes of the experiments in this thesis, the relative permittivity has unfortunately not been measured. Therefore, relative permittivity will not be considered in the data presentation and analysis except for two ionic liquids that have literature values for the relative permittivity.

2.3 Ion Cluster Size

With the emission of current reviewed, a review of the physics of ion clustering will now be explored. Although this is not a well understood phenomena in ionic electro-spray propulsion, some insights will be provided into how the charge-to-mass ratios of

ion clusters could be controlled. The possible methods for the prediction of clustering of ions will be investigated based off of the Born approximation, with a focus on the effects of various propellant properties. The physical phenomena called ‘fragmentation’ will also be explored due to it changing the sizes of clusters after emission and playing an important role in the experimental data.

2.3.1 Predicting Cluster Sizes

The determination of the ion cluster sizes in electrospray thrusters is not a well understood phenomena, with little investigation being done into the fundamentals of its emission. In section 2.1 it was discussed that the ion cluster sizes are not well predicted by the equations used for droplet-dominated electrospray thrusters, such as Equation 2.2. The previous section also discussed some ion kinetics based equations for current emission, which showed some correlation with certain propellant properties. In this section, a method to identify the most possible ion size will be introduced, continuing from Larriba *et al* [16].

Revisiting Equation 2.8, the ion solvation energy is driven by the ion radius, r_i , which corresponds to ion size. This has been plotted in Figure 2.9 using the ionic liquid properties of EMI-BF₄. It can be seen that the ion energy required to emit an ion of a given ion radius has a minimum value. This appears to suggest that the Born approximation can be used to predict an ion size which requires minimum energy to emit and therefore perhaps the most likely ion size to be emitted. It has already been discussed that this equation is likely somewhat inaccurate, however it will be used from here to attempt to predict quantitatively what ions are emitted by an electrospray thruster.

In order to find the minimum energy required to solvate an ion it is possible to differentiate Equation 2.8. Differentiating with respect to r_i produces the equation,

$$\frac{d\Delta G_{Born, \gamma}}{dr_i} = 8\pi\gamma r_i - \frac{(n_q e)^2}{8\pi\epsilon_0 r_i^2} \left(1 - \frac{1}{\epsilon}\right). \quad (2.22)$$

Equation 2.22 has been plotted in Figure 2.10, with a line at $y = 0$ in order to help in indicating the point of zero gradient. It can be seen that the minimum gradient, therefore

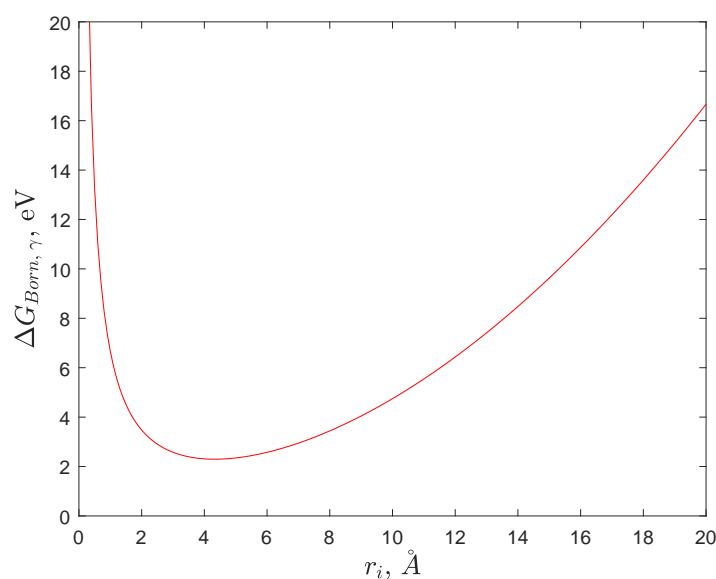


FIGURE 2.9: Ion solvation energy required to emit an ion of various ion radii, taking a minimum at approximately 4 Å possibly corresponding to the most likely ion size to be emitted.

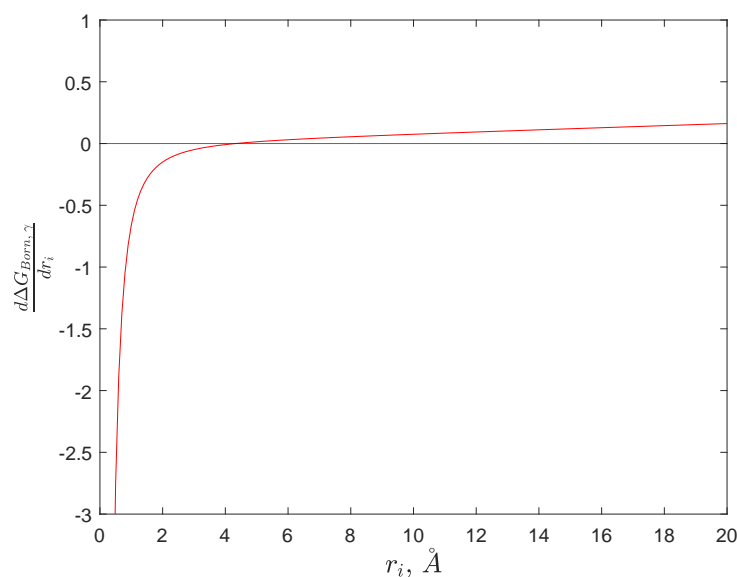


FIGURE 2.10: Gradient of the ion solvation energy required to emit an ion of varying ion radius. A line at $y = 0$ has been added in to help visualise the point of minimum gradient at which the lowest energy is required to emit an ion cluster.

minimum energy, ion radius is approximately 4.3 Å. Using an ion radius approximation [16],

$$r_i = (3m/4\pi\rho)^{\frac{1}{3}}, \quad (2.23)$$

it is possible to estimate the ion radii of EMI-BF₄ ions which are closest to the minimum

energy ion radius. The ion radii of a monomer and a dimer are hence approximated as 3.29 Å and 4.62 Å, respectively. The calculation of these sizes is likely inaccurate as the calculation assumes the ion cluster forms a sphere, which is highly improbable due to the various non-spherical molecular ion shapes and the many different conformers, or arrangements, possible with ion clusters. Nonetheless, assuming the minimum solvation energy ion would be the most likely ion emitted, Equation 2.22 suggests that dimers are the most probable ion emitted by EMI-BF₄.

To further the Born energy model, a statistical approach can be taken. This statistical approach will involve producing a probability distribution of ions from the Born approximation. From this probability distribution, a modelled plume composition can be derived.

The first step in this analysis is to produce a probability distribution of ion emission. In order to represent ion clusters numerically the neutral number n will be used to represent each species, with the scheme for this being introduced in Table 1.1. The approximation of ion radius can thus be rearranged to estimate the neutral number of an ion, therefore allowing for easy classification, by

$$m = \frac{4\pi\rho r_i^3}{3} \quad (2.24)$$

$$m = m_i + nm_n \therefore$$

$$n = \frac{1}{m_n} \left(\frac{4\pi\rho r_i^3}{3} - m_i \right), \quad (2.25)$$

where m_n and m_i are the neutral and ion mass respectively in kg, with the value for these in EMI-BF₄ in AMU being 197.97 and 111.17 respectively². The ion emission probability will be assumed to take the form of a Boltzmann distribution [16],

$$e^{-\frac{\Delta G_s}{kT}}. \quad (2.26)$$

For this model, $\Delta G_s = \Delta G_{Born, \gamma}$, and therefore it can be represented using neutral number in order to produce a distribution based on the neutral number size:

²Ion mass sizes for all ions in this thesis have been acquired from <https://pubchem.ncbi.nlm.nih.gov/> unless specified otherwise.

$$\Delta G_s = \Delta G_{Born, \gamma} = \frac{(ne)^2}{8\pi\epsilon_0 \left(\frac{3(m_i + nm_n)}{4\pi\rho}\right)^{\frac{1}{3}}} \left(1 - \frac{1}{\epsilon}\right) + 4\pi\gamma \left(\frac{3(m_i + nm_n)}{4\pi\rho}\right)^{\frac{2}{3}}. \quad (2.27)$$

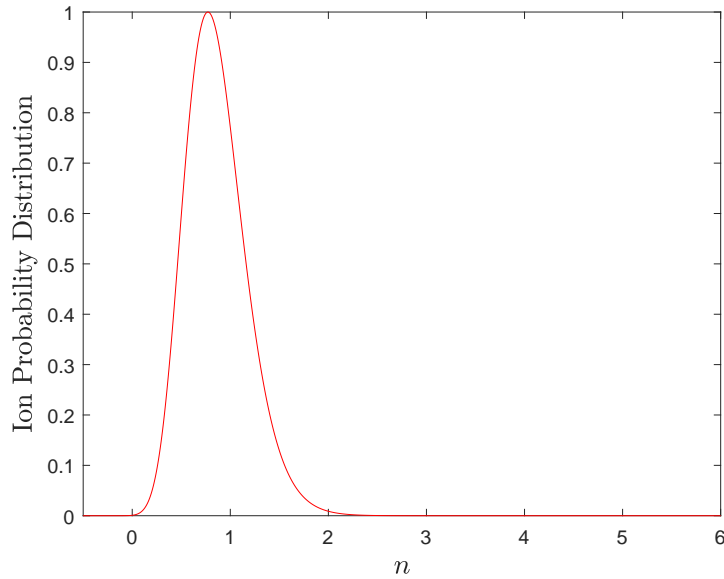


FIGURE 2.11: Probability distribution function for EMI-BF₄ positive ion emission, with the probability normalised with peak probability at $n = 0.777$. This corresponds to the most common emitted ion being close to the size of a dimer.

Equation 2.27 has been plotted in Figure 2.11. It can be seen that the highest probability occurs at $n = 0.777$, with which the rest of the data was normalised to, agreeing with the previously discussed ion radius values. The closeness of this value to $n = 1$ suggests that dimers should be the most common type of ion emitted, agreeing with the experimental data.

2.3.2 Comparison with Experimental Data

To investigate how effectively this model predicts the ion cluster size distribution, a comparison to experimental data will be made in this subsection. As a discrete distribution is produced by experimental data, the probability distribution in Figure 2.11 must be converted into discrete data in order for the data to be comparable. It will be assumed that the probability of a given ion cluster size, $p(n)$, will be equal to the area between $n - 0.5$ and $n + 0.5$. The integral for this equation is:

$$p(n) = \int_{n-0.5}^{n+0.5} e^{-\frac{\Delta G_s}{kT}}. \quad (2.28)$$

In order to produce a modelled distribution of ion cluster sizes, the probability for each ion cluster size shall be divided by the sum of all the probabilities. This can be defined as,

$$P_n = \frac{p(n)}{\sum_{i=0}^2 p(i)}, \quad (2.29)$$

where $P(n)$ is the proportion of an ion cluster of size n . It will also be assumed that no ions bigger than trimers, $n = 2$, are emitted due to a very small probability of emitting quadramers and larger clusters. Using this method the modelled ion cluster distribution for EMI^+ ions has 14.8% monomers, 82.9% dimers and 2.3% trimers. Similarly, for BF_4^- the model predicts an ion plume of 5.7% monomers, 89.9% dimers and 4.4% trimers. These proportions have been summarised in Tab. 2.1.

TABLE 2.1: Monomer, dimer and trimer distributions using the Boltzmann ion cluster distribution.

Proportions of EMI-BF_4 ion clusters.		
Ion Cluster Size	EMI^+	BF_4^-
$n = 0$	0.148	0.057
$n = 1$	0.829	0.899
$n = 2$	0.023	0.044

To validate the model, comparison with experimental data are required. A non-exhaustive selection of EMI-BF_4 data that emit only or mainly ion clusters was chosen and is shown in Tab. 2.2. Two different types of emitters were used for these experimental data, porous [27, 28, 34, 63] and externally wetted emitters [24, 49]. For two of these studies [24, 63], the proportions were calculated using WebPlotDigitizer³. The droplet proportions were not included in these data for [49, 63] as these are assumed to be emitted by a separate phenomena. The quadramers emitted in [34] were also not included in these tables, although the plume was comprised of 2% quadramers for both polarities.

³<https://automeris.io/>

TABLE 2.2: Experimental monomer, dimer and trimer distributions using EMI-BF₄.

Experimental data of EMI-BF ₄ ion cluster distribution.			
Ion Cluster Size	EMI ⁺	BF ₄ ⁻	Reference
$n = 0$	0.509	0.426	[27]
$n = 1$	0.491	0.574	
$n = 2$	0.000	0.000	
$n = 0$	0.685	0.527	[28]
$n = 1$	0.290	0.426	
$n = 2$	0.025	0.047	
$n = 0$	0.478	0.406	[24]
$n = 1$	0.485	0.456	
$n = 2$	0.040	0.138	
$n = 0$	0.45	0.39	[34]
$n = 1$	0.47	0.51	
$n = 2$	0.05	0.08	
$n = 0$	0.56	0.59	[49]
$n = 1$	0.35	0.35	
$n = 2$	0.09	0.06	
$n = 0$	0.274	0.356	[63]
$n = 1$	0.639	0.558	
$n = 2$	0.087	0.084	

Comparing the modelled plume distribution and the experimental plume distributions, a few key points can be determined. The correct types of ions are predicted by the model that are experimentally emitted by pure-ion plumes, with these being monomers, dimers and trimers. However, the modelled composition is not consistent with the experimental data, with the proportion of dimers being greatly over predicted. A similar problem was encountered by Larriba *et al* when using this method as the distribution of ions was not broad enough [16]. The larger sizes of the BF₄⁻ anions seems to agree with half of the experimental data [27, 28, 34], while the other half of the data show similar to smaller sizes of the cations [24, 49, 63].

To summarise, the ion emission model does not produce accurate proportions of ions, although the types of ions that might be emitted from EMI-BF₄ seem to be predicted well. The types of ions emitted by these pure or nearly pure-ion experimental data are primarily monomers, dimers and trimers, all of which are predicted by the model. A better agreement between the ion emission model and the experimental data maybe achieved if the components contributing to ΔG_s are further examined.

2.3.3 Considerations for Ionic Emission

One major inaccuracy of this method is a lack of the representation of the upstream flow conditions within the thruster, which play a key role in determining the ion cluster sizes. This is true for porous electro spray thrusters, shown by experimenting with porous reservoir pore sizes by Courtney and Shea [63]. The changing distributions in Tab. 2.2 might suggest this as well, as the differences in ion cluster distributions are possibly caused by the differences in hydraulic design of different thrusters, affecting the upstream conditions.

However given a lack of the knowledge of how this affects the ion solvation energy, a term for this will not be included. In the experimental work done in this thesis, the emitter and propellant tank design were not changed between experiments in order to eliminate the possibility that this would affect the different propellant data. This should ensure that the ion size distribution in chapter 5 will be comparable due to similar upstream conditions. Nonetheless, a better agreement between the modelled and the experimental data would likely be reached if the effects of the upstream conditions are considered.

Another possible consideration is what temperature the ions are emitted at. So far in this thesis it has been assumed that the ions are emitted at room temperature, 293.15 K. However, theoretical and experimental testing on ionic liquid ion sources has shown that the ion temperature may be much higher than expected. Miller showed that based on experimental testing, the ion temperature could reach as high as 800 K [64, 65]. Petro *et al* [66] showed that good agreement can be reached between experimental and numerical data by varying the temperature of the emitted ion clusters. These studies seem to indicate that the emitted ion clusters could be emitted at temperatures much higher than bulk conditions.

Applying the increased temperature to the ion probability distribution function, the probability distribution will vary due to these temperature changes. This variation arises because both the Boltzmann distribution is a function of temperature and the propellant properties in Equation 2.27 also vary with a changing temperature. In order to examine how the ion probability distribution function varies with temperature, all the propellant properties will be varied first to see each property's contribution to the

ion size distribution. These contributions will also provide an insight into how different ionic liquid properties might affect the ions they emit.

For these calculations, the temperature will be varied from room temperature, 293 K, up to 90% of the EMI-BF₄'s decomposition temperature, $0.9T_d$, which corresponds to a temperature of 613 K. Although this is lower than the ion temperatures from [64, 65], it will be assumed that that conditions at the tip of the Taylor Cone will remain below this temperature. The propellant property values for Equation 2.27 will be the same as for EMI-BF₄, unless stated otherwise.

Assuming no variation in any other variable, the effect of varying surface tension is shown in Figure 2.12. The figure shows that as the surface tension increases, the most probable size of ions emitted decreases, meaning that at higher surface tensions, smaller ions will be emitted. Garoz *et al* [48] tested ionic liquids with various surface tensions. It was found that there was some correlation with surface tension, with higher surface tensions reducing the size of ion clusters emitted. However, it was also noted in [48] that other studies [67] showed similar ion emission with lower surface tension ionic liquids, therefore the relationship between surface tension and the sizes of ions is not necessarily clear.

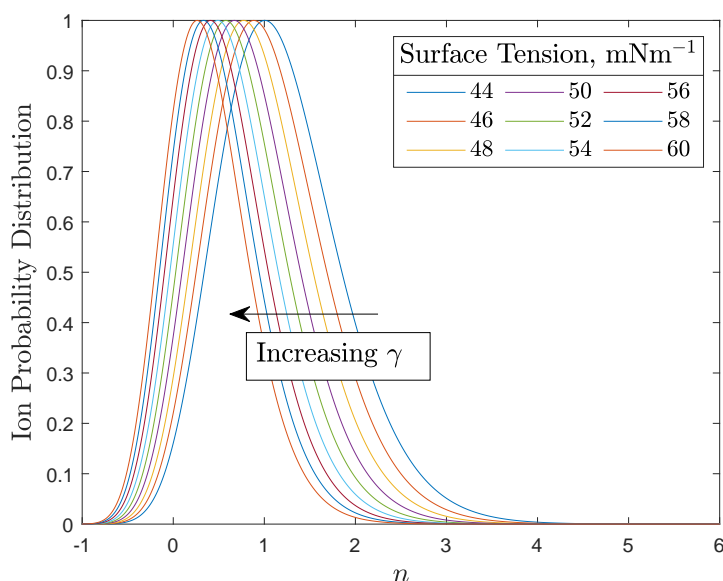


FIGURE 2.12: Probability distribution function for EMI-BF₄ positive ion emission with a varying surface tension from 0.044 to 0.06 Nm⁻¹. As the surface tension is increased, the curve shifts towards a lower n value corresponding to smaller ions being emitted at higher surface tensions.

The surface tension changes as a function of the temperature, described by the equation [68]:

$$\gamma = \gamma_0 \left(1 - \frac{T}{T_C}\right)^{n_\gamma}, \quad (2.30)$$

where γ_0 is a reference surface tension value, T_C is the critical temperature of the liquid and n_γ is an empirical scaling constant taken as $n_\gamma = \frac{11}{9}$ for organic ionic liquids such as EMI-BF₄ [69]. The equation shows that as the temperature is increased, the surface tension decreases and therefore the ions become more clustered when emitted. Assuming that EMI-BF₄ has a surface tension of 0.052 Nm⁻¹ at 293 K, γ_0 can be calculated, allowing for the equation for EMI-BF₄ surface tension to be calculated:

$$\gamma_{EMI-BF_4} = 0.0745 \left(1 - \frac{T}{1148}\right)^{\frac{11}{9}}, \quad (2.31)$$

where T_C is taken as 1148 K [70].

The second component of Equation 2.27 which varies with temperature is the relative permittivity. Firstly, it is important to consider the relationship between the ion emission probability function and a changing relative permittivity. Figure 2.13 shows that as the relative permittivity increases, the probability distribution shifts towards a higher n meaning that larger ions are more likely to be emitted. This effect becomes diminishing with higher relative permittivity, which is shown by the reduction of the distances between each line.

The temperature dependence of relative permittivity for ionic liquids is generally that as the temperature is increased, the relative permittivity decreases in a non-linear manner [71]. However as far as the author is aware, there is not an effective model to predict the effect of temperature on relative permittivity, except for experimental data. For EMI-BF₄ a linear regression model can be used to model the variation of relative permittivity for a range of temperatures up to 338 K [72]. Although the linear regression model will be inaccurate in the range of temperatures that will be used here, up to a maximum of 613 K, it will nonetheless be applied to give a method of varying the relative permittivity with respect to the temperature. In the linear regression model, the relative permittivity for EMI-BF₄ varies with the temperature with a gradient of

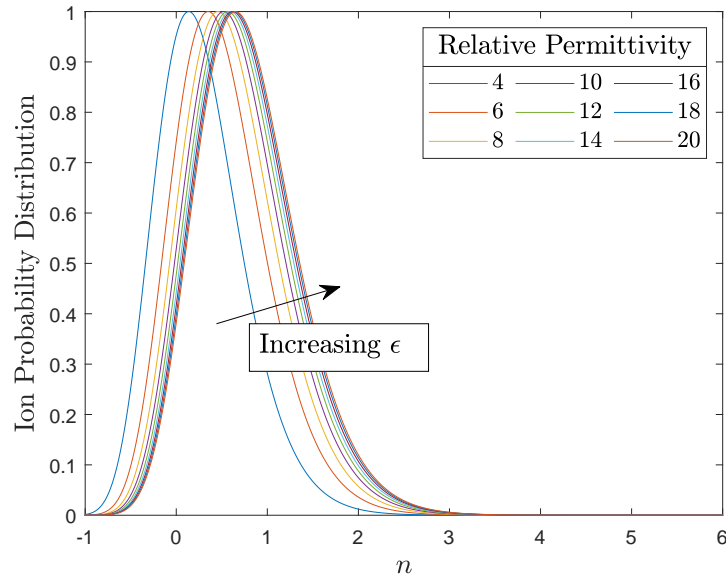


FIGURE 2.13: Probability distribution function for EMI-BF₄ positive ion emission with a varying relative permittivity from 4 to 20. As the relative permittivity increases, the curves shift further right at a higher n value, corresponding to larger ion emission

$\frac{d\epsilon}{dT} = -0.041$. It will be assumed that the relative permittivity will vary with the equation [72]:

$$\epsilon_{EMI-BF_4} = A + \frac{d\epsilon}{dT}T = 26.813 - 0.041T. \quad (2.32)$$

Equation 2.32 produces a relative permittivity of 14.5 at a temperature of 293 K, higher than so far used, however it allows for the extrapolation of the model to $0.9T_d$, at which the relative permittivity would be 1.63. This is inaccurate as the dielectric constant would likely begin to plateau at higher temperatures and therefore would not reach the low values predicted by Equation 2.32. However, lacking a better model, this equation will be used.

The final component of ΔG_s that will vary significantly is the density of the propellant. As with the previous two properties, the effect of changing density on the ion probability distribution will be investigated first. Figure 2.14 shows the relationship between the ion emission probability function and the density. As the density is increased, the ion distribution shifts further right indicating that heavier ions will be emitted. Interestingly, it also seems to broaden probability distribution, meaning a broader range of

ion clusters will be emitted.

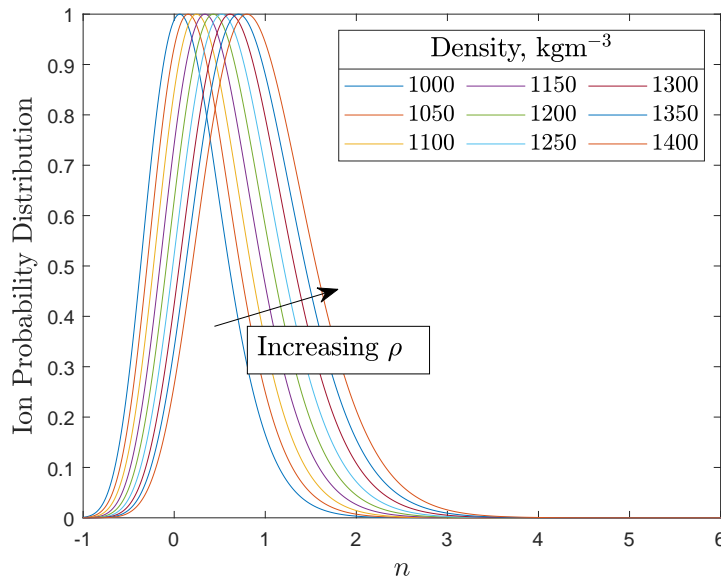


FIGURE 2.14: Probability distribution function for EMI-BF₄ positive ion emission with a varying density from 1000 to 1400 kgm⁻³. Larger ions are more likely to be emitted as the density increases.

The ionic liquid density's dependence on temperature can be modelled using a simple equation [73]:

$$\rho = \frac{m}{NV_0(a + bT + cP)}, \quad (2.33)$$

where N is Avogadro's number, V_0 is the molecular volume at the reference temperature, a , b and c are empirical constants and P is the pressure at which the ionic liquid is maintained. Since the testing is done in vacuum conditions, it is expected that cP is negligible. V_0 is assumed to be the sum of the volumes of each individual ion, which for EMI-BF₄ is equal to 255×10^{-30} m³. The molecular weight for EMI-BF₄ is 0.198 kgmol⁻¹, whilst coefficients a and b have been found to be 8.005×10^{-1} [73] and 6.652×10^{-4} K⁻¹ [74] respectively. Combining these constants together, a density equation for EMI-BF₄ can be produced as only a function of temperature:

$$\rho_{EMI-BF_4} = \frac{1289}{8.005 \times 10^{-1} + 6.652 \times 10^{-4}T}. \quad (2.34)$$

At room temperature, Equation 2.34 provides a density value of 1289 kgm^{-3} , which is in agreement with experimental data.

Having now introduced the temperature variation of all these three components, it will now be possible to investigate how the ion probability function will vary with a variation in the temperature of the meniscus. This will be done in order to have a ‘correction’ factor, which can be used to explain why there maybe a difference in the experimental and modelled data.

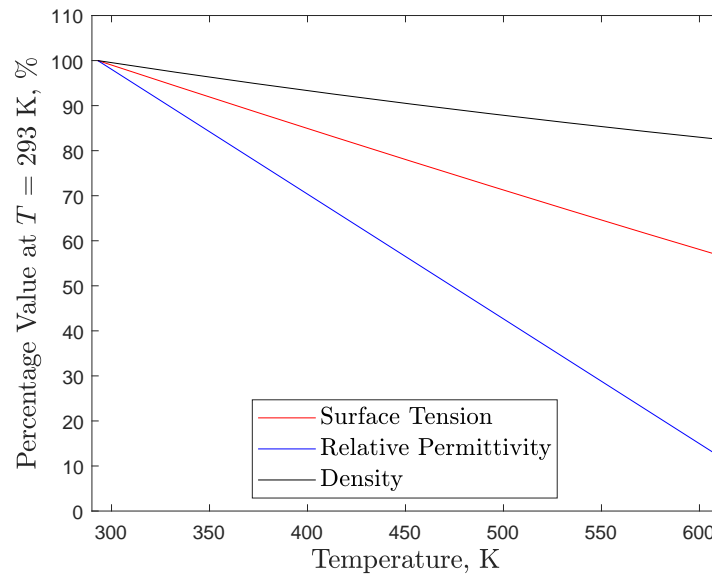


FIGURE 2.15: Percentage change in surface tension, relative permittivity and density for EMI-BF₄. Increasing temperatures cause the each of the propellant properties to decrease, with relative permittivity decreasing the most.

The change in each of the three propellant properties is shown in Figure 2.15. It shows that the surface tension, relative permittivity and the density decrease as the temperature is increased. Furthermore, the relative permittivity of the ionic liquid decreases the most, with a reduction of almost 90% in the range of temperatures considered. The temperature for this figure was varied between 293 K and 613 K, i.e. between room temperature and $0.9T_d$.

Figure 2.16 shows the variation in the ion probability distribution with respect to the temperature of the meniscus, including the effect of temperature on the surface tension, relative permittivity and density. As the temperature is increased, the most probable ion cluster has a larger n , corresponding to higher clustered ions to be emitted on average. The variation is relatively small, with an increasing temperature slightly increasing

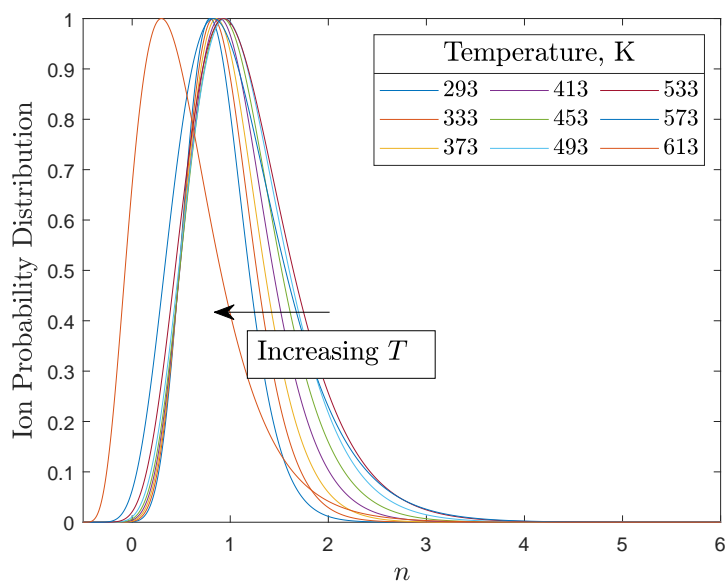


FIGURE 2.16: Probability distribution function for EMI-BF₄ positive ion emission with a temperature varying from 293 to 613 K. As the temperature increases, the likely size of ions increases. At the temperature limit, $T = 613$ K, the probable ion sizes are significantly smaller due to the anomalously low relative permittivity.

the width of the distribution function and moving it more to the left. This would suggest that at higher temperatures, a more varied plume is expected to be seen, with a higher probability for trimer emission.

The exception to this is the furthest left curve which occurs at the highest temperature of 613 K, at which the relative permittivity is 1.68 causing a significant reduction in ΔG_s . From Equation 2.27 it can be seen that the left hand-side term is multiplied by a factor of $1 - \frac{1}{\epsilon}$, which is significantly reduce at a relative permittivity of 1.68 causing the large reduction in ion solvation energy, hence the significant shift in the ion distribution function.

Using the temperature effect, the modelled EMI-BF₄ ion cluster distribution can be recalculated and compared with experimental data. These calculated data are found in Tab. 2.3 for both positive and negative emission. It shows that as the temperature is increased, the plume emits larger ion clusters. However at 613 K, due to the low relative permittivity, the probable ion sizes are significantly lighter, with monomers comprising 47.6% and 37.3% of the plume for positive and negative polarity, respectively.

TABLE 2.3: Ion cluster size distributions calculated to take into account the effect of temperature.

Positive Polarity							
Ion Cluster	Temperature, K						
n	313	363	413	463	513	563	613
$n = 0$	0.116	0.090	0.073	0.063	0.062	0.090	0.476
$n = 1$	0.840	0.812	0.756	0.686	0.623	0.596	0.449
$n = 2$	0.044	0.097	0.165	0.233	0.278	0.266	0.068
$n = 3$	0.000	0.001	0.006	0.019	0.037	0.048	0.008
Negative Polarity							
$n = 0$	0.044	0.036	0.030	0.027	0.029	0.048	0.373
$n = 1$	0.880	0.816	0.734	0.651	0.585	0.574	0.529
$n = 2$	0.076	0.146	0.226	0.296	0.355	0.316	0.087
$n = 3$	0.000	0.003	0.010	0.027	0.051	0.063	0.010

Assuming that the 613 K case for EMI-BF₄ is physical, it would match better with most of the experimental data review in Tab. 2.2. However, it would be unlikely that the relative permittivity would reduce to as low as 1.63. Furthermore, assuming that the temperature discussed here is the temperature of the meniscus, it is also unlikely that the meniscus would be able to get sufficiently hot to reach 613 K. Therefore, although these data show the possibility of this model matching experimental data well, further work is required to explore factors contributing to ΔG_s . These contributing factors might reduce ΔG_s , therefore produce a higher proportion of monomers in the plume.

2.3.4 Alternative Propellants

So far only EMI-BF₄ has been discussed as a propellant for electrospray thrusters. However, many different propellants have been tested in the literature. An overview of a selection of these studies will be provided in this subsection.

EMI-BF₄ is one of the two most common ionic liquids used in electrospray thruster research. The other ionic liquid that is commonly used is 1-ethyl-3-methylimidazolium bis(trifluoromethylsulfonyl)imide (EMI-Im). However, for similar electrospray thrusters, this ionic liquid has a greater propensity to emit droplets [63] making it less suitable for comparison to the ionic cluster emission model presented.

One study where a pure-ionic mission is reached with EMI-Im is by Legge and Lozano [28]. When EMI-Im was tested, it was found to only emit monomers and dimers as opposed to monomers, dimers and trimers by EMI-BF₄. Thus these experimental results can be compared with the ion cluster emission model, given that EMI-Im has a surface tension of 38.8 mN/m [75], a density of 1580 kg/m [75] and a relative permittivity of 13.8 [76].

TABLE 2.4: Comparison of modelled ion cluster size and experimental ion cluster sizes [28] for EMI-Im assuming $T = 293$ K.

EMI ⁺		
Ion Cluster	Modelled	Experimental
$n = 0$	0.030	0.539
$n = 1$	0.939	0.456
$n = 2$	0.031	0.005
Im ⁻		
$n = 0$	0.633	0.641
$n = 1$	0.366	0.330
$n = 2$	0.001	0.029

The modelled ion cluster size distribution compared to the experimental ion cluster size distribution is shown in Tab. 2.4. For the positive polarity, as with EMI-BF₄, it can be seen that the model over-predicts the presence of dimers in the plume. However, interestingly for the negative polarity, the modelled ion cluster distribution matches well with the experimental data. Comparing these results, alongside the EMI-BF₄ comparisons, it can be seen that the types of ion clusters that are emitted are predicted correctly. However, the emission of monomers is not accurately predicted as significantly more positive monomers are seen in the experimental data than in the modelled data.

In the negative polarity, the ion cluster distribution are predicted correctly, to within a few percent. The agreement of the modelled and experimental data in the negative polarity seems to suggest that this model can accurately predict ion cluster emission, however in this case the agreement is likely coincidental. This is because the positive polarity is not modelled accurately, alongside the previous EMI-BF₄ experimental data. These data further suggest that refinements to the ion cluster emission model are required in order to achieve an accurate model.

A further three propellants were also considered by Legge and Lozano. These ionic liquids were: EMI-BF₄, EMI-bis(pentafluoroethyl) sulfonylimide (EMI-Beti) and

1-methyl-3-pentylimidazolium tri-s(pentafluoroethyl) trifluorophosphate (MPI). The properties of these ionic liquids can be found in Table 2.5. Unfortunately, relative permittivity data could not be found for the latter two ionic liquids and the other alternative ionic liquids tested in this section, therefore the emission model can not be tested on these. Nonetheless, these propellants will be discussed in order to show what types of ion clusters are emitted by them.

An interesting trend with these ionic liquids was that the ion cluster size distribution did not vary significantly with their propellant properties. Although the larger ionic liquids (EMI-Beti and MPI) emitted slightly heavier clusters, the actual distribution remained similar with similar propellants. Since conductivity varied by 6 to 8 times between the different propellants, this seems to suggest a diminished influence of the conductivity on the ion cluster sizing.

TABLE 2.5: The different propellant properties for the ionic liquids tested by Legge *et al* [28].

Ionic Liquid	Surface Tension (mN/m)	Conductivity (mS/cm)	Viscosity (cP)	Cation Mass (AMU)	Anion Mass (AMU)
EMI-BF ₄	45.2	14	38	111.2	86.8
EMI-Im	41	8.4	43	111.2	280.2
EMI-Beti	28.75	3.4	61	111.2	380.15
MPI	30.33	1.6 - 2.29	140	153.24	445.01

Based on Equation 1.5, it might be expected that heavier ionic liquids would have a higher thrust that increases with \sqrt{m} . However, in practise it was found that EMI-BF₄, with the lowest ion mass, produced the most thrust compared to any of the heavier ILs. This was because the current produced by EMI-BF₄ was approximately three to six times more than the other ILs that were tested. The thrust-to-power, another key metric in electric propulsion, was calculated as 42.7, 57.7, 72.3 and 77.3 for EMI-BF₄, EMI-Im, EMI-Beti and MPI respectively. The increased thrust-to-power indicates that if the heavier ionic liquids emitted similar currents at similar voltages to EMI-BF₄, i.e. at the same power, the ionic liquids would produce more thrust. Therefore, if higher mass propellants that emit similar currents to EMI-BF₄ could be found, these would emit more thrust, which is desirable for electrospray thrusters [53].

Castro *et al* [25] experimented with six different ILs in order to investigate the effects of different propellant properties on the ions emitted by an electrospray source. The six propellants were grouped into two groups, 'good' and 'bad' propellants. The 'good' propellants were all based on the cation 1-ethyl-3-methylimidazolium (EMI). The anions of these were tetrachlorogallate, dicyanamide and tricyanomethanide (EMI-GaCl₄, EMI-N(CN)₂ and EMI-C(CN)₃). These were selected due to their high conductivity and high surface tension. The 'bad' propellants are made up of larger cations (1-butyl-3-methylimidazolium and 1-hexyl-3-methylimidazolium, shortened to BMI and HMI respectively) and iron-based anions (tetrabromoferrate and tetrachloroferrate, FeBr₄ and FeCl₄ respectively). These were termed poor due to their low conductivities and low surface tensions. A summary of these liquids is provided in Table 2.6 to highlight the differences in the propellant properties.

Similar sizes of ions were emitted by these ionic liquids, irrespective of the conductivity, which varied almost an order of magnitude, and surface tension. This seems to indicate, as with [28], that the emitted ion cluster sizes do not depend on conductivity. Nonetheless, the emitted current was found to remain in good agreement with the conductivity of the ionic liquids.

TABLE 2.6: Different propellant properties for the ionic liquids tested by Castro *et al* [25].

Ionic Liquid	Surface Tension (mN/m)	Density (kg/m ³)	Conductivity (mS/cm)
EMI-GaCl ₄	48.6	1.53	22
EMI-N(CN) ₃	49.05	1.08	28
EMI-C(CN) ₃	47.9	1.11	22
BMI-FeBr ₄	47.1	1.98	5.5
HMI-FeBr ₄	42.01	1.86	2.8
HMI-FeCl ₄	39.37	1.33	4.7

Krejci *et al* tested two ionic liquids different to EMI-BF₄ [31]. These two ionic liquids were 1-ethyl-3-methylimidazolium dicyanimade (EMI-DCA) and 1-ethyl-3-methylimidazolium tetrachlorogallate (EMI-GaCl₄). These had conductivities of 28 and 20 mS/cm, respectively, and viscosities of 21 and 13 cP, respectively. The high conductivities and low viscosities meant that it was likely that these ionic liquids

would emit more current than EMI-BF₄. Furthermore, it is interesting that EMI-GaCl₄ has an anion with a mass of 211.5 (2.43 times larger than BF₄⁻), yet its conductivity properties were improved than EMI-BF₄. This indicates the possibility of a similar emitted current for a heavier ionic liquid, hence a higher thrust.

The plume current data in [31] found that EMI-DCA emitted the most current, followed by EMI-GaCl₄ and EMI-BF₄, reflecting the conductivities of each propellant. Ion cluster size data for EMI-DCA and EMI-GaCl₄ were unfortunately not provided, hence a comparison of ion cluster sizes could not be made. Nonetheless, it is interesting that the heavier ionic liquid EMI-GaCl₄ was able to emit significantly more current than EMI-BF₄, likely leading to increased thrust. It is therefore possible that heavy ionic liquids exist that can emit comparable or higher current than EMI-BF₄, hence producing more thrust. Another point that will be expanded upon in chapter 5 is that this ionic liquid is similar to EMI-BF₄ in terms of the anion that it has. Both BF₄⁻ and GaCl₄⁻ are comprised of a central metalloid atom surrounded by four halogens. This may indicate that using anions with a similar composition to BF₄⁻ could emit similar to larger currents, possibly allow for high masses and high currents, therefore higher thrusts.

Another ionic liquid that has been tested is 1-ethyl-3-methylimidazolium fluorohydrogenate (EMI-(HF)_{2.3}F) by Miller *et al* [32]. EMI-(HF)_{2.3}F has a near magnitude higher conductivity than EMI-BF₄ (100 compared to 14 mS/cm) and a significantly lower viscosity (4.9 compared to 37 cP) therefore likely promoting a higher current. However, the propellant is somewhat acidic meaning it can damage the porous borosilicate glass emitters. For this thruster, carbon xerogel emitters were used to mitigate the acidic effect.

At its highest, the thruster emitted nearly 1 mA of current, which was almost five times higher than the previous tests by Krejci *et al* [31] with the same thruster. This also translated to almost six times more thrust than previous testing with the thruster. However, the propellant caused very strong electrochemical reactions which quickly damaged the emitters, likely due to its acidic nature.

The experiments utilising different propellants show interesting results. They have shown that the sizes of ion clusters do not strongly depend on propellant properties. However, the current emitted has been shown to depend on conductivity, with higher conductivity ionic liquids emitting more current. It has also shown some promise for

ionic liquids that could emit similar current levels to EMI-BF₄ but be comprised of heavier ions, such as EMI-GaCl₄.

2.3.5 Ion Cluster Fragmentation

The clusters of ions that are emitted from electro spray thrusters are typically unstable, breaking apart during flight. The process of ions breaking apart in electro spray thrusters has been termed ‘fragmentation’ and it has significant effect on the performance of thrusters.

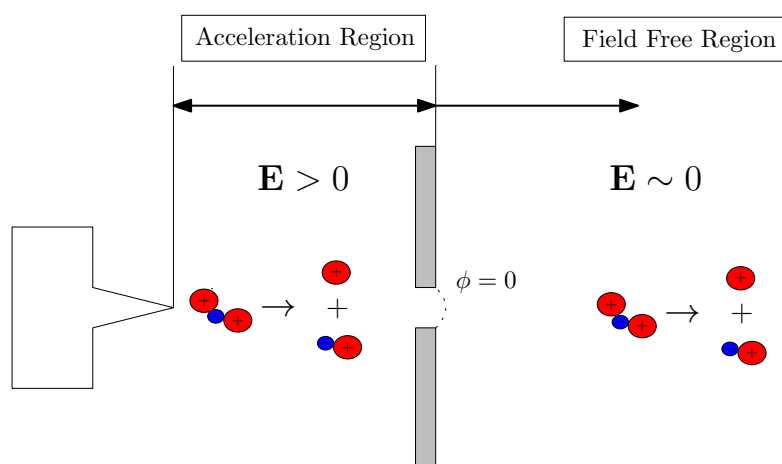
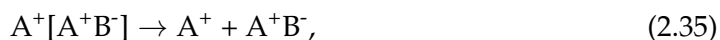
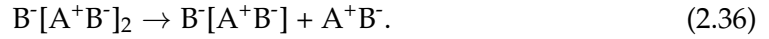


FIGURE 2.17: Fragmentation within an electro spray thruster, alongside the two regions where fragmentation occurs. The acceleration region fragmentation occurs under the influence of the electric field, so that the progeny ions get accelerated, while in the field-free region the progeny ions are outside of the electric field therefore remain at a constant velocity.

When an ion cluster fragments, a parent ion breaks up into a progeny ion and a neutral. As mentioned in Chapter 1, ion clusters can be represented using the general form $A^+[A^+B^-]_n$ or $B^-[A^+B^-]_n$, where n is the number of neutrals within the molecule. With this representation monomers have $n = 0$, dimers have $n = 1$ and so forth. As an example for a singly-charged cation dimer the fragmentation process would look as follows:



which describes a dimer breaking into a monomer and a neutral molecule. Another example will be the fragmentation of an anion trimer, fragmenting into both an anion dimer and a neutral, so that,



Larger ion clusters fragment in the same manner, with an n ion cluster fragmenting into an $n - 1$ progeny ion cluster. Fragmentations where two neutrals break off of a parent ion are assumed to not occur given they do not typically occur in experiments [77].

The physics of fragmentation have been characterised [64] and will be presented here, although the focus will be on the energy and exhaust velocity consideration. In order to fragment, the ion clusters must cross an energy barrier, E_{frag} , before they fragment and therefore can be represented by an Arrhenius type equation:

$$r_f = \frac{1}{\tau} = A \exp\left(-\frac{E_{frag}}{k_b t_i}\right), \quad (2.37)$$

where r_f is the cluster fragmentation rate, τ is the ion cluster mean lifetime, A is a reaction rate constant and t_i is the cluster internal temperature as opposed to the bulk temperature of the propellant. E_{frag} and A are properties of the ion cluster and these vary for different ion cluster sizes and different ionic liquids.

Similar to the ion evaporation process, the energy required by a cluster to fragment is reduced by a factor of $\Delta E_{frag,e}$, dependent on the strength of the electric field. It can be derived in the same manner as G_E ,

$$\Delta E_{frag,e} = \sqrt{\frac{q^3 E(x)}{4\pi\epsilon_0}}, \quad (2.38)$$

where $E(x)$ is the electric field strength at the location of the ion cluster. Finally, as with ion emission, the full rate equation becomes

$$r = A \exp\left(-\frac{E_{frag} - \Delta E_{frag,e}}{k_b t_i}\right). \quad (2.39)$$

Equation 2.39 shows that fragmentation is highest where the electric field is the highest, meaning fragmentation is at a maximum close to the emitter tip and lowest outside of the thruster, where there is no electric field. Two different types of fragmentation are therefore defined, field-free and acceleration region fragmentation. These regions have been highlighted in Figure 2.17 with acceleration region fragmentation occurring inside of the thruster, while field-free fragmentation occurring outside, downstream of the extractor electrode.

2.3.5.1 Field-free Fragmentation

The energy changes caused by fragmentation are important to understand in order to characterise the impacts of fragmentation on electro spray thruster performance. For field-free fragmentation the energy changes have no impact on the performance of a thruster, but have a significant influence on the evaluation of experimental data. In order to evaluate these energies changes, some assumptions will have to be made. Firstly, it is assumed that the energy is conserved during fragmentation. Secondly, the energy after fragmentation does not change as the ion clusters fragment outside the electric field, therefore the initial ion energy will remain the same as the energy after fragmentation. Thirdly, the velocity of the ions remains constant throughout the fragmentation process. The kinetic energy of fragmentation can be described by considering that an ion's variation in kinetic energy is proportional to the variation in electric potential energy [35],

$$q\phi_1 = \frac{1}{2}m_1v_1^2 \quad (2.40)$$

$$q\phi_2 = \frac{1}{2}m_2v_2^2, \quad (2.41)$$

where ϕ is the ion's potential, m is the ion's mass, v is the ion's velocity, and the subscript 1 and 2 denote the energies for the parent and progeny ion, respectively. The ratio of energies can be calculated by dividing Equation 2.41 by 2.40,

$$\frac{q\phi_2}{q\phi_1} = \frac{m_2v_2^2}{m_1v_1^2}. \quad (2.42)$$

Since the velocity remains constant before and after fragmentation, $v_1 = v_2$ and the charge does not change, therefore $q_1 = q_2$. Finally, it is assumed that the initial potential that the ion was accelerated by the potential of the emitter, therefore $\phi_1 = \phi_{emitter}$. Using these three assumptions, Equation 2.42 can be rewritten as

$$\frac{\phi_2}{\phi_{emitter}} = \frac{m_2}{m_1}. \quad (2.43)$$

Equation 2.43 shows that the potential of field-free fragmentation can be determined by the ratios of masses of the ion before and after fragmentation. As an example, for a field-free fragmentation of a cation dimer of EMI-BF₄ the potential of the fragmented ion would be determined by the ratio of A⁺ to A⁺[A⁺B⁻], which is calculated as 0.360. What is important using this technique is that this energy is only dependent on the masses of the ions as opposed to the charge-to-mass of the ions.

2.3.5.2 Acceleration Region Fragmentation

Acceleration region fragmentation has similar assumptions as field-free fragmentation, that the energies and velocities remain the same directly before and after the moment of fragmentation. It will also be assumed that there are no acceleration inefficiencies, so that the ion will be accelerated to the potential applied to the emitter. However, the velocities do not remain the same sometime after fragmentation, due the ions being present in the electric field and therefore are accelerated post fragmentation. For acceleration region fragmentation, the energy up to the point of fragmentation in the acceleration region needs to be considered which takes the form,

$$E_1 = q\phi(x_1) + \frac{1}{2}m_1v_1^2, \quad (2.44)$$

where $\phi(x_1)$ is the potential at the position x_1 , at the position where the ion cluster fragments. Similarly, we can consider the parent ion velocity in the moment before breakup,

$$v_1 = \sqrt{\frac{2q(\phi_{emitter} - \phi(x_1))}{m_1}}. \quad (2.45)$$

Therefore, from Equation 2.45 it can be seen that the initial velocity of the progeny ion will also be v_1 as the velocity remains the same in the moment before and after fragmentation. The electric potential energy for the progeny ion becomes different, and similar to field-free fragmentation is equal to

$$E_{elec,1} = q \left(\frac{m_2}{m_1} \phi(x_1) \right), \quad (2.46)$$

where E_{elec} is the ion's electric potential energy. However, as the progeny ion is present in the electric field it will continue to accelerate post fragmentation. The kinetic energy of the progeny ion will continue to increase after fragmentation as well, however this energy will be lower than a fully accelerated and non-fragmented ion. The progeny ion's velocity will also continue to increase, with the final velocity of the progeny ion being greater than if it did not fragment, due to the progeny ion's increased charge-to-mass ratio. The important properties to consider for this thesis are the potential and the exhaust velocity of the progeny ion, described by the equations,

$$\phi_2 = \frac{m_2}{m_1} \phi(x_1) + (\phi_{emitter} - \phi(x_1)), \quad (2.47)$$

$$v_2 = \sqrt{\frac{2q(\phi(x_1))}{m_1}} + \sqrt{\frac{2q(\phi_{emitter} - \phi(x_1))}{m_2}}. \quad (2.48)$$

Equations 2.47 and 2.48 show the general form of the progeny ion's potential and exhaust velocity equation. The stopping potential for field-free fragmentation can be recovered, if x_1 is set to be at the end of the acceleration region, so that $\phi(x_1)$ is equal to $\phi_{emitter}$ and therefore Equation 2.47 becomes $\frac{m_2}{m_1} \phi_{emitter}$. The velocity from Equation 2.48 also yields the velocity expected for a non-fragmented ion cluster, $\sqrt{\frac{2q\phi_{emitter}}{m_1}}$, further validating the equations.

Similarly, in the opposite case, where fragmentation occurs at the moment after emission, ϕ_1 is effectively zero, therefore ϕ_2 would be equal to $\phi_{emitter}$ and the velocity would be the same velocity as for a non-fragmented $n - 1$ ion cluster, $\sqrt{\frac{2q\phi_{emitter}}{m_2}}$. Considering both the potential and the exhaust velocity of the progeny ion in this case, it would appear that an ion cluster fragmenting in the moment after emission would be advantageous due to the higher ion cluster exit velocity. However, this is not the case when the the second component of fragmentation, the neutral, is considered.

By its definition, a neutral cannot be accelerated by an electrostatic field because it contains no charge. Therefore, when the parent ion cluster fragments, the neutral it produces is essentially 'energetically frozen', with the neutral's velocity and energy remaining the same post-fragmentation. Examining Equation 2.48 again shows that if this ion cluster were to fragment at the moment right after emission the energy and the velocity of the neutral would be zero and the mass of the neutral would act as a considerable mass loss for the system. In the worst case scenario, where a dimer fragments in the moment after emission, for example a cation EMI-BF₄ dimer outlined in Equation 2.35, 64% of the total emitted mass is lost to acceleration region fragmentation.

The impact of acceleration region fragmentation on electrospray thrusters has been previously explored by Courtney and Shea [78], showing how the mass flow rate and thrust are affected by acceleration region fragmentation for EMI-BF₄ and EMI-Im. It was found that the effect of acceleration region fragmentation could increase the actual mass flow rate by over 40% in negative polarity emission of EMI-BF₄. This could translate to a nearly 20% reduction in the specific impulse of the thruster, and about a 10% reduction in total thruster efficiency due to this effect. It is therefore imperative to characterise acceleration region fragmentation when investigating electrospray thrusters.

2.4 Investigating Alternative Propellants for Porous Electrospray Thrusters

This chapter has shown that propellant properties of ionic liquids might affect both the current and the ion cluster sizes of ions emitted by electrospray thrusters. The fundamental kinetics of ion emission have been explored, showing the influence of relative permittivity and surface tension on the ion solvation energies. These ion kinetics were then applied to model how current and ion cluster sizes would vary with propellant properties. The current was shown to increase with increasing conductivity and surface tension and a reducing relative permittivity. The model for ion cluster sizes showed that ion clusters become smaller with an increasing surface tension, and a decreasing relative permittivity and density. In order to characterise these physical

phenomena, experiments are required that adequately measured the current, energy and plume composition.

Chapter 3

Experimental Methods

To investigate the effects of propellant properties on ion clustering alongside other key performance metrics in an electrospray thruster, such as current, experiments have to be conducted. For testing electrospray thrusters using various ionic liquids, three different tests were used in this thesis. These were: current collection, retarding potential analysis and Time-of-Flight Mass Spectrometry (TOF), which provided information about the current, ion energy and ion cluster sizes, respectively. This chapter will provide an overview of the general methods that are applied with these techniques.

3.1 Current Collection

The simplest diagnostic method in electrospray propulsion is the measurement of the ion current. Quantifying the current is essential in order to characterise an electrospray thruster's performance. At its most basic the plume current is collected using a current collector, typically a simple metal plate, which collects the incident ion current it receives, then the collected current is measured. The measurement can be provided by either an ammeter, which measures the current directly, a resistor, where the voltage across the resistor is measured using a voltmeter and Ohm's law applied to calculate the respective current that would produce such a voltage, or a transimpedance amplifier, which converts the current into a voltage which is then measured. Schematics of these three current measurement configurations are shown in Figure 3.1.

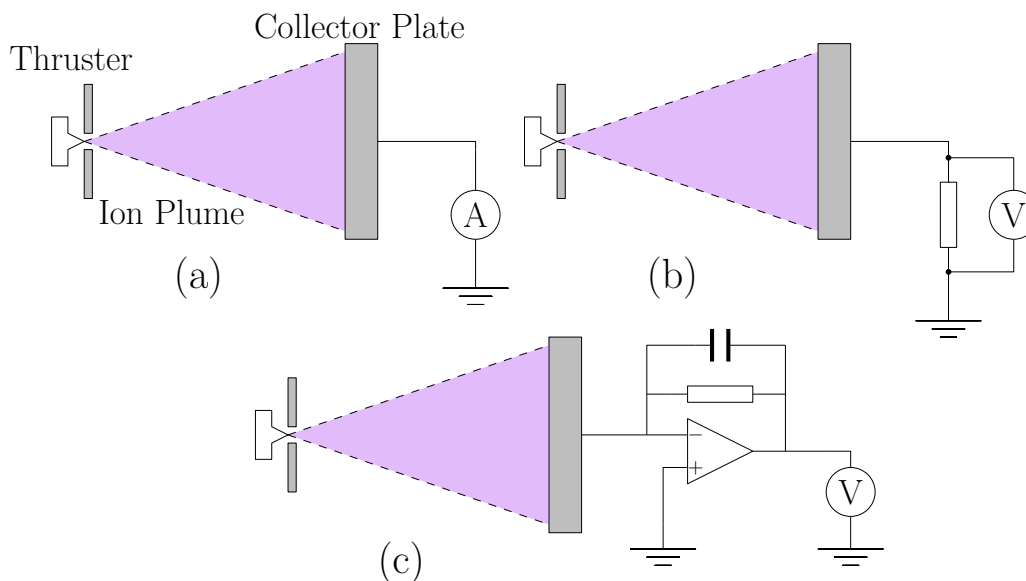


FIGURE 3.1: Three variants a basic current collection setup, with a thruster emitting a plume onto a metal plate. The current measurements methods are as follows: (a) uses an ammeter, (b) uses a resistor and (c) uses a transimpedance amplifier.

For an electro spray thruster, there are three currents which are necessary to understand thruster operation. The plume current, as described, is one such current, with the measurement of the extractor and emitter current also generally required. The extractor can be impinged by a portion of the current emitted, therefore the extractor current is also essential to measure. The impinged plume can accumulate on the extractor leading to shorting between the emitter and the extractor. Extractor current measurements also show a variety of effects, such as sparking, and also help the detection of leakage currents. These effects are a source of inefficiency for the thruster therefore make the extractor current essential to measure. One of these inefficiencies is the transparency efficiency, which is defined as,

$$\eta_{trans} = \frac{I_{em} - I_{ex}}{I_{em}}, \quad (3.1)$$

where I_{ex} is the extractor current and I_{em} is the total emitted current. The transparency efficiency indicates how much of the current exits the thruster and therefore produces thrust.

Measuring the extractor current is achieved similarly to the collector current. The extractor is typically grounded for an electrospray thruster, therefore an ammeter or a resistor can be used to measure the current, with these components placed in between the extractor and the ground. This can be difficult due to the tendency of sparking between the emitter and extractor, possibly causing sudden increases in current that can damage sensitive electrical equipment. Therefore, protection against sparking is required when extractor current measurement is utilised.

The last current typically measured for electrospray thrusters is the emitter current, $I_{emitter}$. This current corresponds to the total current used by the thruster, and therefore is essential for determining the total thruster efficiency. In an ideal thruster, the collector current, I_c , and extractor current, I_{ex} , can be used to define the emitter current by the equation,

$$I_{emitter} = I_c + I_{ex}. \quad (3.2)$$

The emitter current is therefore determined by the sum of the collector current and the extractor current. Nonetheless, it is usually advantageous to measure the emitter current, as Equation 3.2 assumes no current losses, which could possibly lead to overestimating thruster performance if the emitter current is not measured.

Since the emitter current is measured between the high voltage power supply and the emitter, both kept at high voltages, the emitter current is difficult to measure. Two methods will be listed here that can be used to measure the emitter current. A resistor can be used to measure the current, and is typically the most common method applied due to its simplicity and reliability in current measurements. An isolation amplifier is also a possible method, which typically provides a better sampling frequency. However, isolation amplifiers can be difficult to implement. This is because they require bespoke circuits using components that are very sensitive to electrostatic discharges meaning they can be difficult to design and manufacture without specialised knowledge.

Another crucial aspect of current measurement that needs to be considered is the design of the current collector plate. For a collector plate, a few design choices must be evaluated. The necessary area of the collector plate, termed the collection area, should

ideally be sufficient to collect the entire plume current. This required area is clearly dependent on the distance from the thruster, with space available within the vacuum being a consideration. The collector plate being positioned at a greater distance is also beneficial to ensure no interactions between the collector plate and the thruster.

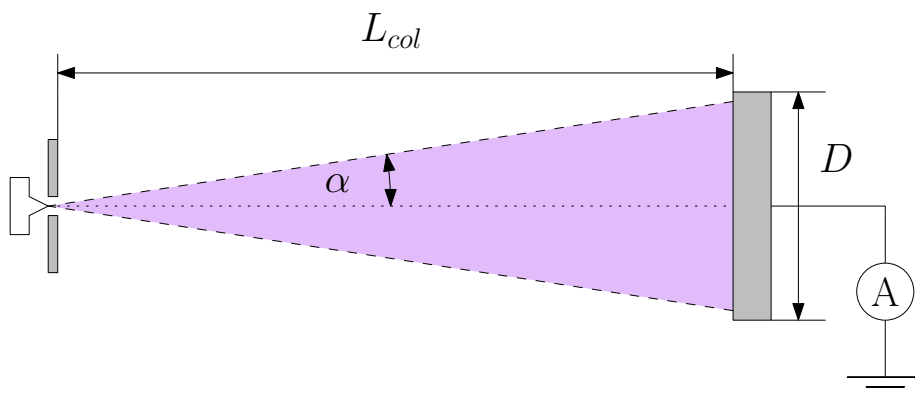


FIGURE 3.2: Key geometrical considerations for designing an electro spray thruster current collector. These include the length between the thruster and the collector plate, the half-angle of the plume and the diameter of the collector plate, assuming a circular collector plate.

For the collector plate to be designed, the width of the collector plate, D , and the distance from the thruster to the collector, L_{col} , must be determined, with these parameters illustrated in Figure 3.2. Both of these parameters are dependent on the half-angle of the plume that is collected by the collector plate, α . This can be defined by the equation,

$$\tan(\alpha) = \frac{D}{2L_{col}} \quad \therefore D = 2 \tan(\alpha) L_{col}, \quad (3.3)$$

where the collector plate is assumed to be circular. The half-angle of an electro spray thruster plume is typically greater than 20° [79, 80], possibly reaching as higher than 60° [31, 81, 82], therefore this variability should be taken into account for adequate collector plate design.

Assuming a distance of 100 mm, the diameter of collector plate required for a half-angle of 20° is 73 mm and for a half-angle of 60° the collector diameter would be 346 mm. With increasing distances from the collector, the collector plate size can become limitingly large, with a doubling of the distance doubling the required diameter to 692 mm.

Secondary Electron Emission (SEE) effects should be considered for current collector design. SEE occurs when a surface is impacted by an ion with significant energy causing the emission of electrons. This effect can decrease the reliability of collector and extractor current readings due to these currents being amplified by the emitted electrons. For example, Klosterman, Rovey and Levin showed that when an aluminium collector plate was used to collect the current of an EMI-BF₄ plume, 2.5 electrons were produced from each positive polarity ion, while almost no electrons were produced from negative polarity ions [83]. It is therefore imperative for SEE to be mitigated to ensure reliable current readings.

One of the methods to mitigate SEE is the selection of a material with a lower secondary electron yield, resulting in fewer electrons emitted per incident ion. Common materials used for collector plates are aluminium, steel and sometimes molybdenum. Aluminium has the highest secondary electron yield, 2.5 electrons per ion, followed by stainless steel, 1.3 electrons per ion, for cations with an energy of 3 keV [83]. The nature of SEE is complicated due to the secondary electron yields being dependent on the type of incident ion and its energy and the material that is impacted by the ion, therefore using solely material selection for SEE mitigation is less commonly utilised.

A more common method to mitigate SEE is using a secondary electron suppression grid. This grid consists of a fine mesh, and is placed close to the surface of the current collector, typically at a distance of ~ 5 mm. A negative voltage is applied to the grid, of the order of 10s of V, with the voltage acting to suppress the emission of secondary electrons. An advantage of this method is its simplicity and effectiveness of secondary electron suppression, therefore it is the commonly implemented.

As a final note on current collection, it is crucial to consider the effect of a grid on the current collector. As the grid has a finite transparency, the reduction in the current must be considered, due to part of the plume being blocked by the grid. Assuming that this transparency is represented by T , the correction for the raw collector current, $I_{col, raw}$, is:

$$I_{col} = \frac{I_{col, raw}}{T}. \quad (3.4)$$

When multiple grids are implemented, the product of the transparencies is used, as in Equation 3.4.

3.2 Retarding Potential Analysis

Retarding potential analysis (RPA) is an experimental method used to analyse the energy of ions. From section 2.3.5, it was shown that ions are emitted from an electro-spray thruster with some energy, which can be represented by a potential ϕ_{ion} . These ions can be repelled by a potential that is greater than ϕ_{ion} , and through the variation of potential the ions are filtered for different energies. This filtering is implemented by using a retarding potential, ϕ_r , at various different voltages to repel incoming ions from a collector plate. Changes in the collected current are produced by the changing the upstream retarding potential, which are then measured and recorded to produce current versus retarding potential data. The data are then analysed to investigate the ion energy distribution, which provides information about the fragmentation of ions.

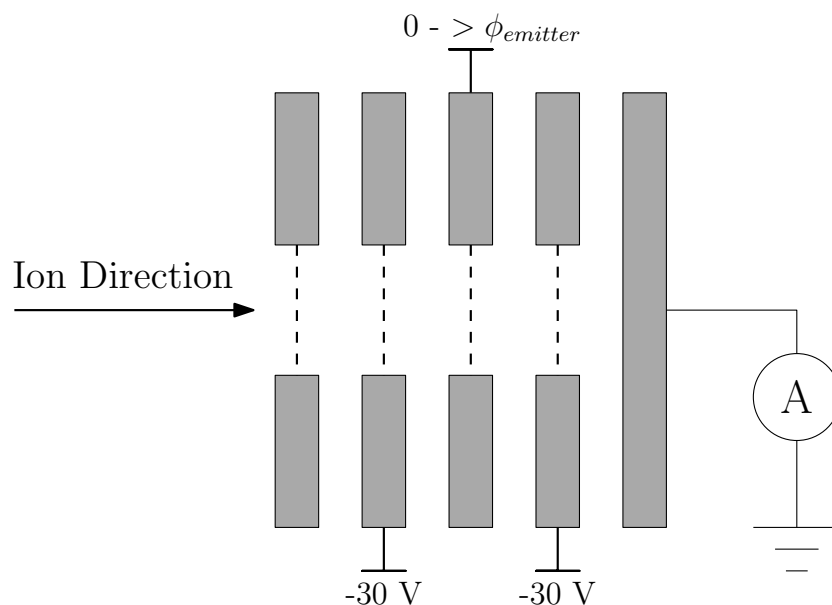


FIGURE 3.3: A four grid RPA, showing to what grid each potential is applied to. From the left hand-side the grids are as follows: floating, electron repelling, retarding and secondary electron suppression.

A retarding potential analyser consists of several grids perpendicularly aligned with the plume direction, illustrated in Figure 4.2. The first grid from the left hand-side of the figure is the floating grid, which reduces plasma perturbations [84]. The next grid is negatively biased to repel electrons from the plasma. The third grid is the retarding

grid on to which ϕ_r is applied hence repelling incoming ions. The final grid is an SEE suppression grid, which is negatively charged. A collector plate or cup is placed at the end of these four grids and collects the filtered ion current.

Although common for other plasma diagnostics, for electro spray thruster research four grids are typically not required as the plume produced by electro spray ionisation is too rarefied to cause plasma effects. Therefore, a typical electro spray retarding potential analyser only consists of three grids, with the floating grid removed and the electron repelling grid grounded to prevent any influence of the electric field on ion energies outside the retarding potential analyser.

3.2.1 RPA Expected Results

The expected results for RPA will be presented in this subsection using the equations for fragmentation from section 2.3.5. These expected results will provide the foundation for the RPA data analysis in chapter 5, linking fragmentation to experimental data.

One of simplest effects measured by RPA, briefly mentioned here as it has impact on all RPA data, is the acceleration efficiency. The acceleration efficiency, η_{acc} , indicates how ions are accelerated by a thruster. Since the thrust produced by a thruster is based on the velocity of the ions emitted, shown in Equation 1.1, the acceleration efficiency is an important metric to determine the performance of a thruster. An emitted ion's final energy, E_ϕ , is the difference between the final and the initial potential energy and can be described by the equation,

$$E_\phi = q\phi_{final} - q\phi_{initial}, \quad (3.5)$$

where the final ion potential is given by ϕ_{final} and the potential of the ion at emission, i.e. in its initial state, is $\phi_{initial}$. It is assumed that the ion has gained no or negligible potential at the moment of emission, $\phi_{initial} = 0$, hence Equation 3.5 can be simplified to equation

$$E_\phi = q\phi_{final}. \quad (3.6)$$

For the most efficient acceleration process the ion should be accelerated by the highest potential difference that is possible from the thruster, which is the potential difference between the emitter and the extractor. Since the extractor is typically grounded, the maximum electric potential energy, E_{max} , gained in an electrospray thruster can be defined as,

$$E_{max} = q\phi_{emitter} - q\phi_{extractor} = q\phi_{emitter}. \quad (3.7)$$

where $\phi_{emitter}$ is the potential of the emitter and $\phi_{extractor}$ is the extractor potential. The extractor is assumed to be grounded, therefore $\phi_{extractor} = 0$. However, some energy will be lost in the emission and acceleration of the ion, therefore the final ion potential will be lower than $\phi_{emitter}$. The lower ion potential reduces the final velocity of the ion, hence reducing the specific impulse and thrust of the thruster. This reduction in performance is described by the acceleration efficiency, η_{acc} , defined as,

$$\eta_{acc} = \frac{E_{\phi}}{E_{max}} = \frac{\phi_{final}}{\phi_{emitter}}. \quad (3.8)$$

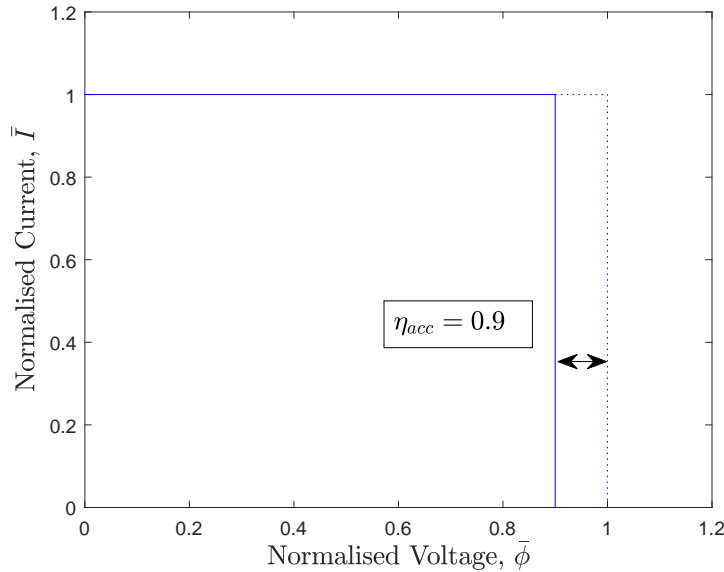


FIGURE 3.4: The effects of an acceleration efficiency of 0.9 on RPA data. The dotted line shows ideal acceleration, where all ions are accelerated to the maximum possible voltage. However, due to the acceleration efficiency this is reduce to 0.9 of the thruster's maximum value.

The effects of the acceleration efficiency on the RPA data are illustrated in Figure 3.4. For this figure, the y-axis is the normalised current, \bar{I} , which is the current for a given measurement divided by the current when no retarding potential is applied. The x-axis is the normalised voltage, $\bar{\phi}$, is the retarding potential divided by emitter potential. In this example a sharp drop in current is seen at the final acceleration voltage of the ions, which for this example was selected to be $0.9 \bar{\phi}$. The drop corresponds to all the ions accelerated by $0.9 \bar{\phi}$ being repelled by a retarding potential of the same magnitude.

3.2.1.1 Field-Free Fragmentation

As described in section 2.3.5.1, field-free fragmentation of ion clusters significantly impacts the energy distribution of the plume. Taking the example of an EMI-BF₄ dimer fragmenting into a monomer from section 2.3.5.1, the field-free fragmentation energy was calculated to be 0.360. It would be expected that this translates into a current drop at a normalised voltage of 0.360, however the field-free fragmentation energy is reduced to 0.324 when an acceleration efficiency of 0.9 is considered. The corresponding RPA data are shown in Figure 3.5, visualising the energy distribution for a plume with a field-free fragmenting EMI-BF₄ dimer. The ‘ideal’ curve is shown with the dotted line,

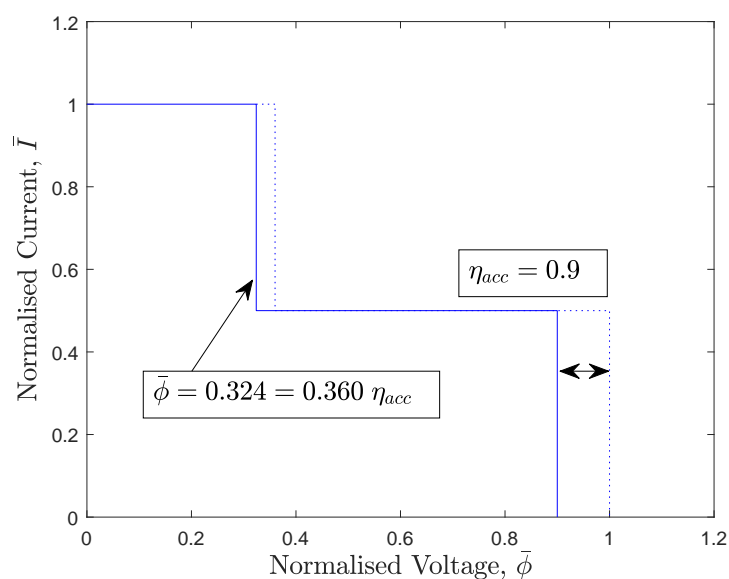


FIGURE 3.5: An ideal energy distribution, shown in the dotted line, with a more realistic energy distribution shown in the solid line showing the effects of field-free fragmentation.

while the more realistic distribution, which considers acceleration efficiency, is plotted in blue.

In this example, 50% of the current is comprised of dimers that fragment in the field-free region, meaning that at least 50% of the parent ions in the plume were initially emitted as dimers. However, this does not provide any further information about the composition of the plume, for example that only 50% of the ions were emitted as dimers. The plume could initially have more emitted dimers, however the RPA data do not necessarily show that this is the case, although it is likely that more dimers are present in the plume due to the finite lifetimes of EMI-BF₄ dimers [65]. To determine the plume composition Time-of-Flight data are required, which will be introduced in the next section.

3.2.1.2 Acceleration Region Fragmentation

Described in section 2.3.5.2, acceleration region fragmentation occurs between the emitter and the extractor, leading to the progeny ions being accelerated after fragmentation. The progeny ions gain energy and therefore exit the thruster with a higher energy than if it field-free fragmented. Since the parent ion can fragment at any point between the emitter and the extractor, a range of energies is produced by acceleration region fragmentation when an electrospray plume is measured using RPA.

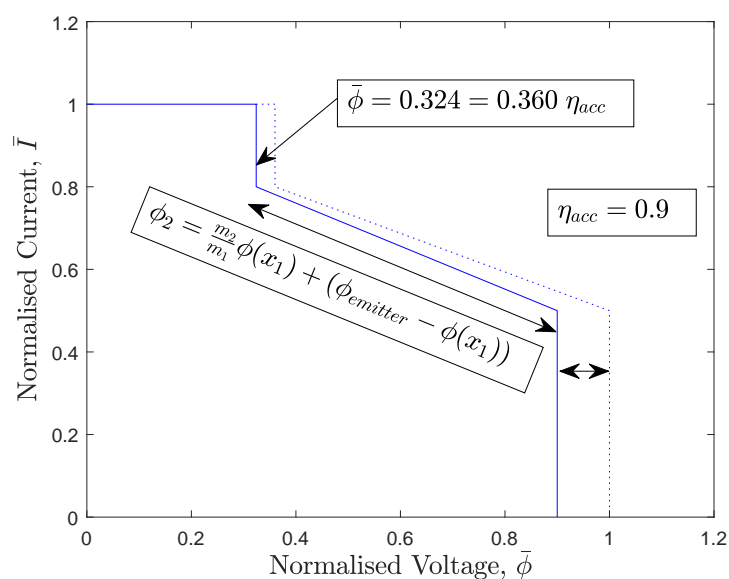


FIGURE 3.6: An idealised version of RPA data, including the effects of acceleration efficiency, field-free fragmentation and acceleration region fragmentation.

It is important to also consider how acceleration region fragmentation affects the RPA data, with an example illustrated in Figure 3.6. It includes the effects of acceleration region and field-free fragmentation, and the acceleration efficiency. It has been assumed that 20% of the fragmenting dimers fragment in the field-free region and 30% of the dimers fragment in the acceleration region.

Acceleration region fragmentation is represented in Figure 3.6 as a straight line between the field-free fragmentation current drop and the fully accelerated ion drop. Ions with an energy closer to the field-free fragmentation energy, 0.324, correspond to ions that have fragmented close to the end of the acceleration region, while ions with energies close to 0.9 correspond to ions that have fragmented close to the emitter. This type of representation agrees quite well with experimental RPA data. An example of experimental RPA data is shown in Figure 3.7 from [35], showing reasonable agreement in term of the broad shape with the idealised plume in Figure 3.6.

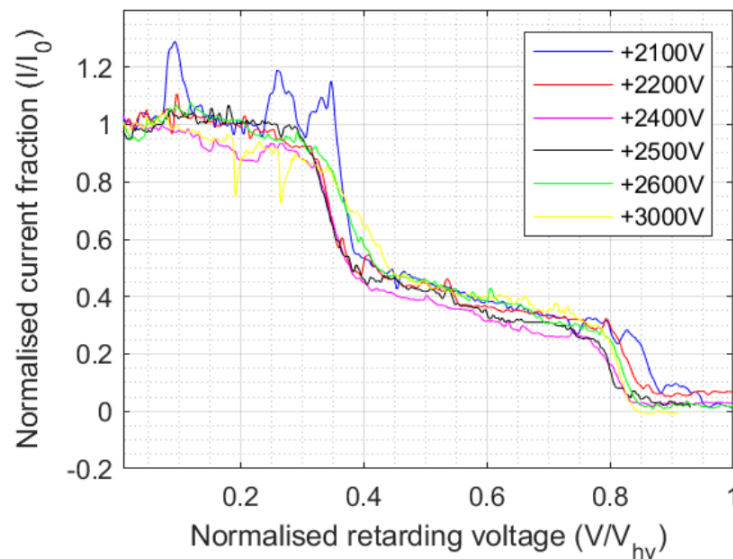


FIGURE 3.7: Example RPA data from a thruster which has similar emitters to the emitters tested in this thesis [35]. The data show field-free fragmentation around an energy of 0.360 as well as acceleration region fragmentation.

This simple analysis can be applied for any ion cluster size, including trimers, quadramers and so forth. However, as the ion clusters become larger, they become less discernible in the RPA data, as typically there are few heavy ion clusters in pure ion plumes hence the current drop would be small. Furthermore, the field-free fragmentation energy of large clusters is closer to that of the highest energy current drop, for example a EMI-BF₄ cation trimer has a field-free fragmentation energy of

0.610. The field-free energy will only increase with larger ion cluster sizes, therefore become less discernible.

3.3 Time of Flight Mass Spectrometry

The final diagnostic that will be reviewed in this chapter is Time-of-Flight mass spectrometry (TOF). TOF allows for the identification of the charge-to-mass ratios of emitted ions, essential in characterising electrospray thruster ion emission.

To understand TOF, some basic equations need to be reviewed. Firstly, when an ion is emitted by an electrospray thruster, it is accelerated by the emitter potential to a velocity, v_{ex} . This can be defined similar to Equation 1.4:

$$v_{ex} = \sqrt{\frac{2q\phi_{emitter}}{m}}, \quad (3.9)$$

assuming that there are no acceleration losses. For TOF the time it takes for an ion to cross a specified length L is measured, giving the technique its name. The time it takes for an ion to cross this length, t_f , can be described the equation $t_f = \frac{L}{v_{ex}}$, which when substituted into Equation 3.9 provides an estimate of the flight time of an ion cluster,

$$t_f = L\sqrt{\frac{m}{2q\phi_{emitter}}}. \quad (3.10)$$

Equation 3.10 can be further rearranged to describe the charge-to-mass ratio based on the time it takes for an ion to cross the TOF mass spectrometer:

$$\frac{q}{m} = \frac{L^2}{2\phi_{emitter} t_f^2}. \quad (3.11)$$

Equation 3.11 shows the charge-to-mass ratio of a charged species can be resolved through measurement of the emitter potential, flight length and time.

Figure 3.8 illustrates a basic design of a TOF system. The ions fly towards the electrostatic TOF gate which periodically opens and closes through the fast application of

the gate voltage, ϕ_{gate} . This prevents the current from entering the flight section, defined as the region between the gate and the collector. The distance covered by the flight section is defined as L , corresponding to the instrument's sensitivity to different charge-to-mass ratios of ion clusters (i.e. the longer the distance the greater the difference in time between the arrival times of different ion clusters). Finally, at the end of the flight section is the current collector which measures the ion current that passes through the gate over time.

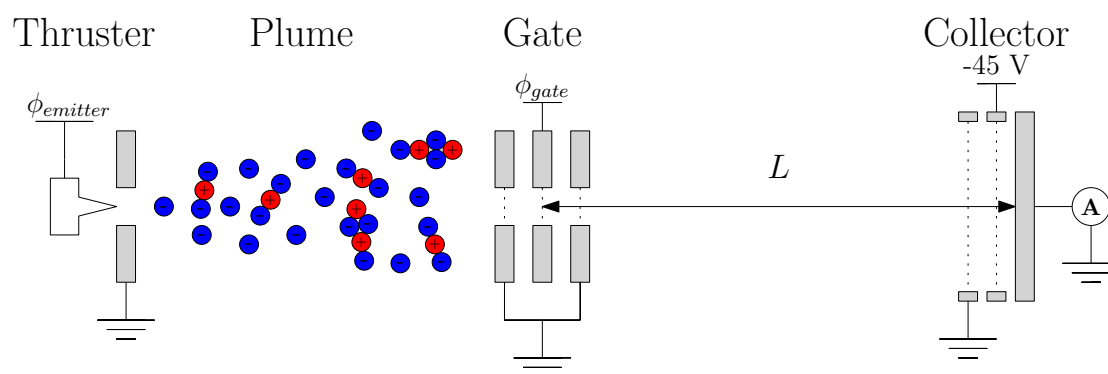


FIGURE 3.8: A basic TOF system showing the two components, the gate and the collector, alongside a plume comprising of monomers, dimers and trimers. The gate will periodically close, causing the current collected to decay, with the drops in the current curve corresponding to different ion species.

3.3.1 TOF Expected Results

Before the components of the TOF system are investigated, the results that are expected from TOF will be reviewed first. In this subsection the expected TOF data will be illustrated, assuming a plume of EMI- BF_4 cations.

Example TOF data for operating in a pure ion regime are presented in Figure 3.9, showing a plume comprised of monomers, dimers and trimers. The y-axis is the normalised current, calculated by dividing the measured current by the current at the arrival time of monomers. The x-axis is the charge-to-mass ratio corresponding to the time the current was recorded after the gate was closed. This is calculated using Equation 3.11. The plume in Figure 3.9 is comprised of 20% monomers, 60% dimers and 20% trimers.

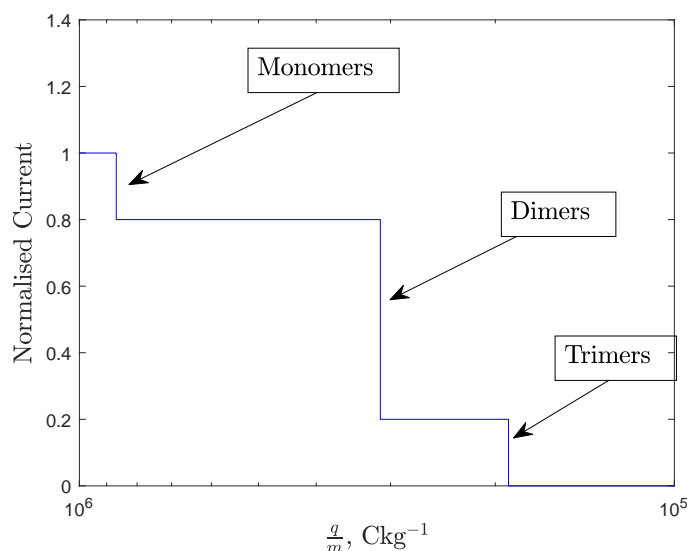


FIGURE 3.9: An example plot of TOF data assuming monomer, dimer and trimer EMI- BF_4 cations. The current drops correspond to the arrival of a given ion species.

The charged species appear as ‘drops’ in the current, with their charge-to-mass ratios corresponding to their expected times of arrival. In the ideal case, where no fragmentation and no non-idealities occur, the current drops are perfectly straight and the current does not change in between the drops.

If the effect of acceleration region fragmentation is included, the data will appear different as acceleration region fragmentation affects the velocities of ions hence their arrival times. Since acceleration region fragmentation is the strongest closest to the emitter, most ions will break-up close to the emitter. This leads to the progeny ion’s velocity being close to its maximum velocity, that of a non-fragmented $n - 1$ ion, where n is the number of neutrals of the parent ion.

The TOF data including the effect of acceleration region fragmentation are illustrated in Figure 3.10. The data show the drops in current corresponding to the arrival of ion clusters. However, in between these drops the current does not remain constant and instead changes due to acceleration region fragmentation increasing the velocity of progeny ions. The high fragmentation rate close to the emitter is shown by the higher change in current close to the current drops.

The variation of ion cluster arrival times due to acceleration region fragmentation can

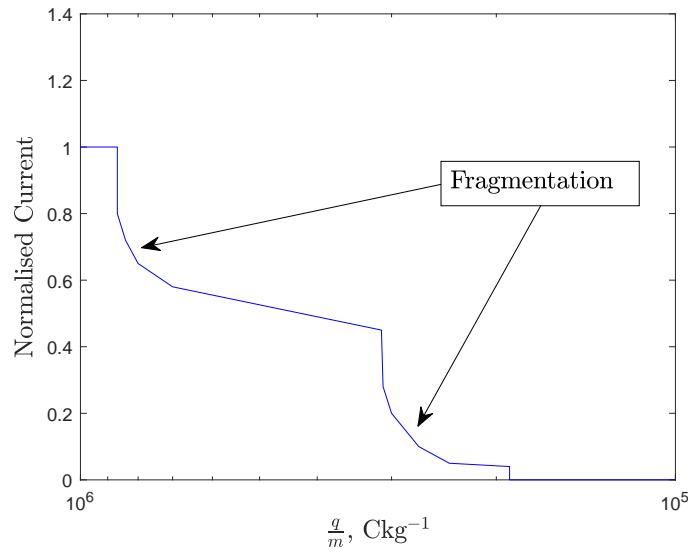


FIGURE 3.10: An example TOF plot which includes the effects of acceleration region fragmentation. Close to the emitter, acceleration region fragmentation is significant therefore having a higher gradient close to the current drops, with the gradient decreasing further way from each consecutive current drops.

make it more difficult to discern different ion species. Taking the case of a dimer acceleration region fragmenting in, its velocity can be described by Equation 2.48:

$$v_2 = \sqrt{\frac{2q(\phi(x_1))}{m_1}} + \sqrt{\frac{2q(\phi_{emitter} - \phi(x_1))}{m_2}}. \quad (3.12)$$

Equation 3.12 can be used to determine the time of flight of the dimer by dividing the flight length by Equation 3.12,

$$\tau_{ar} = \frac{L}{\sqrt{\frac{2q(\phi(x_1))}{m_1}} + \sqrt{\frac{2q(\phi_{emitter} - \phi(x_1))}{m_2}}}, \quad (3.13)$$

where τ_{ar} is the time of flight for an acceleration region fragmented progeny ion. As the position of fragmentation, x_1 , approaches the emitter, the electric potential becomes greater, $\phi(x_1)$. Therefore, τ_{ar} beings to approach the time-of-flight of a monomer ion, which can be described by,

$$\tau_{ar} = \frac{L}{\sqrt{\frac{2q(\phi(x_1))}{m_1}}}. \quad (3.14)$$

At the limit, where $\phi(x_1) = \phi_{emitter}$, the time-of-flight of a monomer and acceleration region fragmented dimer is indiscernible making it impossible to use TOF in order to distinguish the two species. Furthermore, depending on the time resolution of the TOF system, acceleration region fragmentation close to the emitter may also be indiscernible with a non-fragmented ion. A good time resolution is therefore imperative when designing a TOF system to mitigate fragmentation effects.

Other non-idealities exist in the data, such as the finite bandwidth of the electronics used to measure the current. The effect of the bandwidth is that the data have a wider spread in time, therefore the sharp drops seen in Figures 3.9 and 3.10 will become broader. The design of the collector plate will also cause increasingly lower charge-to-mass ratio charged particles to have a broader current drop, eventually leading to a ‘tail’ at the end of the plume that does not have any distinct current drops. The lack of distinct current drops can make the determination of the proportion of large ion clusters difficult, a consideration when designing the collector plate. This will be investigated in the TOF collector subsection.

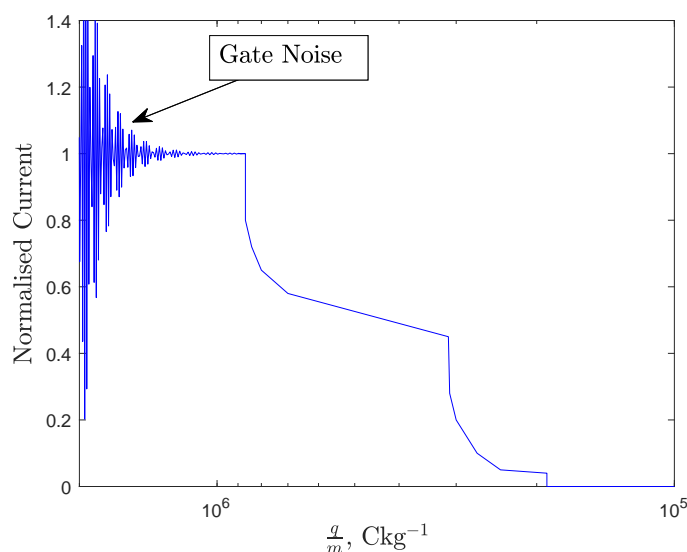


FIGURE 3.11: Example TOF data showing the effect of gate noise. The gate noise manifests as an exponentially decreasing sinusoidal after the gate is closed.

The final effect that will be considered is the noise produced by an electrostatic TOF gate, called the gate noise, as it is a significant source of noise in TOF data. Gate noise manifests as an exponential sinusoidal wave due to it originating from parasitic capacitance in the TOF system, illustrated in Figure 3.11. The illustration shows that gate

noise can have a significant effect on the TOF data if it is not adequately mitigated. The electronics driving the gate likely provide the biggest source of gate noise, due to the large changes in voltages applied in very short periods of times. The current produced by this noise, I_{cap} can be defined as,

$$I_{cap} = C \frac{d\phi_{gate}}{dt}, \quad (3.15)$$

where C is capacitance. Since every conductive surface including wires has some stray capacitance, there will be some noise produced by this rapidly changing signal. As ions travel very rapidly across the flight section, in microseconds to tens of microseconds, the voltage rise time of the gate switch must be as fast as possible, ideally within one percent of the flight-time for the fastest moving ion. Some examples of gate switches include the DEI PVM-4210 [45] and the PVX-4140 [63], having a rise time of 15 and 20 ns respectively.

As the rise time is required to be very low, the other two variables that can be modified are the capacitance and the magnitude of the voltage change, $d\phi_{gate}$. Both of these variables are a function of gate design, therefore the electrostatic gate used for the TOF system must be adequately selected and designed.

3.3.2 TOF Electrostatic Gates

The function of a TOF electrostatic gate is to prevent ions from entering the flight region of the TOF mass spectrometer. There are many different configurations of TOF electrostatic gates, with the most common types of gates used within electrospray thruster research being 'deflecting' and 'reflecting' gates. Illustrations of these gates are provided in Figure 3.12. Both of these gates function by altering the path of an incoming ion, however the method of ion repulsion has practical implications on the operation of the TOF system.

A reflecting gate operates by applying a gate potential, ϕ_{gate} , to an electrode, typically a mesh, that is placed between two grounded meshes, in order to produce a parallel electric field. When an ion with an energy $q\phi_{ion}$ enters the gate, the high gate potential, ϕ_{gate} , is greater than the ion potential, $\phi_{gate} > \phi_{ion}$, therefore the ion will decelerate

to zero velocity and then accelerate in the opposite direction that the ion entered the instrument. This will cause the ion to be ‘reflected’ from the gate.

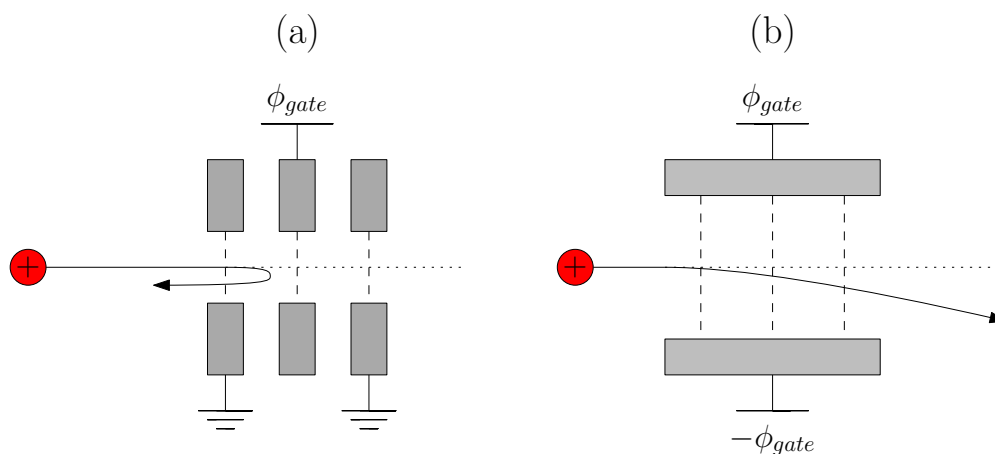


FIGURE 3.12: Two most common TOF gates used in literature, with gate (a) corresponding to a reflecting gate, and (b) to a deflecting gate. A reflecting gate has a greater potential than the ion energy, causing reflection, while a deflecting gate has sufficient potential applied to it to deflect the ions from the collector downstream.

A deflecting gate functions in a similar manner, however two equal potentials in opposite polarities are applied to two parallel electrodes. When an ion enters this gate, the two potentials accelerate the ion in the perpendicular direction to its flight path resulting in a deflection of the charged particle away from the current collector. Given the relatively large distances between the gate and the collector in a typical electrospray TOF system, only a minor deflection is required to prevent ions from reaching the current collector. Therefore, for a deflecting gate the gate potential can be significantly lower than for a reflecting gate, which typically creates less gate noise in the current collector measurements.

There are two other less commonly used types of gates for electrospray research. One of these is the ‘emitter’ gate where rather than a separate electrostatic gate, instead the voltage is applied to the emitter, or extractor, to switch the thruster off with a fast rise time switch. Although these are not technically gates, and can be considered alternative TOF methods, for simplicity these will be termed ‘gates’ in this section. The ‘emitter’ gate is probably the third most common used type of gate behind the deflecting and reflecting types gates, and has been used in various studies [18, 21, 22, 33, 44]. This type of ‘gate’ design can be advantageous as it eliminates the requirement for the design of a separate TOF gate.

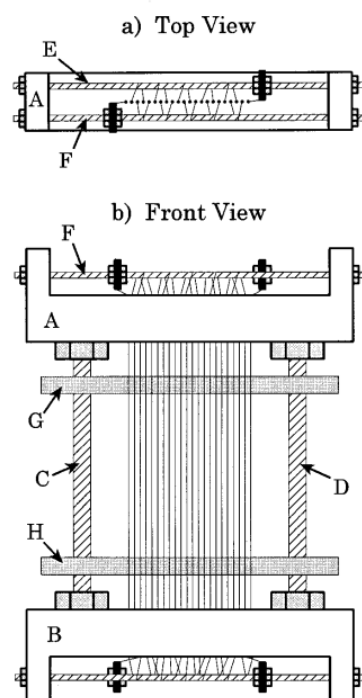


FIGURE 3.13: Design of an interleaved comb gate used in TOF [85]. Two sets of parallel wires are charged to the same magnitude potential but with opposite polarity, similar to a deflection gate.

A further electrostatic gate that has been used in electrospray testing is the interleaved comb gate, having been used only rarely for electrospray TOF tests [25, 86]. This type of gate is comprised of two parallel wires that are kept taut and meshed over an area in order to produce an entrance aperture, shown in Figure 3.13. Opposing polarity voltages of the same magnitude are applied to the two parallel wires hence an electric field is produced in between the parallel wires. The electric field deflects the ions similarly to a deflecting gate. The advantage of this type of gate is that the electric field is confined to a smaller space than with other gates, being significant only close to the wires. The confinement of the electric field enables a higher resolution of charge-to-mass ratios.

However, because of the small size of the electric field, higher voltages are required for it to sufficiently deflect ions, possibly causing issues in testing [25]. It is also significantly more difficult to manufacture this type of gate compared to the latter three gates due to the taut wires being very close to each other.

3.3.3 TOF Current Collection

A current collector is required for a TOF system to measure the decaying ion current when the gate is closed. The operation of the TOF system is significantly impacted by the selection and design of the TOF current collector, therefore it must be carefully evaluated. There are at least four types of collectors that can be used for a TOF mass spectrometer; a collector plate, a Faraday cup, a channel-electron multiplier and a micro-channel plate.

The most basic type of current collector for a TOF system is a current collector plate. Compared to a collector plate used for plume current measurement, an extra grid is added in front of the SEE grid. The function of this grid is to prevent the SEE grid electric field from interacting with ions outside of the current collector. This ensures that the flight times of incoming ions are not affected by the potential applied to the SEE grid.

A current collector design choice that must be considered further for TOF current collectors is the charge-to-mass ratio spread caused by the diameter of the current collector. Since ions will arrive at different points on the surface of the collector, they will arrive with slightly different times. Assuming a plume half-angle of α , the time-of-flight of ions arriving at the edge of the collector can be described as,

$$\tau_{arrival, edge} = \frac{L}{\cos(\alpha)v_{ex}}. \quad (3.16)$$

The time of arrival of on-axis ions is $\frac{L}{v_{ex}}$, therefore the spread in time due to the different distances travelled by the ion would be

$$\Delta\tau = \frac{L}{v_{ex}} \left(1 - \frac{1}{\cos(\alpha)} \right). \quad (3.17)$$

Equation 3.17 assumes that the whole plume is captured by the collector plate, which can have a large half-angle. However, in practise this could lead to significant $\Delta\tau$ and hence uncertainty in the charge-to-mass ratios of ion clusters. The width of the collector can be varied, hence instead of collecting the full plume, a smaller angle is collected,

θ . The angle θ can be defined by Equation 3.3 can be substituted into Equation 3.17 in order to establish the influence of the collector width. The equation is thus defined as,

$$\Delta\tau = \frac{L}{v_{ex}} \left(1 - \sqrt{1 - \left(\frac{D}{2L} \right)^2} \right). \quad (3.18)$$

Equation 3.18 shows that as D is decreased, $\Delta\tau$ is also decreased, meaning smaller collector widths lead to a lower time spread. Another key point is that the width of the collector is dependent on $\frac{1}{v_{ex}}$ meaning higher charge-to-mass ratio ion clusters have lower changes in flight time due to the angular difference, therefore the influence of the width of the collector plate is diminished.

Figure 3.14 illustrates the different times of arrival for different EMI-BF₄ cations at an emitter potential of 2500 V and a flight length of 500 mm. The time spread was calculated using Equation 3.17. It can be seen that for the largest ion (quadramers) the arrival times become larger at a higher rate than for the smaller ions, showing that broader current drops would be produced by lower charge-to-mass ratio ion clusters.

Nonetheless, minimising $\Delta\tau$ is still desirable to achieve very sharp peaks, therefore an increasingly smaller collector will lead to a continually decreasing collector width.

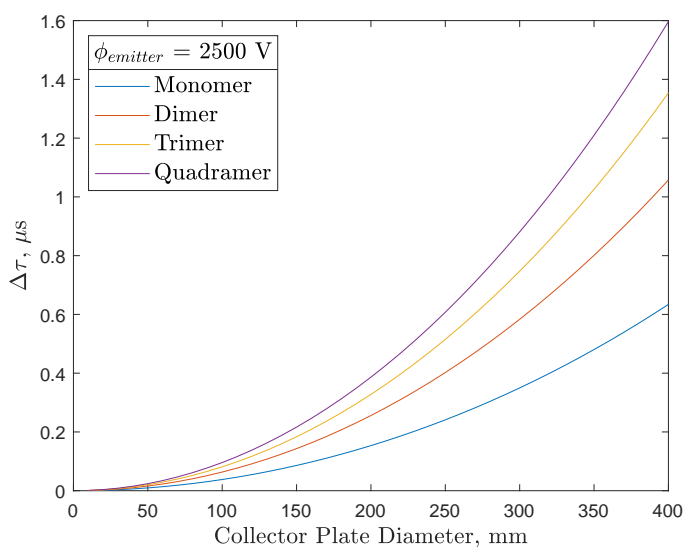


FIGURE 3.14: Time spread induced due to the width of a collector plate assuming a flight length of 500 mm. As the collector plate diameter is increased, the time spread increases. The time spread is also higher for the heavier ion clusters.

Eventually, it becomes beneficial to replace a small collector plate with a Faraday Cup, which can be considered a smaller collector plate surrounded by a grounded shielding. A diagram of a Faraday cup can be seen in Figure 3.15.

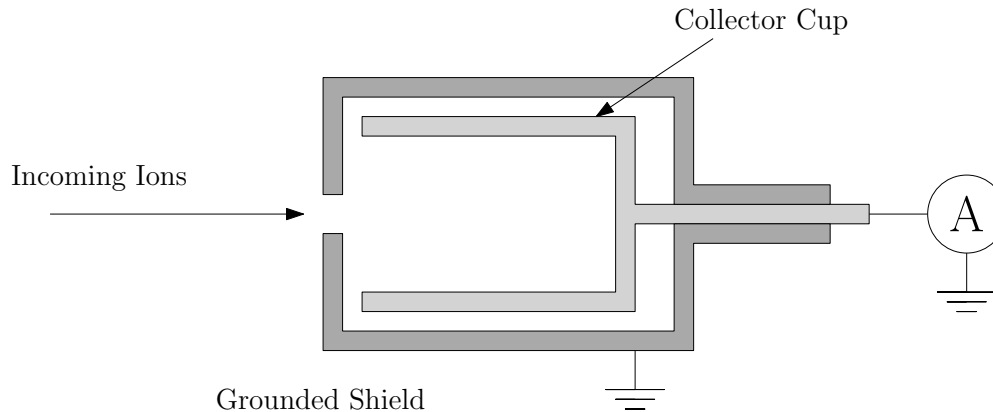


FIGURE 3.15: A schematic of a typical Faraday cup used for ion detection. The collector is a metal cup surrounded by a grounded shield.

A Faraday cup can have some significant advantages compared to a conventional collector plate when used for TOF. Aside from the significant reduction in $\Delta\tau$, the shielded collector significantly reduces electromagnetic noise from external sources.

However, signal-to-noise problems would likely be more common with a Faraday cup, as opposed to a large current collector. This problem originates from the off-axis emission phenomena of single emitter electrospray thrusters. Although it is expected for these emitters to emit a plume of ions on-axis, it has been found that single emitters can emit in various small off-axis beamlets [87].

Figure 3.16 illustrates this effect for a TOF gate. The beam in Figure 3.16(a) is emitted on-axis, with the full area of the TOF gate transmitting current. In Figure 3.16(b), two beamlets are emitted instead of one large beam. This causes significantly lower current to be transmitted through the gate, leading to a significantly reduced signal-to-noise ratio.

A solution to the emission of off-axis beamlets is to use rotational control, however this can be difficult and expensive to implement, especially when two-axes are involved. Two rotational axes are required to fully mitigate off-axis emission in electrospray thrusters. For this reason, larger collector plates are more common as opposed to Faraday cups, because collector plates account of this effect due to their large size.

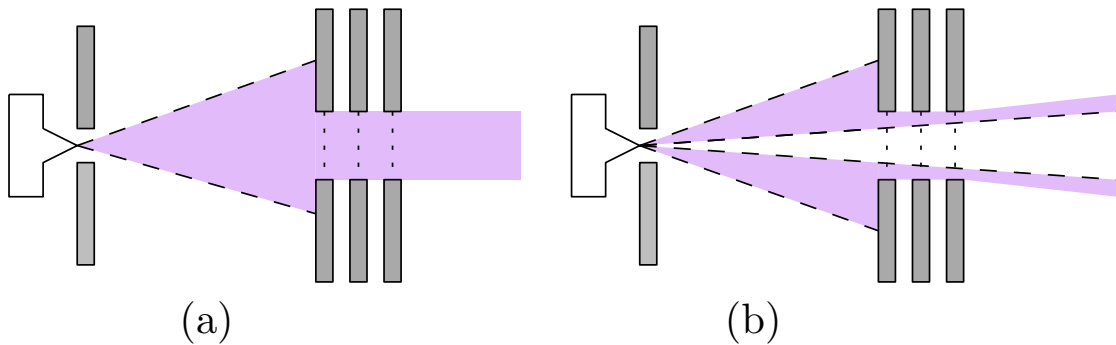


FIGURE 3.16: Effects of off-axis emission for TOF. On-axis emission into a TOF gate is shown in (a) while (b) shows the off-axis emission. During off-axis emission, a significant proportion of the current may be lost due to the misalignment between the beamlets and the TOF gate entrance aperture.

Two other collectors can be used for TOF that are less commonly used. They are a channel electron multiplier (shortened here to channeltron) and a micro-channel plate (MCP). These operate by amplifying incoming ions by utilising the secondary electron emission effect, hence the current of incoming ions is amplified by more electrons being emitted than the number of incoming ions.

A diagram of an electron amplification tube (termed a dynode) is shown in Figure 3.17. The top diagram illustrates an incoming ion from the left hand-side impacting the wall of the dynode and emitting electrons due to SEE. These emitted electrons then liberate further electrons, which repeat the process many more times until the end of the tube is reached. More electrons are emitted due to this process than the single incoming ion that entered the tube, therefore the current is amplified.

The bottom diagram shows an enlarged view of an individual electron within the tube, showing that two more electrons are liberated from the surface of the material than the single incident electron. The movement of the electrons through the tube is enabled by an electric field which is applied between the two ends of the dynode.

A channeltron consists of one of these electron amplification tubes, leading to a small $\Delta\tau$ due to its smaller collector area. Similar to a Faraday cup, the channeltron would encounter similar problems due to the non-axial emission of electrospray thrusters. Alternatively a MCP consists of multiple electron amplification tubes in parallel, forming a large collection area similar to a large current collector. As with a large collector plate, similar design considerations would have to be examined in order to use a MCP effectively for TOF in electrospray thruster testing.

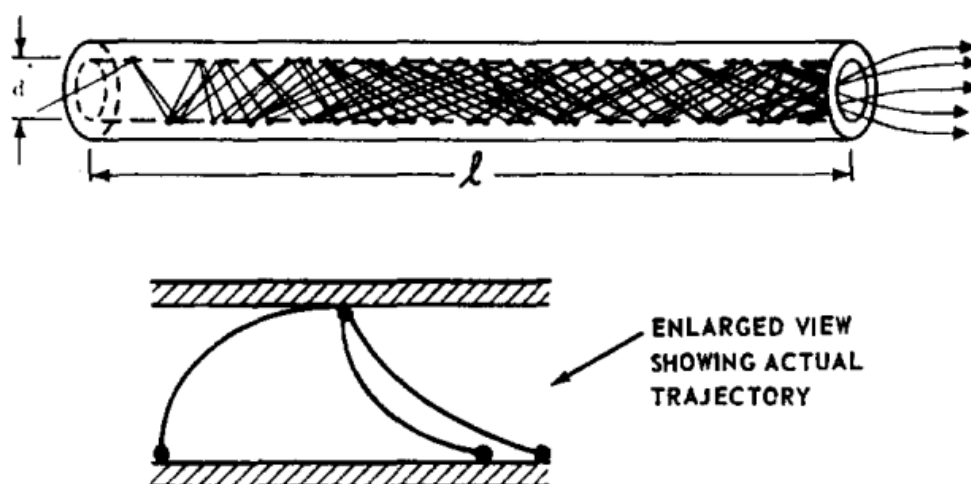


FIGURE 3.17: Use of electron amplification to amplify the current of an incoming ion inside a dynode [88]. As ions impact the interior walls of the dynode, multiple electrons are liberated, creating more net charge than initially hence amplifying the current. The progeny electrons will repeat this process multiple times causing a large gain.

Channeltrons and MCPs have typically better response times and amplification than Faraday cups and large collector plates due to the electron amplification phenomena. The electron amplification effect occurs very quickly, offering quick amplification and response to incoming ions. Meanwhile, electronics to amplify the current are required by Faraday cups and large collector plates. A typical current amplifier used in electro spray thruster TOF is a transimpedance amplifier (TIA). A bandwidth greater than at least 1 MHz is required at typical flight lengths due to the times of arrival of the fastest ions being of the order of a few μs . Although common TIAs are capable of providing bandwidths of 10s to 100s of MHz, due to Faraday cups and large collector plates requiring amplification, the bandwidth decreases from the gain of the TIA increasing. Therefore, the bandwidth is reduced to a few MHz, sufficient for electro spray TOF, however possibly leading to broadening of the data. On the other hand, channeltrons and MCPs only require current to voltage conversion from electronic components, meaning they have a significantly higher bandwidth. The higher bandwidth in TOF would lead to much sharper peaks, reducing the uncertainty in TOF data.

There are however some problems with using channeltrons and MCPs. Two problems are the high cost and complex use of the channeltron and the MCP. A high voltage supply is also required to operate both the channeltron and the MCP to enable effective electron amplification. Another issue is the gain can depend on the type of ion that is

collected, therefore care must be taken in analysing the data. Furthermore, due to the material that MCPs consist of, stricter storage requirements are required. MCPs have to be stored in an inert atmosphere to ensure that they are not damaged.

3.3.4 TOF Systems in the Literature

Electrostatic gate types and collection methods used in previous work are shown in Table 3.1. The most common gates that are used are the reflecting and deflecting gates, followed by the ‘emitter’ and ‘extractor’ gates. The least used electrostatic gate is the interleaved comb gate, being only used three times in literature.

Almost all of the sources found in literature use a conventional collector plate as their collector, with two experimental setups using Faraday cups and only one using a channeltron. It is probable that the more common use of large collector plates is due to their increased signal-to-noise ratio and a lower sensitivity to off-axis beamlets.

The flight lengths for TOF systems are also shown. The range of these distances is varied, however most TOF systems have a flight length greater than 400 mm due to the

TABLE 3.1: Summary of the design choices of different TOF systems in literature. The ‘Emitter’ and ‘Extractor’ gates reference to systems where the gate switch is used on the emitter and extractor. For [44] the flight length is unknown.

Gate Type	Collector Type	Length, L mm	Reference
Emitter	Collector Plate	123	[18]
Reflecting	Collector Plate	410	[20]
Extractor	Collector Plate	500	[21]
Emitter	Collector Plate	441	[22]
Interleaved Comb	Faraday Cup	757	[23]
Interleaved Comb	Collector Plate	300	[25]
Deflecting	Collector Plate	920	[26]
Reflecting	Collector Plate	746	[30]
Reflecting	Collector Plate	1600	[31]
Deflecting	Channeltron	810	[32]
Emitter	Collector Plate	370	[33]
Reflecting	Collector Plate	641	[34]
Reflecting	Faraday Cup	550	[35]
Reflecting	Collector Plate	700	[37]
Reflecting	Collector Plate	116	[38]
Deflecting	Collector Plate	742	[45]
Emitter	Collector Plate	N/A	[44]
Interleaved Comb	Collector Plate	300	[86]

very fast speeds of monomer ions, which is 10s of kms^{-1} . A larger difference between the times of arrival of different species is also enabled by a longer flight length, typically enabling sharper current drops in the TOF data.

3.4 Diagnostic Setups for Electrospray Experiments

With all three key experiments having been reviewed, a summary of them is provided here and how they are essential for electrospray thruster characterisation. Measurement of electrospray thrusters currents, including the plume, extractor and emitter currents, was the first diagnostic method introduced in this chapter. A characterisation of all three of these currents allows for the characterisation of thruster efficiency and thruster power.

RPA is another key diagnostic method which is used for quantifying the energy distribution in electrospray thruster plumes. The energy distribution can be used for characterising the fragmentation occurring within electrospray thruster plumes, an important physical phenomena unique to electrospray thrusters. The effect of fragmentation on data is essential to characterise in order to analyse some of the propellants used later in this thesis.

Finally, TOF characterises the distribution of ion cluster sizes in the plume of an electrospray thruster. The distribution of the ion cluster sizes can be used to evaluate how different ionic liquids electrospray and what characteristics affect the emission of different ion clusters.

With all these three experiments combined, electrospray thrusters can be characterised extensively, enabling the investigation of the effects of propellant properties on ion cluster emission. The next chapter will describe the experimental setup developed to characterise the plumes of various ionic liquids and, specific to this thesis, characterise the sizes of ion clusters produced by these ionic liquids.

Chapter 4

Experimental Setup

In order to characterise ion cluster emission, and also characterise electrospray thrusters, a robust, accurate and reliable experimental setup is required. In the previous chapter, it was specified that the setup must include a full plume current collector, a RPA and a TOF system. Furthermore, to be able to conduct the tests without having to take the thruster out of vacuum, essential for rapid and reliable testing, a rotary stage is also required. This chapter discusses how the previous chapter's theoretical considerations were applied in order to create an experimental setup. The methods for raw data analysis will also be introduced, showing how the data in the next chapter were reached. The methodology used for testing the propellants will also be discussed which will define the standard testing techniques for the results section.

4.1 Diagnostic Tools

In total, three plume diagnostic tools were used for the diagnostic system, a large current collector, a retarding potential analyser and a time-of-flight mass spectrometer. The first two of these were already manufactured or purchased off-the-shelf, therefore only a brief overview of these will be provided. The TOF system was developed as part of this PhD, therefore a more thorough discussion of it will be provided, including the designed choices that were made. Finally, a LabVIEW program was developed to control the system using a NI DAQ system.

4.1.1 Current Collector

The current collector utilised for testing was designed and manufactured by previous PhD student Chengyu Ma. However, an overview of its design and current measurement method are given here.

The collector plate was manufactured from 6061 aluminium with a collection area of 200 x 200 mm. Although aluminium has poor SEE properties, it was readily available, therefore it was selected as the collector material. SEE mitigation was accomplished using an SEE grid and therefore the material of the collector plate does not cause significant SEE issues.

Two grids were placed above the collector plate surface, a grounded grid and a SEE grid. Both of the grids were manufactured from MN20 nickel mesh sourced from Precision EForming. The grids have a transparency of 88% each, consequently a total transparency of 77%. The SEE grid was placed 5 mm from the collector plate surface, a distance found to be adequate in suppressing SEE effects. A SEE voltage of -30 V was applied during testing. The grounded grid was placed a further 5 mm away from the SEE grid. It was kept grounded throughout testing in order to keep the electric field contained within the current collector.

For the current measurement, a transimpedance amplifier (TIA) was used. The model of the TIA was the DHPKA-100, sourced from FEMTO. The DHPKA-100 is a commonly used TIA in the electrospray research field, therefore it was selected due to its reliability. The DHPKA-100 allows for a variable gain, from 10^2 to 10^7 , making it suitable for use as a general purpose current measurement device. The voltage output was recorded using the DAQ system where it was converted to the collector current value and stored.

As the extractor current reader could short with the high voltage power supply, the DHPKA-100 was not used to measure the extractor current. Instead, the measurement of extractor current was achieved by measuring the voltage drop across a resistor. The resistance was selected as 100 k Ω , corresponding to a voltage of 1 V for every 10 μ A of extractor current. In order to prevent damage to the voltmeter due to sparking, a Transient Voltage Suppression diode (TVS) was also implemented in parallel to the measurement resistor as illustrated in Fig 4.1. The function of this diode was to short

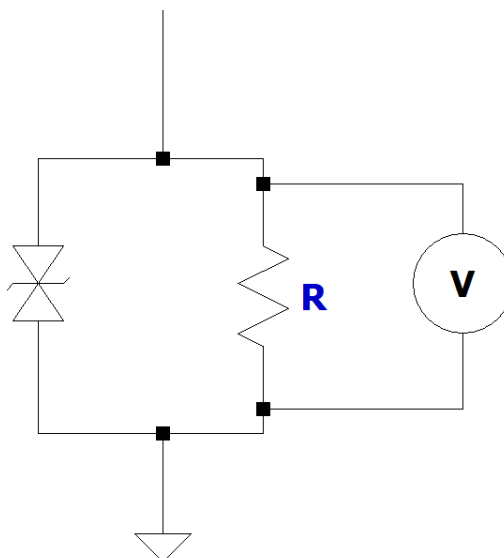


FIGURE 4.1: An example circuit using a TVS diode, made using LTSpice. The voltmeter measures the voltage drop across the resistor, shown on the right, while the TVS is on the left short-circuiting if a the voltage exceeds a certain threshold. This protects the voltmeter from damage during sparking.

circuit when the voltage across the resistor exceeded a certain threshold value, selected to be 10 V.

A digital multimeter, a Keysight 34401A, was used to measure the voltage across the resistor. The multimeter was connected to the LabVIEW program, ensuring the data were recorded synchronously with the collector current data. The sampling frequency of the multimeter was low, at 0.67 Hz, therefore fewer measurements of the extractor current were taken per test than of the collector current, which had a typical sampling frequency of 10 Hz.

4.1.2 Retarding Potential Analyser

Plume energy analysis was essential in the identification of ion clusters of certain ionic liquids and therefore the selection of an appropriate RPA instrument was crucial. In order to simplify the design and manufacturing of the experimental setup, the RPA was purchased off-the-shelf.

The Kimball Physics FC-72 was selected for use in these experiments, which can be used both as a Faraday cup or a retarding potential analyser. The RPA has three grids, with the SEE grid charged to -30 V and the third grid kept grounded. This retarding

potential is applied to the second grid. A schematic of this RPA can be found in Figure 4.2, which shows the three grids as well as the approximate internal structure of the RPA.

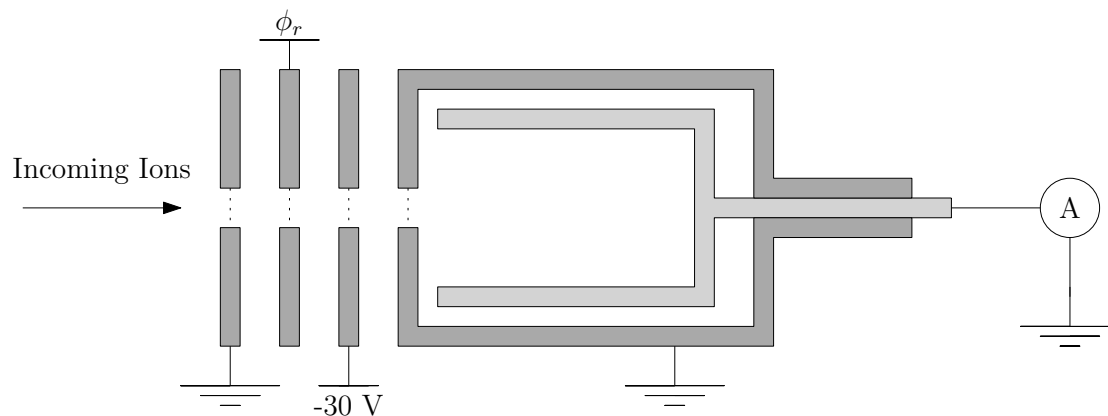


FIGURE 4.2: The schematics of the FC-72 used as an RPA. The RPA has, from left to right, a grounded, a retarding and a SEE grid, terminated by a collector cup surrounded by a grounded shield used for collecting the ion current.

The retarding potential was synchronised with the current measurements using the LabVIEW program. A programmable power supply, a Matusada AMT-5B20, was used which enabled control of the retarding potential. The current measurements were taken with the DHPCA-100, which was also connected to the DAQ system. These were then synchronised using the LabVIEW program, which would record the data concurrently during RPA testing.

4.1.3 Time-of-Flight Mass Spectrometer

The TOF system was developed as part of the diagnostic system as no off-the-shelf solutions were available. Previous work on the TOF system using a reflecting gate produced data that indicated pure ion emission of primarily monomers and dimers, however the data were noisy therefore somewhat unreliable [35]. The TOF system required improvements in order to ensure reliable data and operation with a single emitter.

The TOF system consists of a deflecting gate and a large metal collector, with a flight length of 550 mm. The gate switching was provided by a PVX-4140 high voltage switch, controlled by the LabVIEW program. The current was measured using the DHPCA-100 and recorded using a Wavesurfer 3024 oscilloscope. The gate and large metal collector

were manufactured internally, therefore these were designed in order to minimise the noise of the system.

4.1.3.1 Design of the Electrostatic Gate

The design choices for the gate were made based upon the considerations of gate noise. In section 3.3.2, the gate noise was defined as,

$$I_{cap} = C \frac{d\phi_g}{dt}, \quad (4.1)$$

where I_{cap} is the current produced due to the fast switching of the gate and the parasitic capacitance within the system. The capacitive current is reduced by a lower voltage per time and a lower capacitance, illustrated in Equation 4.1. The gate switch that was selected for the system, the PVX-4140, had a rise-time below 20 ns, which could not be changed. The gate voltage was dependent on the ionic liquid which was used, hence this was also typically constant. Capacitance was therefore the only characteristic that could be significantly reduced for the system.

In order to design the gate with minimum capacitance, the factors contributing to capacitance were investigated. Capacitance between two parallel plates can be defined as,

$$C = \frac{\epsilon A}{d}, \quad (4.2)$$

where A is the area of the plate, ϵ is the relative permittivity of the insulating material and d is the distance between the two plates.

Equation 4.2 provides three design consideration for the gate in order to decrease the capacitance hence decrease gate noise. To reduce relative permittivity polypropylene spaces between the three gate electrodes were used with a lower relative permittivity of 2.2, compared to other readily available spacers. Polypropylene was also found to be suitable for use in vacuum based on outgassing data¹. To further decrease capacitance, the area of the spacers was minimised.

¹<https://outgassing.nasa.gov/outgassing-data-table>

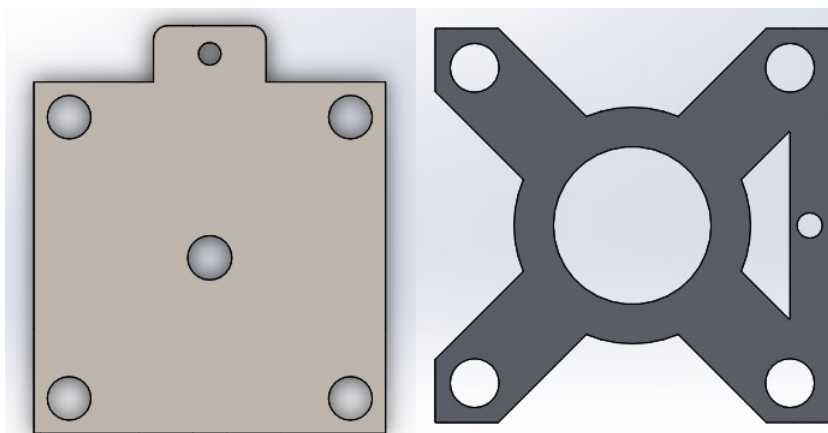


FIGURE 4.3: The previous TOF gate design, shown on the left, with an improved design shown on the right. The area of the gate was reduced between the two designs in order to decrease the capacitance of the system.

Similarly, the area of the gate was also reduced to minimise the capacitance. Figure 4.3 shows the initial designs of the TOF gate on the left hand-side, with the improved design on the right hand-side. The area can be seen to be significantly reduced, with only the central area through which ions were transmitted and the ‘arms’ being kept.

The three electrodes were aligned through the ‘arms’ using an alumina rod, which connected three of these electrodes to form a reflecting gate. Each pair of electrodes was separated using two spacers, for a total inter-electrode distance of 6.4 mm. The diameter of the central transmission area was 15 mm and was covered by a MN20 nickel mesh, similar to the current collector system.

4.1.3.2 Design of the Collector Plate

A large current collector was selected for the TOF current collection. The signal-to-noise ratio was found to be a significant problem in the TOF system, therefore the size of the collector plate was maximised. The largest collector diameter that was possible to fit within the vacuum chamber was 180 mm, which was the diameter of the collector area when manufactured. The material selected for the collector plate was 6061 aluminium due to its availability.

Two grids were also used on the collector plate, the SEE and grounded grid, manufactured from the MN20 nickel mesh material. A voltage of -45 V was applied to the SEE

grid, provided by five 9 V batteries. Batteries were used to provide the SEE voltage as their application minimised the noise of the TOF data.

An image of the TOF collector plate is shown in Figure 4.4. It shows the assembled collector plate prior to being placed in the vacuum chamber. The two grids and collector surface are connected together using three alumina rods. Similar to the TOF gate, two polypropylene spacers were used to separate the grids and the collector surface.

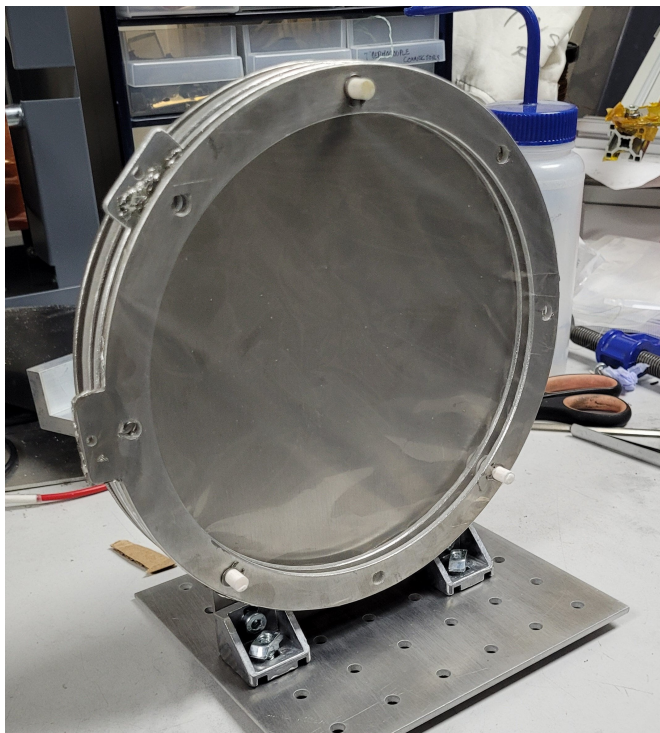


FIGURE 4.4: The large collector plate designed for use with TOF system.

4.1.3.3 Assembled TOF System

A diagram of the fully assembled system is shown in Figure 4.5. The important dimensions of the TOF system have been added to the diagram to help illustrate the design choices made. The spacing of different plates is the same for the gate and the collector plate. During testing, a 'guard' is added behind the TOF gate. The function of this component was to prevent any stray ions or electrons from entering the TOF system. It was made from a 6061 metal plate and was mounted a few centimetres behind the gate.

The current is measured also using the DHPCA-100, with a gain of 10^5 and a bandwidth of 3.5 MHz. The current measurements were averaged using a Wavesurfer 3024 oscilloscope, which was connected to the DHPCA-100. 500 waveforms were averaged per measurement in order to minimise noise by the oscilloscope. However, the oscilloscope did not store the 500 waveforms and each TOF data curve was averaged concurrently, so that only the final averaged waveform was available.

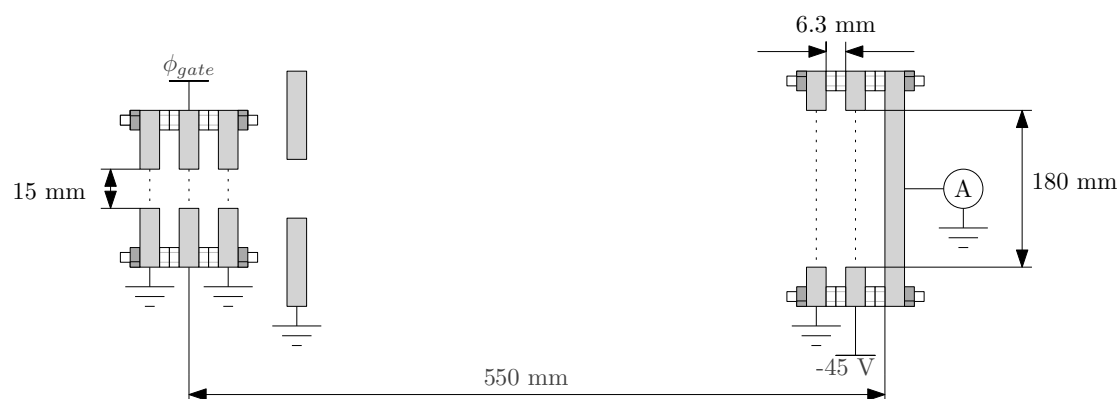


FIGURE 4.5: The assembled TOF system consisting of the gate on the left, the 'guard' behind the gate and the collector on the right. Key dimensions are shown for both the gate and the current collector.

4.2 Electrospray Thruster

A single emitter electrospray thruster was used to test the ionic liquids, as designed by Turan, Ma and Ryan [89]. The emitters were made from P5 BORU borosilicate glass with pore sizes of 1-1.6 μm using CNC machining. The emitters were designed to have a tip sharpness of 100 μm . The emitter tip height was 2 mm, with the base of the emitter also having a height of 2 mm. A diagram showing the dimensions of each emitter is shown in Figure 4.6.

The emitters were made in blocks of 16 emitters, shown in Figure 4.7, in order to minimise manufacturing costs. After manufacture, the glass bottom of the block was removed using sandpaper in order to produce individual emitters. After the separation process, the emitters were cleaned using isopropanol, scanned (this will be covered further in section 5.1.2) and finally stored until testing. A disadvantage of the manufacturing of the emitters was that the mechanical processes involved in producing each

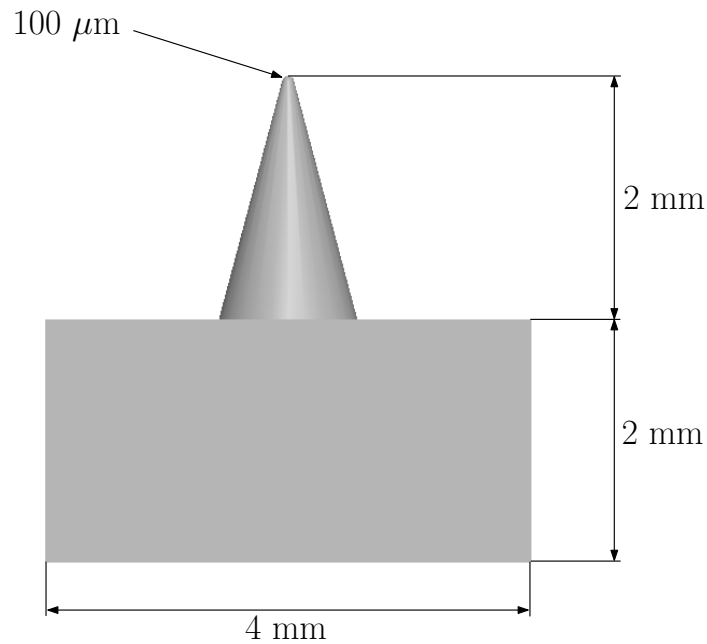


FIGURE 4.6: The designed dimensions of each porous glass emitter.

single emitter reduces the repeatability of the emitter dimensions. This made it essential to measure the tip radii and heights after manufacturing to consider the effects of the manufacturing process.

Propellant was fed to the emitter by a porous stainless steel reservoir, with a porosity of 51% and pore sizes from 39 to 83 μm. The material was sourced from AMESPore and the reservoir was waterjet cut from a sheet of the porous steel.

Figure 4.8 shows a cut-out of the thruster, illustrating the major components. The body was made out of PEEK with a design inspired by the AFET thruster [81]. The emitter was placed into the reservoir and these were mounted using a distal electrode, made out of stainless steel, by four M1.6 bolts. These bolts were also used to ensure emitter alignment. A bolt was used to provide the electrical connect through the back of the thruster, with its hole shown in Figure 4.8.

The extractor was manufactured from AISI 316 stainless steel with a thickness of 0.25 mm. It was waterjet cut from a thin stainless steel plate. The extractor aperture was 1.5 mm. As with the emitter, the extractor was aligned with four M3 bolts, and the emitter-extractor distance was controlled using spacers in between the body of the thruster and the extractor. Using this method, the emitter-extractor distance was kept at approximately 100 μm.



FIGURE 4.7: A block of 16 emitters after CNC manufacturing. The bottom of this block was removed using sandpaper to separate the emitters hence produce 16 individual emitters in a cost-effective manner.

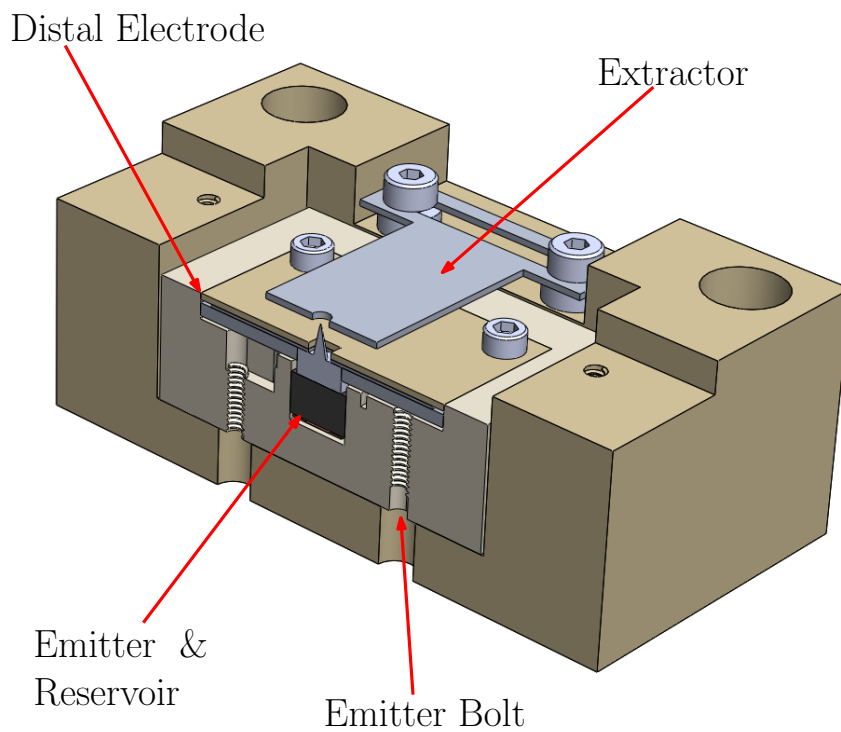


FIGURE 4.8: Cut-out of the thruster with the main components annotated. The emitter and reservoir were kept inside a PEEK casing and the distal electrode, with the electrical connection to the emitter being provided by the emitter bolt. The extractor was connected to the housing using four bolts, allowing for alignment with the emitter.

4.3 Combined Experimental System

This subsection will provide a brief summary for all the remaining components of the combined testing setup. The tests were conducted at the David Fearn Electric Propulsion laboratory at the University of Southampton in the 'Hatch' chamber. The background pressure that the chamber could reach was at minimum 7.4×10^{-7} mBar, however a typical pressure for testing was $\sim 1 \times 10^{-6}$ mBar during emission. The pumps for the chamber are a dry scroll roughing pump and a turbomolecular pump.

In order to rapidly test different ionic liquids, the current collector, RPA and TOF systems were combined to create a testing setup called the Porous Electrospray Thruster Rotating Testing Setup (PET-RTS). This enabled quicker testing as well as an improved reliability of the data. The reliability was improved by ensuring that the wetted emitter, therefore the propellant, had minimum exposure to the atmosphere.

The thruster was mounted on a Velmex V-B4872TS-BK rotary stage, allowing for rotation to orient the thruster towards different diagnostic tools within one experiment. The rotation was controlled by a LabVIEW program which allowed for positional control with an accuracy of 0.1° . The control was enabled by a H-Bridge motor driver, the L298N, which received a digital signal from a NI-9401 DAQ card. The signal controlled a 12 V power supply that powered the coils within the rotary stage.

A diagram of the system is shown in Figure 4.9, showing the different voltages applied to each of the components. A picture of the setup before testing is also provided in Figure 4.10, showing the assembled components.

The LabVIEW DAQ cards that were used were mounted into a cDAQ-9174 chassis. The implemented DAQ cards were: NI-9211, NI-9263, NI-9401 and NI-9205. The NI-9211 was only used for one of the ionic 'liquids', and was used to measure the thermocouple temperature. The specific parts which were used will be presented in section 5.3.2. The programmable power supply was controlled by the NI-9263, which output a ± 10 V voltage to control the ± 5000 V output from the power supply. As previously mentioned, the NI-9401 was used to control the rotary stage using a H-Bridge motor controller, but also functioned to switch the TOF gate during bipolar operation. The NI-9205 measured the voltage output from the DHPKA-100, used for the RPA and current collector.

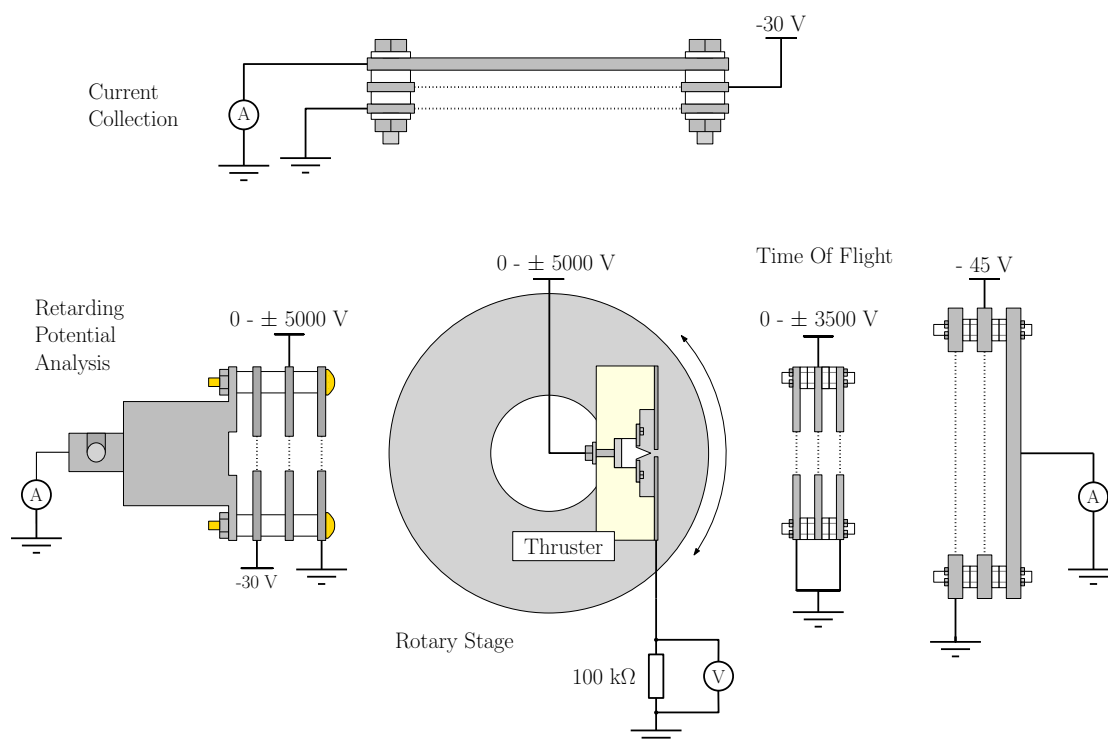


FIGURE 4.9: PET-RTS with the porous electro spray source mounted on the rotary stage. The respective diagram of each of the instruments is shown here with their electrical connections.

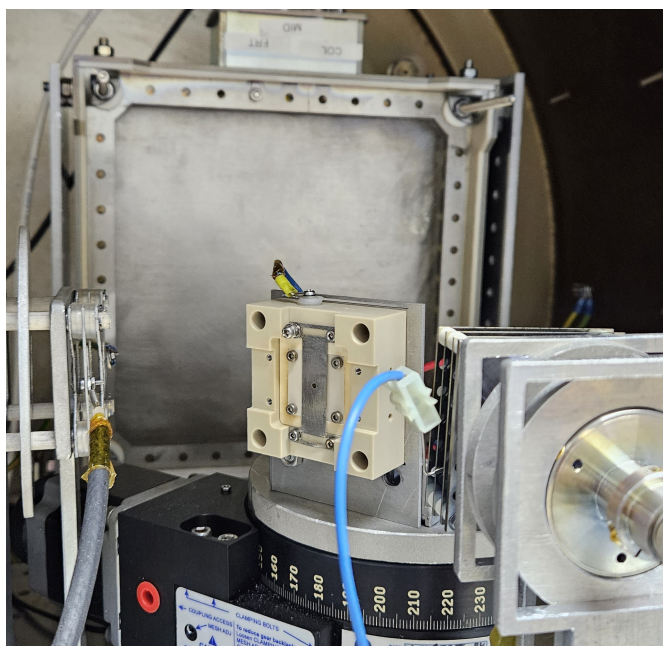


FIGURE 4.10: The thruster, centre, mounted on the rotary stage. On the left hand-side the TOF gate can be seen, positioned behind the thruster is the rotary stage and finally in the bottom right corner is the RPA.

4.4 Data Analysis

In this section, the methods of converting the raw data recorded by the experimental setup will be provided. The collector current was averaged for each voltage and the standard deviation of the collector current was calculated to determine the uncertainty. The RPA current data were binned then averaged for each retarding voltage. Finally, the TOF data were also averaged and noise reduction measures were utilised for the final data.

4.4.1 Collector Current

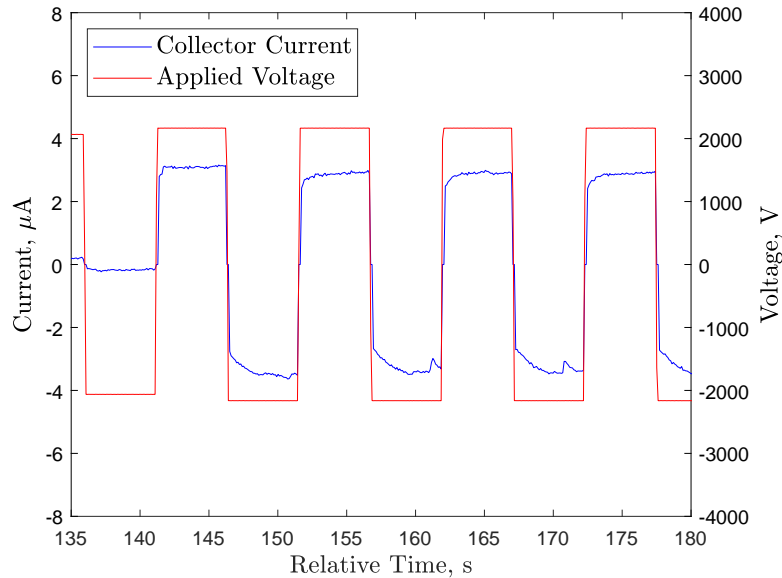


FIGURE 4.11: Current-Voltage data using EMI-BF_4 , with both the current collected and the voltage applied to the emitter.

A sample of the data recorded for each polarity is shown in Figure 4.11. The relative time corresponds to the time since the DAQ system began recording data. Figure 4.11 shows that the collector current was not constant, therefore to ensure that the current was calculated accurately, the current data were averaged per half-wave. Since current is the charge per second,

$$I(t) = \frac{dQ}{dt}, \quad (4.3)$$

where Q is the total charge. The ‘average’ current is calculated by the amount of charge emitted for each polarity, divided by the time the voltage is applied for. The ‘average’ current per cycle, which for simplicity will be I , is given by,

$$I = \frac{\int I(t)dt}{t_h}, \quad (4.4)$$

where t_h is half the period of the applied voltage, applied as a square-wave. In order to achieve this, a simple midpoint rule algorithm was used to calculate $\int I(t)dt$, and the uncertainty was a sum of the amplifier error, 1%, and the standard deviation of the average values.

4.4.2 RPA

Typical raw RPA data are shown in Figure 4.12. These data show a retarding voltage being swept between 0-2800 V to repel ions. The RPA current is also shown, which changes accordingly with the retarding voltage. The current for at least four increasing and decreasing voltage sweeps were averaged per emitter voltage in order to improve the reliability of the RPA data.

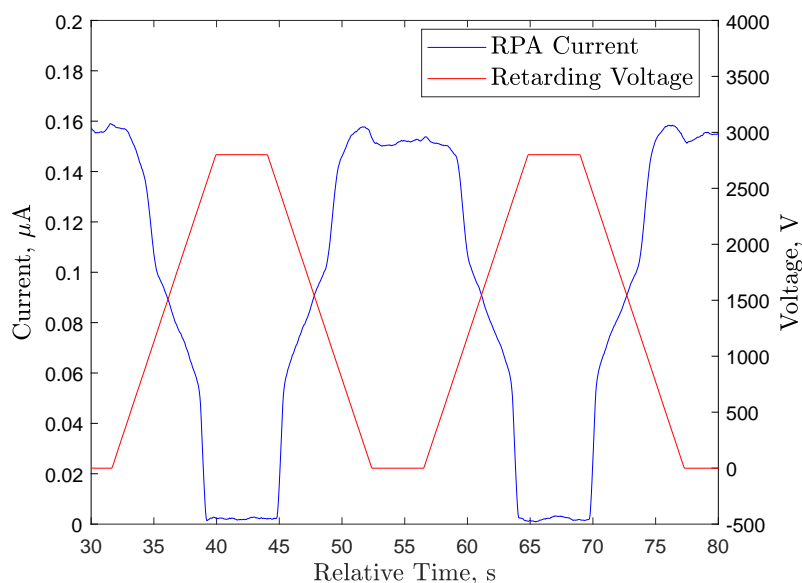


FIGURE 4.12: Raw RPA data using EMI-BF₄ including the retarding voltage applied. As the voltage varies, the current varies accordingly based on the ion energy distribution.

In order to analyse the data, a binning algorithm was developed to average the currents for each voltage. There are 160 bins equally divided into the retarding potential, ϕ_r , with each bin corresponding to a voltage. Each current measurement recorded by the DAQ is assigned to a bin, if the voltage recorded at the time of the current measurement is within $\pm \frac{1}{2}$ of the bin width. Once all the data have been binned, the average for each bin is taken, which gives the average current recorded by the DAQ at the bin voltage. The standard deviation of each bin is calculated, with the uncertainty for each measurement being equal to the sum of the standard deviation and the error from the DHPCA-100, 1%. These data are then plotted using the normalised current, \bar{I} and voltage, \bar{V} , and are calculated as,

$$\bar{I} = \frac{I(V)}{I_{max}} \quad (4.5)$$

$$\bar{V} = \frac{V}{\phi_{emitter}}, \quad (4.6)$$

where I_{max} is the current when ϕ_r is zero.

4.4.3 TOF

The two sets of TOF data were collected for each TOF measurement. One of these data sets was the TOF data during thruster operation at a given voltage. The other set of data was the current without thruster operation. Although gate noise was significantly decreased by the gate design, issues persisted with the gate noise during testing.

One of the gate effects was a change in the current after the gate was activated. Figure 4.13 shows the TOF data recorded without thruster operation. It can be seen that after the gate switches at 0 μ s, a lot of gate noise is initially seen. The magnitude of the gate noise reduces, with it becoming significantly smaller at around 5 μ s. However, likely due to the gate noise, a current decay is seen after the gate was switched. This current decay occurs over a long period, meaning it affects all the TOF data.

This effect can be seen in Figure 4.14, which shows the raw TOF data from the oscilloscope. The data correspond to a TOF curve for EMI-BF₄ operating at a voltage of 2800 V, with a plume comprised primarily of monomers and dimers, with evidence of some

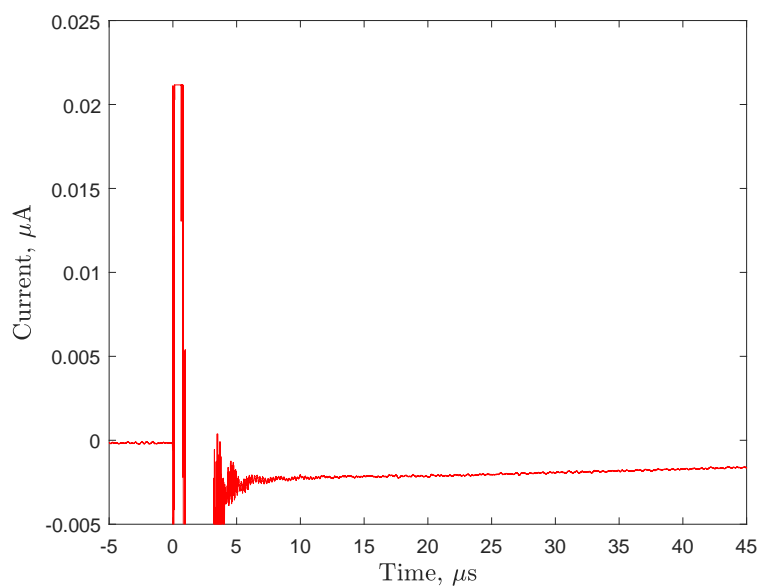


FIGURE 4.13: TOF data recorded without the thruster operating, showing the gate noise occurring after the switching of the gate at 0 μs .

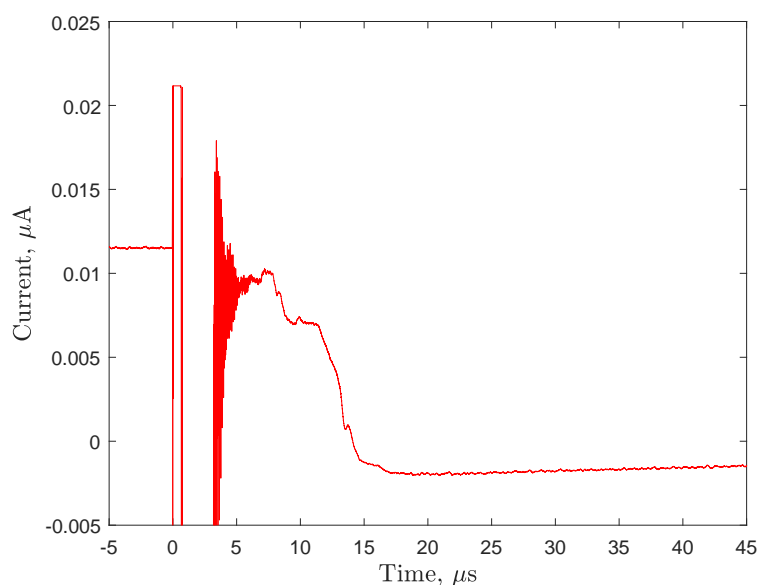


FIGURE 4.14: Raw TOF with no corrections or filtering while the thruster is operating showing a typical TOF curve.

trimers. It can be seen that the decaying current is also seen in these data, which could interfere with identifying larger size ionic clusters.

To minimise this effect, the gate noise data is subtracted from the TOF data. Figure 4.15 shows the TOF data with the gate noise data, shown in Figure 4.13, subtracted

from the raw TOF data, shown in Figure 4.14. It can be seen that the decay in current is significantly reduced, allowing for easier identification of heavier ionic clusters. A slight offset is also seen in the data. Based on long period TOF data taken, it is likely that this is caused by the slight negative offset of the gate noise data, seen at times below 0 μs in Figure 4.13.

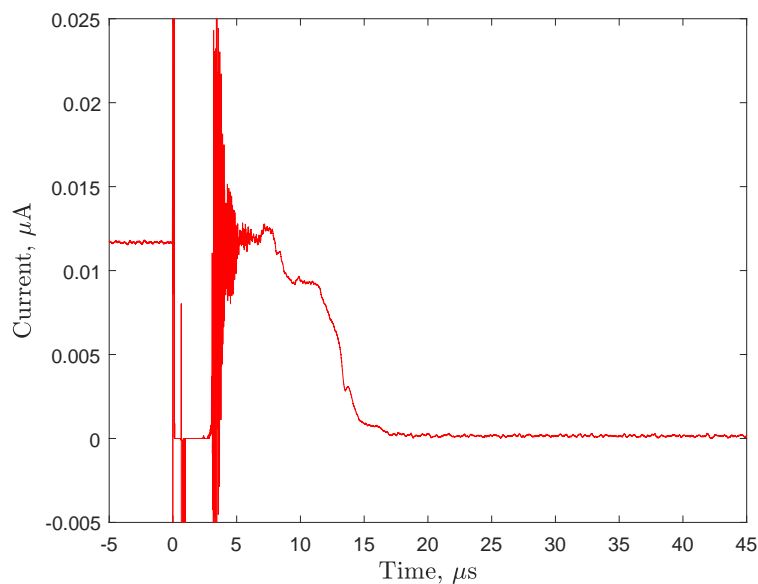


FIGURE 4.15: Reduced noise TOF data, removing the effect of the gate noise by subtracting the gate noise from the raw TOF data.

There are a few final steps to produce the final TOF data which are presented in the next chapter. Firstly, a 5 MHz zero-phase butterworth filter is applied to the data in order to remove some of the higher frequency noise. Using a zero-phase filter prevents the shifting of the current drops caused by typical Butterworth filters, essential in ensuring accurate times of arrival.

The data are also normalised in the current. Each current reading is normalised with the current at the calculated arrival time of monomers $I_{n=0}$, so that:

$$\bar{I} = \frac{I(t)}{I_{n=0}}. \quad (4.7)$$

For presentation the time axis is converted to charge-to-mass ratio. The TOF charge-to-mass ratio equation was defined in section 3.3.2, which is,

$$\frac{q}{m} = 2 \frac{L^2}{\phi_{emitter} t^2}. \quad (4.8)$$

For the TOF data, Equation 4.8 is applied, transforming the arrival times to charge-to-mass ratios, making ionic cluster identification easier. Figure 4.16 shows the final TOF data with the filtering and the transformed time data.

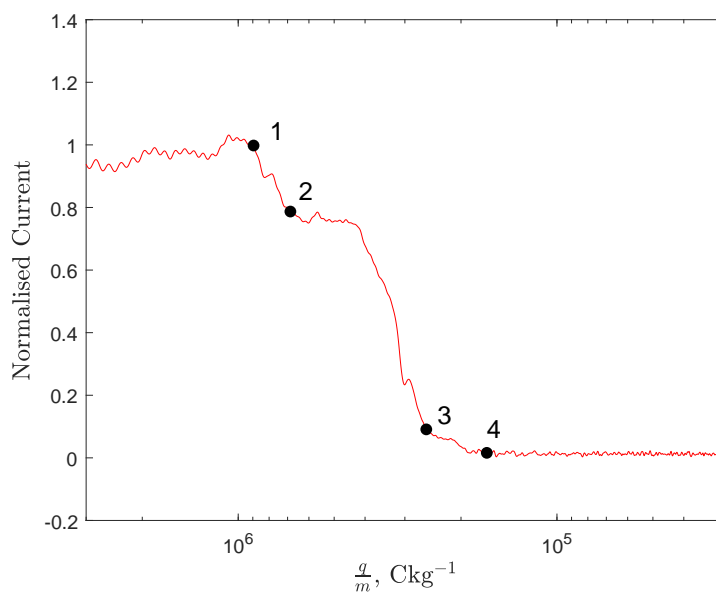


FIGURE 4.16: Filtered and transformed TOF data. The points indicate where the proportions of each species were calculated.

To calculate the relative proportions of each ion species, a manual method was used. The turning points in the data were identified, around the estimated charge-to-mass ratio of each ionic cluster. These are indicated in Figure 4.16 by the numbered points. Although this method was subject to human error, it nonetheless enabled the characterisation of general trends for each ionic liquid. The ion proportions, P_n , were calculated using the formula,

$$P_n = \frac{I_{n+1} - I_{n+2}}{I_1 - I_k}, \quad (4.9)$$

where n corresponds to the neutral number of the ionic cluster ($n = 0$ for monomers, $n = 1$ for dimers etc.) and subscript k corresponds to the last turning point on the data. The uncertainty for each data point is as a sum of the amplifier gain (1%), two times the

standard deviation of the current noise (this is calculated for the 5 μ s before the gate noise is applied) and a factor for human error. Since it is difficult to precisely estimate the uncertainty caused by this, a value of 3% is added to the uncertainty in order to represent human error.

For the example data, the calculated values are provided in Table 4.1, showing a plume primarily comprised of dimers, with a significant amount of monomers and some trimers.

TABLE 4.1: Calculated ion proportions and their uncertainties for the example TOF data.

Ion Type	Proportion	Uncertainty
$n = 0$	0.215	0.055
$n = 1$	0.709	0.055
$n = 2$	0.076	0.055

4.5 Methodology

The procedure applied to all the ionic liquids in preparation for testing will be described in this section. To minimise extraneous effects on the ionic liquid and therefore ensure the reliability of the results, two key steps were taken in the preparation for testing. All the ionic liquids were hygroscopic to a certain degree, and therefore could absorb a significant amount of moisture. Before testing, the propellant was stored in vacuum for at least one day to dry the propellant. When the electro spray thruster was prepared, the assembly time of the thruster was minimised, so that only ~ 1 hour passed between opening the vacuum chamber to atmosphere and the pumping down of the vacuum chamber. After the chamber was pumped down, the thruster was kept in vacuum overnight to further dry the components before finally being able to be tested.

To minimise the cross contamination of ionic liquids, each electro spray thruster component was cleaned using isopropanol and an ultrasonic bath before an experiment. The cleaning process included the liquid reservoir and the components were left to dry in atmosphere for approximately one hour after cleaning. For each test a new emitter

was used. The ionic liquid was fed to the emitter and liquid reservoir with a pipette, with a new pipette being used for each test.

With the electrospray setup, a 'pre-firing' was implemented for 30 minutes to an hour. This involved operating the thruster for a period of time before testing. It was found that the electrospray source would not emit as much current and would onset at a higher voltage until it was pre-fired.

After pre-firing the electrospray source, the current was collected using the large diameter collector plate. The voltage was swept from the electrospray source's onset voltage, V_{onset} , to $V_{onset} + 1000$ V. The electrospray source was operated in a bipolar mode, with a square wave of frequency typically around 0.2 Hz. The low frequency was found to be sufficient to suppress electrochemical effects for most tests, although it was increased to 1 Hz when the collector current exceeded ~ 10 μ A to prevent damage.

Once the total plume current was satisfactorily collected, the electrospray source was rotated and the TOF was collected. The thruster was not necessarily rotated to the exact angle of the TOF gate aperture, as the plume could be emitted a few degrees off-axially. The thruster was therefore rotated until the maximum current was reached, which was assumed to be the centre of the plume. The thruster could be a few degrees off-centre before the maximum current was reached. A similar process was followed for the RPA data. TOF was typically initiated at several hundred volts above onset, at which point a measurable amount of current could be observed on the TOF collector. The emitter voltage would then be incremented in steps of 50 V or 100 V up to at least 400 V above the starting voltage. As some of the ionic liquids had not been previously tested, a cautious approach to testing was implemented.

That last test conducted during an experiment was retarding potential analysis. The emitter voltage range for the RPA was the same as for TOF. The sweeping voltage rose for 8 seconds, rising between 0 V and $\phi_{emitter} + 300$ V. It was then held at the high voltage for a further 4 seconds. The voltage was then reduced from $\phi_{emitter} + 300$ V to 0 V over a period of 8 seconds as well. The retarding voltage was kept at 0 V for 4 seconds, before this process was repeated at minimum four times.

4.6 Summary

An experimental setup containing three different instruments, a large current collector, a RPA and a TOF was created. The setup, called PET-RTS, enabled rapid testing and characterisation of single emitter porous electrospray thrusters, a key aim for testing a broad range of ionic liquids. The system also ensures an increased testing reliability, due to minimising the exposure of any tests to the atmosphere.

The first two diagnostic instruments, the current collector and RPA, were previously available or purchased off-the-shelf, therefore easily integrated into the system. However, the TOF system was developed as part of this PhD in order to increase the reliability of the previous design. The TOF system was comprised of a 'reflecting' gate with a 15 mm entrance aperture, placed 550 mm away from a large current collector plate, which was 180 mm in diameter in order to ensure maximum current collection. This was found to sufficiently increase the signal-to-noise ratio for the electrospray thruster used in this thesis.

Data analysis for all three instruments was also discussed. For the current-voltage tests an average is taken of the current for each given voltage, and the standard deviation alongside the amplifier error is used to represent the measurement error. RPA curves are averaged for each voltage as well, with a similar error calculation method as current collection. The TOF data are averaged over 500 waveforms and the proportions of each ion species are manually calculated, with the error calculated in a similar manner to the previous two methods with the addition of a factor for human error.

A methodology was outlined for the tests, which focuses on minimising the exposure of the ionic liquids to the atmosphere. The ionic liquids are dried before testing using the vacuum chamber, then the thruster is assembled in approximately one hour, then the thruster is left in vacuum over night in order to ensure minimum moisture is present. During testing, the thruster is pre-fired for 30 minutes in order to ensure a higher repeatability of its current-voltage characteristics. Finally, the three tests are conducted, beginning with current-voltage, followed by TOF and RPA.

Chapter 5

Experimental Results

Parts of this chapter were published in following references: [90, 91]

Experimental results from testing with the PET-RTS diagnostic system will be presented in this chapter. Firstly, the propellants used in testing will be introduced covering two types of ionic liquids tested, metal/metalloid halides and multiply-charged ionic liquids. The results will be presented, beginning with the metal/metalloid halides and ending with multiply-charged ionic liquids. For each ionic liquid the current, RPA and TOF data are presented where available. A combined plot of the emitted current will be presented at the end of the chapter to permit easy comparison of the current emitted by the emitters tested. Finally, the experimental data will be compared to the droplet charge-to-mass ratio equation and the ion emission model.

5.1 Experimental Conditions

5.1.1 Ionic Liquids

In total seven ionic liquids were tested in this thesis. The first group of ionic liquids tested is based upon metal/metalloid halides, a group of ionic liquids that contain a single metal/metalloid atom surrounded by halogens. The reason for the choice of this ion type was by their similarity to EMI-BF₄. It was postulated that ions with a similar structure would produce similar ion clusters to EMI-BF₄ due to being nearly identical in

structure. Furthermore, a previous ionic liquid tested from this group, EMI-GaCl₄ [31], discussed in section 2.3.4 had promising results, emitting more current than EMI-BF₄.

A secondary aim was an increased thrust, vital in commercial electrospray thruster performance [53]. In order to pursue this aim, metal/metalloid halide ionic liquids with higher ion masses were selected. Previous heavy ionic liquids typically had significantly lower currents than EMI-BF₄ [28], therefore despite the additional mass favouring more thrust, the overall thrust was found to be lower due to the decreased current.

The first ionic liquid of these that was selected was 1-ethyl-3-methylimidazolium tetrachloroferrate, EMI-FeCl₄, nearly identical in structure to EMI-BF₄. It has a similar conductivity, but a much lower viscosity than EMI-BF₄ and a significantly heavier anion, 2.27 times heavier than BF₄⁻. The second ionic liquid of this group is 1-ethyl-3-methylimidazolium hexafluoroantimonate, EMI-SbF₆. The anion in this ionic liquid is also structurally similar to BF₄⁻, however with two extra halogens. This combined with the inclusion of antimony make it significantly heavier, 2.72 times heavier than EMI-BF₄. This ionic liquid also has a conductivity approximately two times lower and viscosity two times higher than EMI-BF₄, suggesting a lower current emission may occur. The properties of these ionic liquids can be found in Tab. 5.1, showing their conductivities, viscosities, surface tensions, ion molecular masses and their charges.

TABLE 5.1: The conductivities, K , viscosities, μ , surface tensions, γ , masses, m and charges, q , for the ionic liquids tested in this thesis. is solid, therefore the liquid properties are not provided. All the conductivities unless otherwise stated were tested with a Horriba LAQUAtwin EC-33 conductivitymeter. Anion masses were obtained from PubChem, <https://pubchem.ncbi.nlm.nih.gov/>.

Ionic Liquid	K mS/cm	μ cP	γ mN/m	Cat. m AMU	An. m AMU	An./Cat. q e
EMI-BF ₄	14.6	37.2 [92]	52.8 [60]	111.17	86.81	+1/-1
EMI-FeCl ₄	14.4	18 [93]	47.7 [60]	111.17	197.7	+1/-1
EMI-SbF ₆	6.2 [94]	67 [94]	N/A	111.17	235.75	+1/-1
(EMI) ₂ -Co(SCN) ₄	3.42	225	56.0 [95]	222.34	291.30	2(+1)/-2
C ₆ (mim) ₂ -[Im] ₂	0.42	~ 590 [96]	40 [97]	248.30	562.32	+2/2(-1)
C ₆ (mim) ₂ -Co(SCN) ₄	N/A	N/A	N/A	248.30	291.30	+2/-2
(C ₆ mim) ₃ -Dy(SCN) ₆	N/A	N/A	N/A	501.9	517.4	3(+1)/-3

The second group of ionic liquids tested in this thesis were multiply-charged ionic liquids (MILs). These type of ionic liquids are very novel in that they contain ions with more than one charge within them. All the previous ionic liquids mentioned in this

thesis have contained one anion and one cation within them. However, it is possible for an ionic liquid to be comprised of doubly charged ions, such a doubly charged anion, termed a di-anion, B^{2-} , or a doubly charged cation, termed a di-cation, A^{2+} . These have the possibility to increase the current emission of electrospray thrusters due to the extra charge amplifying the electric field, which will be covered at the start of section 5.3.

The first of this group was bis(1-ethyl-3-methylimidazolium) tetrathiocyanatocobaltate, $(EMI)_2-Co(SCN)_4$, an ionic liquid containing one di-anion ($Co(SCN)_4^{2-}$) and two cations (two EMI^+ cations). $(EMI)_2-Co(SCN)_4$ has relatively 'normal' liquid properties, in that its conductivity is not very low, 3.42 mS/cm, however it has a high viscosity and high surface tension suggesting reduced current.

The second of these ionic liquids was 1,6-bis(3-methylimidazolium-1-yl)hexane bis(trifluoromethylsulfonyl)amide, $C_6(mim)_2-(Im)_2$, an ionic liquid containing a di-cation ($C_6mim_2^{2+}$) and two anions (two Im^-). This ionic liquid has a very low conductivity, 34.7 times lower than $EMI-BF_4$, and a very high viscosity, 15.9 times higher than $EMI-BF_4$, indicating that it may emit a significantly lower current than $EMI-BF_4$.

The next ionic liquid was tris(1-hexyl-3-methylimidazolium) dysprosium(III)hexathiocyanate, $(C_6mim)_3-Dy(SCN)_6$, containing a tri-anion ($Dy(SCN)_6^{3-}$) and three cations (three C_6mim^+). Although none of the ionic liquid properties are known for this ionic liquid, from the experimental handling it was clear that $(C_6mim)_3-Dy(SCN)_6$ is even more viscous than the ionic liquid $C_6(mim)_2-(Im)_2$, having a consistency close to honey, suggesting an extremely high viscosity and very low conductivity.

The final 'ionic liquid' tested was bis(3-methylimidazolium)hexyl tetrakis(hexathiocyanato)cobaltate, $C_6(mim)_2-Co(SCN)_4$, containing a di-cation ($Co(SCN)_4^{2-}$) and a di-anion ($C_6(mim)_2^{2+}$). The propellant properties were not known for $C_6(mim)_2-Co(SCN)_4$ as it was solid at room temperature, having a melting point of around 80°C.

A picture of all the ionic liquids are shown in Figure 5.1, showing the six liquids and one solid ionic liquid tested. The molecular diagrams of each cation and anion tested



FIGURE 5.1: Appearance of the different ionic liquids, from left to right; EMI- BF_4 , EMI- FeCl_4 , EMI- SbF_6 , $(\text{EMI})_2\text{-Co}(\text{SCN})_4$, $\text{C}_6(\text{mim})_2\text{-(Im)}_2$, $(\text{C}_6\text{mim})_3\text{-Dy}(\text{SCN})_6$ and $\text{C}_6(\text{mim})_2\text{-Co}(\text{SCN})_4$.

are shown in Figure 5.2, presented to aid the reader in visualising the scale of each ion. All the cations tested are based on an imidazolium cation, shortened to ‘mim’ when discussed in the form $\text{C}_x(\text{mim})_y$. In Figure 5.2 C_2mim^+ corresponds to EMI^+ , however the chemical formula is used in order to highlight the similarities between all the cations. With the exception of Im^- , there are also two groups of anions. The previously mentioned metal/metalloid halides form the first three anions, BF_4^- , FeCl_4^- and SbF_6^- . The second group is metals with thiocyanate ligands, with these ligands appearing like ‘arms’ attached to the central metal atom, these being $\text{Co}(\text{SCN})_4^{2-}$ and $\text{Dy}(\text{SCN})_6^{3-}$.

5.1.2 Emitters Used for Testing

A summary of the emitters is also provided here. As described in section 4.2, a block of emitters was manufactured before testing that was then sanded down to produce the individual emitters. Although this permitted quicker and cheaper manufacturing of emitters, the repeatability of the emitters tip radii was somewhat low. To mitigate this, all the emitters were scanned after manufacturing using an Alicona InfiniteScan profilometer, enabling the measurement of the emitter tip radii and heights.

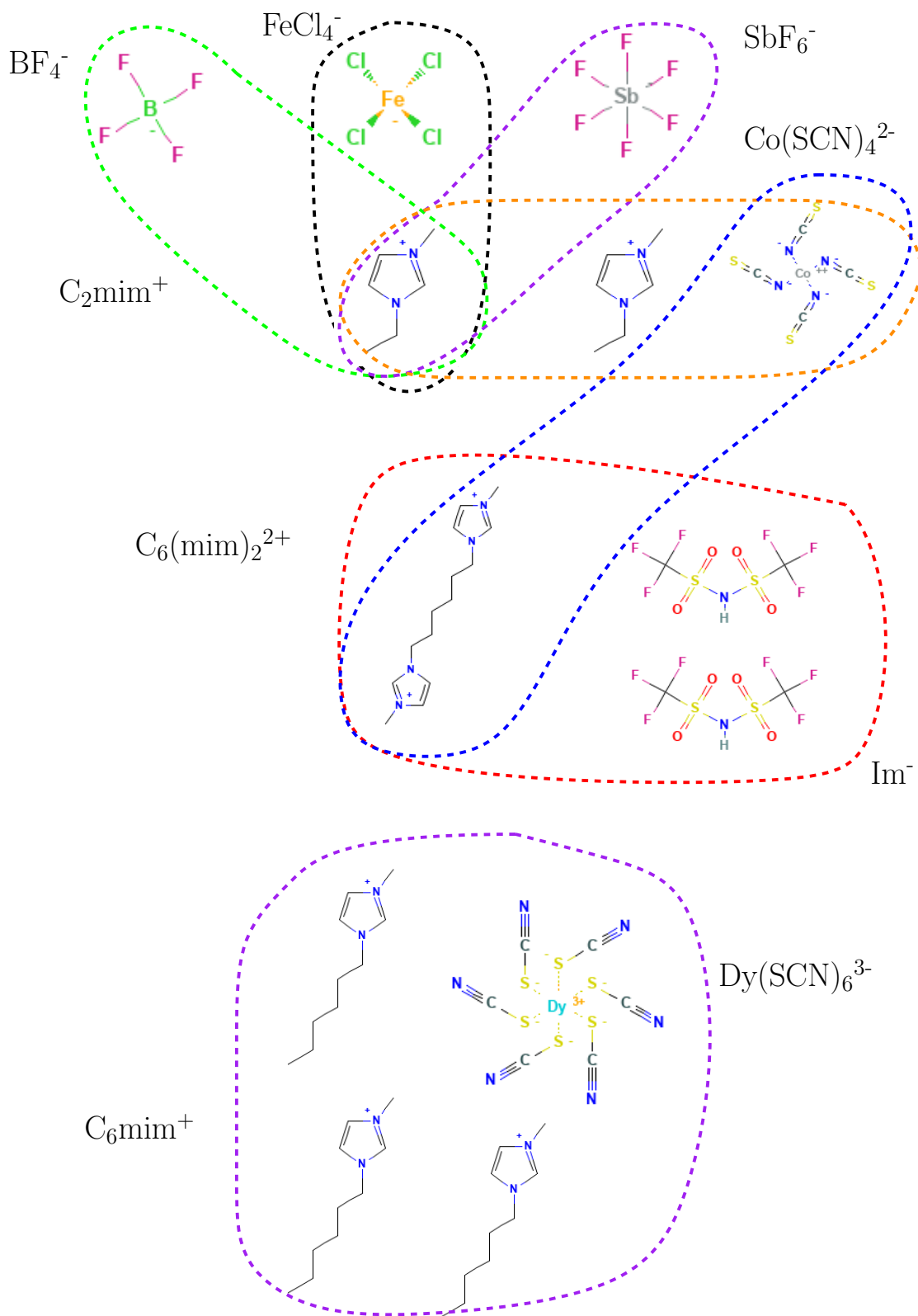


FIGURE 5.2: The ions present in the ionic liquids which were tested in this paper. Each ionic liquids is represented by: EMI- BF_4 - green, EMI- FeCl_4 - black, EMI- SbF_6 - purple, $(\text{EMI})_2\text{-Co}(\text{SCN})_4$ - orange, $\text{C}_6(\text{mim})_2\text{-(Im)}_2$ - red, $(\text{C}_6\text{mim})_3\text{-Dy}(\text{SCN})_6$ - yellow and $\text{C}_6(\text{mim})_2\text{-Co}(\text{SCN})_4$ - blue. The molecular diagrams were sourced from PubChem(<https://pubchem.ncbi.nlm.nih.gov/>).

The measured tip radii and heights are presented in Tab. 5.2. Two different sets of experiments were conducted, where two different tip radii were targeted. Firstly, emitters 2, 1, 10, 6 and 15 (representing the ionic liquids EMI-BF_4 , $(\text{EMI})_2\text{-Co(SCN)}_4$ and $\text{C}_6(\text{mim})_2\text{-(IM)}_2$) were tested to investigate the effects of multiply-charged ionic liquids. Later, emitters 3, 17, 4 and 14 (EMI-BF_4 , EMI-FeCl_4 and EMI-SbF_6) were tested to investigate the effects of metal/metalloid halide ions. Within these two groups, the data are comparable, however the current-voltage data are less reliable due to the variance in emitter tip radii and heights. However, it is assumed that the TOF data, and also RPA data, will not be significantly affected by the tip radii based on previous experimental work various tip radii using externally wetted emitter tips [40].

The last two emitters, 16 and 9 (representing the ionic liquids $\text{C}_6(\text{mim})_2\text{-Co(SCN)}_4$ and $(\text{C}_6\text{mim})_3\text{-Dy(SCN)}_6$ respectively), were tested with insufficient time to produce new emitters. Therefore, the emitters used were some of the last remaining from the emitter block, leading to the large variance in tip radius and height. Even though the data are not reliable enough to produce strong scientific conclusions, they nonetheless provide an insight into what types of ion clusters are emitted by these ionic liquids hence will be presented.

TABLE 5.2: Tip radii and heights of different emitter tips used in testing.

Emitter Number	Liquid	Radius (μm)	Height (μm)
2	EMI-BF_4	108.1	2070
3	EMI-BF_4	78.8	2073
17	EMI-FeCl_4	72.7	1862
4	EMI-FeCl_4	78.2	2143
14	EMI-SbF_6	63.0	2213
1	$(\text{EMI})_2\text{-Co(SCN)}_4$	124.9	2073
10	$(\text{EMI})_2\text{-Co(SCN)}_4$	110.7	2045
6	$\text{C}_6(\text{mim})_2\text{-(IM)}_2$	111.9	2231
15	$\text{C}_6(\text{mim})_2\text{-(IM)}_2$	61.2	2067
16	$\text{C}_6(\text{mim})_2\text{-Co(SCN)}_4$	130.9	1781
9	$(\text{C}_6\text{mim})_3\text{-Dy(SCN)}_6$	50.1	2258

5.2 Metal/Metalloid Halides

5.2.1 EMI-BF₄

5.2.1.1 Current-Voltage

EMI-BF₄ is the most commonly used ionic liquid for electrospray thrusters and as such will be used as the baseline ionic liquid for comparison. The first data that will be presented is the current-voltage data as it is the most basic data that can be collected for electrospray thrusters.

Using emitter 2 the onset of emission is at a voltage of 2000 V, reaching a maximum current of +10.3/-14.9 μA at a voltage of ± 2800 V shown in Figure 5.3. The current levels for a single emitter shown here are very high in comparison to other single emitter tests done in literature [28, 29, 98] possibly due to the porosity of the propellant tank and emitter. For more details on the the emitters and propellant reservoirs used in this thesis, the thesis by Ma provides detail into their development and design choices [82]. For these data the extractor current data are not shown as they are noisy, however the magnitude of the extractor current was negligible for emitter 2.

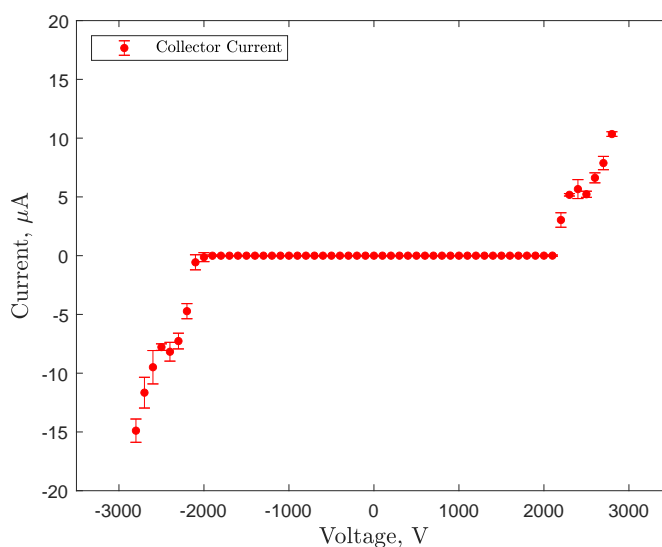


FIGURE 5.3: Current-voltage for data emitter 2 using EMI-BF₄.

The current-voltage data for EMI-BF₄ when using emitter 3 is illustrated in Figure 5.4. The data show a similar pattern to the emitter 2 current data, however a significantly lower current was emitted, with the maximum current being +3.3/-5.3 μA at a voltage of ± 2900 V. The extractor current data are also shown in Figure 5.4, showing that negligible amounts of the plume were impinging on the extractor. The emitter also onset at a voltage of approximately 2000 V, similar to emitter 2.

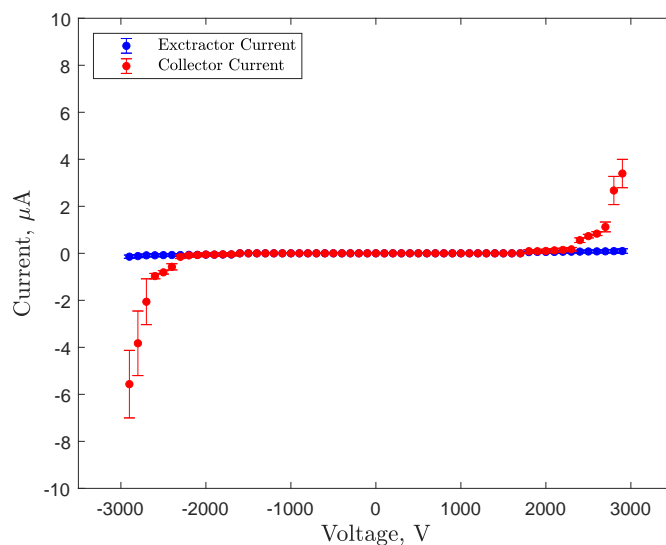


FIGURE 5.4: Current-voltage data for emitter 3 using EMI-BF₄.

Both of these data show that the single emitter thruster is capable of emitting significant amounts of current making these emitters suitable for use for electric propulsion. The radii of emitter 2 and 3 are 108.1 and 78.8 μm respectively, possibly explaining some of the differences in current seen in Figure 5.3 and 5.4. The difference in radii would lead to emitter 2 emitting more current, which is observed, but also on-setting at a higher voltage, which is not observed. It is unclear why the latter effect is not seen, with one possible explanation being that the emitters were at two different levels of wetting (i.e. contained more liquid within them), possibly leading to higher onset voltages and lower amounts of current for emitter 3 if it was less wetted. Another explanation could be that the emitter could have been damaged during assembly or testing leading to this lower current as the emitter scans were taken before testing. Nonetheless, the important data for investigation are the TOF data and therefore the current discrepancies are not relevant.

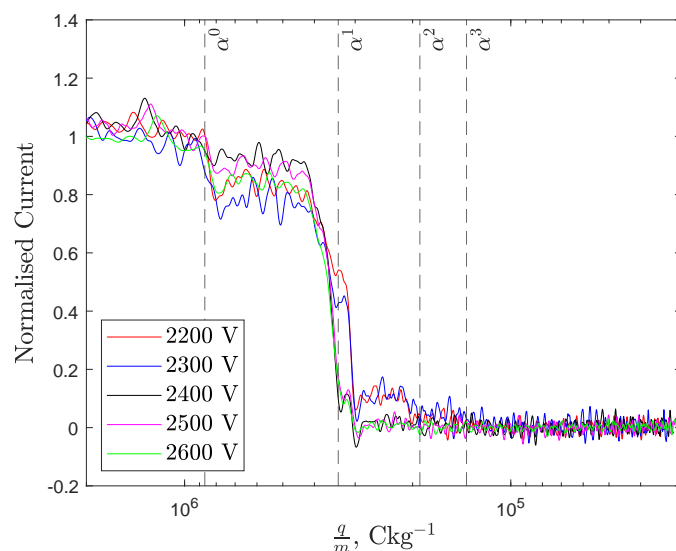
5.2.1.2 Time-of-Flight

For the experimental results chapter, the calculated values for its ions are shown in tables, with the ion table for EMI-BF₄ being Tab. 5.3. Within these tables, from left to right, are shown the ‘ion symbol’ representing each ion (used as it occupies less space when plotted on a graph), the simplified representation of the ion, the chemical formula for the ion, the charge-to-mass ratio of the ion and the calculated field-free fragmentation energy, corresponding to $\frac{\phi_2}{\phi_{emitter}}$. These tables will be used as an easy look up table for all the different ion clusters that will be identified in the TOF and RPA data within this chapter.

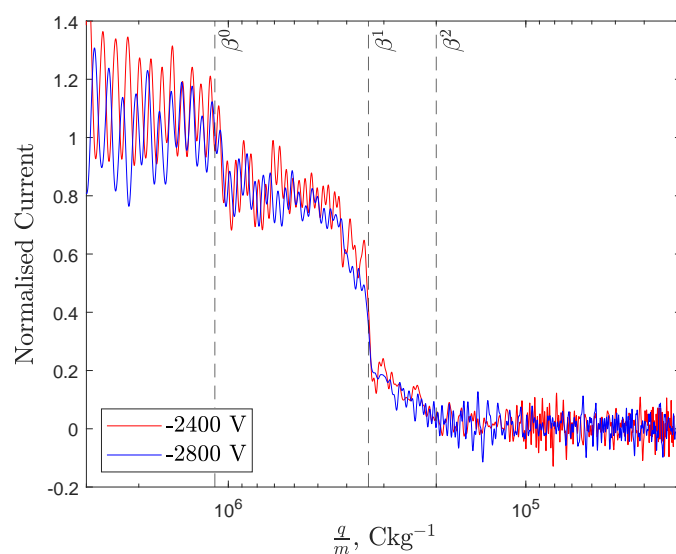
Figure 5.5 illustrates the TOF data collector for emitter 2 for both polarities. They show that both plume polarities are mainly comprised of monomers and dimers, with some trimers also being shown. The data are somewhat noisy, however they show two clear drops in current at the charge-to-mass ratios expected for monomers and dimers, represented by the dashed lines and annotated by their respective symbols from Tab. 5.3. For both polarities, the plume is primarily comprised of dimers with about 80-90% for the positive polarity and 60% for the negative polarity. The ‘tail’ seen in the negative polarity also suggests the existence of trimers within the plume which fragment in the acceleration region of the thruster, while for the positive polarity for 2200 and 2300 V a population of non-fragmenting trimers and quadramers is indicated.

A similar distribution of ion clusters can be seen in the emitter 3 TOF data shown in Figure 5.6. The first two drops from the left correspond to a large population of monomers and dimers, with a majority population of dimers, while the ‘tails’ in both polarities indicate a significant proportion of trimers, quadramers and some larger species corresponding to a somewhat ‘heavier’ plume than emitter 2. However, the emitter 2 and 3 data are very similar showing good repeatability of plume composition across different emitters suggesting the ion beam emitted is broadly in agreement with previous work using similar emitters [35].

Furthermore, the species seen are typical of what is expected from an ionic liquid electrospray source using EMI-BF₄, emitting only ions. Typical EMI-BF₄ plumes emit mostly monomers and dimers, with some larger species also present. The TOF data presented here show that the plume contains a higher proportion of dimers than might



(A) Positive polarity.

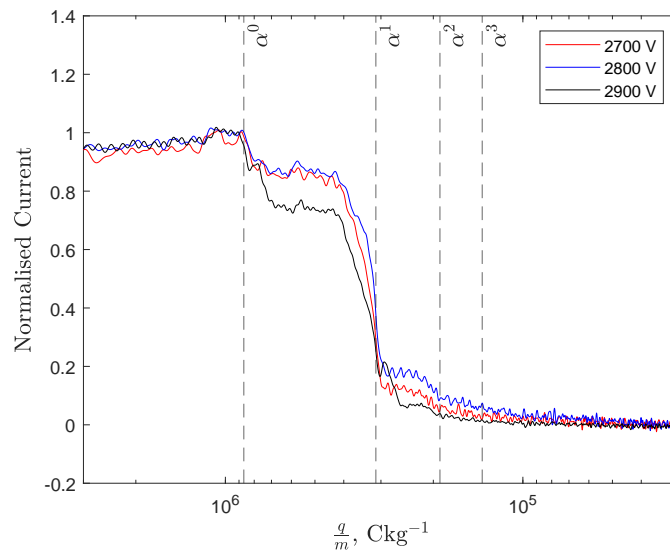


(B) Negative Polarity.

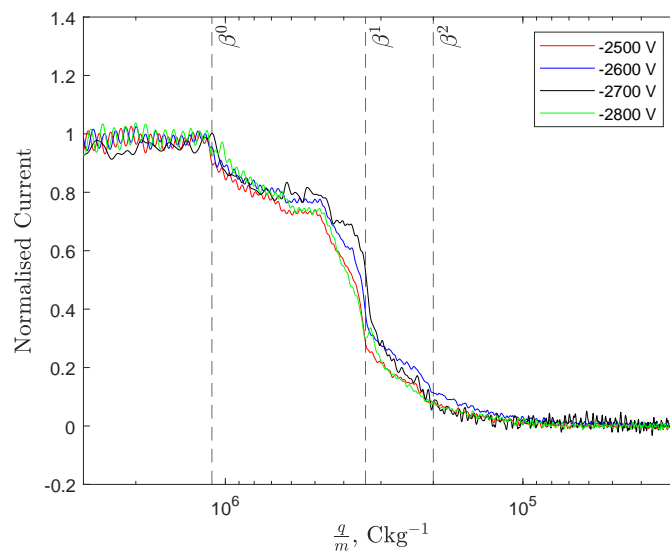
FIGURE 5.5: TOF data for emitter 2 using EMI-BF₄ for both polarities, showing a plume comprised of monomers, dimers and trimers.

be typically expected from an ion emitting electrospray source. This is likely caused by the pores sizes of the emitter and liquid reservoir used in the experiment.

To finish with the EMI-BF₄ TOF data, a long period TOF curve was taken for emitter 2, shown in Figure 5.7. The drops in current show a primarily dimer dominated plume, with evidence of some monomers and trimers, however importantly the long tail shows



(A) Positive polarity.



(B) Negative Polarity.

FIGURE 5.6: TOF data for emitter 3 using EMI-BF₄ for both polarities, with a similar distribution of ions to emitter 2.

that no heavier species are present as there is no decrease in current up to a charge-to-mass ratio of $3 \times 10^2 \text{ Ckg}^{-1}$. Therefore, the data show that the thruster likely operates in a pure ion regime, again confirming previous data on these types of emitters [35].

TABLE 5.3: The various different types of ions calculated which could have been emitted by EMI-BF₄.

Ion Symbol	Simplified Representation	Chemical Formula	Charge-to-Mass Ratio, C/kg	Field-Free Fragmentation Energy
α^0	A ⁺	EMI ⁺	8.67×10^5	Does not fragment
α^1	A ⁺ [A ⁺ B ⁻]	EMI ⁺ [EMI-BF ₄]	3.12×10^5	0.360
α^2	A ⁺ [A ⁺ B ⁻] ₂	EMI ⁺ [EMI-BF ₄] ₂	1.90×10^5	0.610
α^3	A ⁺ [A ⁺ B ⁻] ₃	EMI ⁺ [EMI-BF ₄] ₃	1.37×10^5	0.719
β^0	B ⁻	BF ₄ ⁻	-1.10×10^6	Does not fragment
β^1	B ⁻ [A ⁺ B ⁻]	BF ₄ ⁻ [EMI-BF ₄]	-3.38×10^5	0.305
β^2	B ⁻ [A ⁺ B ⁻] ₂	BF ₄ ⁻ [(EMI-BF ₄) ₂]	-2.00×10^5	0.590

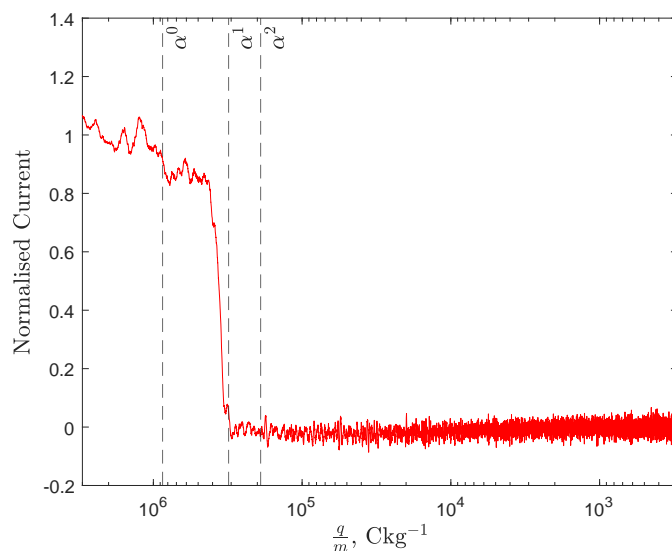


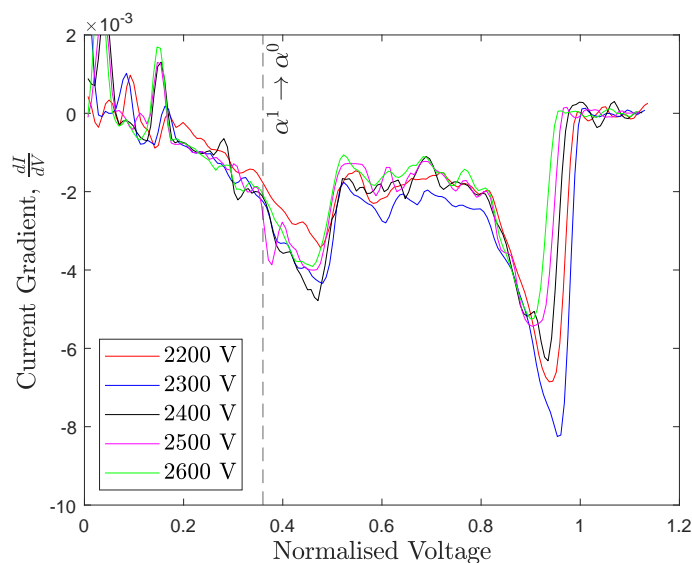
FIGURE 5.7: Long period positive polarity TOF data for emitter 2, showing that the plume emits only ions due to the lack of a 'tail'.

5.2.1.3 Retarding Potential Analysis

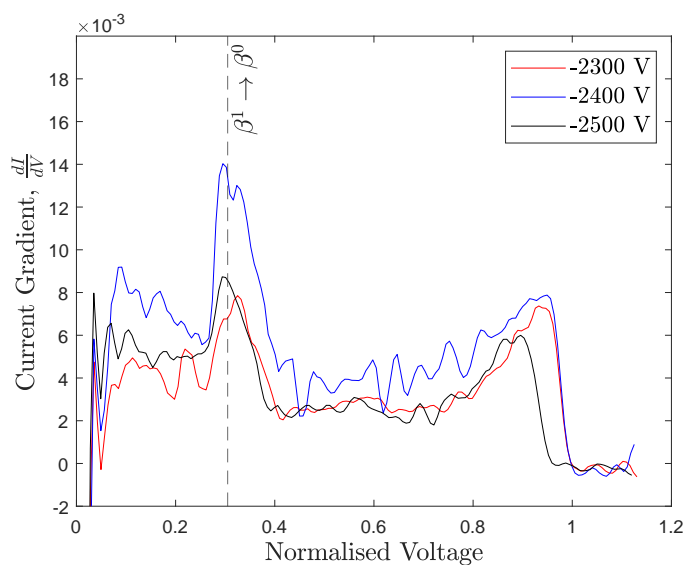
RPA data are used to determine how the emitted ion clusters fragment, indicating both what ion clusters are present and how much propellant is lost due to acceleration region fragmentation resulting in poorly accelerated neutral molecules. The latter effect is not described here due to issues with the retarding potential analyser used in the experimental setup. During testing the RPA had a negative current which did not correspond to any ions, likely being caused by some instrumentation error, therefore obscuring the

acceleration region fragmentation gradient in the data. The RPA data are therefore only used to identify what ions are emitted due to field-free fragmentation.

The positive polarity RPA data for emitter 2 are shown in Figure 5.8a. The figure shows



(A) Positive polarity.



(B) Negative Polarity.

FIGURE 5.8: RPA data for emitter 2 using EMI-BF₄ for both polarities. The peaks around at a normalised voltage lower than 1 correspond to dimer field-free fragmentation in both polarities.

the differentiated current collected during the RPA experiment against the voltage normalised to the emitter voltage. The data show two distinct peaks at different normalised voltages. The peak occurring at a normalised voltage of ~ 0.9 corresponds to ions accelerated by the potential of the emitter tip, representing any emitted ion entering the retarding potential analyser that has not fragmented. An acceleration efficiency of $\sim 90\%$ is indicated by the lower than 1 normalised voltage for the final peak.

The peak occurring at a normalised voltage of ~ 0.4 seems to correspond to the field-free fragmentation of a positive dimer, defined as α^1 in Tab. 5.3. This fragmentation takes the same form as Equation 2.35, with a stopping potential of the ion calculated in Table 5.3, 0.360. The observed peak is more energetic than the theoretically calculated energy. It is unclear why this occurs, as a lower energy is expected due to 90% acceleration efficiency. This misalignment of the expected energy and observed energy is likely caused by instrumentation error. Nonetheless, the lack of other peaks suggests that only dimers are field-free fragmenting, corresponding to the large population of dimers observed in the TOF data. The fragmentation of the α^1 dimer can be represented by



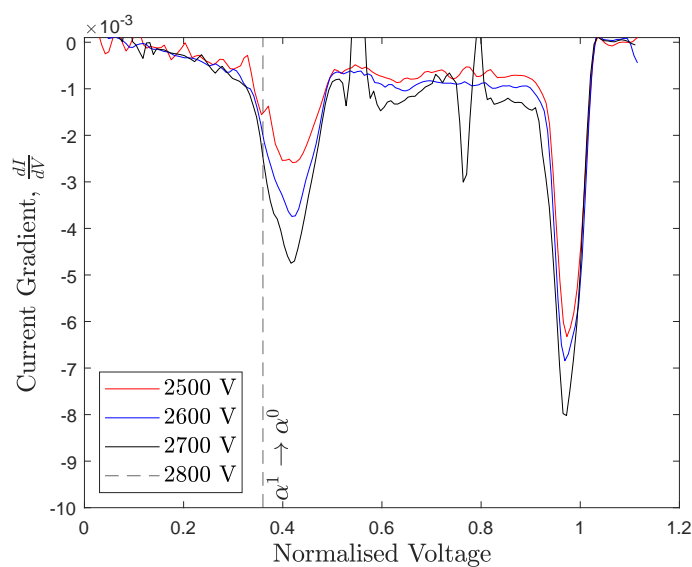
The negative polarity RPA data, shown in Figure 5.8b, indicating similar fragmentation characteristics to the positive polarity data. As with the positive polarity, two prominent peaks can be seen, one of which is around a normalised voltage of ~ 0.3 , indicating the fragmentation of a negative dimer, β^1 . The β^1 field-free fragmentation can be described by



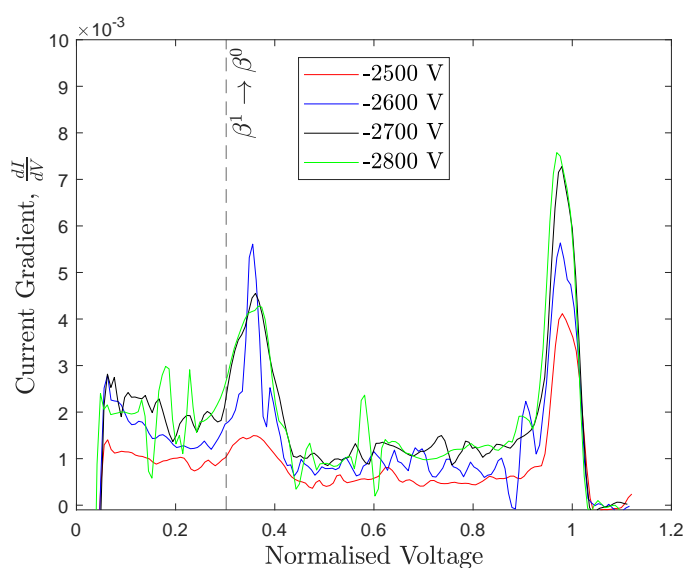
The emitter 3 RPA data are shown in Figure 5.9. The data are similar to the emitter 2 data, with two peaks for both polarities corresponding to ions arriving at the collector of the RPA and field-free fragmentation of dimers, both α^1 and β^1 , respectively. As with the TOF data, the similarity between the two sets of data taken 6 months apart and with different emitters show that the thruster reliably emits monomers, dimers

and some trimers. These ion clusters also fragment in a similar manner as shown by the RPA data.

More energetic peaks than theoretically calculated are seen for both emitters. It is likely that this is caused by instrumentation error due to the RPA already showing an anomalous negative gradient during experimentation. Nonetheless, for the peaks observed in the data, the ion identification was not obscured by this effect.



(A) Positive polarity.



(B) Negative Polarity.

FIGURE 5.9: RPA data for emitter 3 using EMI-BF₄ for both polarities. Similarly to emitter 2, only dimer field-free fragmentation is observed.

5.2.2 EMI-FeCl₄

5.2.2.1 Current-Voltage

Due to its low viscosity and similar conductivity to EMI-BF₄, EMI-FeCl₄ was expected to produce high levels of current. The current-voltage data for emitter 17 are presented in Figure 5.10. For emitter 17 the current emitted can be seen to be approximately equivalent to the highest current emitted using EMI-BF₄ (emitter 2 shown in Figure 5.3), emitting up to +16.6/-14.0 μA at a voltage of ± 2150 V. However, one key difference is a significantly lower operating voltage, with an onset voltage of ± 1200 V. Considering the radius for emitter 17 is 72.7 μm , lower than the emitter 2 radius, tested with EMI-BF₄, the current and the onset voltage should be lower. The similar levels of current could suggest that EMI-FeCl₄ is emitting more current due to its favourable ionic liquid properties.

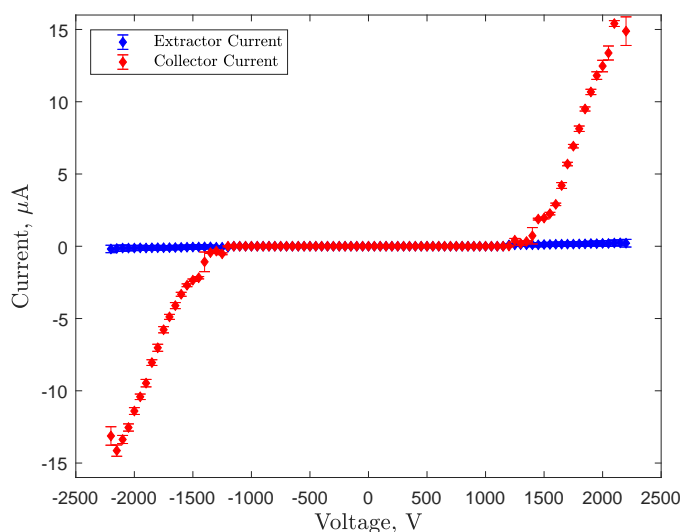


FIGURE 5.10: Current-voltage data for emitter 17 using EMI-FeCl₄, showing a similar magnitude of current emitted to EMI-BF₄, albeit at a significantly lower voltage.

It is difficult to estimate the onset voltage for a porous electrospray thruster. The emitter tip radius [53, 42], emitter-extractor distance [53, 42, 98], pore size [63] and ionic liquid properties will contribute to the onset voltage. One method to approximate the onset voltage is by considering electric field on the surface of a hyperboloid in the proximity of a flat plate [20]. This equation can be defined as

$$V_{onset} = \sqrt{\frac{\gamma r_t}{\epsilon_0}} \frac{\ln\left(\frac{r_t + 2d + 2\sqrt{d(d+r_t)}}{r_t}\right)}{\sqrt{1 + \frac{r_t}{d}}}, \quad (5.3)$$

where r_t is the tip radius and d is the emitter-extractor distance. Although Eq. 5.3 does not consider the effect of porosity which can significantly alter an emitter's onset voltage [63], it might allow for comparison of onset voltages assuming the same porosities. Using the emitter 2 tip radius, 108.1 μm , and emitter 17's tip radius, 72.7 μm , an emitter-extractor distance of 100 μm , and the surface tensions of the two ionic liquids from Tab. 5.1, the onset voltages of emitter 17 and emitter 2 can be approximately calculated. Using Eq. 5.3, the onset voltages are approximately the same for both of the emitters. This is illustrated in Figure 5.11, where two lines are plotted, one showing the onset voltages for EMI- FeCl_4 and one for EMI- BF_4 . It can be seen that the onset values in Figure 5.11 are significantly lower than in experimental data, likely due to the assumption of a flat metal plate.

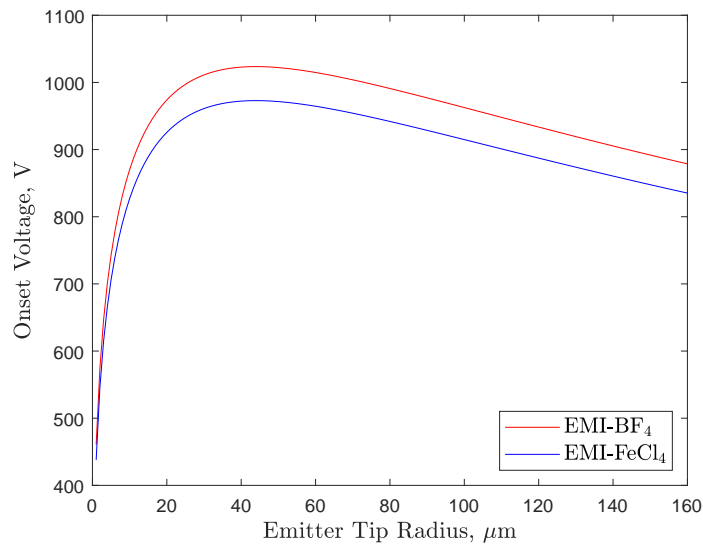


FIGURE 5.11: Estimated onset voltages for EMI- BF_4 and EMI- FeCl_4 , which are lower than experimental onset voltages likely due to the Equation 5.3 assuming a flat plate.

However, emitter tip radii experiments show that the onset voltage should reduce with a smaller tip radius [53, 42]. Since Eq. 5.11 does not provide accurate estimates of the reduction in the onset voltage, it is difficult to quantitatively confirm whether the onset voltage is reduced due to the liquid properties or the geometry. Further experiments

characterising the effects of the emitter and extractor geometry are required to determine this relationship for the specific thruster design used in this thesis.

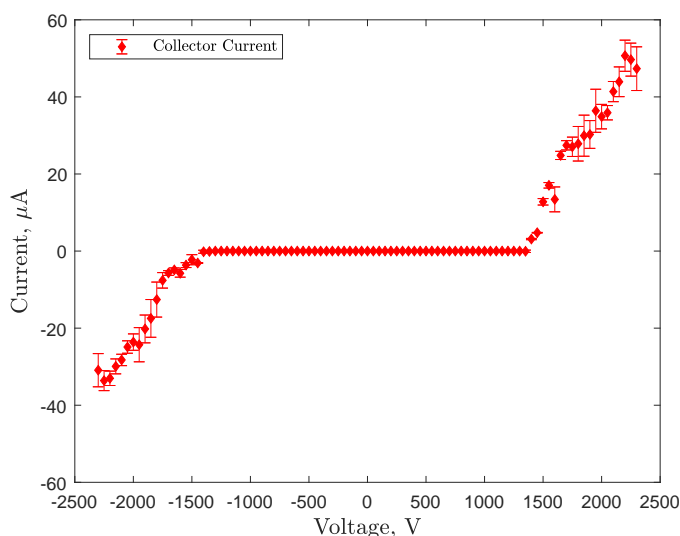


FIGURE 5.12: Current-voltage data for emitter 4 using EMI-FeCl₄. The current emitted is very high in comparison to the EMI-BF₄ tests.

The current-voltage data for emitter 4, the second emitter tested with EMI-FeCl₄, are shown in Figure 5.12. The data show a very large amount of current is emitted, exceeding 50 μA for the positive polarity. The extractor current for emitter 4 was unfortunately not available. Such a high level of current for a single emitter has not been previously recorded and could point towards EMI-FeCl₄ being especially suitable for use in electrospray thrusters, where low thrust restricts electrospray thruster implementation. The level of current is also significantly higher than with emitter 17 even though the radius of the emitter is similar to emitter 17, 78.2 μm for emitter 4 versus 72.7 μm for emitter 17. It is unclear why this maybe the case, possibly being an effect of different wetting. It is also possible that emitter 17 or 4 were damaged during handling, which could create significant differences in the actual emitter tip radii, compared to the measured tip radius. Nonetheless the massively increased current produces compelling evidence for EMI-FeCl₄ possibly being a competitive alternative for EMI-BF₄. Both the increased current and decreased operational voltage being good properties for an electrospray thruster.

Emitter 4 was tested again three days after these data were taken, which is shown in Figure 5.13. For these three days, the thruster was kept assembled inside of the vacuum

chamber, with the chamber being closed during this time, reaching a pressure of ~ 1 mBar due to the pumps not operating. The level of current is seen to be significantly reduced, by an order of magnitude, with the onset voltage remaining approximately the same. The significant reduction in current could suggest that operating the emitter at such a high level of current is not sustainable by a single emitter and either leads to many electrochemical reactions (leading to emitter damage) or damage to the actual emitter due to, for example, sparking. Damage to the emitter is also indicated by the reduction in current after a few days, as this effect was not seen in any of the other repeated current data. The damage can possibly be mitigated by increasing the frequency of voltage alternation, however further tests are required to confirm whether this solution.

A combined plot of all the EMI-FeCl₄ data is shown in Figure 5.14. An additional current-voltage sweep, emitter 17 # 2, has also been added, which is a voltage sweep of emitter 17 taken on a different day. It was kept in a similar condition to emitter 4, except for two days less. It can be seen that the current-voltage data are typically repeatable, except with emitter 4. The cause of this disagreement between the two current-voltage tests of emitter 4 are therefore assumed to be caused by damage to the emitter, possibly by electrochemical reactions. Nonetheless, a repeat of these current-voltage tests are required in order to fully verify the current emission characteristics of EMI-FeCl₄.

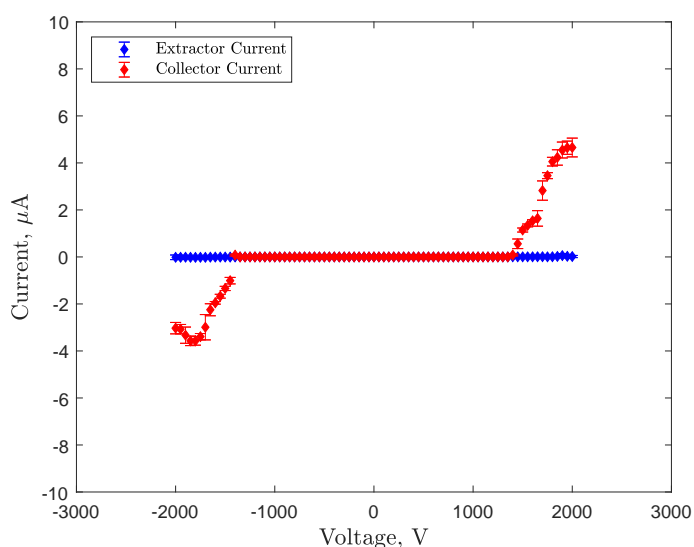


FIGURE 5.13: A repeat test of emitter 4 after three days. The current is seen to be significantly reduced in comparison to the first test with emitter 4, possibly due to emitter damage through electrochemical reactions or sparking.

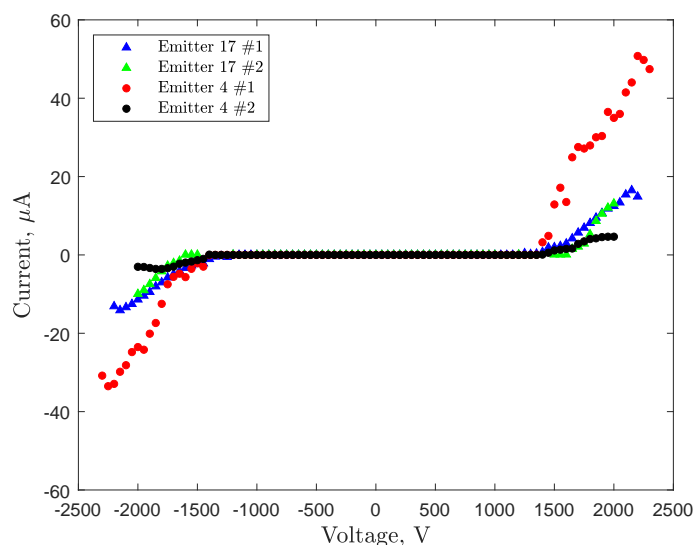


FIGURE 5.14: Combined collector current data for all current data shown, with emitter 17 showing good repeatability compared to emitter 4.

5.2.2.2 Time-of-Flight

Figures 5.15 and 5.16 show the TOF data for both emitters for EMI-FeCl₄, with the ion cluster properties described in Tab. 5.4. The dashed lines show the expected charge-to-mass ratios of for each ion cluster, which from left to right are a monomer, α^0 or β^0 , a dimer, α^1 or β^1 , and trimer, α^2 or β^2 . As in the case with the current-voltage data of EMI-FeCl₄, the TOF data are also quite surprising. In the positive polarity, shown in Figures 5.15a and 5.16a, the thruster emitted a mixture of primarily monomers and dimers with some trimers and larger species between onset and 200 - 300 V above onset. For example, this is shown by the 1400 V, 1450 V and 1500 V data sets included in Figure 5.15a. However, at voltages higher than this range, the emitter almost entirely emitted monomers (as far as the data show), with a low population of dimers for emitter 17 (approximately 10% of the plume).

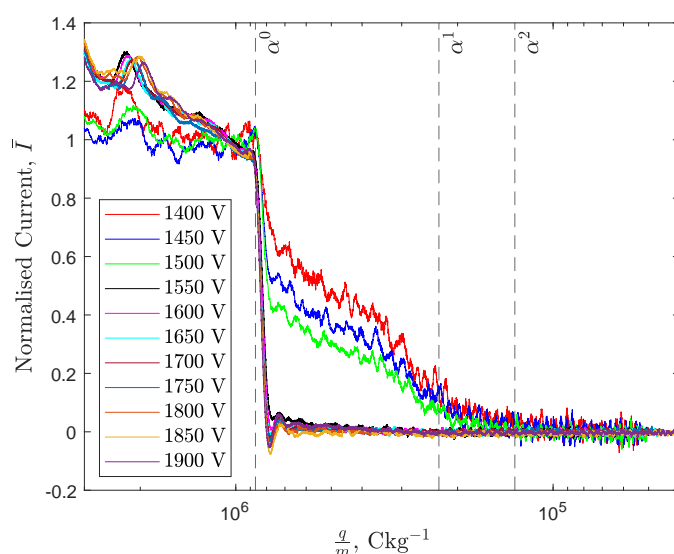
For the negative polarities, shown in Figures 5.15b and 5.16b, a similar trend is seen, with a large population of monomers of at least 50% growing to about 85% at higher voltages for emitter 4, with emitter 17 generally having more monomers than emitter 4. Both of these emitters showed similar plumes at similar voltages above the onset voltage, showing good repeatability for both of the polarities.

The very high amount of monomers, especially in the positive polarity, produces an almost ‘mono-ionic’ plume, that has previously not been reported. A somewhat similar plume was previously observed by Krpoun [20] using EMI-BF₄ and externally wetted emitters, with only monomers being seen at certain voltage. However such a sharp drop seen in these data was not found by Krpoun. From a purely propulsion engineering aspect, for electrospray thrusters this type of plume holds two main benefits. Firstly, emitting only a single type of ion that does not fragment translates to an increase in efficiency due to no mass being lost from acceleration region fragmentation. Secondly, the monomer ion would allow for very high specific impulses due to the monomer’s high charge-to-mass ratio. On the other hand, high charge-to-mass ratio ions mean that the thrust-to-power ratio is lower than other thrusters, translating into a higher power requirement for a similar thrust level. A higher power level can be achieved by EMI-FeCl₄ due to its high current, however it could be problematic for producing propulsion systems for the smallest satellites due to the increased power requirement.

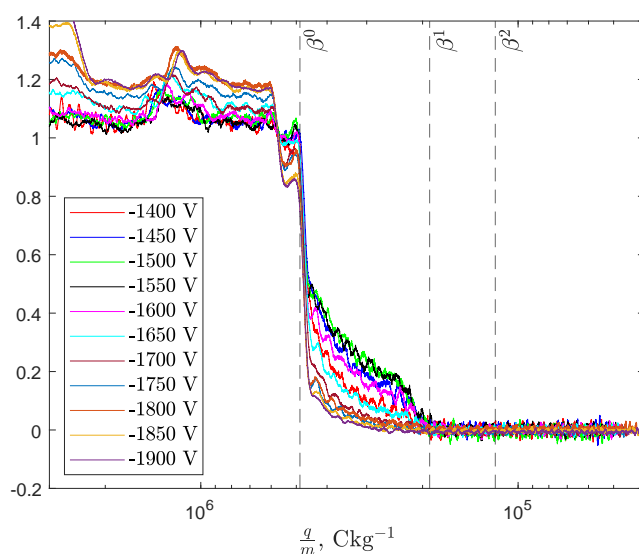
Considering the physics of emission, it is worthwhile to consider why such a plume is produced. There could be a few effects causing the high population of monomers in both polarities. One effect could be that the increasing strength of the electric field, due to the increasing voltage, increases the rate at which dimers fragment in the acceleration region. This would cause the dimers to fragment earlier in the electric field hence reach speeds similar to monomers and appear as monomers using TOF. The second

TABLE 5.4: Various different types of ions calculated which could have been emitted by EMI-FeCl₄.

Ion Symbol	Simplified Representation	Chemical Formula	Charge-to-Mass Ratio, C/kg	Field-Free Fragmentation Energy
α^0	A ⁺	EMI ⁺	8.67×10^5	Does not fragment
α^1	A ⁺ [A ⁺ B ⁻]	EMI ⁺ [EMI-FeCl ₄]	2.29×10^5	0.265
α^2	A ⁺ [A ⁺ B ⁻] ₂	EMI ⁺ [EMI-FeCl ₄] ₂	1.32×10^5	0.576
β^0	B ⁻	FeCl ₄ ⁻	-4.87×10^5	Does not fragment
β^1	B ⁻ [A ⁺ B ⁻]	FeCl ₄ ⁻ [EMI-FeCl ₄]	-1.90×10^5	0.390
β^2	B ⁻ [A ⁺ B ⁻] ₂	FeCl ₄ ⁻ [EMI-FeCl ₄] ₂	-1.18×10^5	0.621



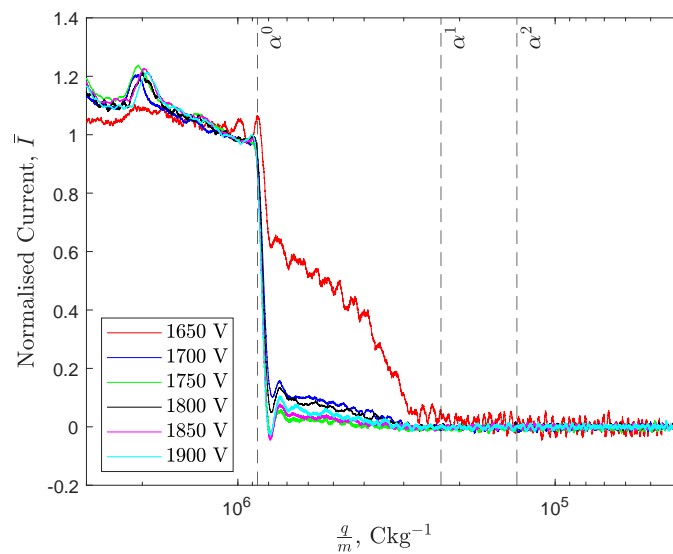
(A) Positive polarity.



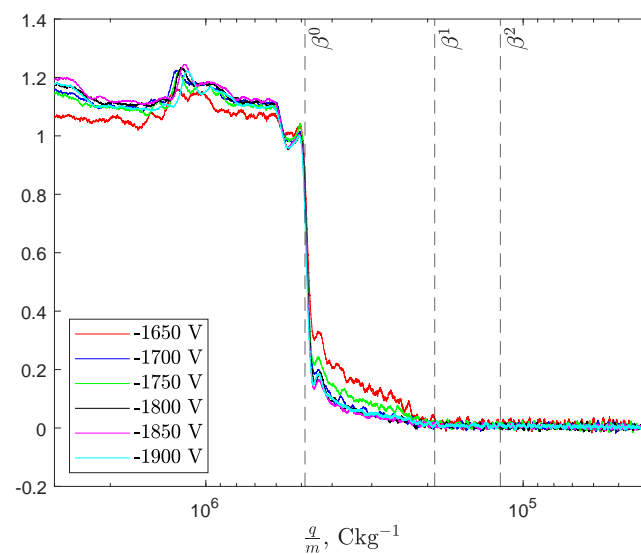
(B) Negative Polarity.

FIGURE 5.15: TOF data for emitter 4 using EMI-FeCl₄ for both polarities, showing an almost purely monomer plume in the positive and negative polarity.

effect could be that the percentage of monomers emitted from the meniscus increases as the voltage increases, increasing the population of monomers relative to the population of dimers in the plume. For increasing fragmentation a gradual decrease in dimer population is expected, seen in the negative polarity. However, in the positive polarity it can be seen that at 1550 V for emitter 4 and 1700 V for emitter 17, the ‘tail’ of the TOF data suddenly disappears, corresponding to a sudden increase in monomer population.



(A) Positive polarity.



(B) Negative Polarity.

FIGURE 5.16: TOF data for emitter 17 using EMI-FeCl₄ for both polarities. Similarly to emitter 4, the plume is almost entirely comprised of monomers in both polarities.

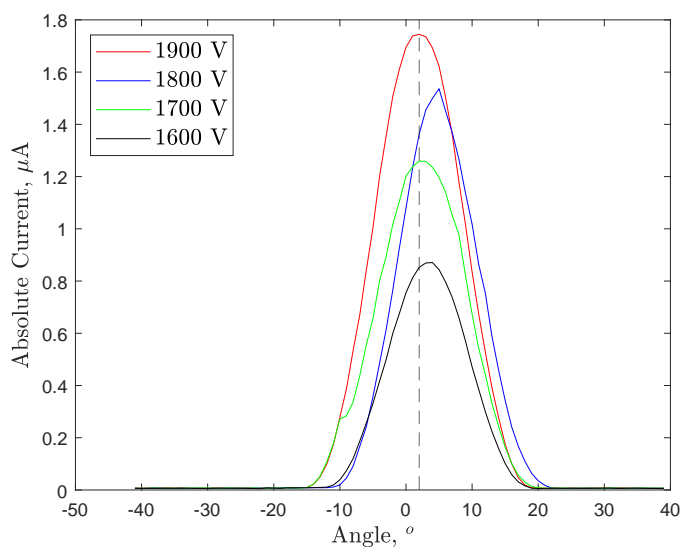
The suddenness of the increase in the monomer population points towards an increase in the emission of monomers as opposed to the gradual increase in acceleration region dimer fragmentation.

A further possibility is that the thruster begins to emit off-axially or begins to emit

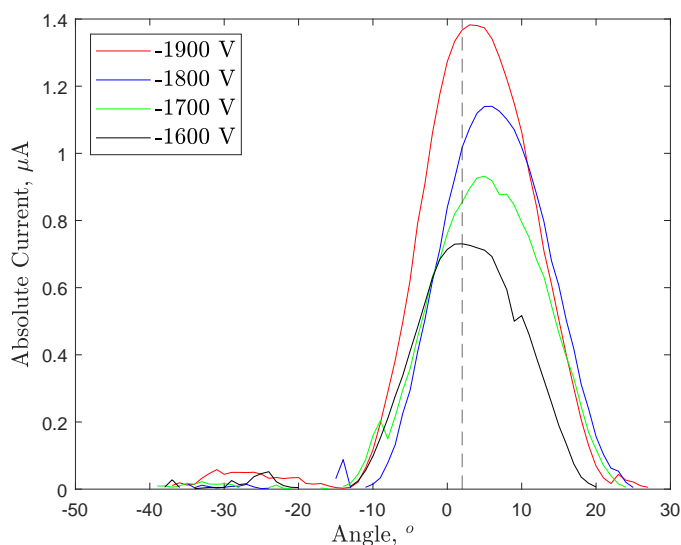
beamlets, previously described in section 3.3.3. The plume composition is likely different radially, therefore the TOF data could significantly vary if off-axis emission occurred. In the positive polarity, a sudden change in composition is seen at voltage of 1550 V and 1700 V for emitter 4 and 17, respectively. This could indicate that the plume could suddenly begin to emit off-axially. Similarly, if the angle between the emitter and the plume or beamlet gradually changed, a gradual change in composition would also be seen, similar to the behaviour in negative polarity. However, it seems likely that the changes in the angle of the beam or beamlet would be the same in both polarities, therefore the same sudden or gradual changes should be observed in both polarities. However, a different behaviour is seen in either polarity, therefore possibly indicating that the plume angle is not significantly changing.

Emitter 17 was rotated using the rotary stage around the RPA, in this case used as a Faraday cup, in order to investigate its angular plume distribution. These data have been plotted in Figure 5.17, showing the plume increasing in current and expanding as the emitter voltage increases. The centre of the plume at 1900 V is indicated by a dashed line in both polarities. Between 1600 V and 1900 V, it can be seen that the angular distribution centre remained relatively constant, with the centre shifting a few degrees at certain voltages. However, a misalignment of a few degrees is probably unlikely to cause a significant variation in the plume composition that is seen in the TOF data. The emitter was only rotated around one axis, therefore it is still possible for off-axis emission to occur that this angular distribution does not capture. Nonetheless, Figure 5.17 seems to indicate that these effects are not caused by off-axis or beamlet emission.

To conclude the EMI-FeCl₄ TOF data, a point will be made of an anomalous drop in current in the negative polarity data. The figures for both of the negative polarity data show a current drop at a charge-to-mass ratio of approximately 1×10^6 CKg⁻¹, a higher charge-to-mass ratio than any of the predicted anions. However, for this to occur, a lower mass or high charge ion would have to be emitted which is unlikely to occur. Therefore, this drop is very likely caused by the TOF gate noise or is an artefact of the noise removal.



(A) Positive polarity.

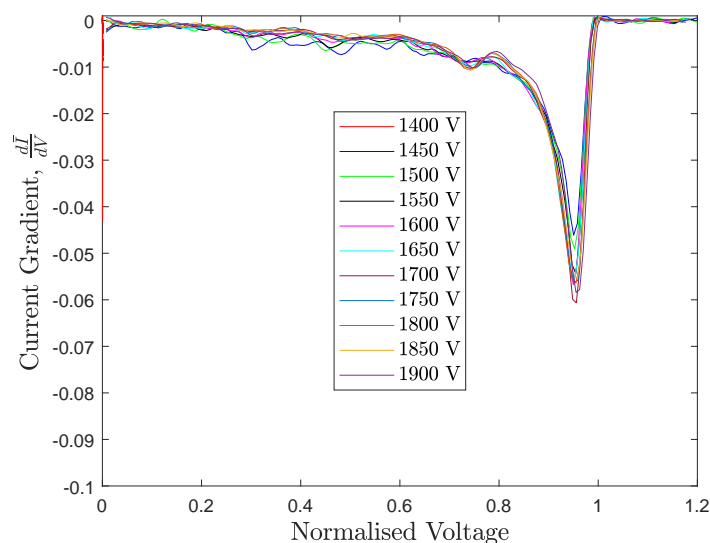


(B) Negative Polarity.

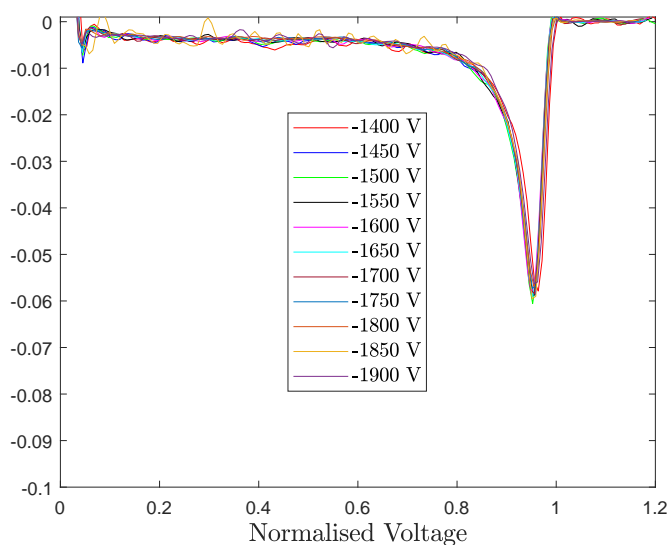
FIGURE 5.17: Angular current distributions for emitter 17 using EMI-FeCl_4 . The alignment of the plume does not vary significantly at the different voltages, showing that plume misalignment likely did not affect the TOF data.

5.2.2.3 Retarding Potential Analysis

Figure 5.18 show the RPA data for EMI-FeCl_4 using emitter 4. The RPA data for emitter 17 were unfortunately too noisy to be reliable and therefore are not presented here. Both of the data show a peak at around a normalised voltage of 0.95. This is expected for TOF



(A) Positive polarity.



(B) Negative Polarity.

FIGURE 5.18: RPA data for emitter 4 using EMI-FeCl₄ for both polarities. A lack of field-free fragmentation is seen, agreeing well with the TOF data.

data that is almost or entirely mono-ionic, as this would cause ions to be accelerated to their full potential without losing energy to fragmentation.

Furthermore, no field-free fragmentation peaks are seen, corresponding well with the fact that all the dimers in the TOF data seem to fragment in the acceleration region. This is evident by a lack of a sharp drop at either the α^1 or β^1 lines. Field-free fragmentation

of dimers would occur as peaks at a voltage of 0.265 and 0.390 for the positive and negative polarity respectively.

5.2.3 EMI-SbF₆

5.2.3.1 Current-Voltage

The final metal/metalloid halide ionic liquid tested was EMI-SbF₆. The ionic liquid was tested only once using emitter 14. The current-voltage plot for this ionic liquid is shown in Figure 5.19, showing an onset voltage of +1900/-2000 V and a maximum current of up to +15.3/-8.5 μA at a voltage of ± 2800 V, similar to EMI-BF₄. A relatively high current is emitted by EMI-SbF₆ despite its high viscosity and low conductivity, having a viscosity about double that of EMI-BF₄ and a conductivity about half of the conductivity of EMI-BF₄. The other propellant property that makes the amount of current emitted by the ionic liquid surprising is its high anion mass, with the mass being around 2.72 times higher than that of BF₄⁻. High ion masses are typically considered to reduce the amount of current emitted due to previous testing with 'heavy' ionic liquids [28]. The emitter's radius was 63.0 μm , making it slightly sharper than previous emitters tested for EMI-BF₄ and EMI-FeCl₄ (emitter 2, 3, 4 and 17), which would also reduce the emitted current.

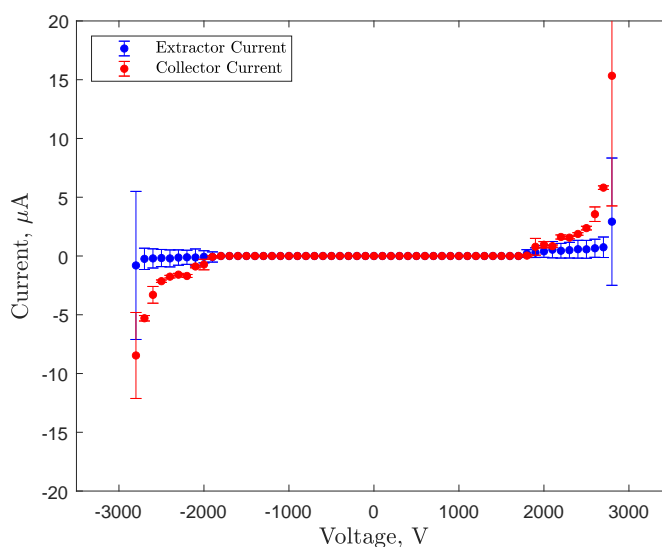


FIGURE 5.19: Current-voltage for data emitter 14 using EMI-SbF₆. A significant amount of current is emitted in comparison to its low conductivity and high viscosity.

The high current emitted by both EMI-FeCl₄ and EMI-SbF₆ suggests a good possibility of using ‘heavier’ ionic liquids, those that have higher ion masses, for electrospray thrusters. This would increase the thrust per unit current from an electrospray emission site, a desired trait to improve currently developed electrospray thrusters.

Considering the ionic liquid properties of EMI-SbF₆, the high current produced using the ionic liquid has implications on ion emission, especially on the effect of conductivity on current emission. This is because EMI-SbF₆'s properties are not well suited for high current emission (on paper), as its properties are more comparable to EMI-Im or EMI-EtOSO₃, a propellant that typically emits lower currents than EMI-BF₄ [49]. For example, in an experiment testing EMI-BF₄, EMI-Im and EMI-EtOSO₃ [49], it was found that EMI-Im emitted 51.1% and 49.6% of EMI-BF₄ current in positive and negative polarity, respectively. Similarly, EMI-EtOSO₃ was found to emit 34.3% and 33.9% of EMI-BF₄ current in positive and negative polarity, respectively. The conductivities of the ionic liquids are 9 and 4 mS/cm for EMI-Im and EMI-EtOSO₃, respectively [49], therefore closer to the conductivity of EMI-SbF₆, 6.2 mS/cm, than EMI-BF₄.

Nonetheless, caution for these preliminary data has to be taken as only one emitter was tested with EMI-SbF₆ and further tests are required for a rigorous conclusion to be ascertained. Furthermore, key aspects for the current-voltage data, such as the emitter-extractor distance, are not characterised in between tests, which may explain some or all of these current-voltage behaviours. Recent experiments [49] have shown a strong correlation between ionic liquids and conductivity, although no metal/metalloid halide ionic liquids were tested in [49], other than EMI-BF₄. Another point to consider is that since the tests in thesis are conducted with a single emitter, there is a higher susceptibility for manufacturing defects to affect the current data. In an array of emitters, such as in [49], many single emitters are manufactured into one block. Therefore many individual emitters are tested simultaneously which should mitigate for defects of individual emitters.

5.2.3.2 Time-of-Flight

EMI-SbF₆ positive polarity data are presented in Figure 5.20. The filter used for these data had a lower cut-off frequency, 2.5 MHz, than the typical cut-off frequency, 5 MHz. This was used due to the increased noise.

Figure 5.20 shows that for all four voltages tested, the thruster emitted only monomers and dimers. The ion charge-to-mass ratios are listed in Tab. 5.5. The distribution of the ion clusters does not vary with the voltage, except a slight difference for 2200 V, showing a similar relationship with voltage as EMI-BF₄. Another similarity is the composition, which is dominated by dimers comprising of up to 80% dimers and with up to 20% monomers. Although the surface tension of this ionic liquid is not known, the lower conductivity could be considered detrimental to the emission of small ion clusters [47], yet the plume remains purely ionic and nearly identical to an ionic liquid with double its conductivity (EMI-BF₄). These data provide more evidence that the relationship between conductivity and the sizes of ion clusters in pure ion emission is not strong, adding to the previous work on pure ionic emission of ionic liquids [28, 40].

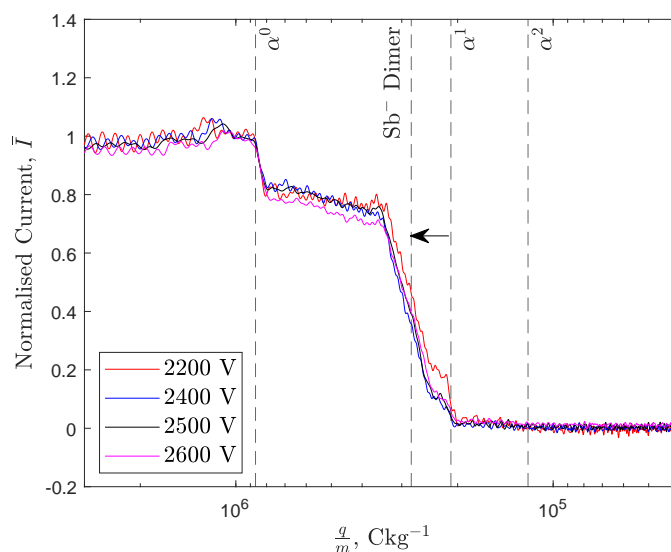


FIGURE 5.20: Positive polarity TOF data for EMI-SbF₆. The arrow indicates how the charge to mass ratio of the dimer ion changes as the anion is reduced in mass. The data show a plume comprised only of monomers and dimers.

However, only a small percentage of the dimers are unfragmented, with this population being represented by the sharp drop at the α^1 line. The rest of the dimers fragment close to the extractor, as shown by the current drop between charge to mass ratios of 2.5 and 3.0×10^5 Ckg⁻¹. This signifies that these dimers arrived at a velocity higher than expected for dimers, corresponding to fragmentation within the acceleration region of the thruster. It is interesting that this pattern does not extend to the monomer expected charge-to-mass ratio, with the gradient of the acceleration region fragmentation changing drastically at a $\frac{q}{m}$ of $\sim 3 \times 10^5$ Ckg⁻¹. This would suggest that the acceleration region

TABLE 5.5: Various different types of ions calculated which could have been emitted by EMI-SbF₆.

Ion Symbol	Simplified Representation	Chemical Formula	Charge-to-Mass Ratio, C/kg	Field-Free Fragmentation Energy
α^0	A ⁺	EMI ⁺	8.67×10^5	Does not fragment
α^1	A ⁺ [A ⁺ B ⁻]	EMI ⁺ [EMI-SbF ₆]	2.10×10^5	0.243
α^2	A ⁺ [A ⁺ B ⁻] ₂	EMI ⁺ [EMI-SbF ₆] ₂	1.20×10^5	0.569
β^0	B ⁻	SbF ₆ ⁻	-4.09×10^5	Does not fragment
β^1	B ⁻ [A ⁺ B ⁻]	SbF ₆ ⁻ [EMI-SbF ₆]	-1.65×10^5	0.405
β^2	B ⁻ [A ⁺ B ⁻] ₂	SbF ₆ ⁻ [EMI-SbF ₆] ₂	-1.04×10^5	0.627

fragmentation becomes much more significant at a distance close to the extractor. This does not seem probable, since the electric field is strongest closest to the emitter and the fragmentation should be promoted by a stronger electric field. It therefore seems contradictory for the dimers to fragment close to the extractor instead of the emitter. In order to verify this effect, the retarding potential analysis data needs to be examined.

One alternative to the peculiar acceleration region fragmentation behaviour is the possibility of a higher charge-to-mass ratio ion being emitted instead of the dimer. Although highly unlikely, the peculiar acceleration region fragmentation behaviour would be prevented if such an ion was emitted. One possibility was the antimony ion losing fluorine atoms in order to lose mass while maintaining a similar charge. This has been plotted in Figure 5.20 with the dashed line labelled 'Sb⁻ Dimer'. It can be seen that although the charge-to-mass ratio of the ion is closer to the point where the current trace gradient dramatically changes, it still does not fully agree with it. Therefore, it is unlikely that such an ion would be emitted, even if the high improbabilities of such an ion existing are not considered. Further discussion about the possibility of such an ion will be discussed in the RPA section.

Negative polarity TOF data are shown in Figure 5.21 for -2600 V. It can be seen that the data are very noisy caused by the lack negative polarity gate noise data, therefore only one voltage is shown. Nonetheless, although a reliable composition cannot be calculated, it can be seen that the TOF data show a clear drop for negative polarity monomers and dimers, and likely show evidence for trimers. These data indicate that

a similar composition of the plume is seen in the negative polarity as with the positive polarity, with possibly more trimers being present.

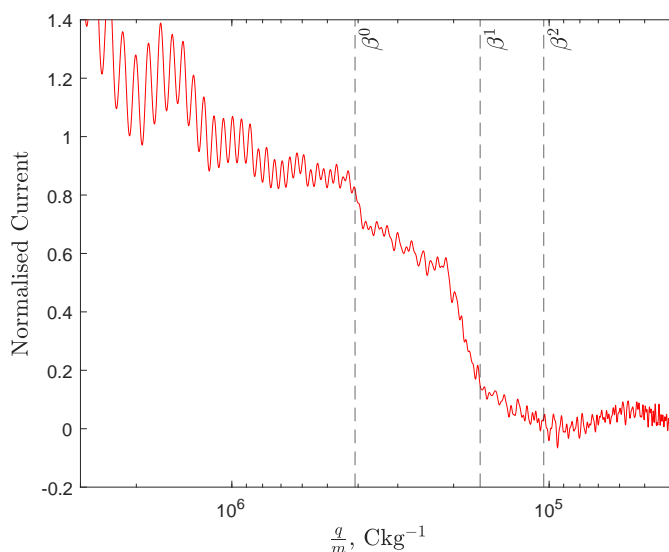


FIGURE 5.21: Negative polarity TOF data for EMI-SbF₆ at a voltage of -2600 V. Although noisy, evidence of monomer, dimer and trimer emission is seen likely indicating a pure ion plume.

5.2.3.3 Retarding Potential Analysis

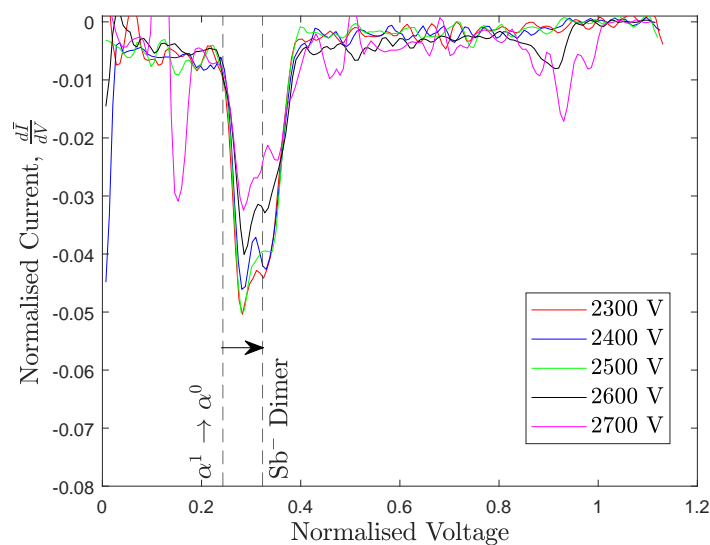
The RPA data are shown in Figure 5.22 showing that in both polarities there is a one significant drop at a normalised voltage of ~ 0.3 and ~ 0.4 for the positive and negative polarity, respectively. However, unlike for the EMI-FeCl₄, this drop does not occur at a normalised voltage of 1 instead occurring at a voltage significantly lower than 1. This signifies that the majority of the dimers fragment.

Beginning with the negative polarity in Figure 5.22b, the drop recorded can be seen to occur at an energy corresponding well to the fragmentation of a β^1 dimer (the energy of field-free fragmentation can be found in Tab. 5.5). The fragmentation can be represented by,

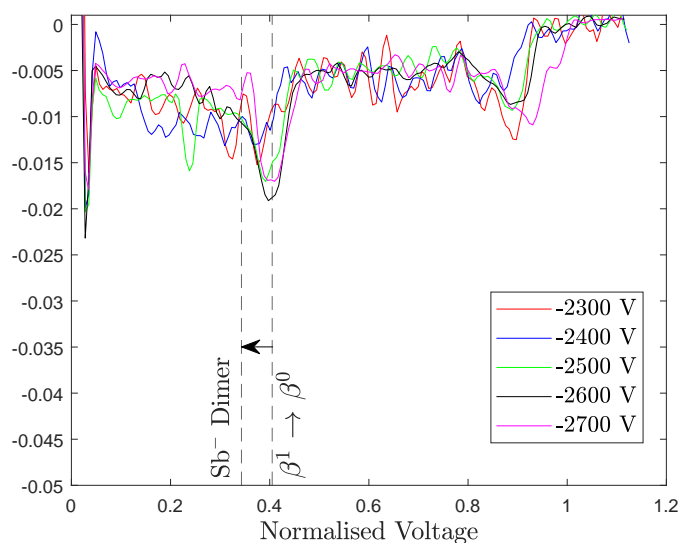


Although there is a lack of reliable TOF data, the evidence for this fragmentation shows that at least some unfragmented dimers are present in the negative polarity plume.

One can further speculate that the lack of any further evidence of larger species field-free fragmenting suggests that, similar to positive polarity, the plume is likely to be dominated by monomers and dimers. However care must be taken as the retarding potential data do not provide any more information about the species present in the plume.



(A) Positive polarity.



(B) Negative Polarity.

FIGURE 5.22: The RPA data for emitter 14 for both polarities. In both polarities significant field-free fragmentation is observed, although the peak in the positive polarity appears more energetic than is expected.

The positive polarity data show a clear peak in current at around a normalised voltage of 0.3. This seems to correspond to field-free fragmentation of positive polarity dimers, α^1 , into monomers, which can be represented as



However, the energy of this field-free fragmentation seems to be lower than the energy at which the peak was recorded, with the drop expected at a normalised voltage of 0.243, indicated by the dashed line. Taking into consideration the TOF data, it can be seen that the fragmentation of dimers into monomers occurs before the ion has exited the thruster meaning that the progeny ion would undergo some acceleration. The acceleration would correspond to the α^1 peak occurring at a slightly higher energy than the expected field-free fragmentation energy, corresponding to a higher normalised voltage to retard the ions using the RPA. The effects of fragmentation occurring just before the extractor can be seen in both the TOF and RPA data which seems to verify the strange fragmentation of the ions.

Nonetheless, this does not seem to provide an adequate explanation for why these ions fragment just before the extractor and why they fragment in such a significant amount, and if they do. Three different possibilities will be presented here in an attempt to be as thorough as possible. One explanation could be that fragmentation occurs due to the work done by the electric field on the ion and therefore once the work done exceeds the amount of work required for fragmentation the ion fragments. This may explain the EMI-SbF₆ TOF and RPA data and also possibly the EMI-BF₄ RPA data. However, one underlying issue would be that it would disagree with previously proposed fragmentation models for electrospray thrusters [99] which predict that the electric field strength alone enables fragmentation in the acceleration region, discussed in chapter 2. Therefore it is unlikely that this is an adequate explanation.

The second possibility could be that the anion, SbF₆⁻, loses some fluorine atoms during emission and therefore has a lower mass than expected. For this speculation, it will be assumed that this ion is possible to be emitted, although this is very unlikely. For analysis we have assumed that the ion loses all of its fluorine atoms to produce an Sb⁻ anion dimer which is indicated by the dashed line in Figures 5.20 and 5.22. The arrows

on the figures indicate how the values change from normal dimers to the reduced mass dimer, and therefore any dimer that has not lost all of its fluorines would have a charge-to-mass ratio and field-free fragmentation energy approximately in this range.

The lower mass of the anion would cause the ion to have a higher charge-to-mass ratio, a higher positive polarity field-free fragmentation energy and a lower negative polarity field-free fragmentation energy, as seen in Figures 5.20 and 5.22. This seems to agree more with the TOF and positive polarity data, although the charge-to-mass ratio of this ion would be too high to be in full agreement with the recorded TOF data. Also, the reduced mass anion brings the data less in agreement with the negative polarity RPA data. The less massive anion proposal seems to bring parts of the data to be more in agreement with each other and parts of the data to be less in agreement with each other meaning that this provides an unsatisfactory answer to problems with the data presented here. Another major problem with the loss of fluorines is that it probably is very unlikely to occur, as six different chemical bonds would have to be broken in order for such an ion to be emitted, likely requiring very large amounts of energy.

Finally, this effect could be caused by a simple instrumentation error with the retarding potential analyser as a higher energy dimer can be seen in both the EMI-BF₄ and EMI-SbF₆ data. This is the most likely explanation as issues were encountered with the RPA throughout testing. However it does not provide an adequate explanation for the TOF data, which can be seen to agree well with the theoretical charge-to-mass ratios of ions and therefore indicate the TOF system working accurately. Further experimentation is required which would characterise the negative polarity TOF data and also verify the repeatability of this effect.

5.2.4 Summary

Reflecting on the three metal/metalloid halide ionic liquids tested, it has been shown that EMI-BF₄ might not be the best ionic liquid that is possible for porous electrospray thrusters. EMI-FeCl₄ emitted similar to significantly more current than EMI-BF₄ promoting a higher thrust. The almost pure monomer plume would reduce the thrust, although the specific impulse of such a thruster would be significantly higher and the reduction in thrust could be offset by the high current emitted.

EMI-SbF₆ was shown to emit similar levels of current to EMI-BF₄, despite EMI-SbF₆ having half the conductivity of EMI-BF₄, while emitting nearly identical ion species in the plumes. The increased molecular mass of the SbF₆⁻ anion translates to a higher total thrust produced by the ionic liquid albeit at a lower specific impulse, meaning it could also be a suitable alternative as a propellant for ionic liquids.

Overall, this section has shown that metal/metalloid halide ionic liquids are a possible group of propellants that could provide an alternative to EMI-BF₄, especially in increasing the thrust of an electrospray thruster. The data also provide evidence of the reduced effect of conductivity on the size of ion clusters in pure ion emission and also possibly on the current emitted. However, further experimentation is required, particularly of the current-voltage data, in order to reduce uncertainties and investigate the repeatability of these results.

5.3 Multiply-Charged Ionic Liquids

Multiply-charged ionic liquids were chosen due to the effect the extra ion charges may have on the kinetics of the ion emission process. The advantage of a multiply-charged ionic liquid can be shown by considering the reduction in evaporation energy due to the presence of an electric field, ΔG_e . In section 2.2.1, this was defined as,

$$\Delta G_e = \sqrt{\frac{(n_q e)^3 E}{4\pi\epsilon_0}}. \quad (5.6)$$

Equation 5.6 shows that $G_e \propto (n_q e)^{\frac{3}{2}}$, which suggests that increasing the charge on the emitted ion should reduce the energy required for ion evaporation for a given intermolecular bonding strength, G_s . The amplification of the electric field would lead to a higher current and potentially higher charge-to-mass ratio ion clusters being emitted by the electrospray thruster. Equation 5.6 can be rearranged to define the critical electric field,

$$E_{crit} = \frac{4\pi\epsilon_0 \Delta G_s^2}{(n_q e)^3}, \quad (5.7)$$

where G_s is the solvation energy required to emit an ion.

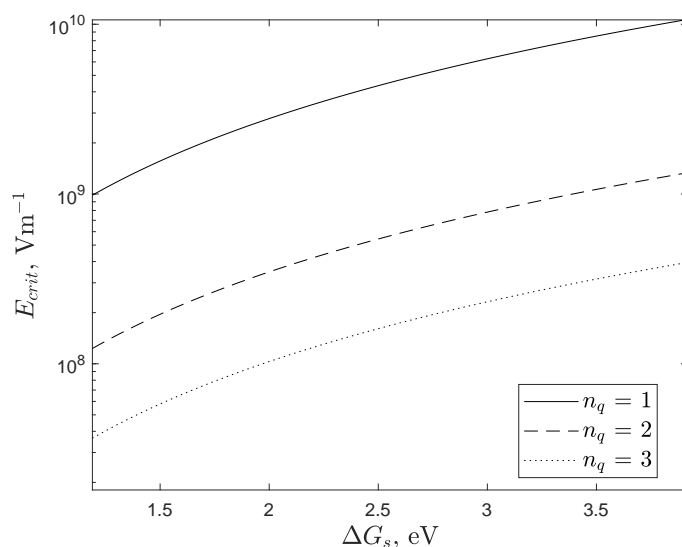


FIGURE 5.23: The critical electric field calculated with different ion charges. As the number of charges is increased, the critical electric field strength for emission decreases.

The effect of increasing charge is highlighted in Figure 5.23. It shows Eq. 5.7 plotted, with the critical electric field required to reach significant ion emission on the y-axis and the ion solvation energy on the x-axis. It can be seen that a significantly lower critical electric field strength is required when the ion charge is increased, possibly leading to an increased current and a lower onset voltage.

5.3.1 (EMI)₂-Co(SCN)₄

5.3.1.1 Current-Voltage

The first multiply-charged ionic liquid that was tested was (EMI)₂-Co(SCN)₄, with two emitters, emitter 1 and 10. The current-voltage for emitter 1 is presented in Figure 5.24, showing the emitter onset at a voltage of +1700/-1800 V, with a maximum current of +3.1/-1.9 μA at a voltage of 2500 V. The emitter 10 data can be found in Figure 5.25, and show that the maximum current achieved was +6.8/-7.2 μA at a voltage of 3100 V, with an onset of +2000/-2500 V. A few key features are therefore shown from these data. Firstly, the current that can be emitted by this ionic liquid can be quite high despite of its 'poor' ionic liquid properties; low conductivity and high viscosity. It is unclear why there was such a significant difference between the two current-voltage

plots of the emitters as the tip radius for emitter 1 was 124.9 μm while for emitter 10 it was 110.7 μm meaning that the tip radii effects would be small. One possible reason could be that emitter 1 was not as well wetted as the other emitter, possibly leading to the difference in current.

Another interesting characteristic for emitter 10 was the significant difference between the onset voltages for each polarity, with an onset voltage of 2000 V in the positive polarity and -2500 V in the negative polarity. As with the differences in the current, it is unclear why this occurred, however one cause that can be speculated is the significant size differences in the two ions that are emitted. The $\text{Co}(\text{SCN})_4^{2-}$ anion is very large with a mass of 291.3 AMU, while each individual EMI^+ ion has a mass of 111.17 AMU, about 38% of the $\text{Co}(\text{SCN})_4^{2-}$ mass, possibly making it easier to emit the di-anion due to its lower mass. Since this was only observed in one of the two tests, further tests are required in order to verify this as a possible effect.

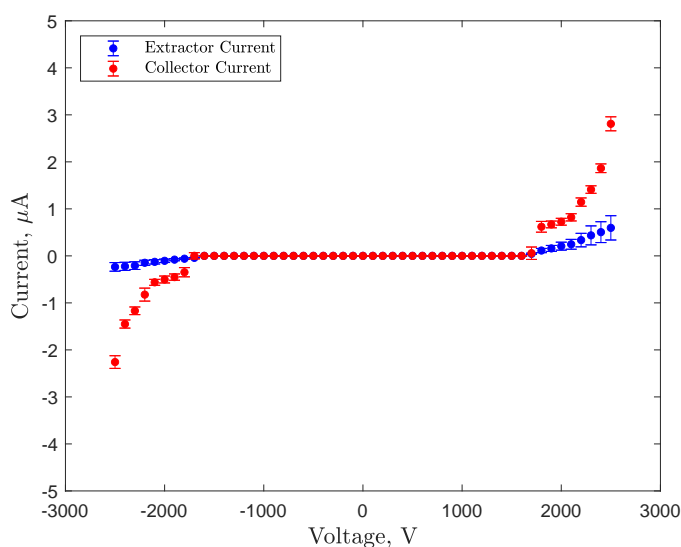


FIGURE 5.24: Current-voltage for data emitter 1 using $(\text{EMI})_2\text{-Co}(\text{SCN})_4$. A significant amount of current is emitted by the multiply-charged ionic liquid, although lower than EMI-BF_4 .

The extractor current for this heavier ionic liquid was also noted to be substantially higher than the previously tested ionic liquids, for which at least two explanations can be offered. Firstly, the extractor could have been less well-aligned with the emitter, causing higher beam impingement. Although this is possible, all the previous data had a low extractor current, which seems to validate the extractor alignment methodology

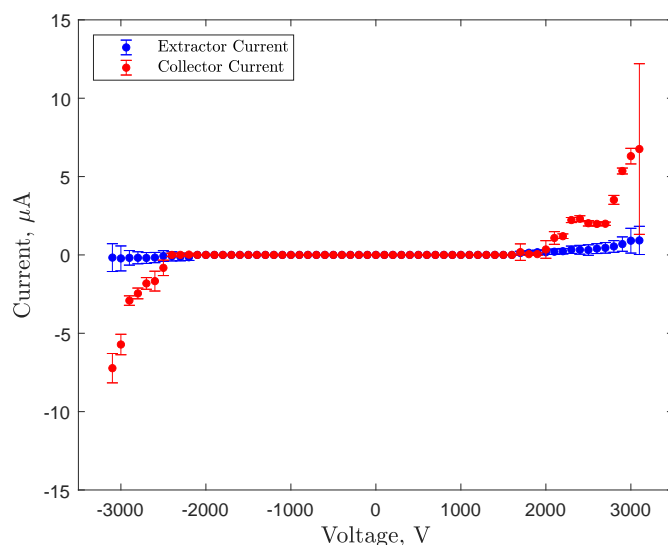


FIGURE 5.25: Current-voltage for data emitter 10 using $(\text{EMI})_2\text{-Co}(\text{SCN})_4$. A large amount of current is emitted compared to emitter 1, with similar currents being emitted to EMI-BF_4 .

hence diminish the likelihood extractor misalignment. A second possibility is that the increased beam impingement indicates that the heavier an ionic liquid is, the more beam impingement might be expected, as higher extractor currents were observed with this ionic liquid and also EMI-SbF_6 .

Finally, a note to the reader is that this liquid could spark easily, causing a lot of failures during experimentation. Further experimentation will require a conservative control of the voltage, with the higher voltage preferably being tested at the end of the experimental campaign.

5.3.1.2 Time-of-Flight

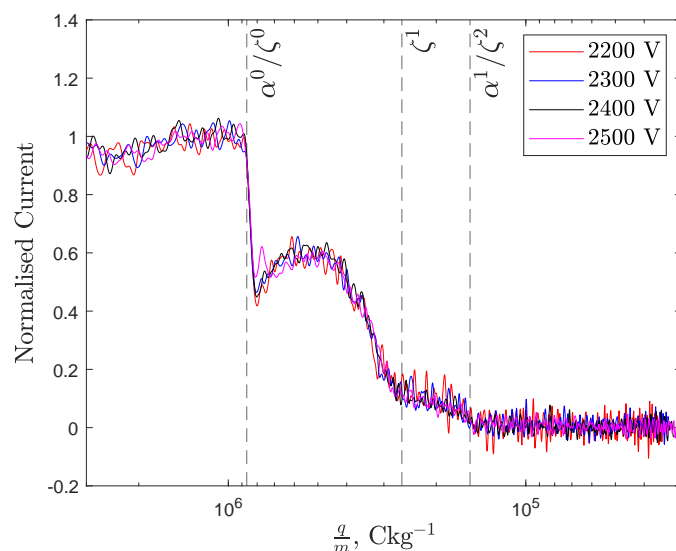
Figures 5.26 and 5.27 show the TOF data when using $(\text{EMI})_2\text{-Co}(\text{SCN})_4$ for the two emitters, emitter 1 and emitter 10 respectively. Due to noise issues when testing emitter 10 in the positive polarity, only a single voltage had a sufficient signal-to-noise ratio during TOF testing to provide clear enough data for analysis. The dashed line on the figures represent the species identified to have been emitted, with the symbol corresponding to the ion shown in Table 5.6. In the negative polarity for both emitters, the data show a sharp peak at around the charge-to-mass ratio of di-anion dimers, β^1 ,

corresponding to a large proportion of the current ($\sim 80\% - 90\%$) being comprised of them. The data also show the presence of di-anionic, β^2 , trimers and quadramers, β^3 , with a small to negligible amount of monomers, β^0 , also shown. It worth mentioning that these ions are made up of doubly-charged anions, or di-anions, represented by B^{2-} . These types of ions have not been previously emitted in electrospray thrusters, and only one multiply-charged ionic liquids, which will also be tested in section 5.3.2, has been previously tested once [97].

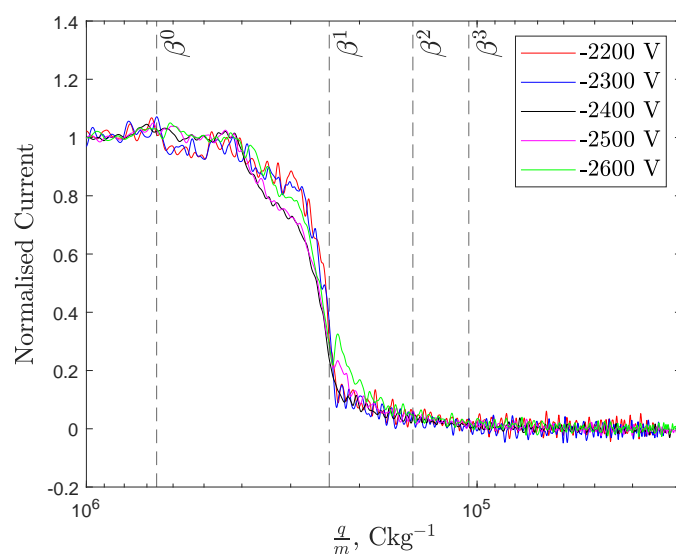
It is also interesting to note that the majority of the plume is made up of dimers, with possibly between 80% - 90% of the negative plume being comprised of dimers for both emitters. This is in stark contrast with the positive polarity plume, which shows a more typical distribution of monomers, dimers and trimers. One of the reasons for these dimers comprising such a large portion of the plume could be the stability of the doubly-charged dimer. Since an extra charge is present in the di-ion, it is likely more stable than a singly-charged dimer [100]. Therefore, it is more likely to be emitted without fragmenting, although some acceleration region fragmentation is evident in the data from the non-horizontal line between β^0 and β^1 . Further evidence of this will be shown in the RPA section.

The thruster was also tested in the positive polarity, showing three distinct drops, corresponding to three ion species emitted. The TOF data appear similar to EMI-BF₄ in having three different drops, however the expected 'single' cations, α , only matched well with two of the drops, both at the charge-to-mass ratio of $8.67 \times 10^5 \text{ Ckg}^{-1}$ and $1.54 \times 10^5 \text{ Ckg}^{-1}$. However, there appears to be a further current drop in between these two currents drops at a charge-to-mass ratio of $\sim 2.7 \times 10^5 \text{ Ckg}^{-1}$.

This current drop could indicate a sudden change in acceleration region fragmentation, due to the change in gradient. However, this would suggest that 'single' cations initially have a constant rate of acceleration region fragmentation (due to the constant gradient) but at a point between the emitter and extractor, the acceleration region fragmentation suddenly and drastically changes, before returning to its original value. As an example, for emitter 1 at 2300 V, the time of this sudden change at this charge-to-mass ratio is approximately 15.7 μs . From this, an energy can be derived, assuming a 100% acceleration efficiency. Rearranging the time of flight equation (Eq. 3.11) for the



(A) Positive polarity.

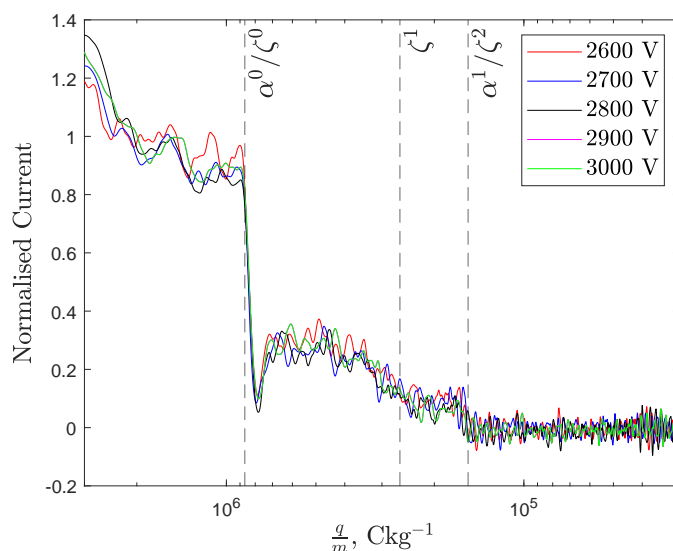


(B) Negative Polarity.

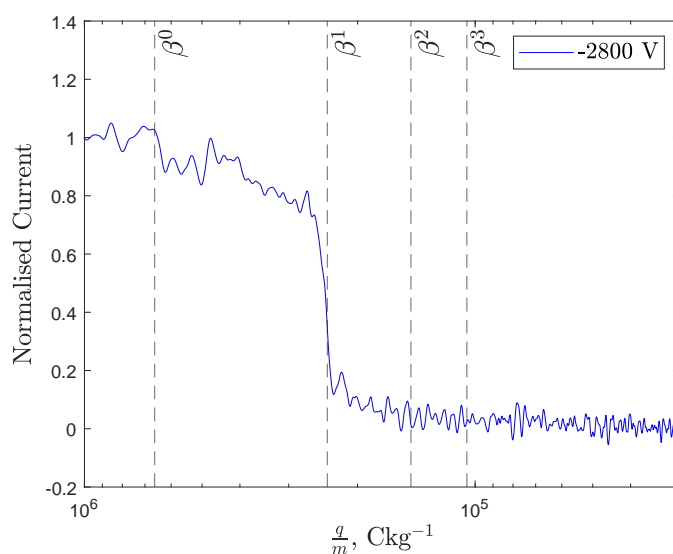
FIGURE 5.26: TOF data for emitter 1 using $(EMI)_2\text{-Co(SCN)}_4$ for both polarities. Monomers, dimers and trimers are seen to be emitted in both polarities, with some quadramers in the negative polarity. Furthermore, ‘double cation’ species are proposed to be emitted in the positive polarity, denoted by ζ^n .

emitter potential and assuming an α^0 monomer, the energy of this fragmentation can be derived. It is defined as,

$$\phi_{ion} = \frac{mL^2}{2qt_f^2}, \quad (5.8)$$



(A) Positive polarity.



(B) Negative Polarity.

FIGURE 5.27: TOF data for emitter 10 using $(EMI)_2\text{-Co(SCN)}_4$ for both polarities.

where ϕ_{ion} is the energy of the acceleration-region fragmented ion. Using a flight length of 550 mm, an arrival time of 15.7 μs and monomer charge-to-mass ratio ($8.67 \times 10^5 \text{ Ckg}^{-1}$), the corresponding energy potential is 708 V. This sudden change of gradient would therefore appear at a normalised voltage of 0.308 and would appear as a large change in gradient at this voltage. In the RPA section, it will be shown that a change of gradient is not seen, therefore making it unlikely that this is explanation for this current drop.

An alternative was to introduce a new species, ζ , which is comprised of a ‘double cation’, $2(A^+)$, as opposed to a cation, A^+ . This naming is also used to distinguish the ions from di-anions and di-cations, B^{2-} and A^{2+} respectively. The ‘double cation’ ions have been given the symbol ζ , and their information can be found in Table 5.6. The current drops in the data well to a ‘double cation’ monomer, ζ^0 , a dimer, ζ^1 , and a trimer, ζ^2 , which have been marked on Figures 5.26a and 5.27a using a dashed line. There has been at least one other study by Gamero-Castaño and De La Mora [101] where a ‘double ion’ species was emitted using formamide and propanol doped with tetraheptyl ammonium bromide. However, this would be the first case that such a species was detected using only an ionic liquid. In the study by Gamero-Castaño and De La Mora, it was shown that both singly charged and doubly charged species were emitted by the thruster. This could also be the case with the data seen here with both the cation and ‘double cation’ monomer, α^0 and ζ^0 , having the same charge-to-mass ratios and the cation dimer and ‘double cation’ trimer, α^1 and ζ^2 , having the same charge-to-mass

TABLE 5.6: Various different types of ions calculated which could have been emitted by $(EMI)_2-Co(SCN)_4$.

Ion Symbol	Simplified Representation	Chemical Formula	Charge-to-Mass Ratio, C/kg	Field-Free Fragmentation Energy
α^0	A^+	EMI^+	8.67×10^5	Does not fragment
α^1	$A^+[2(A^+)B^{2-}]$	$EMI^+[(EMI)_2-Co(SCN)_4]$	1.54×10^5	0.178
α^2	$A^+[2(A^+)B^{2-}]_2$	$EMI^+[(EMI)_2-Co(SCN)_4]_2$	8.46×10^4	0.549
β^0	B^{2-}	$Co(SCN)_4^{2-}$	-6.62×10^5	Does not fragment
β^1	$B^{2-}[2(A^+)B^{2-}]$	$Co(SCN)_4^{2-} [(EMI)_2-Co(SCN)_4]$	-2.39×10^5	0.362
β^2	$B^{2-}[2(A^+)B^{2-}]_2$	$Co(SCN)_4^{2-} [(EMI)_2-Co(SCN)_4]_2$	-1.46×10^5	0.610
β^3	$B^{2-}[2(A^+)B^{2-}]_3$	$Co(SCN)_4^{2-} [(EMI)_2-Co(SCN)_4]_3$	-1.05×10^5	0.720
ζ^0	$2(A^+)$	$2(EMI^+)$	8.67×10^5	0.500
ζ^1	$2(A^+)[2(A^+)B^{2-}]$	$2(EMI^+)[(EMI)_2-Co(SCN)_4]$	2.61×10^5	0.302
ζ^2	$2(A^+)[2(A^+)B^{2-}]_2$	$2(EMI^+)[(EMI)_2-Co(SCN)_4]_2$	1.54×10^5	0.589

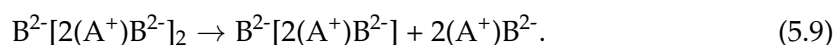
ratios. Further discourse on these two possibilities will be provided in the retarding potential analysis section as retarding potential data is required to see how acceleration region fragmentation varies.

Overall, the sizes of ion clusters emitted by this ionic liquid are similar to the conventional ionic liquids, with the largest ion clusters being quadramers. It is therefore interesting that an ionic liquid with such 'exotic' properties (that the neutral molecule is comprised of three ions: two cations and one di-anion) still emits a similar plume to the metal/metalloid halide ionic liquids such as EMI-BF₄. It is worthwhile noting though that the propellant properties of (EMI)₂-Co(SCN)₄ are the most similar to EMI-BF₄ out of any of the multiply-charged ionic liquids that will be tested, possibly enabling this similar composition.

One interesting deviation from the metal/metalloid halide ionic liquids is that the composition of the positive and negative polarity plumes is significantly different. With the exception of EMI-SbF₆, where no reliable negative polarity TOF data are available, EMI-BF₄ and EMI-FeCl₄ had similar TOF data in both polarities, whereas with (EMI)₂-Co(SCN)₄ data the positive polarity has a significantly higher variation of ion cluster charge-to-mass ratios, but the negative polarity is dominated by dimers. The most likely cause of the effect is the different charge and possibly mass of the cation and anion, with the double charge of the di-anion likely producing more stable dimers due to the strong electrostatic bonding. These TOF data could also reinforce the weird behaviour with the onset voltage being an effect of the ionic liquid itself, rather than experimental error due to the differences also being seen in the plume composition.

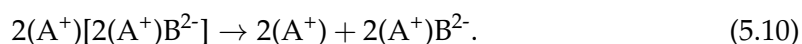
5.3.1.3 Retarding Potential Analysis

The RPA data for both emitters are shown in Figures 5.28 and 5.29. For both emitters in the negative polarity, Figures 5.28b and 5.29b, it can be seen that, as with EMI-BF₄, the most prominent peak is around a normalised voltage of ~ 1 , which corresponds to ions arriving at the collector after being fully accelerated by the emitter potential. However, a second prominent peak can be seen around a normalised voltage of ~ 0.6 . This peak corresponds to the field-free fragmentation of a di-anion trimer fragmenting into a di-anion dimer, $\beta^2 \rightarrow \beta^1$, represented by,



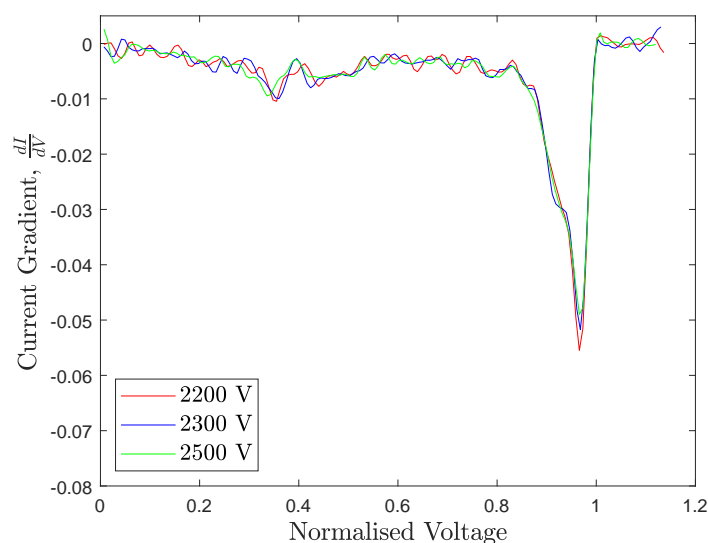
corresponding to field-free fragmentation potential of 0.610. The prevalence of this peak suggests that the trimers, which do not comprise a large proportion of the plume, significantly fragment in the field-free region. However, it's interesting that even with such a large prevalence in the current, there is no evidence in the RPA data for both emitters that the dimers fragment. Furthermore, the sharp current drop in the TOF data suggests little acceleration region fragmentation. Combining both sets of data, the RPA and TOF data seem to reinforce that the doubly-charged dimers emitted by this ionic liquid are more stable than dimers produced by conventional ionic liquids.

Using the positive RPA data it is possible to distinguish which species were emitted based on the field-free fragmentation in the plume. Figures 5.28a and 5.29a shows the positive polarity RPA data for emitter 1 and emitter 10. The emitter 1 data showed no significant peaks, other than around a normalised voltage of 1, which represents non-fragmented ions arriving at the RPA collector. A slight peak can be seen at a normalised voltage of ~ 0.35 , although this is interpreted as noise as opposed to evidence of field-free fragmentation. However, the emitter 15 RPA data show a clear peak at a normalised voltage of ~ 0.302 corresponding to field-free fragmentation of the double cation dimer, ζ^1 , marked on the plot with a dashed line. The fragmentation of the double cation dimer, ζ^1 , can be represented by,

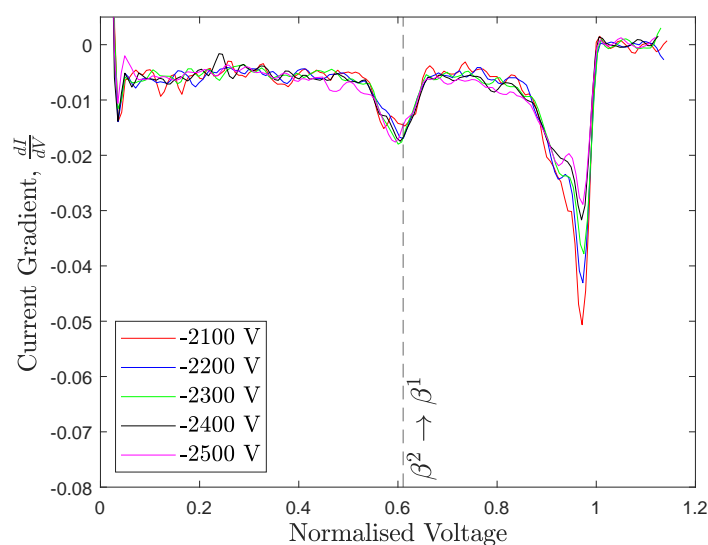


This fragmentation corresponds well to the prevalence of double cation dimers in the TOF data, providing more evidence to the existence of double cation emission. However, the fragmentation of the double cation dimer also provides the largest source of uncertainty within this analysis of the data. This doubt originates from the fact that it would seem the most likely case that the double cation monomer, ζ^0 , would be unstable and therefore break apart immediately after the fragmentation of the double cation dimer, which is described by the fragmentation





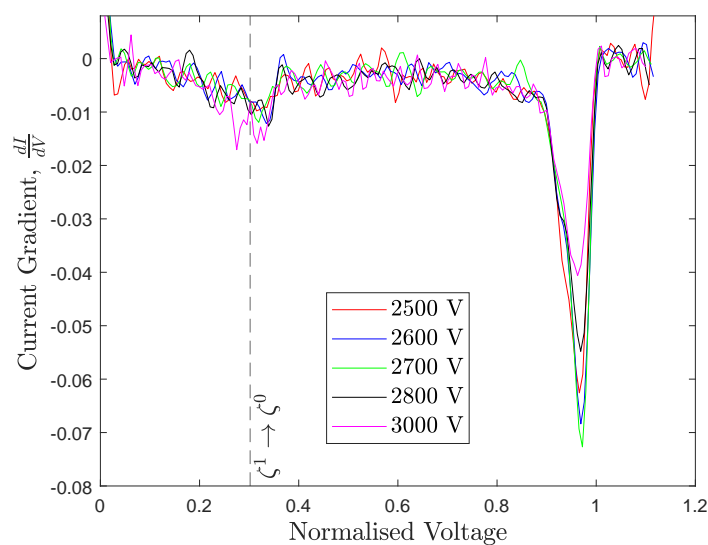
(A) Positive polarity.



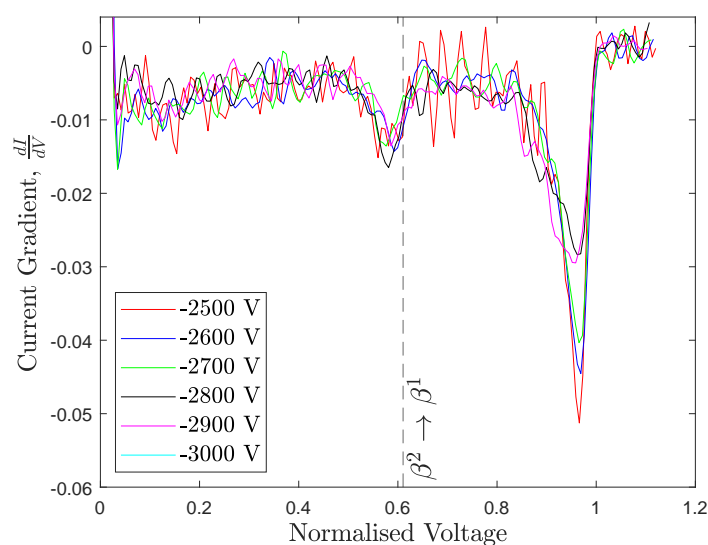
(B) Negative Polarity.

FIGURE 5.28: RPA data for emitter 1 using $(EMI)_2\text{-Co(SCN)}_4$ for both polarities. The positive polarity only shows fully-accelerated ions, however in the negative polarity evidence of trimer fragmentation can be seen.

This fragmentation would appear as a peak at 50% of the energy of field-free fragmentation of ζ^1 , which would be a peak at a normalised voltage of 0.151. However, this peak is not seen in either of the emitters' RPA data. An alternative solution could be the the double cation dimer, ζ^1 , fragments into a cation dimer, α^1 , followed by the cation dimer fragmenting into a cation monomer, α^0 . This fragmentation is described by the equations

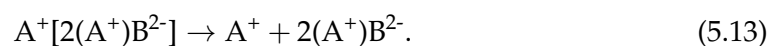
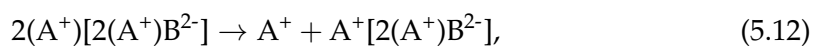


(A) Positive polarity.



(B) Negative Polarity.

FIGURE 5.29: RPA data for emitter 10 using $(\text{EMI})_2\text{-Co}(\text{SCN})_4$ for both polarities. The positive polarity data show evidence of double cation dimer fragmentation, while the negative polarity again shows evidence of trimer fragmentation.



The ions produced by this fragmentation would appear as a peak at the normalised voltages of 0.178 and 0.216 respectively. However, as with the fragmentation of the double cation monomer, no peaks are seen in the RPA data which seem to correspond to these two fragmentations. The consideration of these two alternative fragmentation scenarios, and their lack of evidence within the data, suggests that double cation monomers, ζ^0 , are produced in the fragmentation of double cation dimers, ζ^1 , and the double cation monomers emitted are stable.

In the TOF section, another possibility was that a strong change in acceleration region fragmentation is seen at a normalised voltage of 0.308. Although a drop is seen at around this normalised voltage, what would be expected is a constant change in gradient after this drop. In the RPA data of either emitter, this is not seen. The peaks do not correspond to this a sudden change in acceleration region fragmentation because the expected behaviour of this gradient change would be two different horizontal lines at different constant $\frac{dI}{dV}$ values, whereas after the peak the gradient returns to the original magnitude. Therefore, the data seem to indicate that a sudden change in acceleration region fragmentation does not occur.

Compared to the metal/metalloid halide ionic liquids, the RPA for $(EMI)_2\text{-Co(SCN)}_4$ data show less intense fragmentation peaks overall compared to the peak at a normalised voltage of 1, suggesting decreased field-free fragmentation. Two conclusions exist from this. First, as has been outlined with the negative polarity data, di-anion dimers produced by $(EMI)_2\text{-Co(SCN)}_4$ are much more stable than other ions because of the very sharp current drop in the TOF data and the lack of any evidence of field-free fragmentation.

The second conclusion is that the positive polarity ions likely primarily fragment in the acceleration region. The TOF data show a continuous distribution between the different dashed lines, or in other words no sharp current drops, corresponding to significant acceleration region fragmentation. The lack of peaks in the RPA data suggests that there is little field-free fragmentation of these ions as well, leading to the conclusion that the positive polarity ions are likely less stable. However, in order to fully verify this the retarding potential analyser issues will have to be overcome as due to the anomalous negative polarity gradient, the acceleration region fragmentation cannot be reliably evaluated.

A further discourse on the 'double' ions will be provided with the data tested using the next ionic liquid. However, the $(EMI)_2-Co(SCN)_4$ seem to show an interesting kind of ion being emitted. Although this could correspond to acceleration region fragmentation, this has been shown unlikely, due to the lack of changes in the gradient of the RPA data.

5.3.2 $C_6(mim)_2-(IM)_2$

5.3.2.1 Current-Voltage

Another doubly charged ionic liquid tested was $C_6(mim)_2-(IM)_2$, which is one of the two 'super viscous' ionic liquids that were tested. The viscosity of this ionic liquid is ~ 590 cP from Tab. 5.1, about 17 times that of $EMI-BF_4$, meaning it was expected to emit very little current, if any. This ionic liquid is comprised of a di-cation, $C_6(mim)_2^{2+}$, and two anions, Im^- . This is effectively the opposite of $(EMI)_2-Co(SCN)_4$ which is comprised of two cations and one di-anion.

The data for two emitters tested using $C_6(mim)_2-(IM)_2$, emitter 6 and 14, are shown in Figures 5.30 and 5.31 respectively. Starting with emitter 6, this first emitter was only tested up to a voltage of ± 3000 V, at which it emitted a current of $+1.3/-1.8$ μA . Per emitter, this still remains a high value, however this is a much smaller current compared to the other ionic liquids tested within this thesis. Nonetheless, considering the extremely low conductivity, 34.7 times lower than $EMI-BF_4$, as well as the previously stated viscosity, the level of current seen is still impressive.

Emitter 15 was tested after emitter 6 and at the end of the test it was decided to increase the emitter voltage until the emitter failed. The voltage was constantly increased up to 4200 V, seen in Figure 5.31. For all the other non 'super' viscous tests, a typical maximum voltage was under 3000 V due to the possibility of sparking and damage to the emitter. In these current-voltage tests for $C_6(mim)_2-(IM)_2$, the emitter did not break at 4200 V and continued to emit up to a current of $+4.1/-7.9$ μA . These data seem to provide a remarkable quality of this ionic liquid, that it can maintain stable electrospray emission up to a very high voltage, a voltage where other ionic liquids would fail. High voltage stability could be useful in applications that require higher energy ions, such as etching.

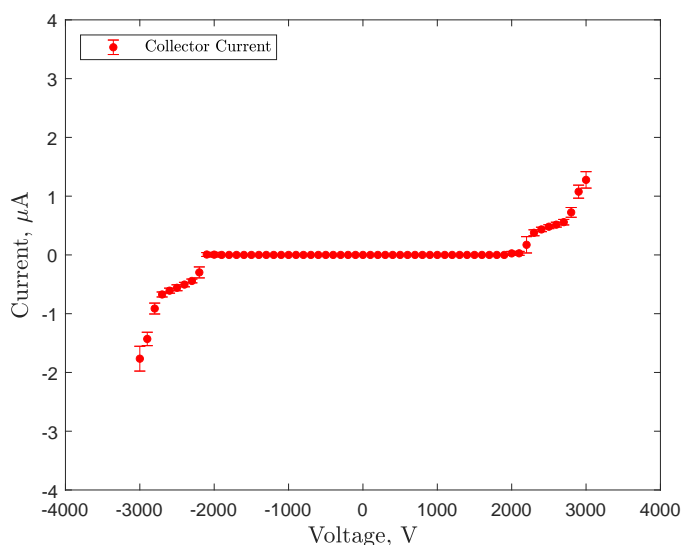


FIGURE 5.30: Current-voltage for data emitter 6 using $C_6(\text{mim})_2\text{-(IM)}_2$. The current emitted is significantly lower than using EMI-BF_4 , although a significant amount is still emitted.

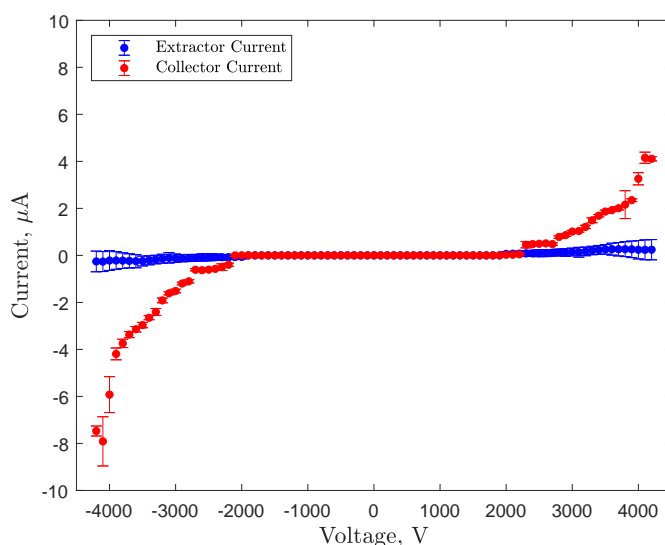


FIGURE 5.31: Current-voltage for data emitter 15 using $C_6(\text{mim})_2\text{-(IM)}_2$. The ionic liquid was able to be operated at significantly higher voltage, up to 4200 V, at which it approached current emission similar to EMI-BF_4

5.3.2.2 Time-of-Flight

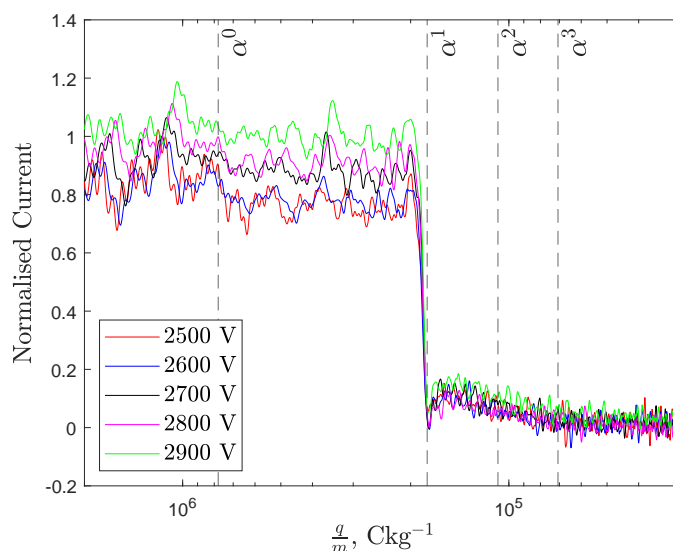
The TOF data for $C_6(\text{mim})_2\text{-(IM)}_2$ for two emitters, emitter 6 and 15, are presented in Figures 5.32 and 5.33. The ionic liquid $C_6(\text{mim})_2\text{-(IM)}_2$ is interesting to compare to $(\text{EMI})_2\text{-Co(SCN)}_4$ as it has a di-cation as opposed to a di-anion. It also is the only MIL

which has had some testing in electrospray propulsion [97]. The ion cluster sizes were calculated and can be found in Table 5.7.

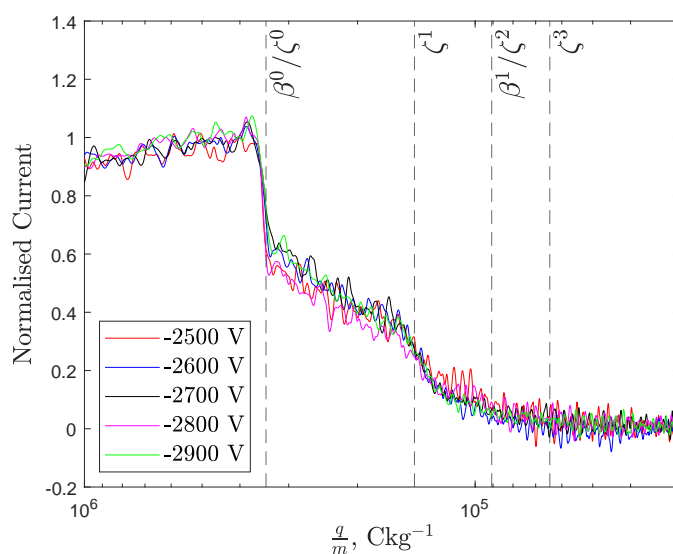
Figures 5.32b and 5.33 show the negative polarity data for emitters 6 and 15, respectively. Similar to $(\text{EMI})_2\text{-Co(SCN)}_4$, but for the opposite polarity, the data show three, possibly four different species of ions. Initially, the single anion species, β , were fit onto the data to determine whether the data could be well explained by single anion ions. The single anion monomer, β^0 , and single anion dimer, β^1 , fit well with the data, as the case was for the positive emission of $(\text{EMI})_2\text{-Co(SCN)}_4$. However, similar to the positive emission data for $(\text{EMI})_2\text{-Co(SCN)}_4$, a better fit can be achieved if a second 'double anion' species, ζ , is introduced. Both the different emitter data show that the emission of 'double anion' monomers, ζ^0 , dimers, ζ^1 , trimers, ζ^2 , and possibly quadramers, ζ^3 , correspond to the location for each significant current drop or change in gradient.

Similarly to the $(\text{EMI})_2\text{-Co(SCN)}_4$ data, it is possible that these changes in the TOF current gradient are caused by a sudden change in the rate of acceleration region fragmentation. Taking emitter 6, two sudden changes occur at charge-to-mass ratio of 1.27×10^5 and $1.64 \times 10^5 \text{ Ckg}^{-1}$. Using the same technique as with the $(\text{EMI})_2\text{-Co(SCN)}_4$ data, it is possible to estimate the normalised voltages where this would occur in the RPA data. As an example, assuming a voltage of -2700 V for emitter 6, the changes in TOF gradient would correspond to potentials of -936 V and -1317 V for the lower and higher charge-to-mass ratio, respectively. These would appear as sudden changes in the RPA gradient at normalised voltage 0.347 and 0.488, respectively. The RPA data will show that a change in gradient is seen at the first drop, however not the latter, again suggesting that changes in acceleration region fragmentation likely do not explain this behaviour.

For emitter 15, the positive polarity TOF data are shown in Figure 5.32a. Unfortunately, the signal-to-noise ratio of the positive polarity was too low for emitter 15 and therefore the data are not shown here. The data show a signal with a steep drop at the charge-to-mass ratio expected for di-cation dimers, α^1 , followed by a steady decrease in current corresponding to the presence of di-cation trimers, α^2 , and quadramers, α^3 . Due to noise it is unclear whether any di-cation monomers are present. Nonetheless, the data show a plume comprised almost purely of dimers. As far as the author is



(A) Positive polarity.



(B) Negative Polarity.

FIGURE 5.32: TOF data for emitter 6 using $C_6(\text{mim})_2\text{-(IM)}_2$ for both polarities. In the positive polarity a very high proportion dimer plume can be seen, while in the negative polarity evidence of double anion ions can be seen.

aware, an electrospray plume which emits such an almost purely dimer plume has not been reported before.

The very dimer heavy plume reflects the previously seen negative polarity (EMI)- $\text{Co}(\text{SCN})_4$ data, where a large majority of the plume also comprised of dimers. It is therefore interesting that with both of these multiply-charged ionic liquids,

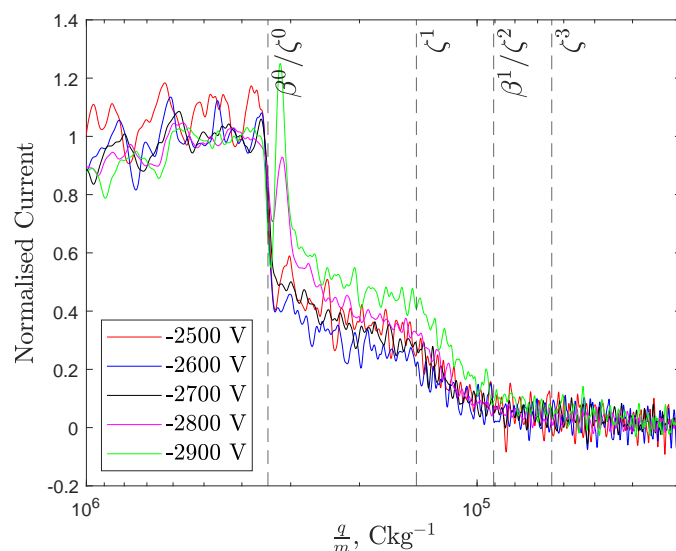


FIGURE 5.33: Negative polarity TOF Data for emitter 15 using $C_6(\text{mim})_2-(\text{Im})_2$. Similar to the emitter 6 negative polarity data, evidence of double anion dimers is seen.

the polarity of the di-ion, the di-anion for $C_6(\text{mim})_2-(\text{Im})_2$ and the di-cation for $(\text{EMI})_2-\text{Co}(\text{SCN})_4$, emitted almost entirely dimers. Therefore, these data seem to indicate that di-ions promote the emission of dimers. However, even if the di-ions promote the emission of dimers it is unclear why such a low proportion of other ions, such as trimers, exists. One possible explanation could be that the dimer is very stable, while all other ions are not stable therefore anything larger than a dimer will fragment into a dimer and remain a dimer. However, the stability of the dimer would not explain the lack of monomers, which should not be affected by this and can clearly form in the other polarity for both of these liquids. What is interesting about this effect is that there seems to be a clear relationship from this ion property (the charge of the ion) and the size of ion cluster it emits, which one could consider an insight into the factors that affect the clustering of ions emitted from porous electro spray thrusters.

As a final thought, the ions emitted by $C_6(\text{mim})_2-(\text{Im})_2$ were similar to the previous ionic liquids that were tested, even though the conductivity of this ionic liquid was extremely low, suggesting that it should emit few ions and more droplets. On a later test with the ionic liquid, it was found that a population of heavier ion clusters and droplets were present, making up about 10% of the plume [90], although it is unclear whether this was due to the emitter having been stored for eight months at that point. Further tests required to confirm these heavier clusters. Nonetheless, these data seem

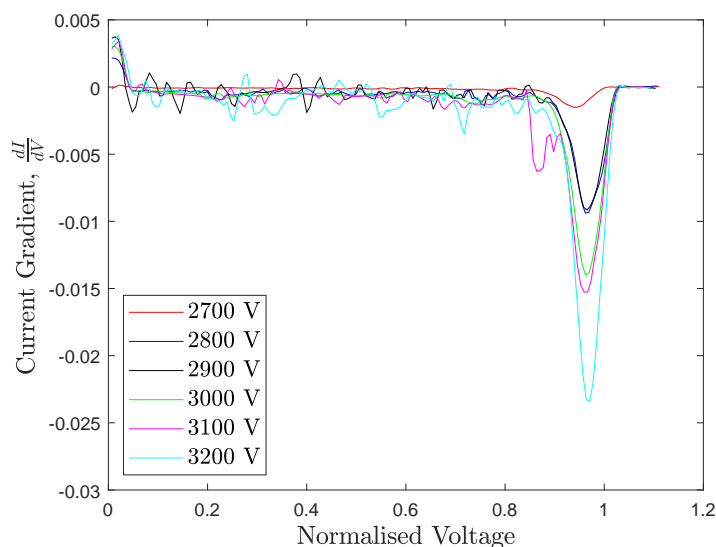
TABLE 5.7: Various different types of ions calculated which could have been emitted by $C_6(\text{mim})_2\text{-(IM)}_2$.

Ion Symbol	Symbol Representation	Chemical Formula	Charge-to-Mass Ratio, C/kg	Field-Free Fragmentation Energy
α^0	A^{2+}	$C_6(\text{mim})_2^{2+}$	7.76×10^5	Does not fragment
α^1	$A^{2+}[A^{2+}2(B^-)]$	$C_6(\text{mim})_2^{2+}$ $[C_6(\text{mim})_2\text{-(IM)}_2]$	1.87×10^5	0.241
α^2	$A^{2+}[A^{2+}2(B^-)]_2$	$C_6(\text{mim})_2^{2+}$ $[C_6(\text{mim})_2\text{-(IM)}_2]_2$	1.06×10^5	0.569
α^3	$A^{2+}[A^{2+}2(B^-)]_3$	$C_6(\text{mim})_2^{2+}$ $[C_6(\text{mim})_2\text{-(IM)}_2]_3$	7.44×10^4	0.699
β^0	B^-	Im^-	-3.43×10^5	Does not fragment
β^1	$B^-[A^{2+}2(B^-)]$	Im^- $[C_6(\text{mim})_2\text{-(IM)}_2]$	-9.07×10^4	0.265
β^2	$B^-[A^{2+}2(B^-)]_2$	Im^- $[C_6(\text{mim})_2\text{-(IM)}_2]_2$	-5.23×10^4	0.576
ζ^0	$2(B^-)$	$2(\text{Im}^-)$	-3.43×10^5	0.500
ζ^1	$2(B^-)[A^{2+}2(B^-)]$	$2(\text{Im}^-)$ $[C_6(\text{mim})_2\text{-(IM)}_2]$	-1.43×10^5	0.419
ζ^2	$2(B^-)[A^{2+}2(B^-)]_2$	$2(\text{Im}^-)$ $[C_6(\text{mim})_2\text{-(IM)}_2]_2$	-9.07×10^4	0.632
ζ^3	$2(B^-)[A^{2+}2(B^-)]_3$	$2(\text{Im}^-)$ $[C_6(\text{mim})_2\text{-(IM)}_2]_3$	-6.64×10^4	0.731

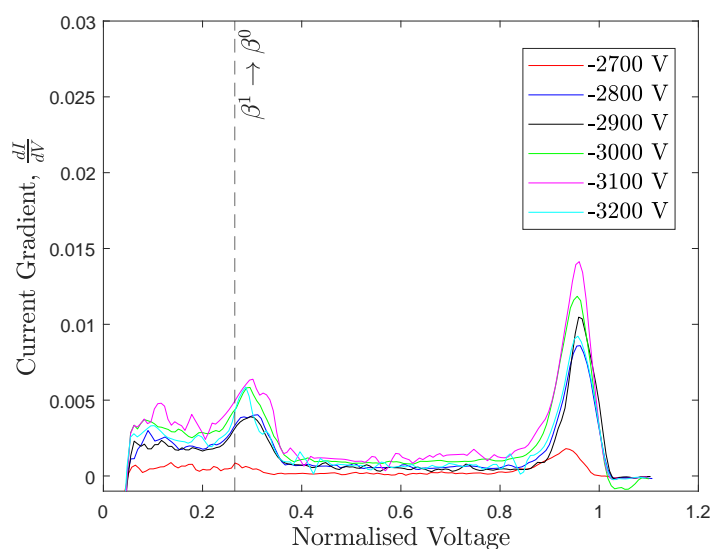
to show that even with a more ‘hostile’ ionic liquid for ion emission (low conductivity, lower surface tension and high viscosity), significant ion emission prevails, even when droplet emission is included, suggesting the prerequisites for ion emission are not significantly based on these traditional propellant properties and rather are based on other properties, whether on the propellant properties or thruster design [63].

5.3.2.3 Retarding Potential Analysis

Problems with the signal-to-noise ratio meant that only the RPA data for emitter 6 were available, shown in Figure 5.34. Beginning with the negative polarity data, the usual peak at around a normalised voltage of ~ 1 is seen, corresponding to fully accelerated ions arriving at the collector. A second peak can be seen at a normalised voltage of



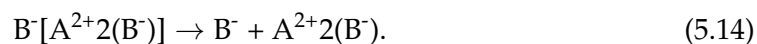
(A) Positive Polarity.



(B) Negative Polarity.

FIGURE 5.34: RPA data for emitter 6 using $C_6(\text{mim})_2-(\text{Im})_2$ for both polarities. In the positive polarity only non-fragmented ions are seen, however in the negative polarity an anion dimer fragmentation peak is seen.

~ 0.33 . The data correspond well with the field-free fragmentation of a single anion dimer, β^1 , into a single anion monomer, β^0 . This can be described by,



The existence of this peak suggests that both types of ions are emitted, single anions, β , and double anions, ζ , as indicated by the TOF data. The possibility that both of these ions are emitted is interesting as it would mean that the conditions within the meniscus of the ionic liquids must enable the two different types of ions to be emitted. Ionic liquids are typically understood to have the individual ions be disassociated within the liquid freely moving around [102], explaining why it is possible for both of these ions to be emitted.

The magnitude of the gradient also changes after the peak. In the TOF subsection it was expected that the RPA gradient in the negative polarity would suddenly change at a normalised voltage of 0.347. Figure 5.34b shows that the magnitude of the gradient does change at around this normalised voltage. However, the change in the magnitude of the gradient is wrong as the TOF data in Figure 5.32b show that the the gradient increases after $1.27 \times 10^5 \text{ Ckg}^{-1}$. The RPA data in Figure 5.34b shows the inverse, that the magnitude of the gradient decreases, in disagreement with what is expected. Furthermore, it was predicted that a second change in the the gradient occurs at a normalised voltage of 0.488, which does not occur. It is therefore likely that these data suggest that changes in the acceleration region fragmentation are not the cause of the sudden changes observed in the TOF current trace.

Negative RPA data show one strong peak at around the emitter voltage, corresponding to ions arriving at the collector after being fully accelerated. The lack of other peaks in the RPA data seems to correspond well with the TOF data, which together suggest a plume of primarily dimers ions which do not fragment either in the acceleration region or the field-free region. The lack of a field-free fragmentation peak at a normalised voltage of 0.241 suggests, as with $(\text{EMI})_2\text{-Co(SCN)}_4$, a very stable dimer is emitted. This is because due to the large proportion of dimers in the plume, it is expected for some field-free fragmentation to occur unless the dimer is especially stable. The trimers and quadramers in the plume seem to fragment in the acceleration region, suggested by the slope seen in the TOF data.

5.3.3 $\text{C}_6(\text{mim})_2\text{-Co(SCN)}_4$

The ionic 'liquid' $\text{C}_6(\text{mim})_2\text{-Co(SCN)}_4$ was tested with only one emitter, emitter 16 (tip radius $130.9 \mu\text{m}$). This ionic liquid was comprised of a di-cation $\text{C}_6(\text{mim})_2^{2+}$ and the

di-anion $\text{Co}(\text{SCN})_4^{2-}$, making it unique as no other singly charged ion was present. It was also the only ionic 'liquid' tested that was solid at room temperature, therefore had a unique testing setup.

A custom kapton heater was purchased to melt this ionic 'liquid'. In order to minimise the risk of shorting, the heater was placed on top of the extractor. This can be seen in Figure 5.35. Although this was a less effective method of heat transfer due to the distance from the emitter tip, it prevented the risk of shorting which, due to limited time, was a higher priority. A thermocouple was placed on top of the heater, likely having a poor thermal contact with the heater. This poor thermal contact would lead to inaccurate temperature measurements, however due to time constraints a more robust system was not developed. Future improvements of this system should integrate the heater and thermocouple into the body of the thruster, closer to the emitter, so that better heat transfer is achieved and a more accurate temperature reading is acquired.

The preparation of the emitter was also unique. Since it was uncertain whether the ionic 'liquid' would operate, a damaged emitter was used, causing the significantly lower height and higher tip radius of emitter 16. Due to time constraints, a second emitter was not tested with this ionic 'liquid'.

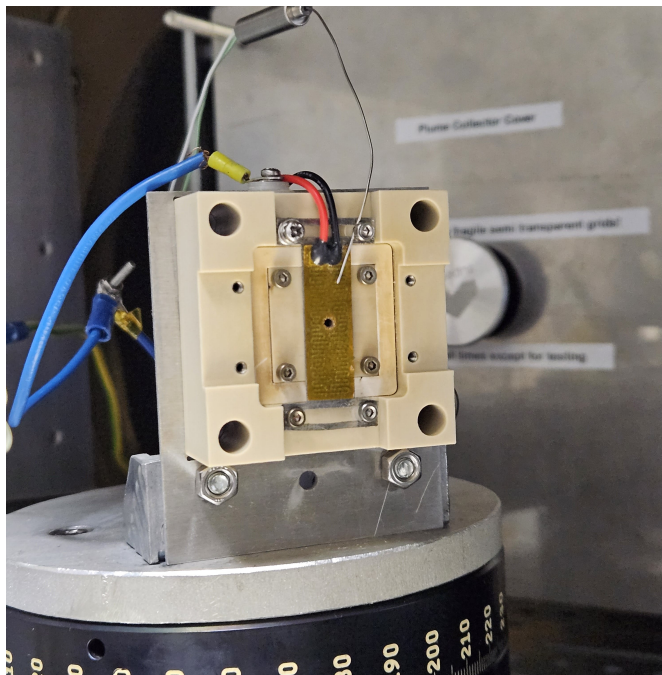


FIGURE 5.35: A kapton heater mounted on the extractor of the thruster.

In order to fill the emitter, an IKA HB eco water bath was used. A Pyrex beaker was then slightly submerged in the surface of the water, held in position by a hand clamp. A small fragment of $C_6(\text{mim})_2\text{-Co}(\text{SCN})_4$ was placed in the beaker, then the temperature of the water bath was set to 88°C , approximately the temperature at which the ionic 'liquid' melted. The emitter was carefully placed into the melted pool of $C_6(\text{mim})_2\text{-Co}(\text{SCN})_4$, ensuring that only the base of the emitter was submerged in the liquid. Capillary forces were used to feed the emitter, and the emitter was removed from the beaker once the emitter tip became the blue colour of the ionic 'liquid'. The filled emitter tip is shown in Figure 5.36. The porous reservoir was filled in a similar manner.



FIGURE 5.36: Emitter 16 after the filling process.

The heater system was controlled by a custom on/off program using LabVIEW. A rudimentary MOSFET control circuit was used, so that a digital signal from the NI-9401 card was able to drive the power to the heater through the MOSFET. The program would turn the heater on when the thermocouple temperature was below the set temperature, and when the temperature was above this set temperature, the heater was switched off. The temperature was increased incrementally to prevent large temperature overshoots. The heater was required to operate at temperatures of approximately 150°C , higher than the melting point of the ionic 'liquid'. This was likely due to the poor thermal connection between the heater and emitter. Nonetheless, current-voltage and TOF data were able to be acquired, and will be presented in the following subsections.

5.3.3.1 Current-Voltage

The data in Figure 5.37 show the current-voltage data recorded for $C_6(\text{mim})_2\text{-Co(SCN)}_4$. It shows that, firstly, it was possible to produce current from an ionic liquid that is solid at room temperature, which has previously not been reported in literature except for mixtures of salts with a solvent [103]. The data show that the current emitted by the ionic liquid was somewhat low compared to the other more conventional ionic liquids, with $+4.6/-1.7 \mu\text{A}$ emitted at a voltage of $\pm 3400 \text{ V}$. The level of current emitted by this ionic liquid is in-between $(\text{EMI})_2\text{-Co(SCN)}_4$ and $C_6(\text{mim})_2\text{-(IM)}_2$, emitting less current than the former and more than the latter. Clearly this is due to the introduction of the long $C_6(\text{mim})_2^{2+}$ di-cation into the liquid, reducing the ion mobility as opposed to the very small EMI^+ cation of $(\text{EMI})_2\text{-Co(SCN)}_4$.

The extractor current for this was highly noisy, which is why the error-bars are not shown, however the data are still plotted here in order to indicate what sort of extractor current might be expected from this ionic liquid.

The onset voltages for this ionic liquid were $+2200/-2500 \text{ V}$, different for either polarity, similar to $(\text{EMI})_2\text{-Co(SCN)}_4$, suggesting that this is possibly a behaviour related to this

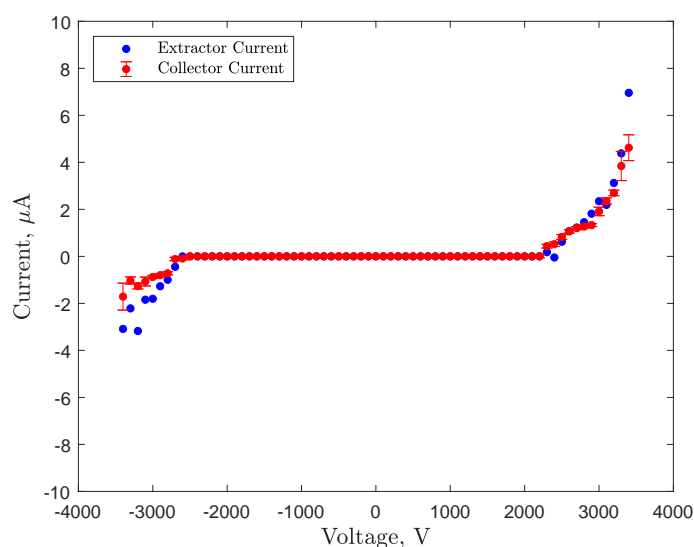


FIGURE 5.37: Current-voltage for data emitter 16 using $C_6(\text{mim})_2\text{-Co(SCN)}_4$. The collector current was lower than EMI-BF_4 and $(\text{EMI})_2\text{-Co(SCN)}_4$, however higher than $C_6\text{-(mim)}_2\text{-(Im)}_2$, reflecting its composition being a mixture of the latter two ionic liquids.

di-anion. This is because $C_6(\text{mim})_2\text{-(IM)}_2$ did not exhibit this behaviour. The strange behaviour hints at the importance of ionic properties themselves in the ionic emission process due to this behaviour seemingly being caused by the di-anion of the ionic liquid.

5.3.3.2 Time-of-Flight

Unfortunately, there were difficulties in collecting both TOF and RPA data for $C_6(\text{mim})_2\text{-Co(SCN)}_4$. Therefore, TOF data for only one voltage was collected, which is shown in Figure 5.38. The data show a clear presence of monomers, dimers and trimers, with monomers comprising most of the plume. There is also what is believed to be noise at lower charge-to-mass ratios.

The shape of the TOF curve resembles the positive polarity TOF curve seen for $(\text{EMI})_2\text{-Co(SCN)}_4$, seemingly further showing the influence of the Co(SCN)_4^{2-} di-anion as it did it with the onset voltage. Also, a recurring trend throughout these data is that this ionic liquid continues to emit ions typical of the standard ionic liquids (that is monomers, dimers and trimers), further reinforcing the limited effect that the ionic liquid properties have on ionic emission. While the liquid properties of this ionic liquid could not be measured, not even the conductivity due to the ionic liquid being solid at room temperature, one can speculate that the liquid properties are somewhere in between that of $(\text{EMI})_2\text{-Co(SCN)}_4$ and $C_6(\text{mim})_2\text{-(Im)}_2$. These ionic liquid properties would seem unfavourable to ion cluster emission, yet despite this significant ion emission is seen. Yet again it seems that ion cluster emission remains feasible despite 'poor' ion emission properties, a continuing trend throughout these ionic liquid tests.

5.3.4 $(C_6\text{mim})_3\text{-Dy(SCN)}_6$

5.3.4.1 Current-Voltage

The final ionic liquid to be tested in this thesis is the triply-charged ionic liquid $(C_6\text{mim})_3\text{-Dy(SCN)}_6$. This was comprised from the triply charged cation, tri-cation, Dy(SCN)_6^{3+} and three anions, $(C_6\text{mim}^+)_3$. Although the propellant properties were not known for it, it was incredibly viscous, almost as viscous as honey, therefore a very low

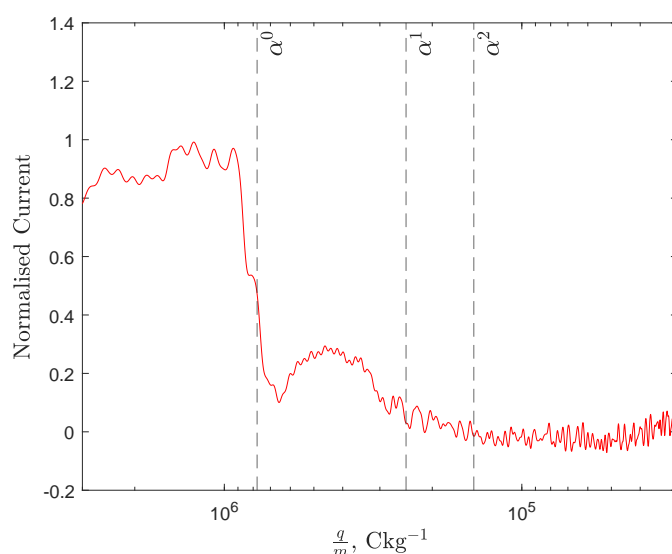


FIGURE 5.38: Positive polarity TOF data for $C_6(\text{mim})_2\text{-Co}(\text{SCN})_4$ at a voltage of 3300 V. As with most of the ionic liquids tested, evidence of monomers, dimers and trimers is seen in the TOF data.

TABLE 5.8: Various different types of ions calculated which could have been emitted by $C_6(\text{mim})_2\text{-Co}(\text{SCN})_4$.

Ion Symbol	Simplified Representation	Chemical Formula	Charge-to-Mass Ratio, C/kg	Field-Free Fragmentation Energy
α^0	A^{2+}	$C_6(\text{mim})_2^{2+}$	7.76×10^5	Does not fragment
α^1	$A^{2+}[A^{2+}B^{2-}]$	$C_6(\text{mim})_2^{2+}$ $[C_6(\text{mim})_2^{2+}\text{Co}(\text{SCN})_4^{2-}]$	2.46×10^5	0.315
α^2	$A^{2+}[A^{2+}B^{2-}]_2$	$C_6(\text{mim})_2^{2+}$ $[C_6(\text{mim})_2^{2+}\text{Co}(\text{SCN})_4^{2-}]_2$	1.45×10^5	0.594
β^0	B^{2-}	$\text{Co}(\text{SCN})_4^{2-}$	-6.62×10^5	Does not fragment
β^1	$B^{2-}[A^{2+}B^{2-}]$	$\text{Co}(\text{SCN})_4^{2-}$ $[C_6(\text{mim})_2^{2+}\text{Co}(\text{SCN})_4^{2-}]$	-2.32×10^5	0.351
β^2	$B^{2-}[A^{2+}B^{2-}]_2$	$\text{Co}(\text{SCN})_4^{2-}$ $[C_6(\text{mim})_2^{2+}\text{Co}(\text{SCN})_4^{2-}]_2$	-1.41×10^5	0.606

current was expected. The viscosity was evident from handling the ionic liquid, which handled similarly to honey. The viscosity was qualitatively evaluated to be higher than $C_6(\text{mim})_2\text{-(Im)}_2$, meaning at minimum the viscosity of $(C_6\text{mim})_3\text{-Dy}(\text{SCN})_6$ is larger than 590 cP. The ionic liquid was so viscous it was uncertain whether it would electrospray, however, even though it was paradoxically very prone to shorting (the only liquid prone to shorting in these tests), it was successfully electrosprayed.

Unfortunately due to the short amount of time available to test this ionic liquid, only one test was conducted with it.

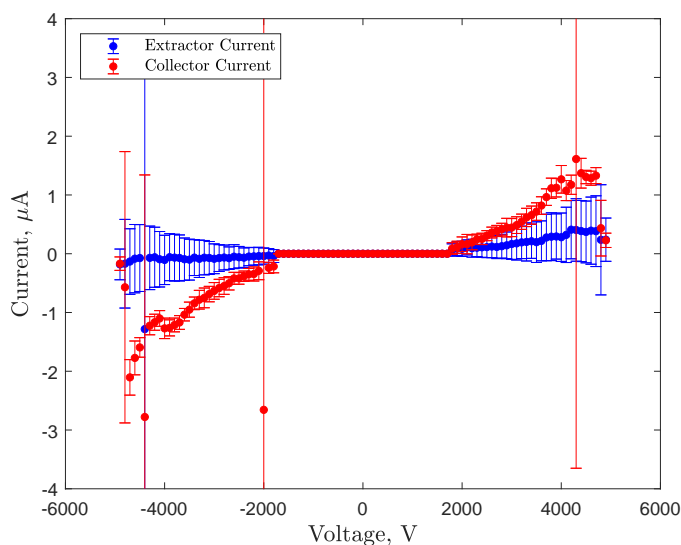


FIGURE 5.39: Current-voltage for data emitter 9 using $(C_6mim)_3-Dy(SCN)_6$. Low current emission is observed, however the ionic liquid was able to be electro sprayed at voltages approaching the limit of the power supply, 5000 V.

The data for its current-voltage test is shown in Figure 5.39. The ionic liquid was taken to a voltage as high as ± 4900 V, with a maximum current of $+1.3/-2.1 \mu A$ at ± 4700 V. The onset voltage was also found to be ± 1800 V. The first observation is that even though a high voltage was required, the ionic liquid still emitted a significant amount of current, over $1 \mu A$ in spite of its incredibly ‘poor’ ionic liquid properties for electro spraying. Similar to $C_6(mim)_2-(Im)_2$, the voltage had to be significantly increased past its onset voltage in order to produce significant current. However, for the vast majority of its voltage range the electro spraying was stable, although above ± 4700 V the current began to decrease. Also, for certain data points the current significantly spiked.

With two ‘super viscous’ ionic liquids tested, some more reliable conclusions can be ascertained. The key finding is that the high viscosity, although reducing emitted current, seemed to enable the ionic liquids to continue stably emitting at much higher voltages. As thrusters ideally require a lower power to produce thrust, the increased voltage likely would not be a good characteristic for propulsion. For applications where energetic ions are required, such as etching, this might prove to be a big advantage therefore

these 'super viscous' ionic liquids may find some application in non-propulsion applications.

5.3.4.2 Time-of-Flight

The TOF data for the tri-ionic liquid $(C_6mim)_3-Dy(SCN)_6$ are shown in Figure 5.40. Due to the low current emitted by the propellant, the TOF data were especially noisy. The cut-off frequency for the butterworth filter was therefore reduced from 5 MHz to 2.5 MHz. The expected ion charge-to-mass ratios are shown in Tab. 5.9, with the cations not shown due to an uncertainty as to how exactly these would form. This is because complex ions were emitted by $(EMI)_2-Co(SCN)_4$ and $C_6(mim)_2-(Im)_2$, possibly making the ions emitted by this ionic liquid more complex due to the three anions and one tri-cation.

The negative polarity TOF data in Figure 5.40 were taken at a -3300 and -3500 V, with the positive polarity data having too much noise for clear TOF data to be shown. These data are particularly interesting as trimers, β^2 , quadramers, β^3 and pentamers, β^4 , match well with the data seen, but monomers, β^0 and dimers, β^1 , do not have a discernible current drop possibly suggesting that the tri-ion promotes trimer emission, similar to the dimers seen with the di-ions. However, at least one other drop exists that does not match with any of the previously listed cations, with the drop at a charge to mass ratio of approximately $1.6 \times 10^{-6} \text{ Ckg}^{-1}$ indicating significant emission of some small ion species, smaller than even the monomer cation. After some investigation, the drop seems to match very well to an $(SCN)^-$ ion, which forms the ligands of the $Dy(SCN)_6^{3-}$ anion.

Due to these ions perfectly aligning at the expected charge-to-mass ratio for $(SCN)^-$, the ligands must be detached almost immediately after the $Dy(SCN)_6^{3-}$ is emitted or these ligands are detached from the ion in liquid phase, being emitted separately from the entire ion. This behaviour was not seen with either of the other propellants comprised of the $Co(SCN)_4^{2-}$ anion, which also have 4 $(SCN)^-$ ligands, therefore it would appear that this behaviour seems to be unique to the $Dy(SCN)_6^{3-}$ tri-anion. The reason for this is unclear, however it could be that each of these ligands is bonding with the dysprosium ion with a lower strength due to the size of the element dysprosium or the size of the molecular ion in general. Further investigation is required to verify this behaviour

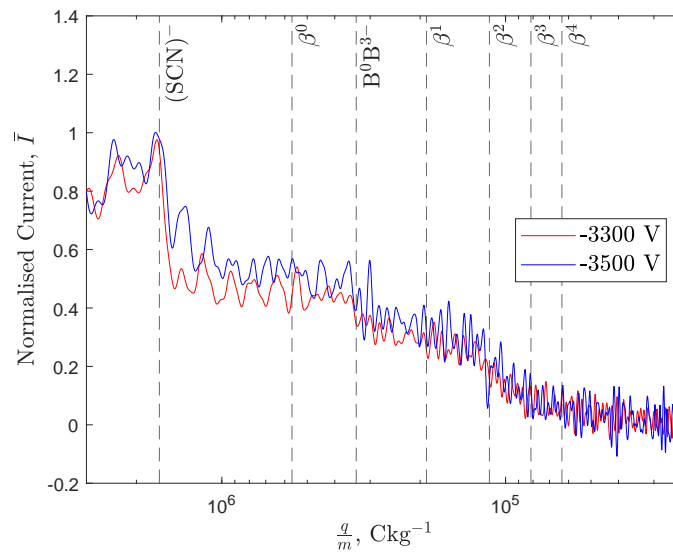


FIGURE 5.40: TOF data for the negative polarity for $(C_6mim)_3-Dy(SCN)_6$. A very complex plume composition was measured, with possibly $(SCN)^-$ ligands being emitted as well as monomers, dimers, trimers and larger species.

for the $Dy(SCN)_6^{3+}$ ion and which exact ions are being emitted by the thruster using this ionic liquid due to the low signal-to-noise ratio.

TABLE 5.9: The various different types of ions calculated which could have been emitted by $(C_6mim)_3-Dy(SCN)_6$.

Ion Symbol	Simplified Representation	Chemical Formula	Charge-to-Mass Ratio, C/kg	Field-Free Fragmentation Energy
β^0	B^{3-}	$Dy(SCN)_6^{3-}$	-5.66×10^5	Does not fragment
β^1	$B^{3-}[3(A^+)B^{3-}]$	$Dy(SCN)_6^{3-}$ $[3(C_6mim^+)Dy(SCN)_6^{3-}]$	-1.90×10^5	0.335
β^2	$B^{3-}[3(A^+)B^{3-}]_2$	$Dy(SCN)_6^{3-}$ $[3(C_6mim^+)^{2+}Dy(SCN)_6^{3-}]_2$	-1.14×10^5	0.601
β^3	$B^{3-}[3(A^+)B^{3-}]_3$	$Dy(SCN)_6^{3-}$ $[3(C_6mim^+)^{2+}Dy(SCN)_6^{3-}]_3$	-8.14×10^4	0.715
β^4	$B^{3-}[3(A^+)B^{3-}]_4$	$Dy(SCN)_6^{3-}$ $[3(C_6mim^+)^{2+}Dy(SCN)_6^{3-}]_4$	-6.34×10^4	0.778

A second unidentified drop is possibly seen at a charge-to-mass ratio of $3.35 \times 10^5 \text{ Ckg}^{-1}$, a charge-to-mass ratio between a monomer and dimer, although this is speculative. The drop was initially not identified due to it not matching well with any of the expected ions. Since the anion has six ligands as is shown in Figure 5.2, up to six ligands can be broken off of the ion due to the ligand breaking phenomena seen in the TOF data.

However, this also gives a large degree of freedom of what ion cluster could be emitted by the thruster operating on this ionic liquid. The ion clusters could contain B^{3-} , B^{2-} , B^{-} and B^0 , with each of these losing one ligand progressively down to neutrality, hence losing one charge and the mass of a thiocyanate group (58.1 AMU) per ligand. It will be assumed that only neutral and negatively charged dysprosium thiocyanate particles can be emitted.

Assuming that any combination of ions could be emitted, at least one ion matches the second drop well. This would be B^0B^{3-} , which chemically would consist of a $Dy(SCN)_3$ bonded with $Dy(SCN)_6$. This would have a charge-to-mass ratio of 3.36×10^5 C/kg and has been plotted on to the TOF data represented by the dashed line labelled ' B^0B^{3-} '. The existence of such an ion would match well with the existence of the $(SCN)^{-}$ ions due to both ions originating from the ligand breaking phenomena. However, the mechanism through which this neutral and ion could bond is uncertain, although it can be speculated that the ligands could possibly act as a way which the two ions could bond together. Further experiments are required as this drop could originate from the noisy data itself and therefore it is uncertain whether it actually exists.

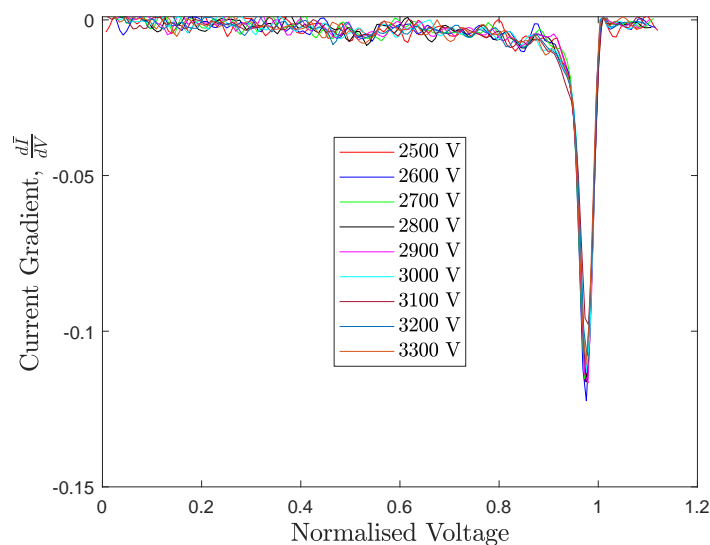
5.3.4.3 Retarding Potential Analysis

The RPA data for both polarities are shown in Figure 5.41. The data for both polarities show a sharp drop at the voltage approximately equal to the emitter potential, suggesting that no significant field-free fragmentation is occurring within the plume of this ionic liquid. The lack of fragmentation is therefore interesting when considering the fact that there seems to be ligand breaking within the plume as there would be an inherent change in the energy seen for this to happen, unless this ligand breaking occurred very close to the emitter. This leads to the conclusion that the ligand breaking of this ion originates either when the ion is still in the liquid phase or when the anion is very close to the emitter.

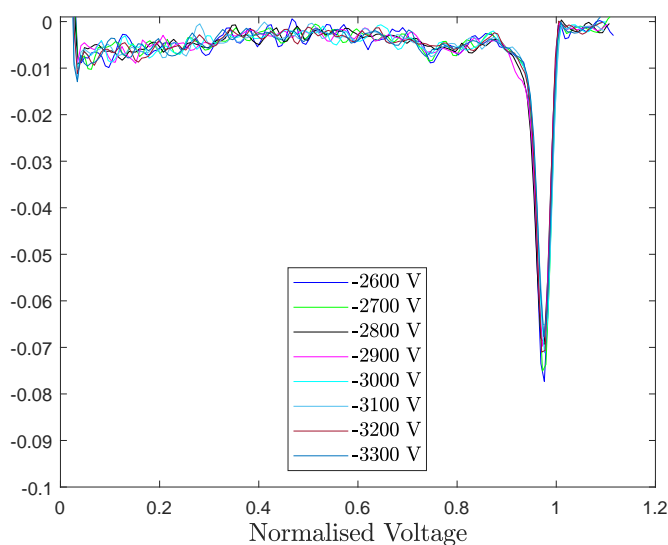
This liquid was found to be not well suited for use as a propellant due to its low current. Furthermore, the ligand breaking seen with the thrusters during emission likely adds a source of inefficiency. However, this ionic liquid definitely is of interest for a scientific review as its probable ligand breaking behaviour has not been seen previously seen in electrospraying.

5.4 Combined Current

The current against voltage data are shown in Figure 5.42 for all the ionic liquids tested. For $C_6(\text{mim})_2\text{-Co}(\text{SCN})_4$, the collector and extractor currents were summed as the extractor current was significant. This was done to accurately represent the total current emitted by the ionic liquid. The current emitted from the different ionic liquids is seen



(A) Positive Polarity.



(B) Negative Polarity.

FIGURE 5.41: The RPA data for emitter 9 for both polarities. No significant fragmentation is observed within the RPA data.

to vary over an order of magnitude, and the ionic liquid operational voltages also vary significantly.

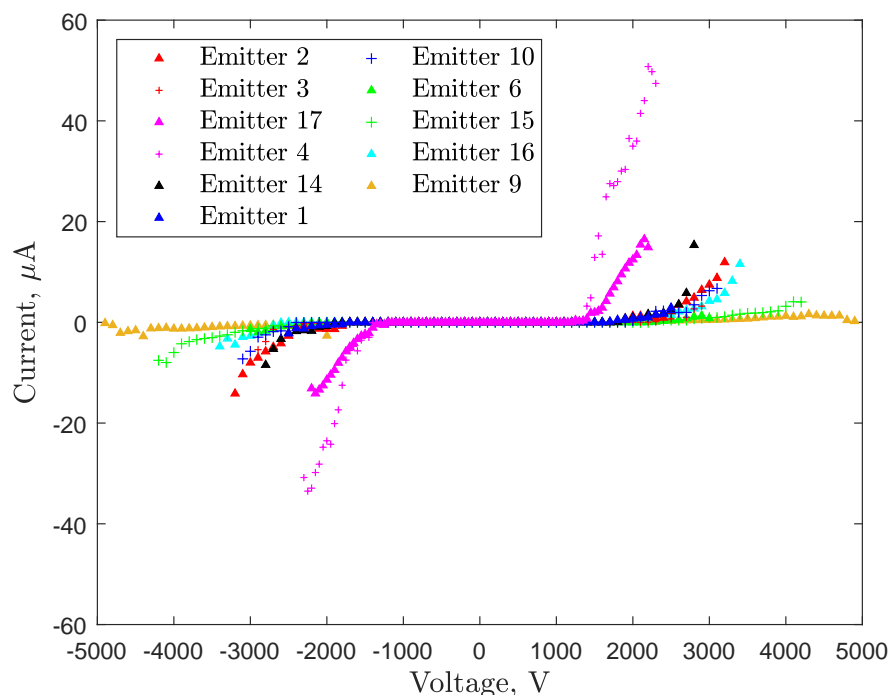


FIGURE 5.42: Current against voltage for the ionic liquids showing the large variation of collector current between the different ionic liquids. The colours represent the following liquids: EMI-BF₄ - red, EMI-FeCl₄ - magenta, EMI-SbF₆ - black, (EMI)₂-Co(SCN)₄ - blue, C₆(mim)₂-(IM)₂ - green, C₆(mim)₂-Co(SCN)₄ - cyan and (C₆mim)₃-Dy(SCN)₆ - orange.

It can be seen that EMI-FeCl₄ onset at significantly lower voltage than the other ionic liquids. Most of the other ionic liquids onset at a voltage of 1800 - 2000 V, whereas EMI-FeCl₄ onset at 1200 and 1400 V. As previously discussed it is unclear whether this arises from the surface tension, emitter-extractor distances or a different ionic liquid property. This is because the emitter was poorly characterised for current-voltage tests. Further current-voltage tests are required to investigate the source of this lowered onset voltage.

Similar levels of current were emitted by EMI-BF₄, EMI-SbF₆, (EMI)₂-Co(SCN)₄ and C₆(mim)₂-Co(SCN)₄. The current was comparable despite the lower conductivity of EMI-SbF₆ (6.2 mS/cm) and (EMI)₂-Co(SCN)₄ (3.42 mS/cm) compared to EMI-BF₄ (14.6 mS/cm). Although the conductivity of C₆(mim)₂-Co(SCN)₄ is unknown due to the

ionic liquid being solid at room temperature, a lower conductivity is expected compared to $(\text{EMI})_2\text{-Co}(\text{SCN})_4$ due to the long $\text{C}_6(\text{mim})_2^{2+}$ di-cation. These data seem to at least suggest that conductivity may have a less significant effect on current than might be expected. However, the tip radii for these emitters varied between $63\ \mu\text{m}$ for EMI-SbF_6 and $130.9\ \mu\text{m}$ for $\text{C}_6(\text{mim})_2\text{-Co}(\text{SCN})_4$. Therefore, there is a large uncertainty whether the similar currents are caused by the properties of the ionic liquids or the emitter and extractor geometry.

A low current was emitted by the super viscous ionic liquids, $\text{C}_6(\text{mim})_2\text{-(IM)}_2$ and $(\text{C}_6\text{mim})_3\text{-Dy}(\text{SCN})_6$. However, a relatively high current was emitted by these liquids considering the very low conductivity of $\text{C}_6(\text{mim})_2\text{-(IM)}_2$ ($0.42\ \text{mS/m}$) and likely even lower conductivity of $(\text{C}_6\text{mim})_3\text{-Dy}(\text{SCN})_6$, although the value of this ionic liquid is unknown. Assuming a linear relationship, a 34.8 times lower current is expected for $\text{C}_6(\text{mim})_2\text{-(IM)}_2$. However, the current for emitter 15 is about 10 times lower in the positive polarity and 7 times lower for the negative polarity at a voltage of $3200\ \text{V}$ compared to emitter 2 using EMI-BF_4 . These data seem to somewhat suggest that even though conductivity does have a significant effect on the current emitted by electro-spray ionisation, the effect of conductivity is somewhat diminished when these ionic liquids are compared.

In order to make the data more comparable, the voltages were normalised with the onset voltage for each emitter. The normalised data are shown in Figure 5.43. These data illustrate a similar picture to the non-normalised current data. However, a few further conclusions can be ascertained. Firstly, excluding emitter 4, the metal/metalloid halides and $\text{Co}(\text{SCN})_4^{2-}$ ionic liquids are found to have similar behaviour, with EMI-FeCl_4 still having the highest current for most of the range.

Notably, EMI-SbF_6 has a higher current for both polarities at $\frac{V}{V_{\text{onset}}}$ of above 1.5 in the positive and 1.45 in the negative polarity. This high current behaviour seems to suggest the EMI-SbF_6 might emit more current than EMI-BF_4 at higher voltages, although the propellant was not tested at the same maximum $\frac{V}{V_{\text{onset}}}$ as EMI-BF_4 . The high current is also emitted despite EMI-SbF_6 having one of the sharpest emitter tips, typically leading to lower current [40, 41, 42]. Further experiments focusing on current-voltage should be conducted, with better control over the tip radii and emitter-extractor distances to

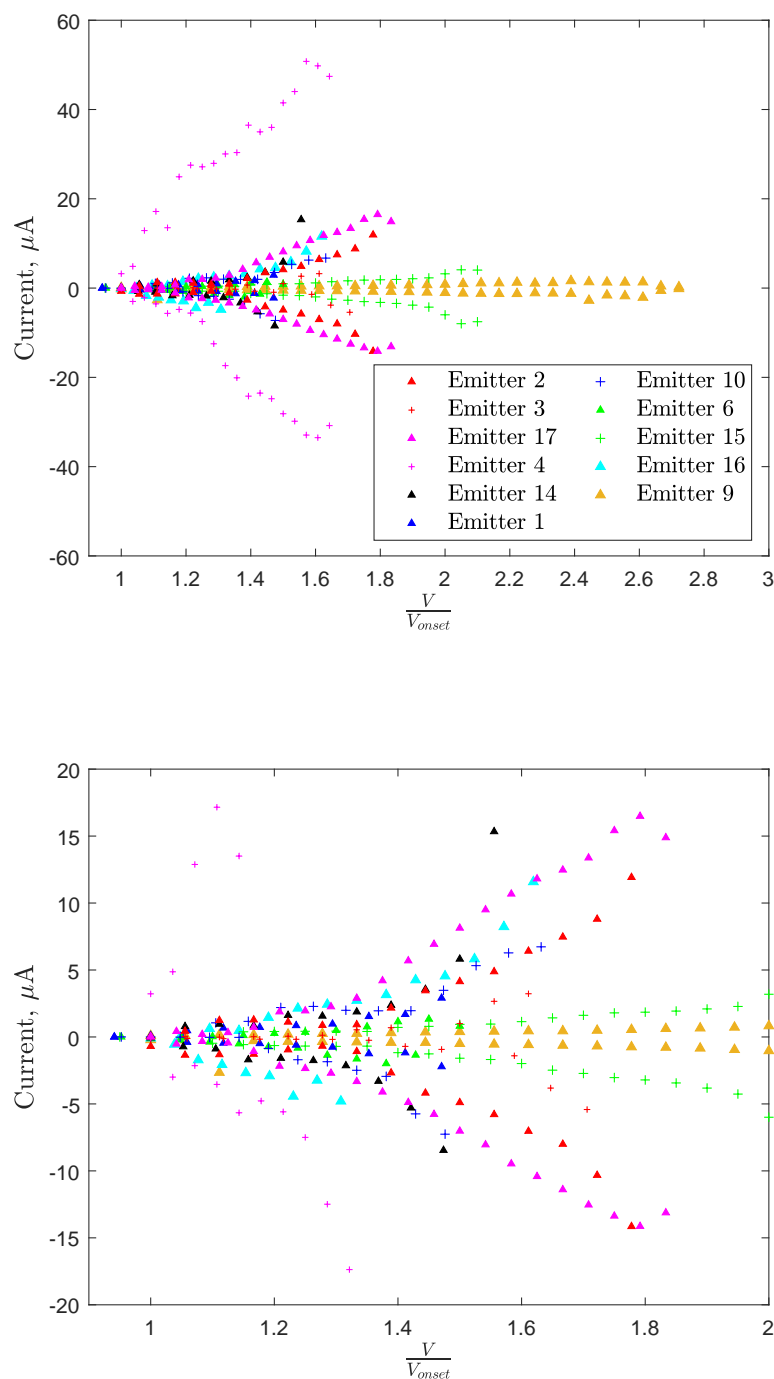


FIGURE 5.43: Current data with a voltage normalised to the onset voltage, showing that similar collector current is achieved between the different ionic liquids when the voltage is normalised. (a) shows the full range of values, while (b) is zoomed in. The colours represent the following liquids: EMI- BF_4 - red, EMI- FeCl_4 - magenta, EMI- SbF_6 - black, $(\text{EMI})_2\text{-Co(SCN)}_4$ - blue, $\text{C}_6(\text{mim})_2\text{-(IM)}_2$ - green, $\text{C}_6(\text{mim})_2\text{-Co(SCN)}_4$ - cyan and $(\text{C}_6\text{mim})_3\text{-Dy(SCN)}_6$ - orange.

establish whether the trend is repeatable. However, these preliminary current-voltage tests seem to show promise for the ionic liquid as a future electrospray propellant.

$C_6(\text{mim})_2\text{-Co}(\text{SCN})_4$ was also observed to emit significant current, with the current exceeding all the other listed propellants in the negative polarity, and nearly exceeding all other ionic liquids in the positive polarity at a $\frac{V}{V_{\text{onset}}}$ of 1.6. Since the temperature was not controlled effectively due to the kapton heater's distance from the emitter tip, it is likely that the conductivity could significantly increase due to an increased temperature. Furthermore, a broken emitter tip was used due to the uncertainty whether it was possible to use a solid ionic liquid, therefore these data are unreliable and require repetition.

It is also notable that $(\text{EMI})_2\text{-Co}(\text{SCN})_4$ had a similar current behaviour to EMI-BF_4 . The current emitted by this ionic liquid was comparable to EMI-BF_4 at all values of $\frac{V}{V_{\text{onset}}}$. If only the lower conductivity, high viscosity and surface tension of $(\text{EMI})_2\text{-Co}(\text{SCN})_4$, it is unclear why the currents would be comparable.

One explanation for the increased current could be that doubly-charged nature of the ions amplifies the electric field, as discussed at the start of section 5.3. This amplification of the electric field would increase the amount of current emitted. Including the low, but nonetheless high considering their propellant properties, current emission of the super viscous ionic liquids, the charge of an ion may be a property that can improve the performance of ionic liquids. The data seem to suggest that the multiply-charged ionic liquids amplify the applied electric field, improving their current emission relative to their quite poor liquid properties.

Overall, the current-voltage data show a few ionic liquids which are promising propellants for electrospray thrusters. Similar to or greater current emission was shown by the two alternative metal/metalloid halide ionic liquids compared to EMI-BF_4 , despite somewhat similar or worse liquid properties and heavier anions used. Furthermore, two ionic liquids with the $\text{Co}(\text{SCN})_4^{2-}$ di-anion also emitted similar current levels, despite the significantly poorer liquid properties, i.e. lower conductivity and higher viscosity. Further investigation with a more robust current-voltage methodology is however required. This is due to the varying emitter tip radii and unknown emitter-extractor distances making it unclear whether the good current emission characteristics are an effect of the ionic liquid properties or the thruster's geometry.

5.5 Analysis of TOF data

To finish the results sections, some of the TOF data will be analysed. Firstly, the experimental data will be compared to the droplet charge-to-mass ratio equation from Pfeifer and Hendricks [47]. Secondly, the ion emission model presented in chapter 2 will be reintroduced and compared with some of the experimental data.

5.5.1 Comparison with Droplet Charge-to-Mass Ratio

The first equation that was introduced in chapter 2 for the approximation of charge-to-mass was by Pfeifer and Hendricks [47]. It has been the only electro spray thruster charge-to-mass ratio equation which has been verified experimentally. However, for purely ionic electro spray thrusters it has been discussed that it is unlikely to be accurate. It was defined in section 2.1.1 as:

$$\frac{q}{m} \propto \left(\frac{K}{Q} \right)^{0.429}. \quad (5.15)$$

Equation 5.15 shows that the charge-to-mass ratio of emitted ions by electro spray thrusters should be proportional to its conductivity divided by volumetric flow rate. For the TOF data of each ionic liquid, the average charge-to-mass ratio, \bar{q}/m , will be determined by calculating the proportion of each ion cluster, then multiplying it by the charge-to-mass ratio of the ion cluster. This can be defined as,

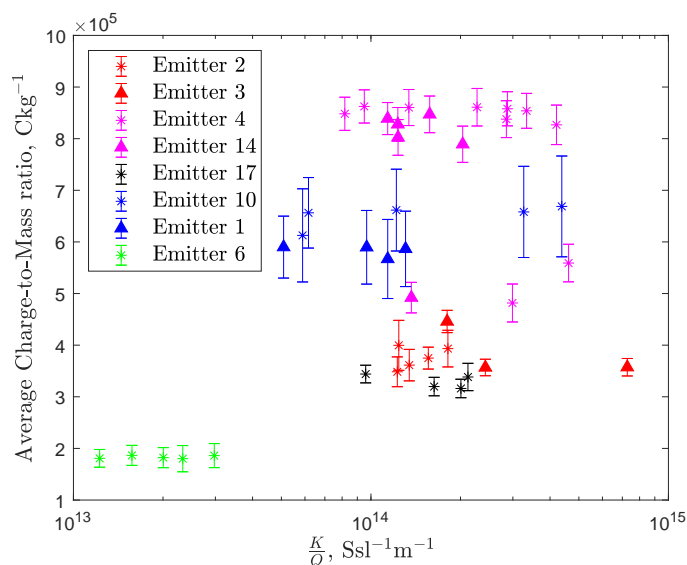
$$\frac{\bar{q}}{m} = \sum_{i=0}^k P_n \frac{q}{m_n}, \quad (5.16)$$

where $\frac{q}{m_n}$ is the charge to mass ratio of an ion cluster with n neutrals.

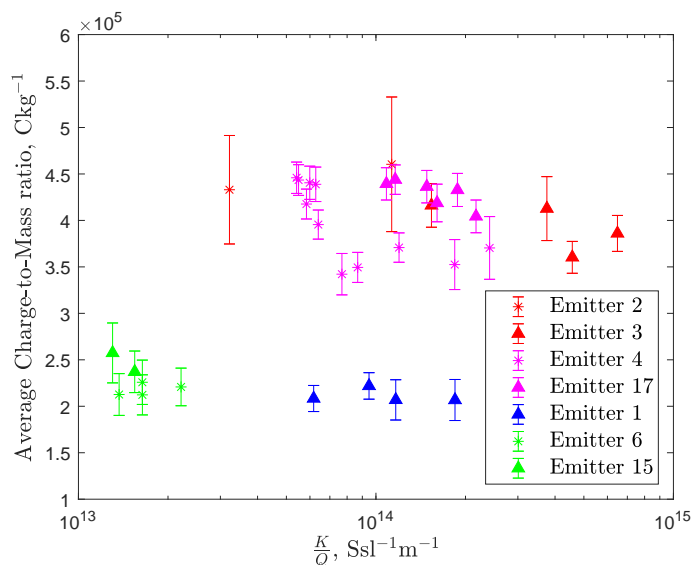
The conductivity of each ionic liquid was defined at the start of this chapter. However, in order to calculate the volumetric flow rate, TOF data will need to be used. The volumetric flow rate can be derived from TOF data by using:

$$Q_{TOF} = -\frac{2I\phi_{emitter}}{\rho L} \int_0^{\infty} I(t)tdt \quad (5.17)$$

where Q_{TOF} is the volumetric flow rate defined from the TOF data, I is the current for the given $\phi_{emitter}$ and $I(t)$ is the TOF current trace.



(A) Positive Polarity.



(B) Negative Polarity.

FIGURE 5.44: Average charge-to-mass ratios against the conductivity per volumetric flow rate for five different ionic liquids. For both polarities and all the ionic liquids it can be seen that the charge-to-mass ratio does not significantly vary with the volumetric flow rate, pointing towards the Pfeifer and Hendricks model being unsuitable for pure ion emission. The colours represent the following liquids: EMI- BF_4 - red, EMI- FeCl_4 - magenta, EMI- SbF_6 - black, $(\text{EMI})_2\text{-Co(SCN)}_4$ - blue and $\text{C}_6(\text{mim})_2\text{-(IM)}_2$ - green.

Using this analysis method, the average charge-to-mass ratios have been plotted in

Figure 5.44 for positive and negative polarities. The ionic liquids $C_6(\text{mim})_2\text{-Co(SCN)}_4$ and $(C_6\text{mim})_3\text{-Dy(SCN)}_6$ were omitted due to the poor quality data. The densities for the plotted ionic liquids were: EMI- BF_4 - 1286 [104], EMI- FeCl_4 - 1420 [93], EMI- SbF_6 - 1850 [94], $(\text{EMI})_2\text{-Co(SCN)}_4$ - 1288 [95] and $C_6(\text{mim})_2\text{-(IM)}_2$ - 1540 [105] kg/m^3 .

From Eq. 5.15, it would be expected that as the volumetric flow rate is decreased, the charge-to-mass ratio would increase. In Figure 5.44 this is mostly not observed, with the average charge-to-mass ratio remaining practically constant at all volumetric flow rates for each ionic liquid. The only clear positive correlations seen are with emitter 2 in the positive polarity and emitter 4 in the negative polarity. The constant charge-to-mass ratios show that changes in volumetric flow rate do not correspond to significant changes in the charge-to-mass ratio of emitted ions in these tests.

Although the constant charge-to-mass ratio of ion clusters for pure ion emission is not a novel conclusion, the application of this to multiply-charged ion clusters is. It can be seen that the average charge-to-mass ratio remains approximately constant for both of the multiply-charged ionic liquids. This seems to show that the physics governing the ion cluster emission of multiply-charged ionic liquids are similar to conventional ionic liquids as they follow similar behaviour.

The charge-to-mass ratios of each ionic liquid's emitted ions also appear to be similar. Although the conductivity varies by almost two orders of magnitude between the highest and lowest conducting ionic liquid, the differences in the charge-to-mass ratios is at maximum approximately 4 times between $C_6(\text{mim})_2\text{-(Im)}_2$ and EMI- FeCl_4 in the positive polarity. Similarly, the other propellant properties do not seem to have a significant contribution to the charge-to-mass ratios of the ion clusters.

There are however a few uncertainties with the analysis. Firstly, a higher volumetric flow rate is emitted by the thruster than has been calculated for the analysis. This is due to the acceleration region fragmentation increasing the volumetric flow rate due to a neutral flux [78] and also potentially anomalous mass fluxes being present in electro-spray thrusters [81, 106]. For the data, it is likely that approximately the same increase in flow rate would be seen for each emitter's data points. Therefore, there should be a negligible effect on the correlation between the charge-to-mass ratio and conductivity per volumetric flow rate, hence the conclusions from the data would remain the same.

A large source of uncertainty, not represented in the error of the data, is the possibility that measured ion clusters are not representative of the full beam. Only a small portion of the plume could be measured by the TOF system if off-axis beamlets are emitted. These beamlets could also be comprised differently to the main plume. Although the thruster was controlled in one axis of rotation, partially mitigating this, a second axis of rotation would be required to ensure full mitigation of this effect. Another possibility to mitigate this effect is to repeat the experiment, as the same beamlets would likely not be produced by different emitters. All the ionic liquids, except for EMI-SbF₆, have been repeated once also mitigating the uncertainty. However more emitters for each ionic liquid would have to be tested to ensure that off-axis emission is fully mitigated.

The final uncertainty is the lack of long period tests of some of the ionic liquids, particularly C₆(mim)₂-(Im)₂. On a repeat experiment with emitter 6, it was found that large ion clusters and droplets were emitted [90]. Since these were repeated after the emitter was kept in atmosphere for a long period of time, it is unclear whether this is representative of the emitter 6 experiments in this analysis. EMI-BF₄ and (EMI)₂-Co(SCN)₄ both have long period TOF data, although the latter is very noisy, therefore their plumes are reliably purely ionic. The EMI-FeCl₄ and EMI-SbF₆ data are also very likely to be purely ionic, due to their constant current trace at charge-to-mass ratios below 1×10^5 Ckg⁻¹. While the same is true for most C₆(mim)₂-(IM)₂ data, to confirm the pure ion emission further long period tests are required. The data are nonetheless presented in Figure 5.44 under the assumption of pure ion emission.

To summarise, the data strongly suggest that the charge-to-mass ratios of ion clusters emitted by the different ionic liquids remain constant despite large changes in the ionic liquid properties. This seems to disagree with droplet charge-to-mass equations, which have been experimentally verified to predict droplet charge-to-mass ratios. However, uncertainty remains in the analysis due to potential for off-axis emission and the lack of longer period TOF data. Nonetheless, it is likely that the lack of correlation between the charge-to-mass ratios of emitted ions and conductivity and volumetric flow rate is quite reliable.

5.5.2 Comparison with Ion Emission Model

To finish the analysis, the ion cluster distributions will be compared with the modelled cluster distributions using the ion emission model introduced in section 2.3.2. One problem with analysing the data using the ion emission model is that the relative permittivity could only be found for EMI-BF₄ and EMI-FeCl₄, 12.8 and 13.1 [76] respectively. Therefore, analysis will only be conducted on these two ionic liquids.

5.5.2.1 EMI-BF₄

The modelled cluster for EMI-BF₄ was calculated in section 2.3.1, therefore will be presented here as well for ease of reading. This distribution is shown in Tab. 5.10. It can be seen that for both of the polarities, it is predicted that dimers will comprise the vast majority of the plume, with 82.9% of the positive and 89.9% of the negative polarity plume being comprised of dimers. The positive polarity is expected to have significantly more monomers as well, compared to the negative polarity.

TABLE 5.10: Modelled ion cluster size distribution for EMI-BF₄.

Ion cluster size	EMI ⁺	BF ₄ ⁻
$n = 0$	0.148	0.057
$n = 1$	0.829	0.899
$n = 2$	0.023	0.044

Tables 5.11 and 5.12 show the estimated ion cluster distribution for emitters 3 and 2. Similar to the experimental data found in literature, the distribution of ion clusters that were modelled is found to be insufficiently broad. A significant population of trimers is seen across all voltages and both polarities. The negative polarity of emitter 3 was

TABLE 5.11: Experimental ion cluster size distributions for emitter 3 using EMI-BF₄.

Positive Polarity					
Voltage	Ion cluster Size				
V	$n = 0$	$n = 1$	$n = 2$	$n = 3$	$n = 4$
2700	0.110	0.777	0.074	0.039	0.000
2800	0.128	0.713	0.098	0.038	0.000
2900	0.254	0.691	0.044	0.011	0.000
Negative Polarity					
-2500	0.119	0.613	0.187	0.043	0.038
-2600	0.092	0.597	0.234	0.057	0.019
-2700	0.163	0.519	0.240	0.057	0.022
-2800	0.146	0.652	0.130	0.056	0.017

TABLE 5.12: Experimental ion cluster size distributions for emitter 2 using EMI-BF₄.

Positive Polarity					
Voltage	Ion cluster Size				
V	$n = 0$	$n = 1$	$n = 2$	$n = 3$	$n = 4$
2200	0.177	0.703	0.080	0.032	0.008
2300	0.190	0.691	0.072	0.023	0.025
2400	0.089	0.830	0.040	0.017	0.024
2500	0.102	0.853	0.027	0.001	0.018
2600	0.132	0.794	0.061	0.002	0.011
Negative Polarity					
-2400	0.197	0.623	0.139	0.041	0.000
-2800	0.168	0.608	0.188	0.036	0.000

comprised an especially high amount of trimers, between 13.0% at -2800 V and 24.0% at -2700 V. Also some quadramers, up to 5.7% for the negative polarity emitter 3 data at -2600 and -2700 V, and pentamers are also observed, with up to 3.8% seen in the negative polarity emitter 3 data at -2500 V. Furthermore, the ion cluster distributions in both polarities are approximately similar, whereas the modelled data predicts more lighter ions in the positive polarity.

Similar to the modelled data, the majority of the plume is comprised of dimers. For emitter 3 about 70% - 80% of the plume is comprised of dimers in the positive polarity, somewhat similar to the 82.9% predicted by the model. For emitter 2, the dimer proportion varies from ~70% up to 85.3% at 2500 V. However, in the negative polarities approximately 60% dimers are observed for both emitters, significantly lower than the 89.9% predicted by the ion cluster emission model.

Overall, the types of emitted ion clusters are somewhat accurately predicted. Therefore,

although the model does not accurately predict ion cluster proportions, more investigation into the model may be warranted due to its ability to predict the type of ion clusters emitted.

5.5.2.2 EMI-FeCl₄

The modelled values for EMI-FeCl₄ at a temperature of 293 K are shown in Tab. 5.13. It shows that for both polarities, the plume is predicted to have more monomers than the EMI-BF₄ plume. The distribution in the positive polarity is 20.9% monomers, 78.8% dimers and 3.5% trimers. Similarly to EMI-BF₄, the majority of the plume is predicted to be comprised of dimers. In the negative polarity however, a monomer dominated plume is predicted, with 66.4% of the plume being comprised of monomers and 33.6 % of dimers.

TABLE 5.13: Modelled ion cluster size distribution for EMI-FeCl₄.

ion cluster size	EMI ⁺	FeCl ₄ ⁻
$n = 0$	0.209	0.664
$n = 1$	0.788	0.336
$n = 2$	0.035	0.000

For the experimental data, only data every 100 V will be shown instead of 50 V, due to the similarity of each data point. For both emitters, the data are presented in Tab. 5.14 and 5.15. It can be seen that in both data sets, the positive polarity has the most monomers, reaching > 95% for both emitters. For the negative polarity, this is not the case, where for both emitters, the proportion of monomers increases at a lower rate, remaining below 90% for all voltages tested.

However, at the lowest voltages, ± 1400 V for emitter 4 and ± 1650 V for emitter 17, the experimental ion cluster size distribution is closer to the modelled distribution.

TABLE 5.14: Experimental ion cluster size distributions for emitter 4 using EMI-FeCl₄.

Positive Polarity				
Voltage	ion cluster Size			
V	$n = 0$	$n = 1$	$n = 2$	$n = 3$
1400	0.385	0.540	0.065	0.010
1500	0.583	0.347	0.109	0.000
1600	0.960	0.040	0.000	0.000
1700	0.988	0.012	0.000	0.000
1800	0.991	0.009	0.000	0.000
1900	0.975	0.255	0.000	0.000
Negative Polarity				
-1400	0.611	0.373	0.016	0.000
-1500	0.517	0.464	0.019	0.000
-1600	0.612	0.373	0.014	0.000
-1700	0.770	0.216	0.014	0.000
-1800	0.844	0.156	0.000	0.000
-1900	0.862	0.138	0.000	0.000

TABLE 5.15: Experimental ion cluster size distributions for emitter 17 using EMI-FeCl₄.

Positive Polarity			
Voltage	ion cluster Size		
V	$n = 0$	$n = 1$	$n = 2$
1650	0.414	0.572	0.014
1750	0.969	0.031	0.000
1850	0.956	0.044	0.000
Negative Polarity			
-1650	0.722	0.278	0.000
-1750	0.770	0.230	0.000
-1850	0.855	0.145	0.000

Although as with the EMI-Im data discussed in section 2.3.4 the agreement is most likely coincidental, it will be assumed it is not in order to speculate why the agreement between the model and experimental data might change if the model was accurate.

The first possibility why the model might become less in agreement with the experimental data could be that as the voltage increases, a beam could change into beamlets or emit off-axially. The current collected using a TOF system could then become less representative of the whole plume current. This might explain the disagreement in the modelled and experimental data, and the sudden change in ion cluster sizes in the positive polarity. However, similar to the considerations given at the end of section 5.5.1, this is unlikely to be the case. The gradual increase in monomer population in the negative polarity is also likely attributable to the increase in the electric field

strength, therefore providing further evidence against this possibility. This is because the sudden changes in the composition should be observed in both polarities if off-axial or beamlet emission occurs. Furthermore, the thruster was rotated in one axis in order to mitigate off-axis emission.

Another possibility could be that the changing size distribution is caused by the changing volumetric flow rate, affecting the upstream conditions. As discussed in section 2.3.3, the size of ion clusters is affected by changing upstream conditions [63]. However, although this could explain the EMI-FeCl₄ data in isolation, this explanation would not be sufficient for the remainder of the ionic liquids. Changes in ion cluster size distribution across different volumetric flow rates are mostly not observed, as shown in Figure 5.44.

To briefly summarise the ion cluster emission model, the predictions of the model seem to somewhat predict experimental data. Similar sizes of ion cluster are predicted to the ion clusters that are experimentally observed. However, the predicted distributions of these ion clusters are not accurate, both in the proportions of the ion clusters and the general trends. For example, the model predicts lighter ions in the negative polarity of the EMI-FeCl₄ plume, which is not seen except for the lowest voltages. A more robust model might be produced if the factors contributing to the model, especially ΔG_s , are further investigated.

5.6 Summary

In this chapter, seven ionic liquids were tested with eleven emitters in order to investigate ion cluster emission from porous electrospray thrusters. Three of these ionic liquids were metal/metalloid halide ionic liquids, ionic liquids which contain an EMI⁺ cation and an anion comprised of a metal/metalloid atom surrounded by halogens. The second group was multiply-charged ionic liquids, which are comprised of ions that contain more than one charge.

The metal/metalloid halide ionic liquids showed promise as alternative propellants for electrospray thrusters. Both the alternative metal/metalloid halide ionic liquids, EMI-FeCl₄ and EMI-SbF₆, showed similar to higher collector currents compared to EMI-BF₄. EMI-FeCl₄ in particular emitted up four to five times more current than EMI-BF₄.

using emitter 4, although more data is required to ensure repeatability. TOF data also showed that both ionic liquids emitted pure ion plumes, with EMI-SbF₆ emitting a similar plume to EMI-BF₄. EMI-FeCl₄ was unique in that at certain voltages, an almost pure monomer plume was emitted for both of the emitters. High currents and pure ion plumes suggest that these two ionic liquids would be suitable to use as alternative propellant options for electrospray thrusters.

The multiply-charged ionic liquid tests showed a variety of results. Firstly, the ionic liquids (EMI)₂-Co(SCN)₄ and C₆(mim)₂-Co(SCN)₄ showed currents similar to EMI-BF₄ despite their likely unfavourable ionic liquid properties, which possibly suggests a diminished effect of conductivity on current emission. The 'super viscous' ionic liquids, C₆(mim)₂-(Im)₂ and (C₆mim)₃-Dy(SCN)₆, did not emit as much current, however they were able to be electrosprayed at very high voltages, exceeding 4000 V. Interesting ion species called 'double ions' were proposed to be emitted by (EMI)₂-Co(SCN)₄ and C₆(mim)₂-(Im)₂ based on the TOF data. These ions could point towards how ion clusters are formed in the meniscus of a Taylor cone. Poor TOF data was collected for C₆(mim)₂-Co(SCN)₄ and (C₆mim)₃-Dy(SCN)₆ making observations unreliable. However, a pure ion plume was likely emitted by C₆(mim)₂-Co(SCN)₄ and a complex plume composition was found to be emitted by (C₆mim)₃-Dy(SCN)₆, including multiple species of ions such as ligands originating from the Dy(SCN)₆³⁻ tri-anion.

A comparison between the average charge-to-mass ratios of ions emitted by the various ionic liquids and the conductivity divided by the volumetric flow rate, $\frac{\kappa}{Q}$ was made, showing that the charge-to-mass ratio did not depend on $\frac{\kappa}{Q}$. The lack of a correlation between the charge-to-mass ratio and $\frac{\kappa}{Q}$ indicated that the droplet emission model does not apply to pure ion emission using ionic liquids. An alternative model, the pure ion emission model, was applied to EMI-BF₄ and EMI-FeCl₄, however it was found that experimental data were not reproduced due to the narrow ion distribution of the model.

Chapter 6

Conclusions and Future Work

In this thesis, ion cluster emission from a porous electrospray thruster was experimentally investigated. Three experimental techniques, full plume current collection, retarding potential analysis and TOF mass spectrometry, were combined into an experimental setup, with the TOF system being developed in this thesis. It was designed with a 'reflecting' type gate, a large current collector and a flight length of 550 mm. These experimental tools were then used to test seven different ionic liquids which were classified into two different classes, metal/metalloid halides and multiply-charged ionic liquids.

Alternative metal/metalloid halide ionic liquids were found to emit similar, to significantly higher currents than EMI-BF₄. Notably, EMI-FeCl₄ was found to emit over 50 μ A in one of the current-voltage tests, a significantly higher amount of current than the other ionic liquids that were tested. However, repeat tests did not reproduce similar levels of current. Nonetheless, high currents were reached by both alternative metal/metalloid halide ionic liquids compared to the current of EMI-BF₄ despite these alternative propellants having heavier ions contained within them.

The higher current behaviour of these liquids shows the possibility of using metal/metalloid halide ionic liquids to produce more thrust for electrospray thrusters, due to their higher mass. Improvements in porous electrospray thruster performances could be achieved with higher thrust as current electrospray thrusters produce only low

amounts of thrust compared to other types of thrusters. The low thrust is one of the barriers in implementing electrospray thrusters as a type of propulsion for small satellites, which these ionic liquids show promise in improving.

Interesting current-voltage characteristics were observed with the use of multiply-charged ionic liquids. It was found that the ionic liquids with the $\text{Co}(\text{SCN})_4^{2-}$ di-anion emitted similar levels of current to EMI-BF_4 , despite their poor ionic liquid properties. These poor properties were primarily the low conductivity and high viscosity in comparison with EMI-BF_4 . An amplification of the electric field due to the extra charge was interpreted from the comparable current. The use of these extra charges could be useful in ionic liquids with high conductivity as this could amplify the current, therefore produce more thrust.

Low current emission of, at maximum $7 \mu\text{A}$ and $2 \mu\text{A}$ was shown by the 'super' viscous ionic liquids $\text{C}_6(\text{mim})_2\text{-(Im)}_2$ and $(\text{C}_6\text{mim})_3\text{-Dy}(\text{SCN})_6$, respectively. The low current was likely caused by their very high viscosities. However, a high stability at significantly higher voltages was observed, with most of the ionic liquids being operated up to 3000 V , whereas these 'super' viscous ionic liquids operated stably above 4000 V .

Although not necessarily applicable to electric propulsion, applications where high energy ions are required could benefit from these ionic liquids. One such application is ionic liquid ion etching, where high energy ions are used to etch into various materials [107]. An advantage of using an ionic liquid which can reach such high voltages is the simplification of the system used to etch, as typical ionic liquid ion etching applications require the extractor to be raised to a high voltage to provide the high energy. This means that care must be taken to ensure that the potential difference between the extractor and emitter is always maintained at a given level in order to prevent damage from the occurring to the emitter. It also makes any polarity switching more complicated. The 'super viscous' ionic liquids provide a simple solution to these problems as the extractor may be able to be kept grounded for a similar ion energy, preventing potential damage to emitters and simplifying polarity switching.

For the TOF tests it was found that all the ionic liquids tested emitted purely ionically, possibly except $\text{C}_6(\text{mim})_2\text{-(Im)}_2$ and $(\text{C}_6\text{mim})_3\text{-Dy}(\text{SCN})_6$. These latter two require longer period TOF data to ensure pure ion emission. Pure ion emission seemed to be resistant to the large variation in ionic liquid properties, with pure ion emission

being observed at conductivities ranging from 14.6 mS/cm down to 3.42 mS/cm for $(EMI)_2-Co(SCN)_4$. If $C_6(mim)_2-(Im)_2$ is assumed to have emitted purely ionically, this range extends down to 0.42 mS/cm. It seems that pure ion emission can be achieved even with low conductivities, high viscosities and with ionic liquids with more exotic properties, such as extra charges within the cations or anions or both.

The findings with pure ion emission have interesting implications on the physics of ion emission. The relationship between conductivity and charge-to-mass ratios has been suspected to not be significant, however it has not been directly evaluated for pure ion emission. In this thesis it has been shown that even with a broad range of ionic liquid properties, the pure ion emission is retained. This indicates that the factors contributing to pure ion emission are more complex than simple propellant properties. One clear correlation is the porous reservoir Laplace pressure [63] which clearly influences the emission of ions from porous electro spray thrusters.

Since different plume compositions are produced by similar porous electro spray thruster geometries with different ionic liquids, the properties of those ionic liquids must impact the plume composition hence the ion emission. One observation which may indicate which ionic liquid properties impact the is the stability of the dimers emitted by $(EMI)_2-Co(SCN)_4$ and $C_6(mim)_2-(Im)_2$. It was found that both of the dimers that were emitted when using these ionic liquids were particularly stable, evident from the lack of field-free fragmentation of these ionic liquids. A large influence of the molecular properties are therefore hinted by this observation, due to the electrostatic bonding strength being increased by the double charge hence decreasing fragmentation and possibly increasing the emission of dimers. The impact of the molecular properties on the electro spray ion emission should therefore be investigated in order to evaluate if this may provide a better method to predict the sizes of emitted ion clusters.

The average charge-to-mass ratios of each ionic liquid tested was compared with the conductivity rate per volumetric flow, in order to test the applicability of the droplet charge-to-mass equation to pure ion emission. It was found that the charge-to-mass ratio did not vary with the volumetric flow rate, showing that for the pure ion emission observed in this thesis, the equation was not valid. This points towards a new model

of ion emission being required in order to accurately predict the charge-to-mass ratios of pure ion emission.

An alternative model, the ion cluster emission model, was compared with the experimental results in order to determine whether it was a possible alternative. Only EMI-BF₄ and EMI-FeCl₄ were compared as the relative permittivity values were only available for these two ionic liquids. It was found that, similar to the literature review, the model was inaccurate in predicting the compositions of the plume. Similar ion clusters to the emitted ion clusters were predicted. However, the model has a tendency to predict a very narrow distribution whereas a much broader ion cluster distribution was experimentally observed.

One of the reasons for this narrow distribution could be that the model does not consider other effects of the ionic liquid. One effect that was introduced is the effect of surface tension on the energy required for an ion to be emitted. It is likely that the energy required for ion emission is influenced by other factors, for example the porous reservoir Laplace pressure. The development of the pure ion emission model, if it is in fact an accurate method to model pure ion emission, could lead to ion plume compositions being predictable, which could have significant impact on the design process of electrospray thrusters and applications where electrospray ionisation is used, such as electrospray ionisation mass spectrometry and ionic liquid ion etching. This would reduce the time and experimental work required to design a given electrospray source and allow for reliable and repeatable electrospray emission.

6.1 Future Work

Although much work has already been done to characterise these alternative ionic liquids, more work is required in order to minimise the uncertainty in the data. In this section a brief summary of the different tasks required will be provided.

One constant source of uncertainty throughout this thesis has been the thruster design, more specifically the emitter-extractor alignment. The method to align the emitter and extractor is imprecise. Therefore, a large uncertainty for the current-voltage data is whether the results are caused by ionic liquid properties or the thruster design. An

overhaul of the single emitter thruster is required to allow for precise emitter-extractor alignment.

Another change to the thruster design is a better integration of a heater within the thruster body. Since the heater was attached to the extractor, accurate control of the emitter temperature was not possible, therefore the actual emitter temperature was uncertain. Although this was only tested for one ionic liquid, two benefits could be seen by the integration of the heater. Firstly, ionic ‘liquids’ that are solid at room temperature could be utilised, which enables the use of a larger range of propellants. These could provide interesting benefits for propulsion, such as minimising the risk of shorting between the emitter and the extractor. Secondly, changing the temperature of normal ionic liquids would allow for another dimension of ion cluster emission, the temperature, to be investigated, possibly allowing for a more robust dataset.

Emitter tip radii and heights are not very repeatable due to the the manufacturing technique utilised in this thesis. Therefore, improvements to this technique would enable for more reliable tests to be conducted due to similar emitter geometries. One of the likely sources of this low repeatability is the separation of individual emitters from a single block. Although this could be achieved by manufacturing each emitter individually, this was significantly more expensive, therefore a refinement of the current manufacturing technique is advised.

The emitter current can also be implemented into the LabVIEW program. Although the emitter current can be measured using a multimeter, the lack of implementation into the program complicates the synchronisation of the current and emitter voltage data. Furthermore, an isolation amplifier could also be implemented. While work has been conducted on implementing an isolation amplifier, it was not completed by the time of experimentation. The implementation of an isolation amplifier would enable a better sampling frequency of the emitter current.

The retarding potential analyser was unreliable for acceleration region fragmentation throughout testing. This unreliability was caused by a constant negative gradient. In order to make the retarding potential data more reliable, this negative gradient must be removed. The negative gradient could be caused by a wrong implementation of the retarding potential analyser, however it is likely a new retarding potential analyser is required.

The TOF system still requires significant improvements. The gate noise is a consistent source of uncertainty as it produces a decreasing current after gate activation which reduces the reliability in detecting heavier species. Further refinements of the gate design are required in order to reduce the gate noise to a minimum.

One of the possible TOF refinements is adding a second axis of rotation for the rotary stage. Off-axis emission is likely to cause the low signal-to-noise ratio for some of the ionic liquid data, increasing the effect of the gate noise. The influence of this effect was evidenced by the varying level of current into the TOF system at similar plume currents, as well as previous experience with using a Faraday cup in the TOF system. Accurate angular position is required for the second axis, therefore simply using a stepper motor is insufficient instead requiring robust positional control. The advantage of implementing such a system would also be that the ion clusters sizes and energies could be characterised at various angular positions. This may also enable a smaller collector to be used, further decreasing the uncertainty in time and producing much sharper data.

The TOF system could also be further implemented into the LabVIEW system. Currently, the system is operated semi-manually, meaning that constant supervision of the system is required. If the system were fully integrated into the LabVIEW program, it could be fully automated, allowing for significantly more TOF data to be taken. With the integration of two-axis rotation, a full plume characterisation in both angular directions could be implemented, enabling very robust plume composition data.

The analysis of the TOF data could also be improved. Since the analysis of the data is achieved manually, human error becomes a large source of uncertainty for the ion cluster distributions. The implementation of a Bayesian inference algorithm would ensure that these data are analysed to a much better accuracy [108]. Furthermore, it would accelerate the processing of the data, which currently requires a long period of time.

For all the TOF tests, a broader range of charge-to-mass ratios, down to $2 \times 10^2 \text{ CKg}^{-1}$, should be taken. This ensures that the pure ion emission, therefore further increasing the reliability of the data.

So far, only future work based on improving the current experimental setup has been discussed. However, the field of pure ion emission is complicated due to the molecular of ionic liquids. Therefore, there are many different areas to explore in order to unravel the physics of pure ion emission.

The metal/metalloid halide ionic liquids showed promise in their use as a propellant and also revealed interesting physics due to the very monomer-rich plumes of EMI-FeCl₄. Therefore, further exploration of this type of ionic liquid might produce further insights into pure ion emission. At least one ionic liquid, EMI-AlCl₄ or 1-ethyl-3-methylimidazolium tetrachloroaluminate, was considered to be tested during this thesis. However, due to it being corrosive it was not selected. There are other metal/metalloid ions which could produce ionic liquids, such as CuCl₄²⁻ or AuCl₄⁻. Therefore, further metal/metalloid halide ionic liquids could be tested in order to determine whether the good current characteristics of these ionic liquids remain.

One constant throughout all of the ionic liquids that were tested in this thesis was that the same type of cation was used, made up of imidazoliums. However, interesting emission behaviour maybe revealed if different types of cations are used. For example, pyrrolidinium or piperidinium cation ionic liquids could be used instead to further explore what ion clusters are emitted by such ionic liquids.

There are certainly more multiply-charged ionic liquids that could be used. One of these that has already been mentioned, CuCl₄²⁻, however there are certainly many more multiply-charged anions and cations that could form ionic liquids. Further exploration of these may reveal whether dimers, or possibly larger ions, are especially stable when these are electrosprayed.

Testing with C₆(mim)₂-(Im)₂ revealed that it is possible to test with solid ionic 'liquids'. These solid ionic 'liquids' maybe interesting to investigate, as many more combinations of cations and anions that form solid ionic 'liquids' become testable. These solid ionic 'liquids' could also be beneficial for electrospray thrusters as they may minimise the risk of shorting between the emitter and extractor when the thruster is not operating.

The ionic liquids tested in this thesis have only been tested with single emitters. However, a robust method to ensure that these ionic liquids, such as EMI-FeCl₄, make good propellants is by testing them with a large array of emitters. These tests could include

direct thrust and mass flow rate measurements, which would ensure that their performance is improved over EMI-BF₄.

Chapter 7

Appendix

7.1 Appendix A: Review of electrospray thrusters

These data here provide each individual source for the data plotted in section 1.2 in Figure 1.6. An annotated graph and a table are provided for each type of emitter, indicating the thrust, specific impulse, power and reference for each thruster. Where the sources do not provide a thrust or specific impulse, these were calculated by initially calculating the ionic cluster distribution with WebPlotDigitizer. Next, the contribution of each species was summed in order to find the total thrust and specific impulse. This can be defined as

$$T = \sum_{i=0}^k P_n T_n, \quad (7.1)$$

$$I_{sp} = \sum_{i=0}^k P_n I_{sp, n}, \quad (7.2)$$

where k is the largest n size of ionic cluster, P_n is the proportion of the ionic cluster of size n and T_n and $I_{sp, n}$ are the thrust and specific impulse of a plume entirely comprised of an ionic cluster of size n . The thrust and specific impulse for each ionic cluster can be calculated using the equation,

$$T_n = I\sqrt{2\phi_{emitter}}\sqrt{\frac{m_n}{q}}, \quad (7.3)$$

$$I_{sp, n} = \frac{1}{g_0}\sqrt{2\phi_{emitter}}\sqrt{\frac{q}{m_n}}, \quad (7.4)$$

where I is the full plume current and m_n is the mass of an ionic cluster of size n .

7.1.1 Capillary Thrusters

Capillary thrusters have a broad range of thrusts and specific impulses, shown in Figure 7.1. This is evidenced by the almost two orders of magnitude difference in specific impulse, and four orders of magnitude difference in thrust. The specific impulses achievable by capillary thrusters are also high, with up to 4000 s of specific impulse being achieved.

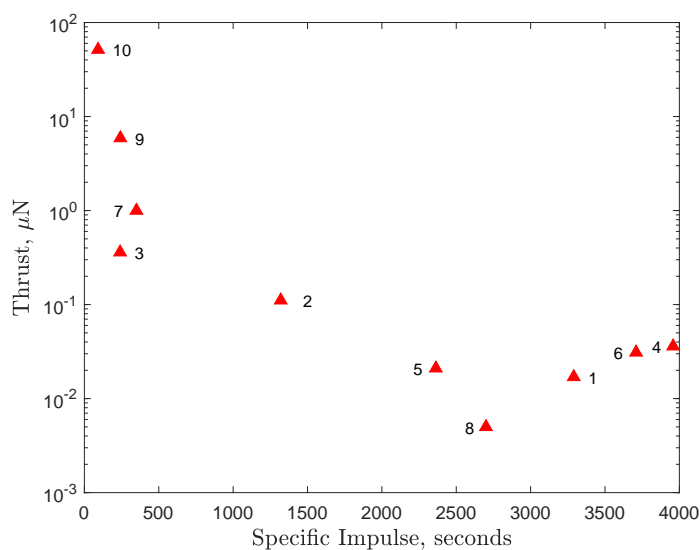


FIGURE 7.1: Performance of different capillary thrusters. The specific impulse, thrust and power are found in Tab. 7.1.

TABLE 7.1: Summary of the thruster parameters from various sources for capillary thrusters.

Point Number	Specific Impulse s	Thrust μN	Power (Current/Voltage) W ($\mu\text{A}/\text{V}$)	Ref.
1	3290	0.017	0.000319 (0.290/1100)	[18]
2	1320	0.111	0.00072 (0.600/1200)	[19]
3	240	0.36	0.00043 (0.227/1900)	[19]
4	3958	0.036	0.00075 (0.500/1500)	[19]
5	2363	0.021	0.00024 (0.345/703)	[20]
6	3709	0.031	0.00055 (0.394/1404)	[20]
7	350	1	0.0054 (6/900)	[21]
8	2700	0.005	0.0083 (7.9/1050)	[21]
9	242	5.9	0.012 (6.82/1752)	[22]
10	92	51.5	0.043 (24.42/1752)	[22]

7.1.2 Externally Wetted Thrusters

The externally wetted thrusters are presented in Figure 7.2, showing a mostly higher specific impulse than capillary emitters. The highest thrust levels of externally wetted thrusters are similar to capillary thrusters. However, specific impulses of over 5000 s can be achieved, as well as most thrusters having a specific impulse higher than 3000 s.

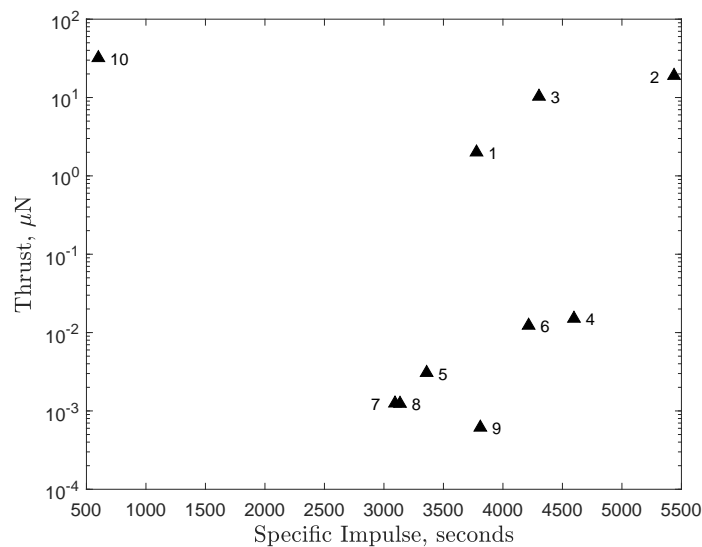


FIGURE 7.2: Performance of different externally wetted thrusters. The specific impulse, thrust and power are found in Tab. 7.2.

TABLE 7.2: Summary of the thruster parameters from various sources for externally wetted thrusters.

Point Number	Specific Impulse s	Thrust μN	Power (Current/Voltage) W ($\mu\text{A}/\text{V}$)	Ref/
1	3728	2	0.05 (36/1400)	[23]
2	5438	19	0.50 (174/2900)	[23]
3	4303	10.3	0.28 (185.7/1500)	[24]
4	4597	0.015	0.0003 (0.151/1844)	[25]
5	3359	0.0045	4.7×10^{-5} (0.045/1045)	[25]
6	4216	0.012	0.0002 (0.135/1729)	[25]
7	3093	0.0013	1.7×10^{-5} (0.0085/1967)	[25]
8	3135	0.0135	1.7×10^{-5} (0.014/1255)	[25]
9	3810	0.0006	1.1×10^{-5} (0.008/- 1432)	[25]
10	600	32	0.28 (200/1400)	[26]

7.1.3 Porous Electropray Thruster

The porous electropray thruster that were reviewed are shown in Figure 7.3. The data show that porous thrusters have had the highest specific impulse and thrust out of any of the other types of emitters. This is likely due to the higher currents emitted by them, which can be found in Tab. 7.3. The thrust and specific impulse values can vary significantly as well, with up to a 7222 s theoretical specific impulse possible. The thrust levels are also the highest, with a thrust of over 100 μN reached with two different thrusters. Porous electropray thrusters are also the most developed, as shown by the number of sources available for comparison.

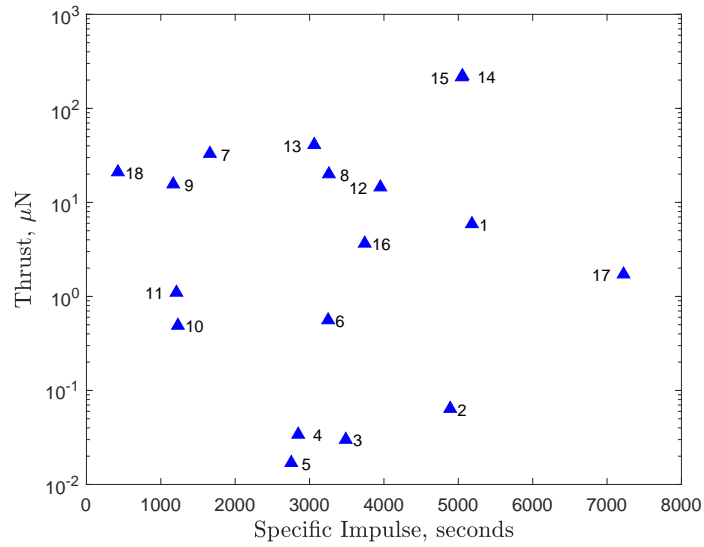


FIGURE 7.3: Performance of different porous thrusters. The specific impulse, thrust and power are found in Tab. 7.3.

TABLE 7.3: Summary of the thruster parameters from various sources for porous thrusters.

Point Number	Specific Impulse (s)	Thrust (μN)	Power (Current/Voltage) W ($\mu\text{A}/\text{V}$)	Ref.
1	5183	5.9	0.16 (66/2350)	[27]
2	4891	0.064	0.0015 (0.696/2200)	[28]
3	3487	0.030	0.00052 (0.237/2200)	[28]
4	2847	0.034	0.00047 (0.214/2200)	[28]
5	2754	0.017	0.00022 (0.102/2200)	[28]
6	3250	0.56	0.014 (5.8/2400)	[29]
7	1660	33	0.48 (240/2000)	[30]
8	3260	20	0.49 (200/2450)	[30]
9	1167	15.6	0.13 (150/865)	[31]
10	1230	0.49	0.0055 (4.4/1260)	[32]
11	1210	1.1	0.013 (9.1/1420)	[32]
12	3952	14.5	0.34 (105/3200)	[33]
13	3063	41	1.29 (700/1840)	[34]
14	5056	221	16.7 (4775/3500)	[35]
15	5047	215	6.00 (1580/3800)	[36]
16	3742	3.66	0.069 (34.7/2000)	[37]
17	7222	1.72	0.036 (12/2983)	[38]
18	423	21	0.11 (145/760)	[39]

References

tocchapterReferences

- [1] D. M. Goebel and I. Katz, *Fundamentals of Electric Propulsion: Ion and Hall Thrusters*. John Wiley & Sons, 2009.
- [2] D. Krejci and P. Lozano, "Space propulsion technology for small spacecraft," *Proceedings of the IEEE*, vol. 106, no. 3, pp. 362–378, 2018.
- [3] G. L. Bennett, "Introduction to space nuclear power and propulsion," *Encyclopedia of Nuclear Energy*. Elsevier, pp. 155–167, 2021.
- [4] M. D. Sambora, "Demonstration rocket for agile cislunar operations (draco)." Accessed: 14/10/2024.
- [5] S. Mazouffre, "Electric propulsion for satellites and spacecraft: established technologies and novel approaches," *Plasma Sources Science and Technology*, vol. 25, no. 3, p. 033002, 2016.
- [6] J. Climer, "Boeing stacks two satellites to launch as a pair." <https://boeing.mediaroom.com/2014-11-12-Boeing-Stacks-Two-Satellites-to-Launch-as-a-Pair>, 2014. Accessed: 05/02/2024.
- [7] D. R. Lev, G. D. Emsellem, and A. K. Hallock, "The rise of the electric age for satellite propulsion," *New Space*, vol. 5, no. 1, pp. 4–14, 2017.
- [8] NASA, "Dawn." Accessed: 25/10/2024, <https://science.nasa.gov/mission/dawn/>.
- [9] I. Levchenko, D. M. Goebel, and K. Bazaka, "Electric propulsion of spacecraft," *Physics Today*, vol. 75, no. 9, pp. 38–44, 2022.

- [10] C. Ryan, "Spacecraft propulsion module lecture notes," 2021. SESA6071: Spacecraft Propulsion, Lecture 2.
- [11] W. G. Seo, J. W. Kuk, H. Kim, D. Kang, and J. Huh, "Micro/nano scale emission tip fabrication for field emission electric propulsion," in *2023 IEEE 22nd International Conference on Micro and Nanotechnology for Power Generation and Energy Conversion Applications (PowerMEMS)*, pp. 252–255, 2023.
- [12] M. Swartwout, "The first one hundred cubesats: A statistical look," *Journal of small Satellites*, vol. 2, no. 2, pp. 213–233, 2013.
- [13] D. Krejci and A. Reissner, "The first 100 FEEP propulsion systems in space: A statistical view and lessons learnt of 4 years of ENPULSION," in *37th International Electric Propulsion Conference*, 2022.
- [14] A. R. Katritzky, R. Jain, A. Lomaka, R. Petrukhin, M. Karelson, A. E. Visser, and R. D. Rogers, "Correlation of the melting points of potential ionic liquids (imidazolium bromides and benzimidazolium bromides) using the codessa program," *Journal of chemical information and computer sciences*, vol. 42, no. 2, pp. 225–231, 2002.
- [15] Y. Guan, Q. Shao, W. Chen, J. Zhang, X. Zhang, and Y. Deng, "Flow-induced voltage generation by driving imidazolium-based ionic liquids over a graphene nano-channel," *Journal of Materials Chemistry A*, vol. 6, no. 25, pp. 11941–11950, 2018.
- [16] C. Larriba, S. Castro, J. Fernandez De La Mora, and P. Lozano, "Monoenergetic source of kilodalton ions from taylor cones of ionic liquids," *Journal of applied physics*, vol. 101, no. 8, 2007.
- [17] J. Iribarne and B. Thomson, "On the evaporation of small ions from charged droplets," *The Journal of chemical physics*, vol. 64, no. 6, pp. 2287–2294, 1976.
- [18] I. Romero-Sanz, R. Bocanegra, J. Fernandez De La Mora, and M. Gamero-Castaño, "Source of heavy molecular ions based on taylor cones of ionic liquids operating in the pure ion evaporation regime," *Journal of Applied Physics*, vol. 94, no. 5, pp. 3599–3605, 2003.

- [19] Y.-H. Chiu, B. L. Austin, R. A. Dressler, D. Levandier, P. T. Murray, P. Lozano, and M. Martinez-Sanchez, "Mass spectrometric analysis of colloid thruster ion emission from selected propellants," *Journal of Propulsion and Power*, vol. 21, no. 3, pp. 416–423, 2005.
- [20] R. Krpoun, *Micromachined electrospray thrusters for spacecraft propulsion*. PhD thesis, EPFL, 2009.
- [21] C. Ryan, A. Daykin-Iliopoulos, J. Stark, A. Salaverri, E. Vargas, P. Rangsten, S. Dandavino, C. Ataman, S. Chakraborty, D. Courtney, *et al.*, "Experimental progress towards the microthrust mems electrospray electric propulsion system," in *33rd International Electric Propulsion Conference*, (Washington, DC, USA), 2013.
- [22] E. Grustan-Gutierrez and M. Gamero-Castaño, "Time-of-flight characterization of a microfabricated electrospray thruster emitter array," in *35th International Electric Propulsion Conference*, (Atlanta, GA, USA), 2017.
- [23] P. Lozano, B. Glass, and M. Martinez-Sanchez, "Performance characteristics of a linear ionic liquid electrospray thruster," in *29th International Electric Propulsion Conference*, vol. 9, (Princeton, NJ, USA), 2005.
- [24] B. L. P. Gassend, *A fully microfabricated two-dimensional electrospray array with applications to space propulsion*. PhD thesis, Massachusetts Institute of Technology, 2007.
- [25] S. Castro, C. Larriba, J. Fernandez de La Mora, P. Lozano, S. Sümer, Y. Yoshida, and G. Saito, "Effect of liquid properties on electrosprays from externally wetted ionic liquid ion sources," *Journal of Applied Physics*, vol. 102, no. 9, 2007.
- [26] D. Villegas, M. Wijnen, S. Correyero, G. Arboleya, and P. Fajardo, "Impact of the propellant temperature on the performance of externally wetted electrospray thrusters," in *37th International Electric Propulsion Conference*, (Boston, MA, USA), 2022.
- [27] R. Legge, P. Lozano, and M. Martinez-Sanchez, "Fabrication and characterization of porous metal emitters for electrospray thrusters," in *30th International Electric Propulsion Conference*, (Florence, Italy), 2007.

- [28] R. Legge and P. Lozano, "Performance of heavy ionic liquids with porous metal electro spray emitters," in *44th AIAA/ASME/SAE/ASEE Joint Propulsion Conference & Exhibit*, (Hartford, CT, USA), p. 5002, 2008.
- [29] D. G. Courtney and P. Lozano, "Characterization of conical ionic liquid ion sources for 2-d electro spray thruster arrays on porous substrates," *Transactions of the Japan Society for Aeronautical and Space Sciences, Aerospace Technology Japan*, vol. 8, no. ists27, pp. Pb_73–Pb_78, 2010.
- [30] D. G. Courtney, S. Dandavino, and H. Shea, "Comparing direct and indirect thrust measurements from passively fed ionic electro spray thrusters," *Journal of Propulsion and Power*, vol. 32, no. 2, pp. 392–407, 2016.
- [31] D. Krejci, F. Mier-Hicks, R. Thomas, T. Haag, and P. Lozano, "Emission characteristics of passively fed electro spray microthrusters with propellant reservoirs," *Journal of Spacecraft and Rockets*, vol. 54, no. 2, pp. 447–458, 2017.
- [32] C. E. Miller, D. Krejci, C. Bates, D. Getty, and P. C. Lozano, "Characterization of EMI-(HF) 2.3 F using carbon xerogel electro spray thrusters," in *The 35th International Electric Propulsion Conference*, (Atlanta, GA, USA), 2017.
- [33] C. Chong, C. Maolin, and Z. Haohao, "Characterization of an ionic liquid electro spray thruster with a porous ceramic emitter," *Plasma Science and Technology*, vol. 22, no. 9, p. 094009, 2020.
- [34] M. Natisin, H. Zamora, W. McGehee, N. Arnold, Z. Holley, M. Holmes, and D. Eckhardt, "Fabrication and characterization of a fully conventionally machined, high-performance porous-media electro spray thruster," *Journal of Micromechanics and Microengineering*, vol. 30, no. 11, p. 115021, 2020.
- [35] C. Ma, T. Bull, and C. N. Ryan, "Plume composition measurements of a high-emission-density electro spray thruster," *Journal of Propulsion and Power*, vol. 37, no. 6, pp. 816–831, 2021.
- [36] J. Hanwu, C. Maolin, L. Xuhui, C. Chong, Z. Haohao, Z. Hao, and H. Zhicong, "Experimental study of a porous electro spray thruster with different number of emitter-strips," *Plasma Science and Technology*, vol. 23, no. 10, p. 104003, 2021.

- [37] Y. Yang, D. Guo, X. Li, L. Deng, B. Che, and M. Cheng, "Development and characterization of a novel porous-media borosilicate glass ion sources for electrospray thruster," *Aerospace*, vol. 8, no. 10, p. 297, 2021.
- [38] A. C. Adduci, J. L. Rovey, C. T. Lyne, Z. R. Putnam, M. F. Lembeck, C. Ma, C. N. Ryan, and S. P. Berg, "Characterization of ionic liquid multimode propellant operating in a porous glass electrospray thruster," in *37th International Electric Propulsion Conference*, (Boston, MA, USA), 2022.
- [39] S. Shaik, O. Jia-Richards, and P. C. Lozano, "Characterization of a single-polarity electrospray propulsion system," in *37th International Electric Propulsion Conference*, (Boston, MA, USA), 2022.
- [40] S. Castro and J. Fernández De La Mora, "Effect of tip curvature on ionic emissions from Taylor cones of ionic liquids from externally wetted tungsten tips," *Journal of Applied Physics*, vol. 105, no. 3, 2009.
- [41] A. Quraishi, S. Dworski, C. Ma, C. N. Ryan, A. Ferreri, G. Vincent, H. Larsen, E. R. Azevedo, E. Dingle, A. Garbayo, M. Vozarova, and E. Neubauer, "Designing and commercialization of porous emitter electrospray thruster for space applications," in *AIAA SCITECH 2023 Forum*, (National Harbor, MD, USA), 2023.
- [42] K. Takagi, R. Tsukizaki, Y. Yamashita, and Y. Takao, "Effects of tip curvature on multiple emitted ion beams in porous ionic liquid electrospray thrusters," in *AIAA SCITECH 2024 Forum*, (Orlando, FL, USA), p. 1346, 2024.
- [43] T. Kerber, H. Sargent, K. Lemmer, and C. Ryan, "Effects of extractor axial position on porous ionic liquid ion source performance," in *37th International Electric Propulsion Conference*, (Cambridge, MA, USA), 2022.
- [44] M. Gamero-Castaño and V. Hruby, "Electrospray as a source of nanoparticles for efficient colloid thrusters," *Journal of Propulsion and Power*, vol. 17, no. 5, pp. 977–987, 2001.
- [45] P. C. Lozano-Tovar, *Studies on the ion-droplet mixed regime in colloid thrusters*. PhD thesis, Massachusetts Institute of Technology, 2003.

- [46] I. G. Loscertales and J. Fernández De La Mora, "Experiments on the kinetics of field evaporation of small ions from droplets," *The Journal of chemical physics*, vol. 103, no. 12, pp. 5041–5060, 1995.
- [47] R. J. Pfeifer and C. D. Hendricks, "Parametric studies of electrohydrodynamic spraying.," *AIAA Journal*, vol. 6, no. 3, pp. 496–502, 1968.
- [48] D. Garoz, C. Bueno, C. Larriba, S. Castro, I. Romero-Sanz, J. Fernandez de La Mora, Y. Yoshida, and G. Saito, "Taylor cones of ionic liquids from capillary tubes as sources of pure ions: The role of surface tension and electrical conductivity," *Journal of Applied Physics*, vol. 102, no. 6, 2007.
- [49] D. Villegas-Prados, J. Cruz, M. Wijnen, P. Fajardo, and J. Navarro-Cavallé, "Emission and performance characterization of ionic liquids for an externally wetted electrospray thruster," *Acta Astronautica*, vol. 219, pp. 97–107, 2024.
- [50] G. I. Taylor, "Disintegration of water drops in an electric field," *Proceedings of the Royal Society of London. Series A. Mathematical and Physical Sciences*, vol. 280, no. 1382, pp. 383–397, 1964.
- [51] J. F. De La Mora and I. G. Loscertales, "The current emitted by highly conducting taylor cones," *Journal of Fluid Mechanics*, vol. 260, pp. 155–184, 1994.
- [52] M. Gamero-Castaño and J. Fernandez De La Mora, "Direct measurement of ion evaporation kinetics from electrified liquid surfaces," *The Journal of Chemical Physics*, vol. 113, no. 2, pp. 815–832, 2000.
- [53] A. Quraishi, S. Dworski, E. Batchelor, A. Gonzalez Machado, C. Ryan, A. Ferreri, G. Vincent, A. Croos, A. Garbayo, M. Vozarova, *et al.*, "Development of a 50 w porous emitter electrospray thruster towards flight," in *74th International Astronautical Congress*, (Baku, Azerbaijan), 2023.
- [54] Busek Co. Inc., "Bet-max." <https://www.busek.com/bet-300p>, 2023. Accessed: 22/01/2024.
- [55] C. Coffman, M. Martínez-Sánchez, F. Higuera, and P. C. Lozano, "Structure of the menisci of leaky dielectric liquids during electrically-assisted evaporation of ions," *Applied Physics Letters*, vol. 109, no. 23, 2016.

- [56] P. W. Atkins, J. De Paula, and J. Keeler, *Atkins' physical chemistry*. Oxford university press, 2006.
- [57] C. Wakai, A. Oleinikova, M. Ott, and H. Weingärtner, "How polar are ionic liquids? determination of the static dielectric constant of an imidazolium-based ionic liquid by microwave dielectric spectroscopy," *The Journal of Physical Chemistry B*, vol. 109, no. 36, pp. 17028–17030, 2005.
- [58] A. Borner, Z. Li, and D. A. Levin, "Modeling of an ionic liquid electrospray using a molecular dynamics model," in *28th International Symposium on Rarefied Gas Dynamics*, vol. 1501, (Zaragoza, Spain), pp. 887–894, American Institute of Physics, 2012.
- [59] F. J. Higuera, "Model of the meniscus of an ionic-liquid ion source," *Physical Review E*, vol. 77, no. 2, p. 026308, 2008.
- [60] M. Tariq, M. G. Freire, B. Saramago, J. A. Coutinho, J. N. C. Lopes, and L. P. N. Rebelo, "Surface tension of ionic liquids and ionic liquid solutions," *Chemical Society Reviews*, vol. 41, no. 2, pp. 829–868, 2012.
- [61] C. B. Whittaker and B. A. Jorns, "Modeling multi-site emission in porous electrosprays resulting from variable electric field and meniscus size," *Journal of Applied Physics*, vol. 134, p. 083301, 08 2023.
- [62] P. L. Wright and R. E. Wirz, "Multiplexed electrospray emission on a porous wedge," *Physics of Fluids*, vol. 33, no. 1, 2021.
- [63] D. G. Courtney and H. Shea, "Influences of porous reservoir laplace pressure on emissions from passively fed ionic liquid electrospray sources," *Applied Physics Letters*, vol. 107, no. 10, 2015.
- [64] C. E. Miller, *Characterization of ion cluster fragmentation in ionic liquid ion sources*. PhD thesis, Massachusetts Institute of Technology, 2019.
- [65] C. E. Miller and P. C. Lozano, "Measurement of the dissociation rates of ion clusters in ionic liquid ion sources," *Applied Physics Letters*, vol. 116, no. 25, 2020.
- [66] E. M. Petro, X. Gallud, S. K. Hampl, M. Schroeder, C. Geiger, and P. C. Lozano, "Multiscale modeling of electrospray ion emission," *Journal of Applied Physics*, vol. 131, no. 19, 2022.

- [67] P. Lozano and M. Martinez-Sanchez, "Ionic liquid ion sources: characterization of externally wetted emitters," *Journal of colloid and interface science*, vol. 282, no. 2, pp. 415–421, 2005.
- [68] E. A. Guggenheim, "The principle of corresponding states," *The Journal of Chemical Physics*, vol. 13, no. 7, pp. 253–261, 1945.
- [69] H. F. Almeida, A. R. R. Teles, J. A. Lopes-da Silva, M. G. Freire, and J. A. Coutinho, "Influence of the anion on the surface tension of 1-ethyl-3-methylimidazolium-based ionic liquids," *The Journal of Chemical Thermodynamics*, vol. 54, pp. 49–54, 2012.
- [70] M. Součková, J. Klomfar, and J. Pátek, "Surface tension of 1-alkyl-3-methylimidazolium based ionic liquids with trifluoromethanesulfonate and tetrafluoroborate anion," *Fluid Phase Equilibria*, vol. 303, no. 2, pp. 184–190, 2011.
- [71] University of Cambridge, Department of Materials Science & Metallurgy, "Effect of temperature on the dielectric constant." <https://www.doitpoms.ac.uk/tlplib/dielectrics/temperature.php>. Accessed: 17/05/2024.
- [72] J. Hunger, A. Stoppa, S. Schrödle, G. Hefter, and R. Buchner, "Temperature dependence of the dielectric properties and dynamics of ionic liquids," *ChemPhysChem*, vol. 10, no. 4, pp. 723–733, 2009.
- [73] R. L. Gardas and J. A. Coutinho, "Extension of the ye and shreeve group contribution method for density estimation of ionic liquids in a wide range of temperatures and pressures," *Fluid Phase Equilibria*, vol. 263, no. 1, pp. 26–32, 2008.
- [74] C. M. Neves, K. A. Kurnia, J. A. Coutinho, I. M. Marrucho, J. N. C. Lopes, M. G. Freire, and L. P. N. Rebelo, "Systematic study of the thermophysical properties of imidazolium-based ionic liquids with cyano-functionalized anions," *The Journal of Physical Chemistry B*, vol. 117, no. 35, pp. 10271–10283, 2013.
- [75] A. Aljasmí, A. S. AlJimaz, K. H. A. E. AlKhalidi, and M. S. Al-Tuwaim, "Dependency of physicochemical properties of imidazolium bis(trifluoromethylsulfonyl)imide-based ionic liquids on temperature and alkyl chain," *Journal of Chemical & Engineering Data*, vol. 67, no. 4, pp. 858–868, 2022.

- [76] E. L. Bennett, C. Song, Y. Huang, and J. Xiao, "Measured relative complex permittivities for multiple series of ionic liquids," *Journal of Molecular Liquids*, vol. 294, p. 111571, 2019.
- [77] P. C. Lozano, "Energy properties of an emi-im ionic liquid ion source," *Journal of Physics D: Applied Physics*, vol. 39, no. 1, p. 126, 2005.
- [78] D. G. Courtney and H. Shea, "Fragmentation in time-of-flight spectrometry-based calculations of ionic electrospray thruster performance," *Journal of Propulsion and Power*, vol. 31, no. 5, pp. 1500–1504, 2015.
- [79] A. Thuppul, A. L. Collins, P. L. Wright, N. M. Uchizono, and R. E. Wirz, "Mass flux and current density distributions of electrospray plumes," *Journal of Applied Physics*, vol. 130, p. 103301, 09 2021.
- [80] S. Dandavino, C. Ataman, C. N. Ryan, S. Chakraborty, D. Courtney, J. P. W. Stark, and H. Shea, "Microfabricated electrospray emitter arrays with integrated extractor and accelerator electrodes for the propulsion of small spacecraft," *Journal of Micromechanics and Microengineering*, vol. 24, p. 075011, jun 2014.
- [81] M. R. Natisin, H. L. Zamora, Z. A. Holley, N. Ivan Arnold, W. A. McGehee, M. R. Holmes, and D. Eckhardt, "Efficiency mechanisms in porous-media electrospray thrusters," *Journal of Propulsion and Power*, vol. 37, no. 5, pp. 650–659, 2021.
- [82] C. Ma, *Design and characterisation of electrospray thrusters with high emission density*. PhD thesis, University of Southampton, Department of Aeronautical and Astronautical Engineering, 2020.
- [83] M. Klosterman, J. Rovey, and D. A. Levin, "Ion-induced electron emission from emim-bf₄ electrospray plume-surface interactions," in *AIAA SCITECH 2021 Forum*, (Virtual), p. 1975, 2021.
- [84] Y. Azziz, *Experimental and theoretical characterization of a Hall thruster plume*. PhD thesis, Massachusetts Institute of Technology, 2007.
- [85] P. R. Vlasak, D. J. Beussman, M. R. Davenport, and C. G. Enke, "An interleaved comb ion deflection gate for m/z selection in time-of-flight mass spectrometry," *Review of scientific instruments*, vol. 67, no. 1, pp. 68–72, 1996.

- [86] R. A. Dressler, B. St. Peter, Y.-H. Chiu, and T. Fedkiw, "Multiple emission sites on porous glass electrospray propulsion emitters using dielectric propellants," *Journal of Propulsion and Power*, vol. 38, no. 5, pp. 809–821, 2022.
- [87] C. Guerra-Garcia, D. Krejci, and P. Lozano, "Spatial uniformity of the current emitted by an array of passively fed electrospray porous emitters," *Journal of Physics D: Applied Physics*, vol. 49, no. 11, p. 115503, 2016.
- [88] G. W. Goodrich and W. C. Wiley, "Continuous Channel Electron Multiplier," *Review of Scientific Instruments*, vol. 33, pp. 761–762, 07 1962.
- [89] N. Turan, C. Ma, and C. N. Ryan, "Optical emission characterization of a single emitter electrospray thruster interacting with surfaces," in *AIAA SCITECH 2023 Forum*, (National Harbor, MD, USA), p. 1409, 2023.
- [90] S. Dworski and C. N. Ryan, "Investigating the ions emitted by multiply charged ionic liquids from a porous electrospray ion source," *Journal of Applied Physics*, vol. 136, p. 133301, 10 2024.
- [91] S. Dworski and C. Ryan, "Analysis of plumes produced by novel ionic liquids in electrospray thrusters," in *38th International Electric Propulsion Conference*, 2024.
- [92] F. Yang, B. Wang, Y. Jiao, H. Tan, and X. Wang, "Density and viscosity of three ionic liquids with 2, 2, 2-trifluoroethanol," *The Journal of Chemical Thermodynamics*, vol. 181, p. 107038, 2023.
- [93] Y. Yoshida and G. Saito, "Influence of structural variations in 1-alkyl-3-methylimidazolium cation and tetrahalogenoferrate (iii) anion on the physical properties of the paramagnetic ionic liquids," *Journal of Materials Chemistry*, vol. 16, no. 13, pp. 1254–1262, 2006.
- [94] K. Matsumoto, R. Hagiwara, R. Yoshida, Y. Ito, Z. Mazej, P. Benkič, B. Žemva, O. Tamada, H. Yoshino, and S. Matsubara, "Syntheses, structures and properties of 1-ethyl-3-methylimidazolium salts of fluorocomplex anions," *Dalton Transactions*, no. 1, pp. 144–149, 2004.
- [95] M. Geppert-Rybczynska, J. K. Lehmann, T. Peppel, M. Kockerling, and A. Heintz, "Studies of physicochemical and thermodynamic properties of the paramagnetic 1-alkyl-3-methylimidazolium ionic liquids (emim) 2 [co (ncs) 4] and (bmim) 2 [co

- (ncs) 4],” *Journal of Chemical & Engineering Data*, vol. 55, no. 12, pp. 5534–5538, 2010.
- [96] M. Chakraborty, S. Barik, A. Mahapatra, and M. Sarkar, “Effect of lithium-ion on the structural organization of monocationic and dicationic ionic liquids,” *The Journal of Physical Chemistry B*, vol. 125, no. 47, pp. 13015–13026, 2021.
- [97] X. Gallud and P. C. Lozano, “The limited effect of electric conductivity on the ion current evaporated from electrospray sources,” *arXiv preprint arXiv:2305.14714*, 2023. Unpublished.
- [98] T. V. Kerber, “Development of a single emitter ionic liquid ion source research platform,” Master’s Thesis, Western Michigan University, 2020.
- [99] C. E. Miller, “Characterization of ion cluster dissociation in ion electrospray thrusters using time of flight mass spectrometry,” in *37th International Electric Propulsion Conference*, (Boston, MA, USA), 2022.
- [100] Professor Patricia Hunt. “Personal Communication”. Victoria University of Wellington, July 2024.
- [101] M. Gamero-Castano and J. F. De La Mora, “Mechanisms of electrospray ionization of singly and multiply charged salt clusters,” *Analytica Chimica Acta*, vol. 406, no. 1, pp. 67–91, 2000.
- [102] N. V. Plechkova and K. R. Seddon, *Ionic liquids completely uncoiled: Critical expert overviews*. John Wiley & Sons, 2015.
- [103] N. Turan, S. Dworski, and C. Ryan, “Investigation of cation and anion emission mechanisms from porous electrospray thrusters using ionic liquid mixtures,” in *38th International Electric Propulsion Conference*, (Toulouse, France), 2024.
- [104] H. Zarei and V. Keley, “Density and speed of sound of binary mixtures of ionic liquid 1-ethyl-3-methylimidazolium tetrafluoroborate, n,n-dimethylformamide, and n,n-dimethylacetamide at temperature range of 293.15–343.15 k: Measurement and pc-saft modeling,” *Journal of Chemical & Engineering Data*, vol. 62, no. 3, pp. 913–923, 2017.

-
- [105] Y. Zhang, P. Yu, and Y. Luo, "Absorption of CO₂ by amino acid-functionalized and traditional dicationic ionic liquids: Properties, Henry's law constants and mechanisms," *Chemical Engineering Journal*, vol. 214, pp. 355–363, 2013.
- [106] M. Caballero-Pérez and M. Gamero-Castano, "Increasing specific impulse in electrospray devices through emitter design," in *38th International Electric Propulsion Conference*, 2024.
- [107] C. S. Perez Martinez, *Engineering ionic liquid ion sources for ion beam applications*. PhD thesis, Massachusetts Institute of Technology, 2016.
- [108] O. Jia-Richards, "Quantification of ionic-liquid ion source beam composition from time-of-flight data," *Journal of Applied Physics*, vol. 132, p. 074501, 08 2022.